Demonstrating the use of Multiple Experimental Techniques to Investigate Helium-Hydrogen Synergies in Tungsten

A Dissertation Presented for the

Doctor of Philosophy

Degree

The University of Tennessee, Knoxville

Wendy A. Garcia

August 2022

Dedication

I dedicate this work to my cat Mitzi, as well as first generation immigrants and first generation college students who all are pursuing an education despite the hardships and sacrifices it entails.

Acknowledgements

I would like to thank all of those that formed a part of my life and career in the last six years starting with Dr. Brian D. Wirth who from the very beginning saw my potential and never stopped believing in me. He has been the best mentor I could have asked for as he has guided me not only academically but career wise and in personal life matters. My research and PhD coursework completion was possible because of him and for that I will forever be grateful.

I would like to thank Dr. David C. Donovan for always being open to answering questions, and teaching even if I was no longer taking his classes. Likewise, Dr. Steven J. Zinkle, who has been ever so kind with me taking his time to explain concepts, and questions outside of class. Dr. Lang who pushed me in the very beginning when I doubted myself and my abilities to continue the PhD. Finally, Dr. William J. Weber who very willingly and happily accepted to form part of my PhD committee, thank you for your disposition and enthusiasm.

In addition to my UTK professors, many people from ORNL highly contributed and made possible my research and the completion of my PhD. I would like to thank Dr. Xunxiang Hu who always supported me and was essentially my mentor at ORNL even though that was not his official title nor responsibility. He always financed any materials I needed at ORNL without any hesitation and was always open and willing to share knowledge and in lab skills with me. I would also like to single out and thank Dr. Ezekial Unterberg who was always ever so patient with me answering all my hundreds of questions. He always had an open door policy for me to pop in and exchange ideas with him. Thanks to him I have gained a tremendous amount of knowledge on LIBS and as a result I feel very confident in my LIBS knowledge, abilities, and skills to continue employing them in my future job. I would like to thank and acknowledge Charles (Chuck) Schaich, and Thomas (Tom) Muth who were

instrumental in the development of the permeation system and always had an open door or email system for me to run in and exchange ideas with them. Travis Dixon who prioritized my work within all the samples entrusted to him and always expedited mine understanding the time crunch I was under. Chad Parish who analyzed many of my samples helping me realize the extent of my experiments success and sharing that success with me as well as always expediting my samples with the best disposition and enthusiasm. I would like to thank Dr. Weicheng Zhong who essentially took over Dr. Hu's position and became my biggest support at ORNL after Dr. Hu left. Thank you for backing all of my projects and entrusting me with my knowledge of the lab. Last but not least I would like to thank Ze Chen who shared with me his knowledge of permeation systems and experiments and helped become proficient enough to conduct my own permeation experiments and data analysis.

I would like to thank all my friends and the friendships found and developed during these 6 years. They became my little Knoxville family and a home away from my hometown. To Jason Rizk for always being my biggest cheerleader and closest friend in Knoxville, Jose March-Rico for always being the light of reason and encouragement, Dasgupta Dwaipayan for believing in me and valuing me as a scientist, Li Yang for her many laughs, goofy moments spent together, her close friendship and belief in me, Robin Rhodea for her friendship, pure optimism and outlook on life as well as our shared love of cats, Kirtan Davda for teaching me everything that goes on behind the curtain of LIBS and electronic diagnostics, his friendship and eternal patience with questions regarding the filterscope system, Shawn Zamperini for his friendship and constant party mood to go about the town an form memories of a lifetime, Ryan Sweet for his optimism and support within the research group, David Martin for his support and helping me with my transition from a physics only background to nuclear engineering courses, Andrew Payant for his optimism, friendship, and keeping in contact through the years even after leaving Knoxville two years into my PhD, David Sikorski for the many laugh filled moments,

Sassy Ann's dancing, and his support during the early years of grad school, Devon Drey for his friendship and kindness, Payson Dieffenbach for his friendship and many memories together, Guinevere Shaw for sharing all of her in lab knowledge with me and always being open to conversation and answering questions.

I would also like to thank my family present during these 6 years if even from afar. My mom making my life better however she could even if by sending care packages not only to me but to my cat as well, thank you mom. To my best friend Lizette thank you manta for always being there for me regardless of distance and time. Finally, but certainly not least of all I would like to thank my three pets Mitzi, Tinker, Daisy. Mitzi who has been a constant light in my life waking up every morning and walking straight to the desk ready to work as well as spending many late nights up with me studying. Tinker who I only knew for a short one year but she meant the world to me, and to Daisy who helped me immensely with Tinker's passing and to continue pushing in the last steps of my PhD where it seemed so close yet so far.

Thank you to all who formed a part of my life during these 6 years and helped in any way, shape, or form, to complete such a milestone of a lifetime.

Abstract

Tungsten (W) is the leading candidate for plasma facing materials in future fusion reactors and the divertor material in ITER, will face a challenging environment during reactor operation. W will be subject to an intensive flux of particles (hydrogen (H) isotopes, helium (He), and 14 MeV neutrons) as well as high heat flux. As a result, W will experience He bubble formation, displacement damage surface erosion, and impurity deposition all of which can influence H isotope recycling and retention. A key concern for the W divertor is H isotope retention and permeation, influenced by the near surface formation of He bubbles. Therefore, understanding He - H isotope synergies in W, is crucial to further the development of fusion reactors.

Polycrystalline W sample discs measuring 6 mm by 0.5 mm have been exposed to a low energy (70 eV) He plasma using a low flux (1.3×10^{17}He m^{-2} s^{-1}) [1.3 times 10 to the 17 He per meter squared per second] ECR source located at the University of Tennessee, followed by material characterization and gas-driven deuterium permeation. The samples were exposed to three different He fluences ($5 \times 10^{19} He\ m^{-2},\ 5 \times 10^{20} He\ m^{-2}, and\ 5 \times 10^{21} He\ m^{-2}$) [5 times 10 to the 19 He per meter squared, 5 times 10 to the 20 He per meter squared, 5 times 10 to the 21 He per meter squared] at surface temperatures of ~300, 600 and 900 K. These He fluences and temperatures provide a systematic study to evaluate the deuterium permeation behavior in W, as a function of He fluence and sample surface temperature. Laser-Induced Breakdown Spectroscopy (LIBS) and Laser Ablation Mass Spectrometry (LAMS) experiments were subsequently performed to determine the spatial depth and quantity of He present within the W. Deuterium was introduced into W using the gas permeation system located in the Low Activation Materials Development and Analysis (LAMDA) at Oak Ridge National Laboratory (ORNL). LIBS/LAMS experiments were then performed again, to determine the location and quantity of deuterium and He, and to construct spatial profiles of deuterium and He within W. The results of these experiments provide insight into existing synergies between H and He in W and the effects of He fluence and W surface temperature on deuterium retention and permeation.

Table of Contents

Chapter 1 Introduction and Motivation 1

1.1 History and Projection of Energy Consumption 1

1.2 Renewable Energy Sources 3

1.3 Fusion Energy 4

1.4 Tritium in Fusion 7

1.4.1 Tritium Sources and Production 7

1.5 Helium Sources in Fusion 9

1.5.1 Computational Evidence of H-He Synergies 10

1.5.2 Experimental Evidence of H-He Synergies in W 10

1.6 Motivation and Objective 19

Chapter 2 Characterization of the ECR Plasma Source 25

2.1 Initial Flux Measurements Taken by a Faraday Cup 26

2.2 Testing the System Against SPECS Standards 27

2.2.1 Chamber Pressure Effect on Plasma 27

2.2.2 Magnetron Current Effect on Plasma 29

2.2.3 Anode Voltage Effect on Plasma 33

2.2.4 Extractor Voltage Effect on Plasma 37

2.3 Ion Energy Readings Performed by a Retarding Field Energy Analyzer (RFEA) 39

2.3.1 Grid Biasing and Voltage Sweeping of the Retarding Field Grid 41

2.3.2 Finding Argon Plasma Ion Energy Peaks as Proof of Method 42

2.3.3 Finding Helium Plasma Ion Energy Peaks 46

2.4 Testing the Temperature Stage 50

Chapter 3 He Plasma Exposures 55

3.1 Loading Stage Design 55

3.2 Sample Preparation 55

3.3 Sample Loading 57
3.4 He Plasma Sparking Conditions and Parameters 58
3.5 Reading He Flux Measurements and Total Fluence 60
Chapter 4 LIBS and LAMS Measurements of Plasma Exposed Tungsten 61
4.1 A Brief Description of LIBS and LAMS 61
4.2 Our LIBS/LAMS System 62
4.3 Preliminary System Testing 65
4.4 LIBS/LAMS Calibrations 67
4.4.1 LIBS Gain Calibration 67
4.4.2 LIBS Absolute Calibration 71
4.4.3 LAMS Standard Leak Calibration 79
4.5 Crater Volume Analysis 83
4.5.1 Volume Analysis Algorithm Correction 83
4.5.2 D Prime (Pseudo Diameter) Derivation 86
4.6 SRIM Implantation Profile Correction 94
4.6.1 SRIM Profile Implementation 94
4.6.2 Addressing the Heat Affected Zone in Future Experiments 96
4.7 Benchmarking LIBS/LAMS 96
4.7.1 Top Hat LIBS Data Using Updated Volume Correction Algorithm 98
4.7.2 LAMS Comparison to Cluster Dynamics Experiments Results 100
Chapter 5 Permeability Measurements of Hydrogen Isotope 102
5.1 Gas Permeability in Metals 102
5.1.1 Arrhenius Dependence 103
5.2 Comparison of Permeability Literature 107
5.3 Permeation System 110
5.3.1 Standard Leak Calibration 114
5.3.2 High Temperature Permeability System Design 114
5.4 Permeability Experimental Methods 119

5.5 Preliminary High Temperature System Testing 121
5.6 Permeability Summary 123
Chapter 6 SEM, Permeability, and LIBS/LAMS measurements of He-plasma exposed Tungsten: pre and post permeation 124
6.1 SEM Evidence of Successful He Exposure 124
6.2 LAMS Measurements for He Exposed Samples 126
6.3 LIBS Plasma Plume Evolution as a Function of He 128
6.4 Permeability Results 134
6.5 Post-permeation LAMS Results 138
6.6 LIBS/LAMS, Permeability Results Summary 143
Chapter 7 WEST Samples 146
7.1 Experimental Setup at WEST 146
7.2 SEM Analysis 147
7.3 LIBS/LAMS Experiment Details 147
7.3.1 SEM Evidence of Heat Affected Zone through W and O filters 149
7.3.2 LIBS Qualitative Assessment of Oxide Layer and Content 151
7.4 LAMS Measured He content 153
7.5 LIBS Plasma Plume Evolution as a Function of He 155
7.6 WEST C4 Campaign LAMS Summary 159
Chapter 8 DIIID 160
8.1 Experiment Details 160
8.1.1 PISCES and DIII-D Exposures 160
8.2 ERDA Results 162
8.3 PISCES DIII-D LAMS He and H Results 164
8.3.1 PISCES DIII-D LAMS H Results 167
8.4 Comparison of ERDA and LAMS He Results 168
8.5 PISCES-DIIID Exposures Summary 173
Chapter 9 Summary and Future Work 175

9.1 Summary 175
9.2 Future work 177
9.2.1 Continued work on He-D synergies 177
9.2.2 Characterizing plasma plume evolution in future experiments .. 178
9.2.3 Nanosecond vs Femtosecond Laser Ablations 180
List of References 183
Appendix 189
Vita 193

List of Tables

Table 1-1. Experimental parameters used for the design and development of He bubble networks in W for the study of He-H synergies in fusion relevant environments. 24
Table 5-1 Parameters and experimental conditions for Hydrogen permeability in tungsten as a function of temperature, as reproduced in Ref [9] 109
Table 8-1 PISCES-A (He) and DIII-D (D) exposure conditions, as reproduced from Ref. [8] 161
Table 8-2 Sample specific exposure conditions and their identification labels, as reproduced from Ref. [2] 161
Table 8-3 161
Table 8-4 ERDA measured He content in atoms cm^{-2} units compared against first ablation LAMS He content measurements in atoms cm^{-2} and appm. 169

List of Figures

Figure 1.1. History of energy consumption as a function of the energy sources used such as petroleum, natural gas, coal, nuclear, biomass, renewables, and hydroelectric, as reproduced from Ref. [11]. 2

Figure 1.2. Historical and projected worldwide energy use as a function of the energy sources such as petroleum, natural gas, coal, renewables, and nuclear, as reproduced from Ref. [4]. 2

Figure 1.3. Schematic illustration of the three types of fusion reactions considered for fusion reactors, as reproduced from Ref. [6]. 6

Figure 1.4. Cross sections for the fusion reactions considered in fusion energy production. The yellow line marks the temperature at which the ITER reactor will operate at, as reproduced from Ref. [10]. 6

Figure 1.5. Depiction of physical processes in plasma facing components as a results of large ion flux, as reproduced from Ref. [15]. 8

Figure 1.6. Atomistic configurations of a high pressure 2 nm diameter He bubble with H initially placed at the center of it, as reproduced from Ref. [12]. H atoms are shown to move towards the periphery of the bubble as the simulation time increases. 11

Figure 1.7. MD simulations of H distribution in a 3 He/V and 0.5 H/V bubble in W(111) at 1800K, as reproduced from Ref. [12]. H atoms start inside the bubble and quickly after migrate to the outer periphery. 12

Figure 1.8. TDS spectra of ITER grade polycrystalline W exposed to pure Deuterium plasma and a combination plasma consisting of 10%He-90%D, as reproduced from Ref. [17]. 13

Figure 1.9. Integrated Deuterium retention values as a function of temperature. Calculations performed for both pure D plasma and He-seeded D plasma, as

reproduced from Ref. [17]. Higher D retention is observed for the pure D plasma while lower D retention is observed for the He-seeded D plasma..... 15
Figure 1.10. NRA measurements for D only vs 5%He seeded D plasma. Deeper permeation of D is mitigated in the presence of the He seeded plasma, while D retention increases linearly as a function of fluence in the D only case, as reproduced from Ref. [18]. 16
Figure 1.11. Reduction of D permeation in Was a function of increasing He fluence and temperature for 3keV He irradiation as reproduced by Ref.[19]. 18
Figure 1.12. Evidence of saturation in reduction of D permeation in W as a function of increasing He fluence and temperature for 3keV He irradiation as reproduced from Ref. [19]..... 18
Figure 1.13. Experimental matrix of dissertation work. An array of fluences are used in combination with temperatures to design and control the He bubble layer formation within W..... 21
Figure 2.1. SPECS ECR source measured beam current as a function of chamber pressure as reproduced from Ref. [1]. 28
Figure 2.2. University of Tennessee ECR source He plasma flux dependence on chamber pressure..... 28
Figure 2.3. University of Tennessee ECR source flux dependence on magnetron current. 30
Figure 2.4. SPECS measured beam current as a function of magnetron current as reproduced from Ref. [1]. 32
Figure 2.5. University of Tennessee ECR source flux dependence as a function of current and anode voltage. 34
Figure 2.6. SPECS ECR source measured beam current as a function of anode voltage reproduced from Ref. [1]. 36
Figure 2.7. SPECS ECR source measured beam current as a function of extractor grid voltage reproduced from Ref. [1]. 38

Figure 2.8. Diagram of an RFEA plasma diagnostic used to read current and identify the plasma ion energy peak as reproduced from Ref. [16]. 40
Figure 2.9. Retarding grid voltage sweeps, from 0V to 80V and back down from 80V to 0V, that plot the measured current versus time for five different argon plasmas. 43
Figure 2.10. Data and best fit curves for the current versus voltage for five anode voltage dependent argon plasmas. Each data point represents a voltage dependent current average over 30 data points. 45
Figure 2.11. Ar plasma ion energy peaks found during the upwards voltage sweep from 0 V to 80. V. 47
Figure 2.12. Ar plasma ion energy peaks found during the downwards voltage sweep from 0 V to 80 V. 47
Figure 2.13. Retarding grid voltage sweeps, from 0 V to 80 V and back down from 80 V to 0 V, that plot the measured current versus time for seven different helium plasmas. 49
Figure 2.14. Data and best fit curves for the current versus voltage for seven anode voltage dependent helium plasmas. Each data point represents a voltage dependent current average over 30 data points. 51
Figure 2.15. He plasma ion energy peaks found during the upwards voltage sweep from 0 V to 80 V. 52
Figure 2.16. He plasma ion energy peaks found during the downwards voltage sweep from 0 V to 80 V. 52
Figure 2.17. Temperature versus current measurements from two heating element tests performed for temperature increments of 0 to 650°C (Red) and 0 to 100°C(Green). 53
Figure 3.1. Sample holder BN plate design showing the lip cutout and the throughput holes for the thermocouple and heating element rods. All units are shown in inches. 56

Figure 4.1. Picture of the LIBS and LAMS system found at ORNL. Some of the components are shown in the colored circles for easier identification of them. The turbo pump is shown in green, the light collecting optics in blue, the laser in red, and the QMS in yellow[3]. Image modified from reference [3]..... 63
Figure 4.2 Diagram showing the main components pertaining to the LIBS LAMS system located at ORNL in the LAMDA lab[3]..... 64
Figure 4.3. Plots showing the crater depth dependence on number of ablations(left) and the crater width dependence on number of ablations(right). Both are fir with polynomials to interpolate values between 10, 15, and 20, as reproduced from Ref. [3]. 66
Figure 4.4. Excel sheet recording of every shot taken during the 2021 Gain calibration of the ORNL filterscope. 69
Figure 4.5. ORNL filterscope Tube 2 output plots produced from executing the fscope_gain_calibration.py main function. Polynomial fit coefficients shown in the first plot (top). 70
Figure 4.6. QMS output during calibration of the LAMS system performed on February 4th 2022. 80
Figure 4.7. Diagram demonstrating the shape of a crater by averaging over 3 shapes, cylinder, cone, and truncated cone, of the same dimensional proportions, as reproduced from Ref.[3]. 84
Figure 4.8. Visual representation of the volume analysis for the three different shapes (cylinder, cone, and truncated cone) to be used in creating the final shape that most closely resembles that of the ablation induced crater. 84
Figure 4.9 Depiction of four accumulated ablations for the truncated cone crater shape approximation. 87
Figure 4.10 Graphics showing the derivation of intermediate diameter found at level 1 for the second ablation crater. Figure a) showsthe geometrical relationship

between crater 1 and two. Figure b) shows the trigonometry formulas needed for derivations of d' (intermediate diameter). 89
Figure 4.11 Diagrams showing the removed volume (at different levels) as a result of the 3rd consecutive ablation. Additionally, intermediate diameters are shown to demonstrate the need for them and how they are useful in volume calculations. 92
Figure 4.12 Demonstration of the volume removed by the 3rd ablation, found by summing all the blue shaded regions. 93
Figure 4.13. Diagram showing the linear and near surface concentration profiles alongside the truncated cone representation of a crater. Linear profile as reproduced from Ref. [3] 95
Figure 4.14. Results from LIBS, LAMS, and ERDA experiments performed by Dr. Shaw on a W flat top sample to benchmark the LIBS/LAMS system depth profiling characterization abilities. Good agreement is seen amongst all four data sets, as reproduced from Ref. [3]. 97
Figure 4.15. LIBS results for Dr. Shaw's flat top sample used to initially benchmark the LIBS-LAMS systems. Profile is composed over the average of seven different spots ablated to ten cumulative ablations. 99
Figure 4.16. LAMS and Cluster Dynamics result for He implanted and annealed PCW samples. Good agreement is seen between the predicted SRIM depth dependence profile and the implanted He results. Agreement for a reduced magnitude of the annealed curve is also evident amongst LAMS and cluster dynamics results. 101
Figure 5.1 Permeation data for Eurofer 97 steel, showing a linear relationship between the steady state permeation flux and the square root of the upstream gas pressure. Permeability measurements for performed for 5 temperatures shown from bottom to top 350°C (brown), 400°C (blue), 450°C (red), 500°C (magenta), 550°C (green), as reproduced from Ref. [7]. 104

Figure 5.2 Arrhenius plot of tritium permeability in polycrystalline W. Permeability measurements performed at 573K, 623K, 673K, 723K, 773K, 823K, and 873K at 100Pa HT gas pressures. As reproduced from Ref. [9]. 106
Figure 5.3 Comparison of Hydrogen isotope permeability in tungsten as function of sample type (tungsten tubes, rolled sintered tungsten rods, tungsten discs), permeability experiments(gas-driven permeation, gas desorption/evolution, isovolumetric gas-phase desorption), and temperatures (555K - 1666K), as reproduced from Ref [9] 108
Figure 5.4 Gas driven permeation system for deuterium permeability in structural materials, or tungsten, analysis. Located in the Low Activation Materials Design and Analysis at Oak Ridge National Lab. 111
Figure 5.5 Diagram showing all the essential upstream, sample heating, and downstream components of our permeability system. The standard leak calibration system is also included in the diagram even though it is only used when calibrating the system and not as a part of every permeability experiment. 113
Figure 5.6 Permeation system component found within the heating source. The two inconel flanges hold the sample of interes, copper gaskets, and the inconel C-rings. Image rendered by Thomas Muth Sr. Scientist at ORNL..... 116
Figure 5.7 Side and top view of Inconel C-rings. Outer diameter is equatl to 0.242 inches (06.15mm). Inner diameter is equal to 0.147 inches (03.73 mm). 118
Figure 5.8 High temperature permeation system component showing the inconel tubes welded onto the flange. During this work, the system is surrounded by a quartz tube (8) to hold argon shown in purble. 118
Figure 5.9 Deuterium in Eurofer 97 permeability measurements performed at 350°C, 400°C, 450°C, 500°C, 550°C, and at four different pressures within each temprature regime. As reproduced from Ref [7]. 120

Figure 5.10 Permeation flux vs the square root of the upstream pressure plot (left) showing a clear linear relationship. Deuterium in Tungsten permeability data plotted against previous works within the same temperature regime (right). 122
Figure 6.1 SEM images produced by Chad Parish showing the He induced W surface damage. 125
Figure 6.2 LAMS results for all UTK He plasma exposed W samples. Plots arranged in order of increasing temperature and fluence. 127
Figure 6.3 Raw voltage signal plotted as a function of LAMS quantified, He in appm. Observable inverse relationship between raw voltage signals and He content. 129
Figure 6.4 Adjusted LIBS calculated He appm to equivalate LAMS He appm by changing the size of the plasma plume cross section. 131
Figure 6.5 Ratio of calculated LAMS He content to LIBS calculated He content while plasma plume size remained unchanged. 133
Figure 6.6 Permeation flux to square root of upstream deuterium pressure plots showing the expected linear relationship for steady state permeation. 135
Figure 6.7 Arrhenius dependence shown for all work alongside Dr. Hu's work. The data has been normalized for direct comparison between all works. 137
Figure 6.8 Post-permeation LIBS/LAMS measurements for UTK He exposed samples. He quantities in appm (left), D quantities in appm (right). Reference sample results (top), 5E19 He m^{-2} 900 K results (bottom). 139
Figure 6.9 Post-permeation LIBS/LAMS measurements for UTK He exposed samples. He quantities in appm (left), D quantities in appm (right). 5E20 He m^{-2} 900 K sample results (top), 5E21 He m^{-2} 900 K results (bottom). 140
Figure 6.10 Pre and post permeation LAMS measured He content for first ablations a) and sum of first three ablations b), as a function of He plasma exposure fluences. Results shown for a Reference sample, 5E19 He m^{-2} 900 K, 5E20 He m^{-2} 900 K, and 5E21 He m^{-2} 900 K exposed samples. 142

Figure 6.11 First ablation and third ablation LAMS measured D content, as a function of He plasma exposure fluences, for a Reference sample, and 5E19 He m^{-2} 900 K, 5E20 He m^{-2} 900 K, and 5E21 He m^{-2} 900 K exposed samples. 144
Figure 7.1 SEM and STEM image produced by Chad Parish for the R1 WEST C4 campaign sample. Surface characterization shows evidence of 'coral' type surface features and a 70-100 nm oxide capping layer. 148
Figure 7.2 SEM images produced by Chad Parish using a W filter (a) and an O filter (right). Image c) and d) are zoomed in images of a) and b), respectively. 150
Figure 7.3 Relative O signals (red) as a function of consecutive ablations (left to right). The W signals are shown in balck and the He signals are shown in an array of rainbow colors near 1E17 ph/s-str-m^2 152
Figure 7.4 LAMS measured He content and depth dependent profiles for R1 (left, R2 (middle), and R3 (right). 154
Figure 7.5 LIBS plasma plume analysis as a function of He content for the three WEST samples and a reference W sample. 156
Figure 7.6 Comparison of LIBS plasma plume volume evolution for UTK He plasma source exposures and WEST He exposures. 158
Figure 8.1 He content in W samples as a function of W temperature for PISCES, DIII-D H mode and L mode, as reproduced from Ref. [5] 163
Figure 8.2 ERDA results of PISCES-DIII-D W sample exposures alongside He concentration profiles demonstrating the location of implanted He layer, as reproduced from Ref. [5] 163
Figure 8.3 LAMS results for PISCES samples exposed at 800 K. 165
Figure 8.4 LAMS results for PISCES examples exposed at 600 K. 165
Figure 8.5 LAMS results for the reference sample and samples not exposed in PISCES, only DIII-D. 166
Figure 8.6 LAMS vs ERDA measurements showing degree of agreement. Dotted line is representative of a perfect one to one relationship. 171

Figure 8.7 PISCES-DIII-D LAMS measured He content integrated over the first three ablations. 172
Figure 9.1 All the LAMS analysis results in this dissertation work plotted as a function of He fluence during exposures. Specific data sources include UTK exposures, PISCES - DIII-D, WEST C4 campaign, and 10 keV He exposures. 176
Figure 9.2 ICCD camera resolved images of plasma plume evolution. Top images a) evolution of fs laser ablation produced plasma plume. Bottom images b) evolution of ns laser ablation produced plasma plume. Figure reproduced from Ref. [13] 179
Figure 9.3 LPP images taken by an ICCD camera showing the difference in plasma formation for a ns vs a fs laser. Next to them are the corresponding AFM produced images of the surface morphology and topography. Ref [14], [20](Unpublished) 181

Chapter 1

Introduction and Motivation

1.1 History and Projection of Energy Consumption

Energy consumption in the United States has continued to steadily increase throughout the years with a record high demand of 101 quadrillion (3E13 kilowatt-hours) reached in 2018. Current and projected energy consumption [11] is shown in Figure 1.1. A clear increase in energy consumption occurred in the early 1900's following the invention of electricity making energy obtainable. A second sharp increase was observed during the mid-1900's due to the second industrial revolution, which is also referred to as the Technological revolution. As well, there is evidence of a strong correlation between energy consumption and social economic growth [21].

Figure 1.2 shows the history and projected energy consumption based on the type of energy source [11]. The U.S. Energy Information Administration (EIA) projects that worldwide energy consumption will see a 50% increase by the year 2050 [22]. Countries that are not part of the Organization for Economic Cooperation and Development (OECD) are the largest contributors to the expected increase in energy demand and consumption. The majority of that economic growth is anticipated to occur in Asia due to its rapid development. Petroleum is still projected to be the largest energy source followed by non-renewable and carbon-emitting sources such as natural gas and coal. These are all contributors to the emission of greenhouse gases into the atmosphere [23]; and thus, an increase in renewable energy sources is expected. Nuclear energy is projected to be the smallest contributor of energy sources due to poor public perception of fission produced nuclear energy, in addition to very high capital costs [24].

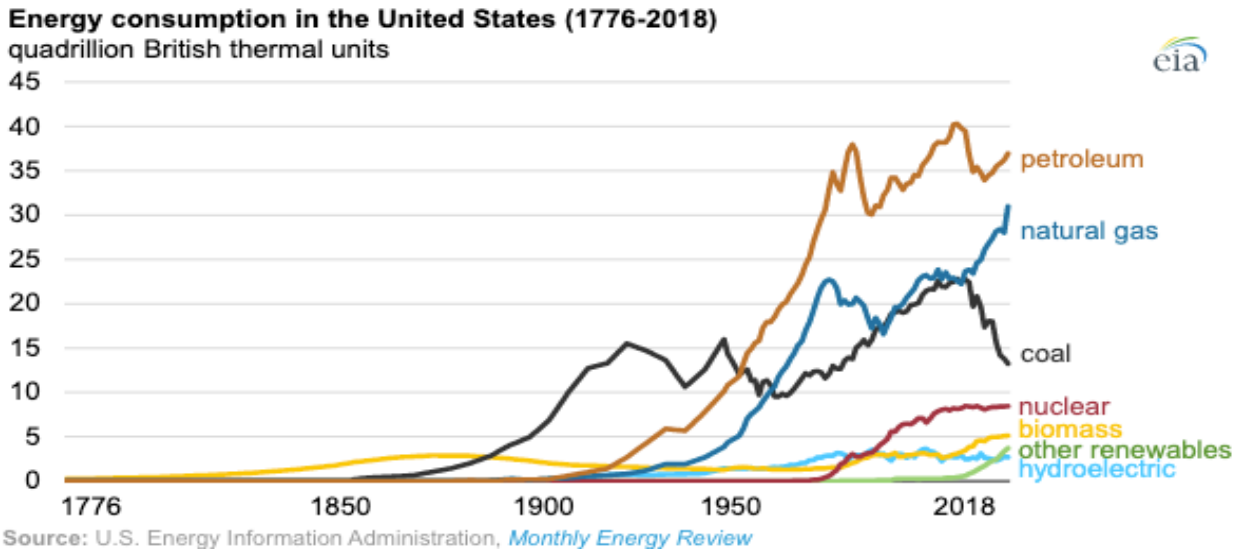

Figure 1.1. History of energy consumption as a function of the energy sources used such as petroleum, natural gas, coal, nuclear, biomass, renewables, and hydroelectric, as reproduced from Ref. [11].

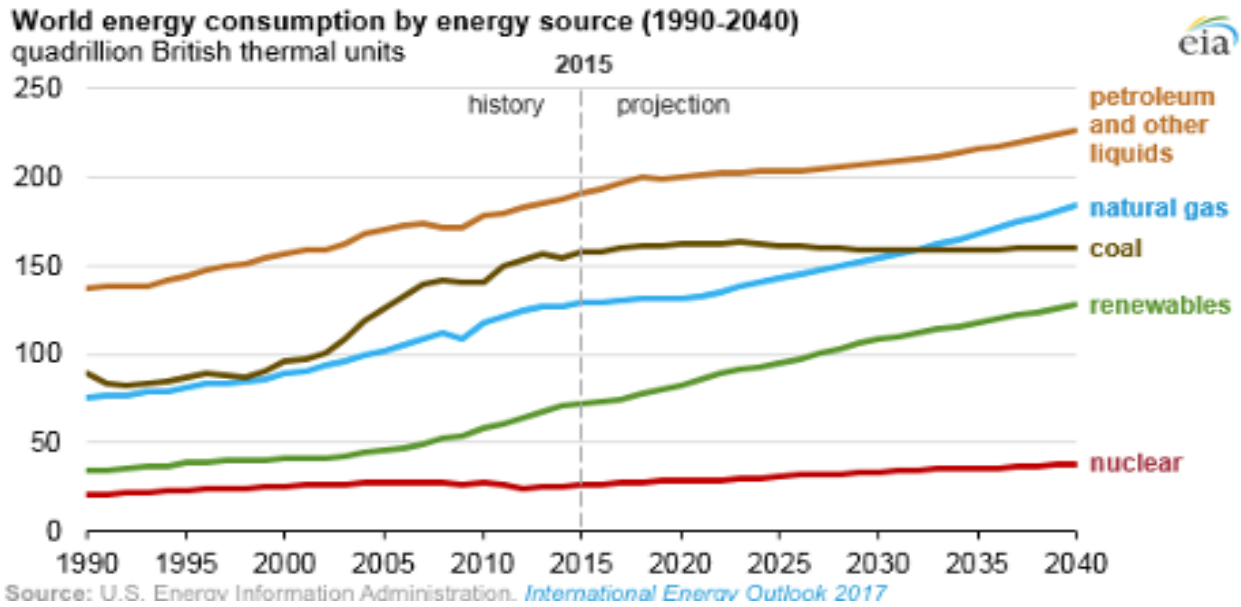

Figure 1.2. Historical and projected worldwide energy use as a function of the energy sources such as petroleum, natural gas, coal, renewables, and nuclear, as reproduced from Ref. [4].

1.2 Renewable Energy Sources

An expected consistent increase in the future energy demand, combined with an ever-increasing environmental consciousness, has resulted in the development of renewable energy sources such as solar, wind, hydroelectric, geothermal, ocean, and biomass[25]. Solar energy is a nearly infinite energy source and while the sun is constantly emitting energy, the energy received on the surface of the earth varies with time, throughout the day, throughout the year, and is highly impacted by weather patterns; and therefore is not a dependable energy source[26]. Wind energy is a another nearly infinite energy source but also highly dependent on weather patterns. It requires the building of large windmills in remote areas from where the produced electricity has to be transported through long distances resulting in an increase of the final electricity costs [27]. There are also concerns for the impact wind energy has on the environment and wildlife. The powerful windmill blades cause harm and kill many wild bird populations[28]. Hydroelectric power is another energy source that takes advantage of nature's power, in this case the power found in rivers. Although the fuel reserves are nearly endless, this method of energy harnessing also harms wildlife, changes water levels and currents, and disrupts migration paths for many fish ecosystems[29]. Geothermal energy leaves little footprint on land as a result of being built underground where the energy source is extracted. There is no risk of depleting this energy source within the human timescale. However, due to being underground, implementation of geothermal energy can be challenging in regions of the world prone to earthquakes[30]. Similar to rivers being used for hydroelectric power, ocean waves are used to produce power. Ocean waves provide predictable cycles based off the moon cycle. However, this means that to take advantage of this energy source one must live near the ocean or else the electricity would have to be transmitted across extremely long distances resulting in an increase of the final electricity costs. Similarly, to wind power, implementing energy

harnessing devices along the ocean coast could also negatively impact ecosystems and wildlife in the area. Biomass is another potential fuel source, however it releases carbon dioxide into the atmosphere, in opposition worldwide efforts to reduce CO_2 emissions[31]. Additionally, as opposed to the other forms of renewable energy, biomass fuel requires plant source to be planted, grown, and harvested; this produces further CO_2 emissions resulting from the machinery needed to produce and process the biomass.

Since all renewable energy sources have shortcomings [26, 27, 32], significant effort has focused on finding an energy source with limited impact on the environment and animal ecosystems, that provides an effectively infinite source, and is attainable World-wide. Fusion energy has emerged as the primary candidate for future energy production given it is sustainable, efficient, and attainable energy production qualities[33, 34]. Focus has been placed on the deuterium(D)-tritium(T) fusion reaction for the production of energy[35]. Fusion energy will most likely be achieved by fusing D and T ions within a fusion reactor called a tokamak. Given the lack of ability on Earth to gravitationally compress a plasma to pressures of 250 billion atomospheres [36] and ion temperatures of ~15 million K, as in the sun. The plasma found within tokamak reactors will be heated to much higher temperatures in the range of 150 million $°C$ in order to overcome the repulsive Coulomb barrier[37].

1.3 Fusion Energy

Energy can be obtained through an array of different fusion reactions. The sun produces energy by fusing a proton with another proton, called the p-p chain reaction [38]. Although the p-p chain reaction has a large energy output of 25 MeV it requires a multitude of sequential fusion reactions that must take place in order to reach the reaction that releases 25 MeV of energy [38], making fusion increasingly more complex. Energy output through the p-p chain is only possible within the sun due to its large size and gravitational force allowing the particles to encounter one another

with large frequency and force [6]. Figure 1.3 shows the three most viable routes to fusion energy production. The top reaction involves the fusion of D-D in which two D atoms fuse and produce a 3He particle, a neutron, and release 3.27 MeV of energy. A secondary path of D-D fusion produces a T, proton, and 4.03 MeV of energy. The middle of Figure 1.3 shows another reaction where D fuses with T and produces an alpha particle, a neutron, and 17.59 MeV of energy. The last fusion reaction illustrates the fusion of D with 3He resulting in an alpha particle, a proton, and 18.3 MeV of energy [6].

The D-D fusion reaction is an attractive candidate due to the absence of radioactive T as a fuel source and the essentially unlimited supply of D. The D-3He reaction has the largest energy output making it another candidate of interest. However, the probability of interaction, defined by the cross section, of each D-D and D-3He, is lower than the D-T reaction across all temperatures[10]. Cross sections for the discussed fusion reactions are plotted in Figure 1.4. The yellow line shows the temperature ITER will operate at. At the ITER operating temperature, the D-T reaction has the largest cross section of the three reactions. In addition to the largest cross section, the D-T reaction has the lowest energy threshold; meaning fusion starts and peaks at lower energies making it more feasible in the absence of large gravitational forces.

The highly energetic particles will be confined to the plasma core by poloidal and toroidal magnetic fields yet some will manage to escape confinement and impact the tungsten divertor [39]. As a result, the divertor will face an extremely hostile environment characterized by high transient temperatures of 3000 K [40], intense particle fluxes of $10^{24} m^{-2} s^{-1}$, and high heat fluxes ranging from $10 - 20\, MW \cdot m^{-2}$. [41]. Plasma material interactions (PMI) will result from the large ion flux to the surrounding components and divertor. This will lead to W material degradation in the form of surface erosion, migration, and redeposition as well as impurity transport, imposing significant challenge to W performance.

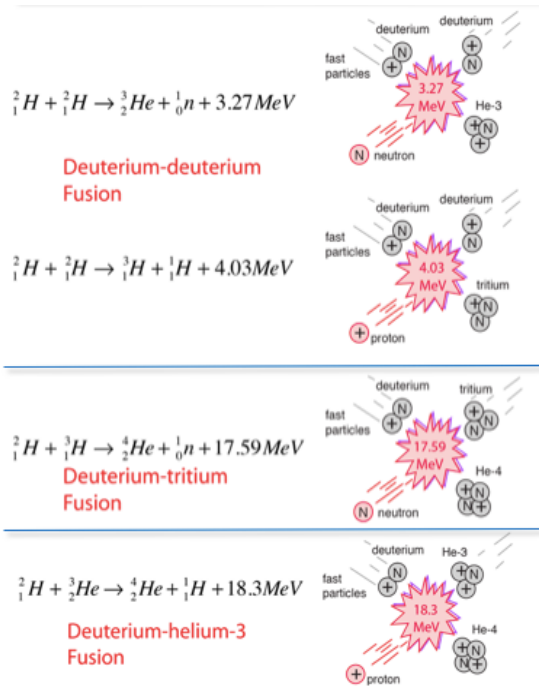

Figure 1.3. Schematic illustration of the three types of fusion reactions considered for fusion reactors, as reproduced from Ref. [6].

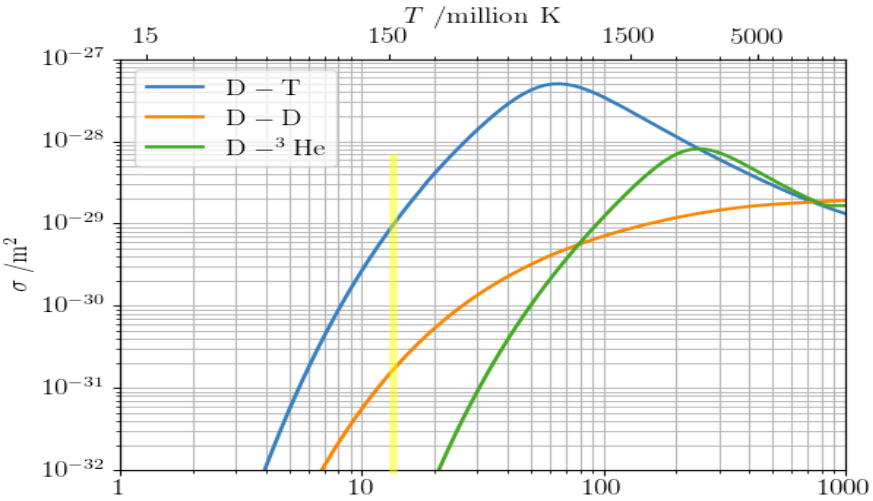

Figure 1.4. Cross sections for the fusion reactions considered in fusion energy production. The yellow line marks the temperature at which the ITER reactor will operate at, as reproduced from Ref. [10].

Figure 1.5 shows the extent of particle removal, implantation, reflection, emission, excitation, ionization, redeposition, exchange, etc [15] that plasma facing materials (PFMs) will experience. Incident ions can be reflected, adsorbed and even modify the surface as a result of ion implantation. PFMs will suffer material sputtering or erosion. The eroded atoms can be transported throughout the reactor with the possibility of becoming a plasma impurity and cooling the plasma due to radiation. T from the fusion fuel will implant in the W microstructure, and can lead to inventory and safety concerns.

1.4 Tritium in Fusion

Fuel retention is of significant concern for future tritium/deuterium fusion reactors. This is due to both the radioactive nature of tritium and the desire to operate future fusion reactors continuously, with ITER planning to demonstrate 400 seconds fusion operation [42]. Materials found within the first wall of the fusion reactor will have to withstand deuterium and tritium particle fluxes in the range of $10^{21} m^{-2} s^{-1}$ while divertor materials will face deuterium and tritium particle fluxes of $10^{24} m^{-2} s^{-1}$ or higher [43]. The divertor will also be exposed to a combination of He-H plasma with an incident ion energy of up to 100eV and temperatures between 600 and 1200 K, at steady-state, with transient surface temperatures as high as 3000K [44].

1.4.1 Tritium Sources and Production

Deuterium is extensively available world-wide in ocean water with an average quantity of 33 grams per cubic meter of sweater. Tritium is not as readily available as deuterium since tritium is radioactive and the only source of tritium results from the cosmic-ray interactions in the atmosphere. Cosmic neutrons interact with either nitrogen or oxygen to form carbon and tritium or nitrogen and tritium, respectively. There is an estimated 20kg of tritium reserves in the world [45]. ITER guidelines for

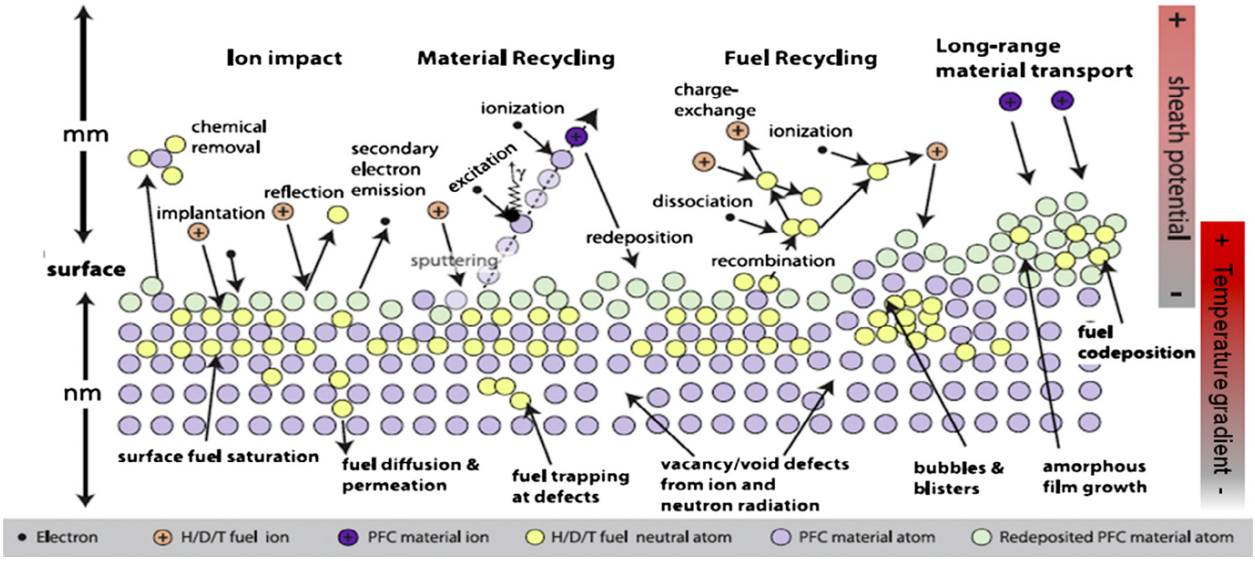

Figure 1.5. Depiction of physical processes in plasma facing components as a results of large ion flux, as reproduced from Ref. [15].

safety operation limit the amount of tritium released/stored in the vacuum vessel to 350 grams. At normal operating conditions this limit will be reached within 70 discharges [42].

Some tritium will be lost due to permeation into the W divertor and other PFMs. In order to make up for the tritium losses, tritium will be replaced through fuel injection shots or by producing it through a breeding blanket[42]. ITER has proposed the inclusion of a test blanket module consisting of a self-cooled lithium (Li) tritium breeding blanket[46] where thermalized neutrons will undergo the ${}^{6}_{3}Li(n,\alpha){}^{3}H$ reaction with the lithium located within the breeding blanket[43]. Thermalized neutrons will collide with the surrounding Li material resulting in the following nuclear reactions:

$$ {}^{6}_{3}Li + n \rightarrow {}^{3}_{1}T + {}^{4}_{2}He \qquad (1\text{-}1) $$

$$ {}^{7}_{3}Li + n \rightarrow {}^{3}_{1}T + {}^{4}_{2}He + n \qquad (1\text{-}2) $$

These reactions replace the tritium lost to permeation. However, this will increase the amount of tritium available to permeate through the fusion reactor.

1.5 Helium Sources in Fusion

Tokamak PFMs will be subjected to fusion-produced 3.5MeV $\boldsymbol{\alpha}$ particles with a flux of ~$10^{16}m^{-2}s^{-1}$[47]. Most particles will be confined, within the plasma, by magnetic fields. After undergoing multiple collisions, less than one percent will escape and reach PFMs with an average energy of ~100eV. Tritium beta decay, where a neutron emits an electron, proton, and a neutrino, will also contribute to the accumulation of He within PFMs. This He source will be significant within materials containing stationary tritium, such as storage containers, with an estimated 150 appm of ^{3}He created daily under a 1:1 tritium to host atoms ratio[47]. Once breeding

blankets are incorporated into ITER, the breeding reaction itself will be the largest contributor of He in the form of (n, $\boldsymbol{\alpha}$) nuclear reactions[47].

1.5.1 Computational Evidence of H-He Synergies

MD simulations performed by Bergstrom, and co-workers with a high pressure 2 nm diameter bubble containing 3 He/vac and a random distribution of 0.5 H/vac at 1800K to investigate the behavior of H in the presence of He in W[12]. Figure 1.6 shows the atomistic configurations from the MD simulations. Initially, at time=0 the H is located within the He bubble. Soon after at ~100 ps the H is observed to quickly migrate to the bubble periphery where it essentially remains trapped.

This raises tritium trapping and inventory concerns. The plot in Figure 1.7 demonstrates the segregation behavior by showing the location of H in relation to the He bubbles as a function of time. The solid black line shows H initially placed inside the bubble at time = 0. The solid symbols show the H location with respect to the He bubble just after 100 ps where it is evident the H has migrated towards the periphery of the bubble. At 1 ns H moves past the shaded region that denotes the boundary of the expanding, elliptical, bubble, towards the outside of the bubble. Both images show that H segregates towards the high-pressure He bubble W matrix interphase where it remains trapped.

1.5.2 Experimental Evidence of H-He Synergies in W

Thermal Desorption Spectra (TDS) of D in ITER grade polycrystalline W was performed by Olga Ogordnikova[17]. Distinctive W samples were exposed to different sets of conditions, pure D, and 10% He-seeded D plasma both at 329K to a fluence of $2 \times 10^{25}\ D\ m^{-2}$. The heating rate for the pure D exposed W was 0.25 K/s and 0.5 K/s for W exposed to the mixed D-He plasma. Figure 1.8 shows the Ogordnikova

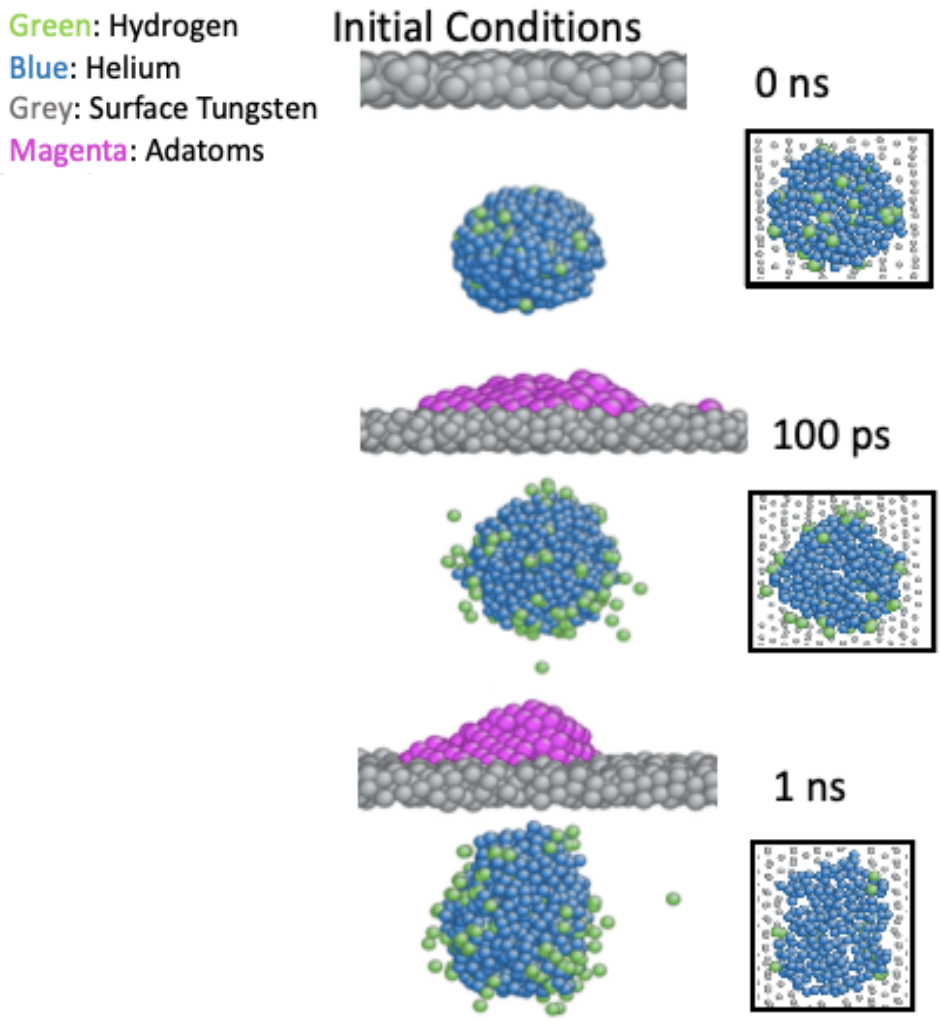

Figure 1.6. Atomistic configurations of a high pressure 2 nm diameter He bubble with H initially placed at the center of it, as reproduced from Ref. [12]. H atoms are shown to move towards the periphery of the bubble as the simulation time increases.

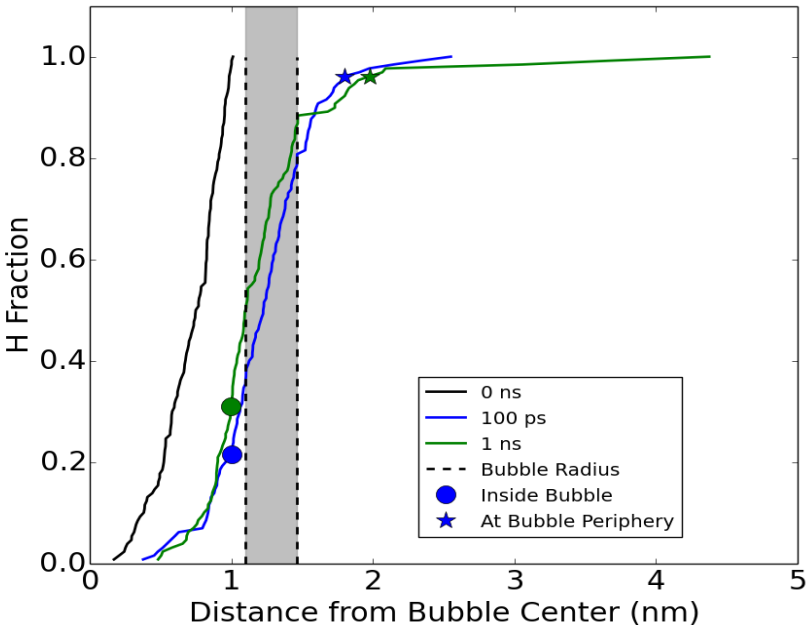

Figure 1.7. MD simulations of H distribution in a 3 He/V and 0.5 H/V bubble in W(111) at 1800K, as reproduced from Ref. [12]. H atoms start inside the bubble and quickly after migrate to the outer periphery.

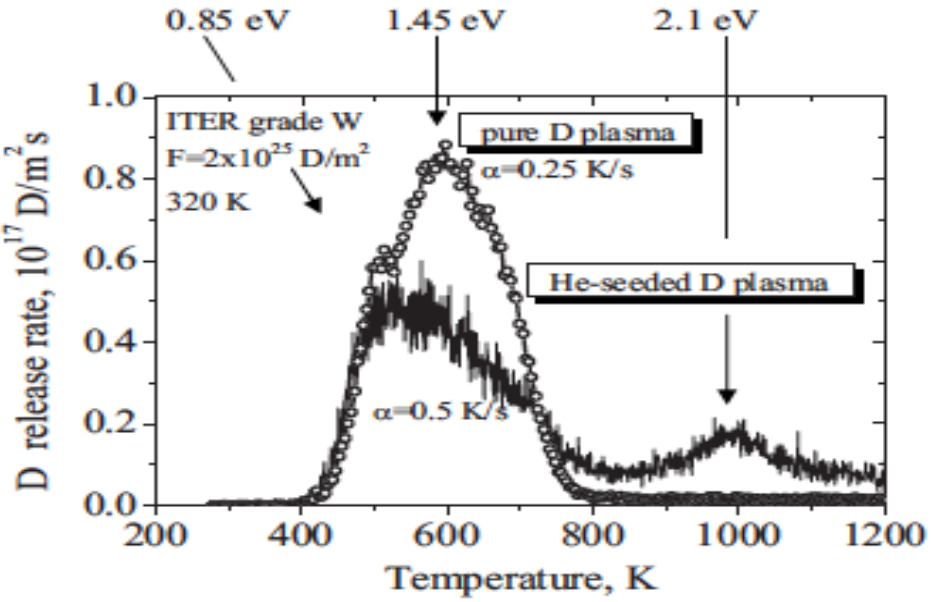

Figure 1.8. TDS spectra of ITER grade polycrystalline W exposed to pure Deuterium plasma and a combination plasma consisting of 10%He-90%D, as reproduced from Ref. [17].

experimental TDS spectra where an initial peak emerges at an approximate temperature of 600 K for the pure D plasma exposed W. Under the He-seeded D plasma the peak at 600 K decreases while the emergence of a secondary peak is observed to occur around 1000 K. This suggest that there could be an increase in the trapping strength of D that releases at high temperatures possibly due to He bubbles.

D and He retention as a function of exposure temperature are shown in Figure 1.9. Pure D plasma exposure (solid black line with filled in squares) shows higher quantities of D permeation over all temperatures and thereby significant concentrations of retained D. Under mixed plasma exposure (Solid black line with filled in circles and dashed line with open stars), a decrease in retained D is observed across all temperatures. Additionally, a sharp decrease is observed near 400K showing an even further significant reduction of retained D at higher temperatures.

NRA measurements were performed by Doerner[18] on W samples exposed to pure D plasma, and 5%He-seeded D plasma, respectively. The W exposed to D only plasma shows and approximate linear increase in D retention in Figure 1.10 with increasing fluence (shown in red), and no indication of reaching a saturation point. When measuring the He-seeded D plasma (shown in green) little to no D retention is detected, registering near the detection limit. The integrated measurements show that far less D retention occurred in the He-D exposure as opposed to the D only exposure. This is a clear indication of He-D synergies that need to be further investigated and understood in order to advance the development of fusion energy.

Effects from He-H synergies will highly impact the evolution of cavities as well as other microstructures. This could further exacerbate the swelling and radiation hardening that structural materials will experience in the extreme fusion environment. It is thought that He-H synergistic effects will have a larger impact on PFMs than displacement defects alone [48]. Vacancy migration energy (E^{V}_{m}) calculations conducted by Liu showed He bound with vacancies forming He-V clusters with an increase in the vacancy migration energy[49]. H-V clusters were possible but

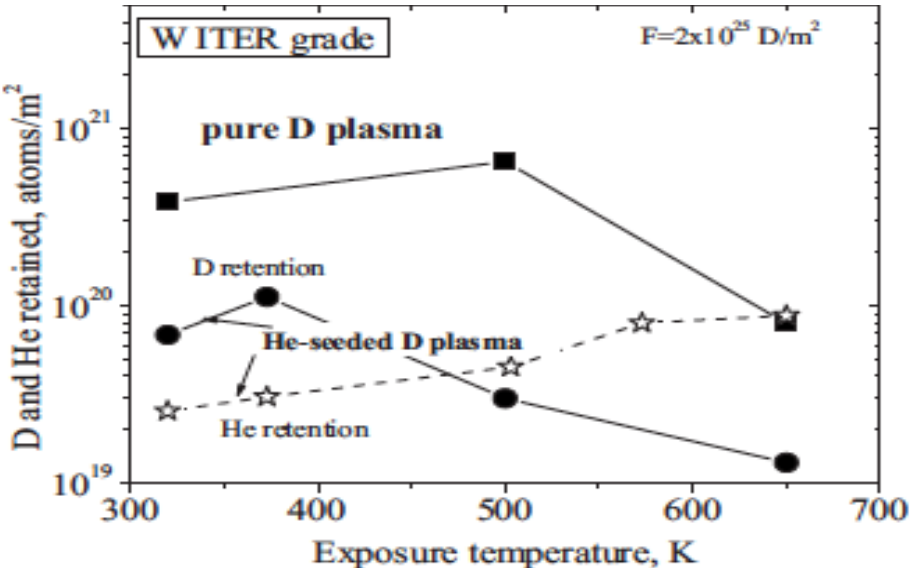

Figure 1.9. Integrated Deuterium retention values as a function of temperature. Calculations performed for both pure D plasma and He-seeded D plasma, as reproduced from Ref. [17]. Higher D retention is observed for the pure D plasma while lower D retention is observed for the He-seeded D plasma.

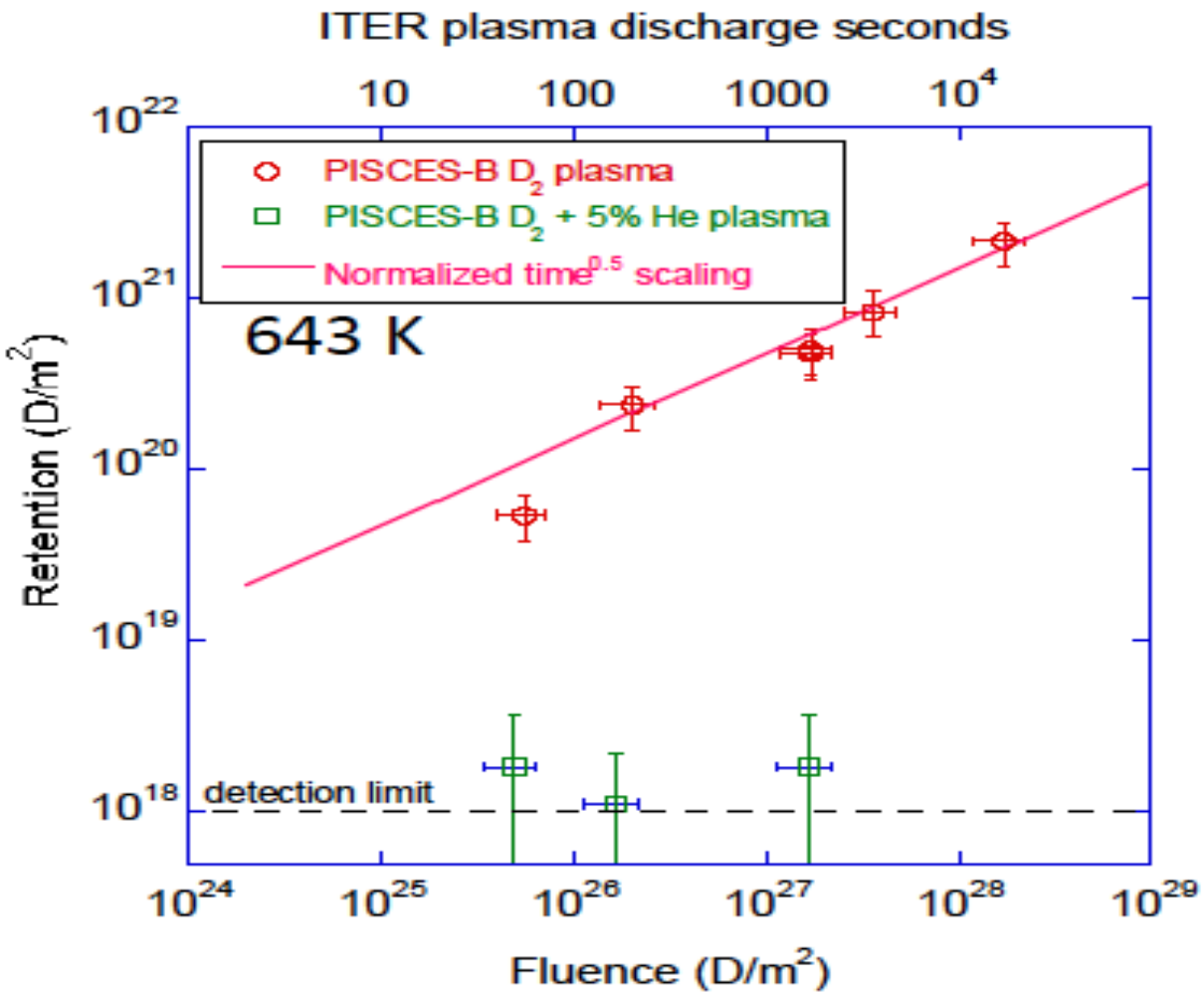

Figure 1.10. NRA measurements for D only vs 5%He seeded D plasma. Deeper permeation of D is mitigated in the presence of the He seeded plasma, while D retention increases linearly as a function of fluence in the D only case, as reproduced from Ref. [18].

to a weaker degree with a lower vacancy migration energy than He-V. Additionally, H seemed to strengthen the binding of He and V, resulting in He-H-V clusters with even higher vacancy migration energy than He-V alone. H seemed to strengthen the binding of He and V. A strong binding interaction between He, H, and V would result in an accumulation of vacancies and cavity formation promoting radiation-induced swelling [50]. The degree to which He can stabilize vacancies and promote cavity nucleation is dependent and affected by temperature[51].

This is due to cluster migration, as well as formation and growth of cavities being strongly dependent on temperature. As a result, a systematic, controlled experiment matrix is necessary to investigate and understand He-H synergies dependence on temperature and on the ratio of present species, and the total He and H fluences. This would provide a more comprehensive understanding of He-H synergistic effects and damage on structural materials [50].

Uemura performed permeability measurements for independent W samples exposed to a different He fluences shown in Figure 1.11 and Figure 1.12. The dotted line and the open upright triangles show the permeation of an un-damaged non He implanted W calculated by Zakharov [52] and Uemura [19]. In Figure 1.11, the lower range of the fluences, $3 \times 10^{19} He/m^2$ (open squares, green box) showed no significant reduction in permeation as is depicted by the overlap of the open upright triangles and the open squares. The next larger fluence $3 \times 10^{20} He\ m^{-2}$ showed some decrease in permeation. This means that the onset of reduced permeation behavior is somewhere between $3 \times 10^{19} He\ m^2$ and $3 \times 10^{20} He\ m^2$. As He fluence increases D permeation decreases. This decrease in permeation can be seen by the downward open triangles, and the solid circles that lie below the undamaged W sample permeation results. The reduced permeation effect is the largest for the highest fluence of $3 \times 10^{21} He/m^2$ in Figure 1.11. The data points for the $3 \times 10^{21} He/m^2$ fluence (black filled circles) are located the farthest below the undamaged W dotted line.

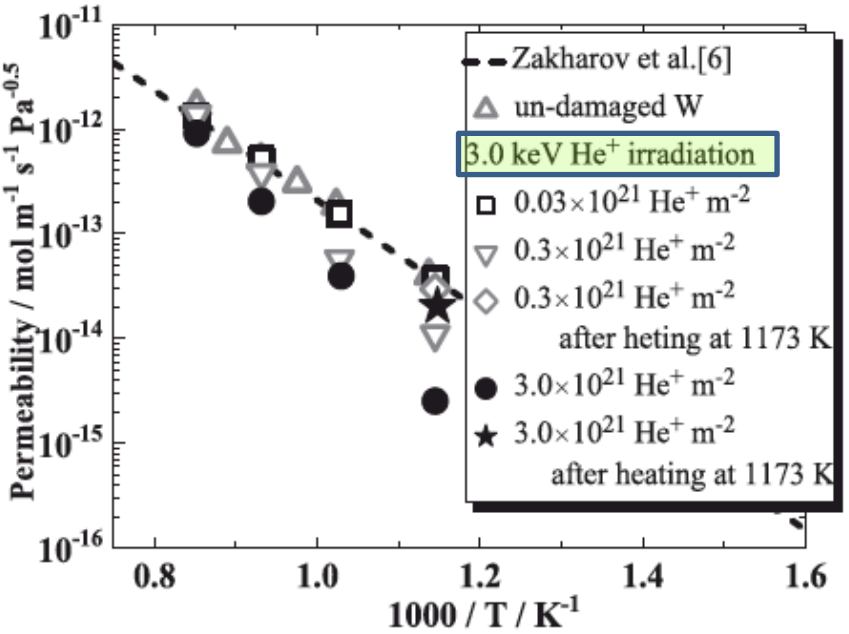

Figure 1.11. Reduction of D permeation in Was a function of increasing He fluence and temperature for 3keV He irradiation as reproduced by Ref.[19].

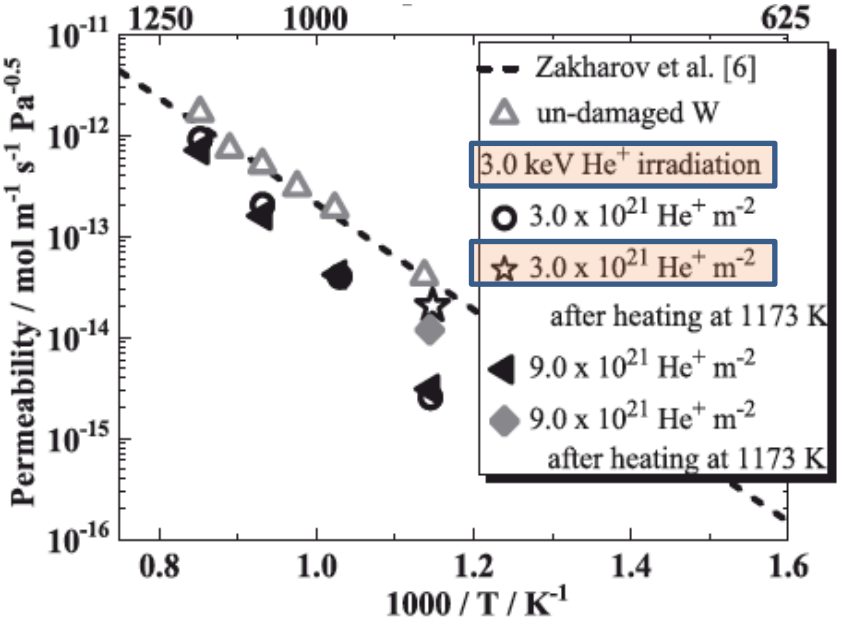

Figure 1.12. Evidence of saturation in reduction of D permeation in W as a function of increasing He fluence and temperature for 3keV He irradiation as reproduced from Ref. [19].

Figure 1.12 focuses on the comparison of permeation behavior between an even larger fluence, $9 \times 10^{21} He/m^2$, with permeation behavior due to $3 \times 10^{21} He/m^2$ the largest fluence studied in Figure 1.11 (orange boxes). No significant further reduced permeation behavior is observed for a fluence of $9 \times 10^{21} He/m^2$, shown by the overlap of the solid triangles with the open circles. The permeation behavior is essentially the same for both fluences indicating that a possible saturation point in reduced D permeability has been reached.

It is shown in Uemura's work that permeation does not continuously decrease as a function of increasing He fluence. There is an onset point where reduced permeation behavior takes off, decreases as fluences increase, and eventually plateau's causing no further reduction in permeation. This threshold and saturation point fluences were used in the design of my experimental matrix.

TEM analysis was performed on Uemura's W samples exposed to $3 \times 10^{21} He/m^2$ and $9 \times 10^{21} He/m^2$ for different temperatures[19]. It was evident that the density of dislocation loops (black dots) increased as He fluence increased. Likewise, the size of the He bubbles (white circled) show a correlation with He fluence and become faceted as the He fluence increases. This means that by exposing individual W samples to different fluences in combination with different sample temperatures I can design and develop different types of He bubble layers within the material. Low temperature, low fluence produces a layer composed of a high density, small He bubble network. High fluence, high temperature exposures produce a low-density bubble network comprised of large sized bubbles. Exposure performed in-between these ranges result in mid-size density networks of medium sized bubbles.

1.6 Motivation and Objective

Due to the limited availability of tritium(T), it is imperative to understand hydrogen behavior in fusion plasma facing materials to accurately predict the distribution and transport of T. He bubbles will greatly affect the microstructure and

mechanical properties of the materials used in fusion reactors. He and T do not exist in isolation in the reactor, they interact with each other making the bubble dynamics increasingly more complex.

Experimental and computation evidence shows that D tends to bind to the surface of He bubbles [12]. D location has been found to be strongly correlated with the location of He implantation [53]. Using a combination of experimental techniques will allow us to gain a more comprehensive understanding of the H-He synergies that exist within W, such as T permeation and T retention.

In this dissertation, I demonstrate a research approach and a multi technique experimental workflow to quantify the importance of He bubble size, density, and depth on tritium migration, permeation, and retention in W. The He bubble size and density was controlled by changing the He plasma fluence and temperature of the W sample. An experimental matrix has been designed to evaluate the onset of reduced permeability and a saturation point at which permeability is not further reduced [19].

Fluence and temperature have been shown to have a large effect on bubble layer characteristics such as bubble size and density. However, the effect on D permeability have not been systematically quantified. The goal of this dissertation is to correlate reduced D permeability with bubble network characteristics such as He bubble size and density. I have designed and controlled bubble size and bubble density networks through a systematic experimental matrix of He fluence and temperature.

Due to the large effect that fluence and temperature have been observed to have on He bubble size and density, these implantation parameters can be controlled to design the desired He bubble network within W and study the effects it has on D permeability as shown in Figure 1.13. The figure shows that at lower temperatures and lower fluences (upper left corner) a network of high number density, small ~1 nm sized He bubbles is formed. Keeping the temperature constant at room temperature,

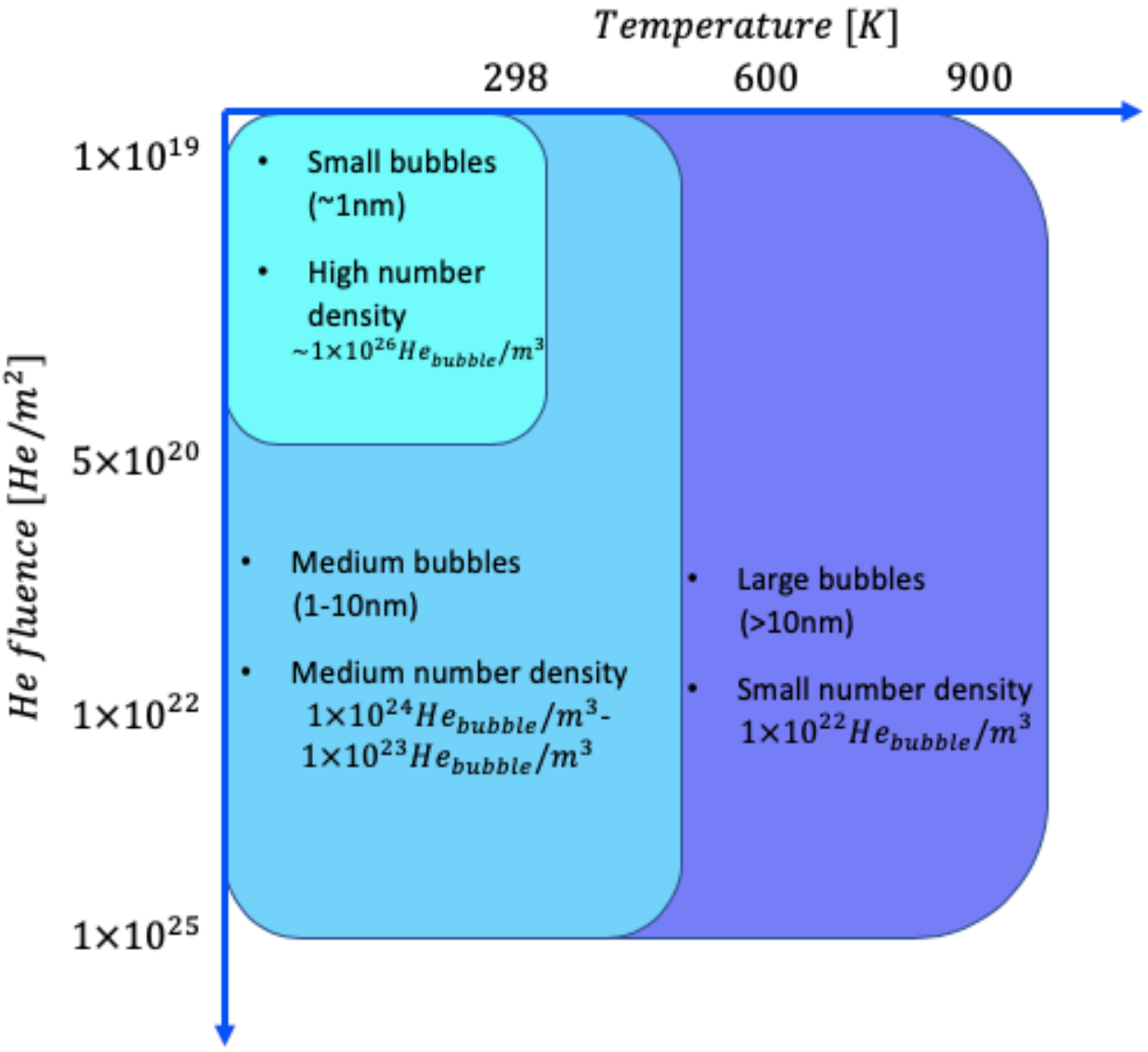

Figure 1.13. Experimental matrix of dissertation work. An array of fluences are used in combination with temperatures to design and control the He bubble layer formation within W.

while increasing He fluence (moving downwards in the y-direction) results in a medium number density bubble network composed of medium 1 to 10 nm sized He bubbles. Increasing the temperature along with high fluences (bottom right corner) produces a small number density of large >10 nm sized bubbles.

For this dissertation work I implanted polycrystalline W discs, measuring 6 mm by 0.5 mm, in the experimental matrix of combination shown in Figure 1.13. Uemura [19] indicates no significant changes in permeability for the $3 \times 10^{19} He/m^2$ fluence therefore, a fluence of $5 \times 10^{19} He/m^2$ has been chosen as the lowest fluence in an attempt to capture the onset of reduced D permeability. A secondary fluence of $5 \times 10^{20} He/m^2$ has been used to observe the continuous reduction in D permeability. Saturation of reduced permeability is expected to take place near $1 \times 10^{22} He/m^2$ therefore $5 \times 10^{21} He/m^2$ is the upper limit fluence used in this work. These fluences were chosen to stay within bounds of null permeability changes regimes. This experimental matrix has been extended to different implantation temperatures from room temperature (298 K) to 600 K to 900 K.

Since the He fluences of interest are relatively low, it was essential to use a low flux plasma source that would allow me to He plasma expose samples in small enough increments to reach total He fluences with higher accuracy. A high flux plasma source would be capable of reaching the entire desired fluence in 1 second or less. Using said source could lead to a large margin of error. Simply high flux plasma exposing for an addition second, or two, would double, or triple, the total He fluence in the sample. A lower flux plasma source naturally has a higher resolution in accumulation of the total He exposure. By using a lower flux, it takes longer to reach the desired fluence and overexposure can be avoided.

The plasma source was also required to operate at a low ion energy source for several experimental reasons. 1) The Helium bubble layer had to be located in the near surface region to closely represent fusion relevant environment plasma facing materials where He is located very near the surface. 2) Avoid He induced W fuzz

formation that forms above a threshold ion energy of ~20 eV at high temperatures in the range from 900 K to 2000 K [54]. This experimental matrix avoids this W fuzz formation regime. Additionally, using a low ion energy would allow for a closer comparison against other works investigating similar ranges of He-H in W permeation behaviors with similar extents of radiation damage.

Parametrizing, characterizing, and benchmarking an Electron Cyclotron Resonance (ECR) plasma source was performed as part of this dissertation. I parametrized and characterized the UTK ECR plasma source in the laboratory of Professor David Donovan using a Retarding Field Energy Analyzer (RFEA) diagnostic to determine the plasma He ion energies. The flux was determined by using a Faraday cup and later converting the current on the sample surface, during exposure, to $He\, m^{-2}\, s^{-1}$. I have He exposed all the W samples with low flux ECR plasma source located at the University of Tennessee. The D was later introduced through gas-driven permeation using joint UTK-ORNL gas driven permeation system in the ORNL LAMDA laboratory. Table 1-1 lists the experimental conditions the W samples were exposed, as well as the number of samples exposed.

Table 1-1. Experimental parameters used for the design and development of He bubble networks in W for the study of He-H synergies in fusion relevant environments.

Fluence [He/m^{2}]	Ion Energy [eV]	Surface Temp [K]	Material
5E19	70	298	PCW, qty 3
5E19	70	600	PCW, qty 3
5E19	70	900	PCW, qty 3
5E20	70	600	PCW, qty 3
5E20	70	900	PCW, qty 3
5E21	70	298	PCW, qty 3
5E21	70	600	PCW, qty 3
5E21	70	900	PCW, qty 3

Chapter 2
Characterization of the ECR Plasma Source

The Electron Cyclotron Resonance (ECR) Plasma Source used to expose the W materials investigated in this dissertation is located at University of Tennessee in Knoxville. It is part of Dr. Donovan's research group located in the Zeanah Engineering Complex. This ECR source is a small commercially available stainless steel ultra high vacuum (UHV) compatible source with a full-length water-jacket cooling system. A high-density plasma is achieved through the implementation of the electron cyclotron resonance phenomenon where radially symmetric GHz microwave fields are coupled with ions located on the surface of a multi-polar magnetic array. This source is the Plasma Cracker Source-Electron Cyclotron Resonance (PCS-ECR) manufactured by SPECS.

SPECS conducts routine testing of their systems to ensure proper performance. This source had been out of operation for several years prior to its use to He expose the W samples in this dissertation, and its performance and reliability were unknown. The plasma sparking had not been parametrized nor the plasma characterized, so the reproducibility of a specific desired plasma was not known. Sparking of an (uncharacterized) Argon plasma was easy, predictable, stable, and could be sustained for indefinite periods of time. However, sustaining of a He plasma had proven difficult and unpredictable. If and when the sparking of a He plasma was achieved; stabilizing, and sustaining of this plasma was challenging and resulted in a He plasma that could only be held for an average of 10 minutes before extinguishing. Additionally, this plasma was not characterized, and reproducibility

was unknown. This meant that it was crucial to understand and test the system, find the best conditions for sparking and sustaining a He plasma, characterize the plasma output, and parametrize the system so a plasma of desired characteristics could be consistently reproduced. All these conditions had to be met before any He plasma exposures could take place.

In the following sections I describe in detail the testing of the plasma source system to ensure it was working according to the manufacturing standards. I demonstrate how a He plasma was sparked and sustained for three hours for the first time. Once I was able to spark and sustain an (uncharacterized) He plasma repeatably, I characterized the plasma output. Understanding the ion energy and flux that was being produced at those system parameters allowed me to adjust accordingly and identify the necessary parameters to produce the desired plasma.

2.1 Initial Flux Measurements Taken by a Faraday Cup

A Faraday cup is a small cup made of conductive material capable of measuring a small current. This current is proportional to the number of incoming ions and therefore can be used to calculate the incident flux [55]. The Faraday cup is biased to a negative voltage to repel incoming electrons, attract incoming ions, and reduce secondary electron emission[56]. This produces a current that is then converted to an ion flux through Equation (2-1). The flux, ϕ, is calculated by taking the Faraday Cup current measurement in Amps and dividing by the quantity of the Faraday Cup aperture surface area, in meters squares, multiplied by 1.602E-19C, the elementary electric charge. This returns a value in terms of particles per meter squared per second. It is through this method that the preliminary system testing flux readings were acquired.

$$\phi = \frac{FC_{current}[A]}{\pi*(R_{aperture})^2*1.602E^{-19}C} = \frac{C/s}{m^2*C} = \frac{He}{m^2\,s} \qquad (2\text{-}1)$$

2.2 Testing the System Against SPECS Standards

2.2.1 Chamber Pressure Effect on Plasma

Given the difficulty associated with sparking and sustaining a He plasma, I knew I had to understand the He plasma behavior and identify the conditions that predictably sparked and sustained the He plasma. Figure 2.2 shows nine flux readings where the relationship between flux and chamber pressure is analyzed. Two of the data points nearly overlap at 5.36E-3 Torr and 9.9E17 He m^{-2} s^{-1} so there appears to be only eight but there are nine data points. The initial pressure was 5.45E-3 Torr and then it was slowly decreased to a final pressure of 3.12E-3 Torr. A flux reading was taken for the He plasma sparked at every pressure increment. It is important to note that at each pressure the system was optimized to spark and sustain a stable He plasma. This means that the system parameters are different for all the He plasmas and as a result, all the flux readings are different as well. The system and plasma parameter must be adjusted accordingly to produce a plasma that is stable at each different pressure. It is not possible to maintain the same magnetron current, anode voltage, and extractor voltage while changing the pressure because this changes the conditions of the plasma and, if the conditions are not ideal, the plasma can be extinguished. A stable plasma requires a very particular combination of magnetron current, anode voltage, extractor voltage, and chamber pressure. Therefore, it can be summarized that the flux values shown in Figure 2.2 were attained for different stable plasmas found at different pressures. It is evident, from the plot, that a lower pressure provides a stable plasma with higher flux. As the chamber pressure is increased, the flux of the resultant stable plasma is reduced. This inverse relationship of flux to chamber pressure is demonstrated in the manufacturer system testing [1], shown in Figure 2.1. A higher beam current is observed at lower pressures. As the chamber pressure increases, the beam current

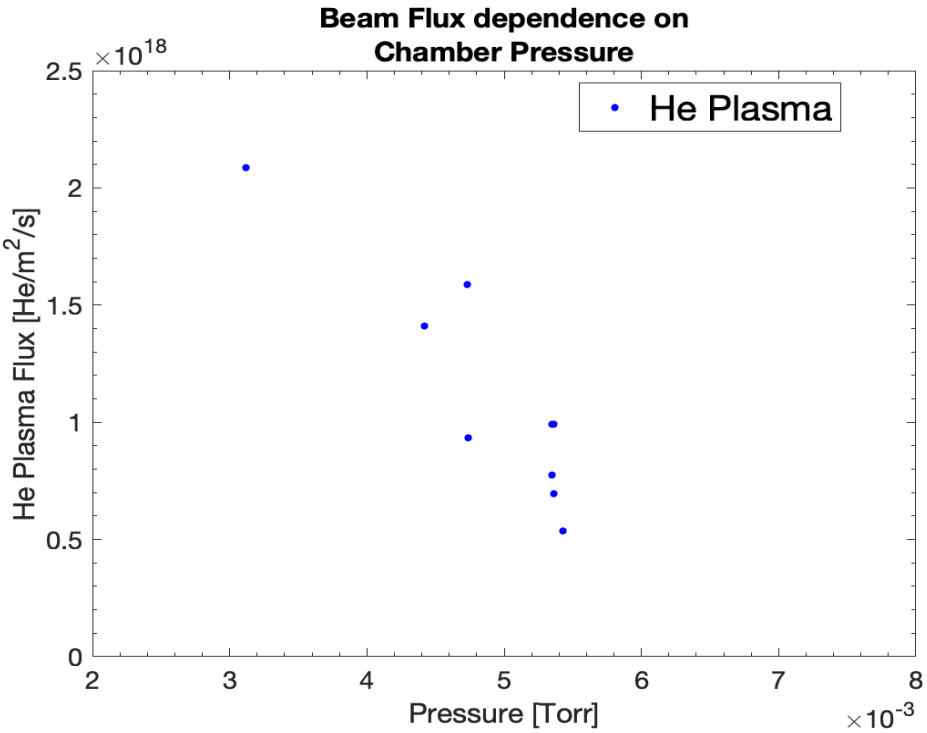

Figure 2.2. University of Tennessee ECR source He plasma flux dependence on chamber pressure

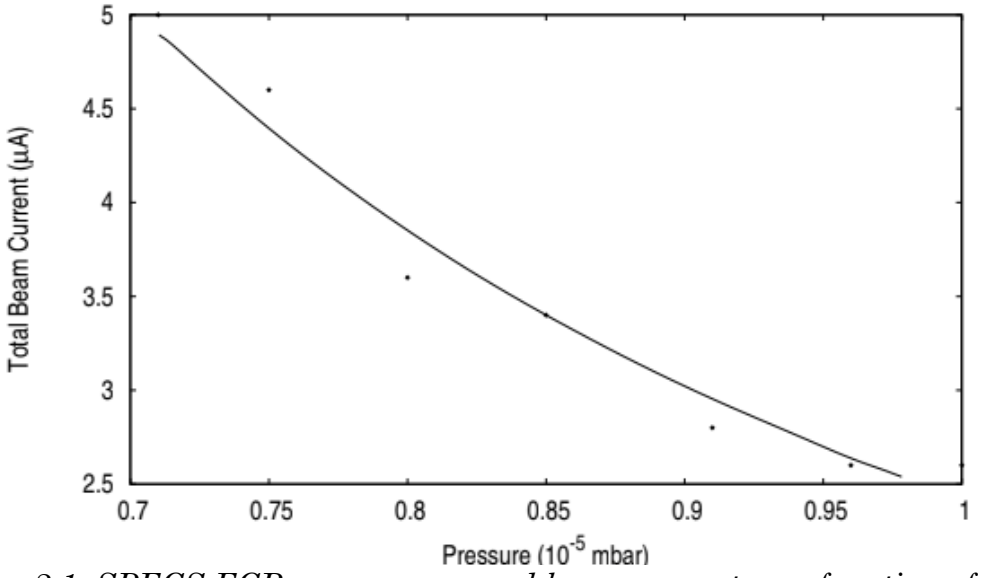

Figure 2.1. SPECS ECR source measured beam current as a function of chamber pressure as reproduced from Ref. [1].

decreases. This is due to ions being scattered or neutralized at larger pressures. Given that the beam current proportionally translates to a flux, we can conclude that this relationship is the same seen in our system and that our system is working appropriately in terms of chamber pressure.

It is not known if this flux to chamber pressure is a linear relationship for our system as is indicated in the manufacturer documentation. I did not perform additional systematic stable plasma flux readings across a broader range of chamber pressures because the goal was not to understand the flux to chamber pressure relationship across the entire spectrum. The goal of these tests was to obtain a general understanding of a regime where stable plasmas were possible, to study the effect that chamber pressure had on flux and to identify the pressure, if any conditions would yield a higher flux, stable, He plasma. From these early He plasma tests, I learned that lower chamber pressures produce a higher flux plasma and that plasmas are highly sensitive to chamber pressures. Therefore, for all the following plasma optimization studies I used the lowest pressure needed to sustain a stable plasma.

2.2.2 Magnetron Current Effect on Plasma

Once a stable plasma was repeatably achieved, I focused on studying the effect of the magnetron current on the produced plasma. As stated in section 2.2.1, it takes a combination of magnetron current, anode voltage, extractor voltage, and chamber pressure to produce a stable plasma. The same nine stable plasmas studied in section 2.2.1 are studied here, but as a function of the magnetron current rather than the chamber pressure, as show in Figure 2.3. For the set of pressures, anode voltages, and extractor voltages used in the nine plasmas; the lowest current capable of sustaining a stable plasma was 20 mA. This is the reason a lot of data points congregate around 20 mA. Higher fluxes are attainable at the same approximate

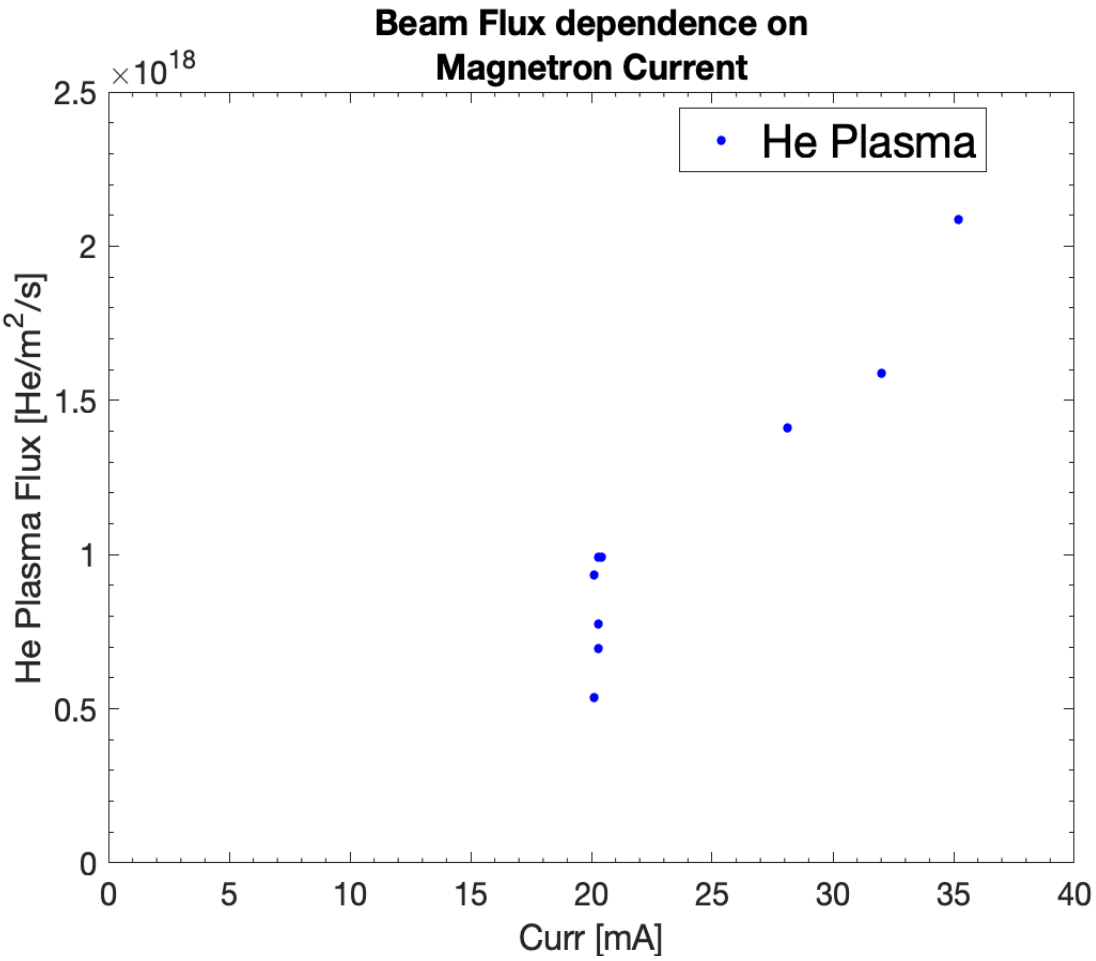

Figure 2.3. University of Tennessee ECR source flux dependence on magnetron current.

current of 20mA due to the different chamber pressures. These five data points provide further insight into the flux to chamber pressure relationship studied in section 2.2.1. Thus, I performed a flux to chamber pressure analysis then revert to flux to magnetron current relationship studies.

For these five data points the magnetron current and the extractor voltage were kept constant at ~20 mA and 200 V, respectively. However, due to the changing chamber pressure, stable plasmas were not possible with all other parameters remaining unchanged, and therefore the anode voltage was increased from 400V to 500V to 600V and 630V (for two data points). Higher fluxes were achieved, despite the same magnetron current, because chamber pressures were adjusted to stabilize the plasma. The higher fluxes (of the five data points discussed) share a strong inverse relationship with chamber pressure. From this point forth the discussion resumes to analyzing all the data shown in Figure 2.3.

From Figure 2.3 it is evident that the He plasma flux increases as the magnetron current increases. Ignoring the five data points in the vicinity of the 20mA magnetron current value, the data appears to follow an approximately linear relationship between plasma flux and current. This flux to magnetron current linear relationship is also documented in the manufacturer flux to magnetron current system testing shown in Figure 2.4 [1]. A higher beam current is observed with higher currents. As the magnetron current increases, the beam current increases. Given that the beam current proportionally translates to a plasma beam flux, we can determine that this relationship is also recreated in our system and that our system is working appropriately in terms of magnetron current.

A limited number of current dependent tests were also performed. The goal in these tests was to gain an understanding of the effect that the magnetron current has on the produced plasma flux, although not necessarily to investigate the flux to current relationship throughout the entire range of all possible magnetron currents.

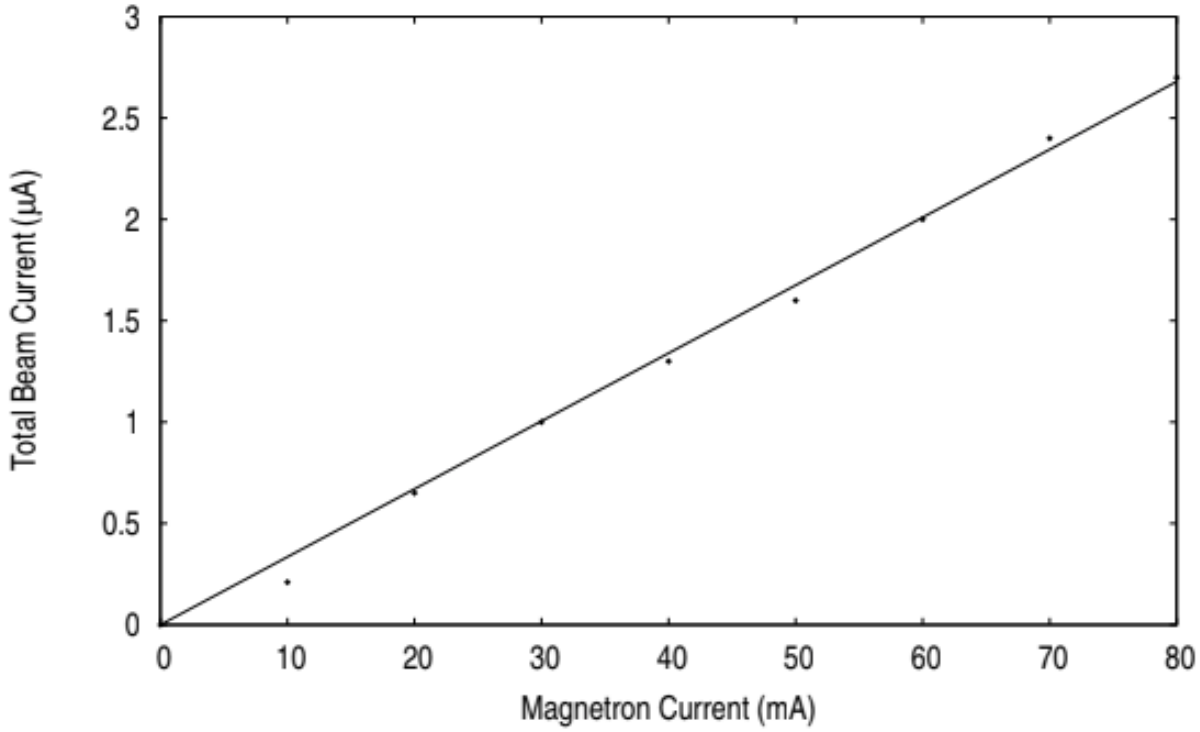

Figure 2.4. SPECS measured beam current as a function of magnetron current as reproduced from Ref. [1].

From these early He plasma tests, we can conclude that magnetron current roughly linearly increases the produced plasma flux. Therefore, for all the following plasma optimization studies I use a combination of the lowest pressure and highest current necessary to yield a stable plasma.

2.2.3 Anode Voltage Effect on Plasma

Once the sparking of a stable plasma was better understood as a function of chamber pressure and magnetron current, I was able to investigate the effect of anode voltage on plasma characteristics. Aside from the chamber pressure and the magnetron current, the anode voltage was the third parameter that was manipulated to stabilize the previously discussed plasmas conditions. The extractor voltage was kept at 200V for all the plasmas produced during testing of the ECR source. Figure 2.5 shows data for twenty-three stable plasmas in addition to the nine stable plasmas mentioned in section 2.2.1 and 2.2.2. The nine previously discussed plasmas are shown in blue. The additional eighteen produced plasmas with an anode voltage of 600V and 700V are shown in green, and the five plasmas with an anode voltage of 800V are shown in magenta.

Once there was an understanding of chamber pressure and magnetron current regime that provided the right conditions for sustaining a plasma; I was able to produce He plasmas with as low as 10mA of magnetron current by increasing the anode voltage from 400V to 600V, 700V, and eventually 800V. A higher anode voltage appeared to aid in not only the stabilizing of the plasma but also increased the beam current, and therefore flux. The chamber pressure for the additional twenty-three samples ranged from 3.11E-3 to 3.26E-3 Torr. Therefore, the effect the pressure had on the flux is minimum and expressed as scatter in the data. With the extractor voltage held constant at 200V we can assume that the plasma was a function of the anode voltage and the magnetron current only.

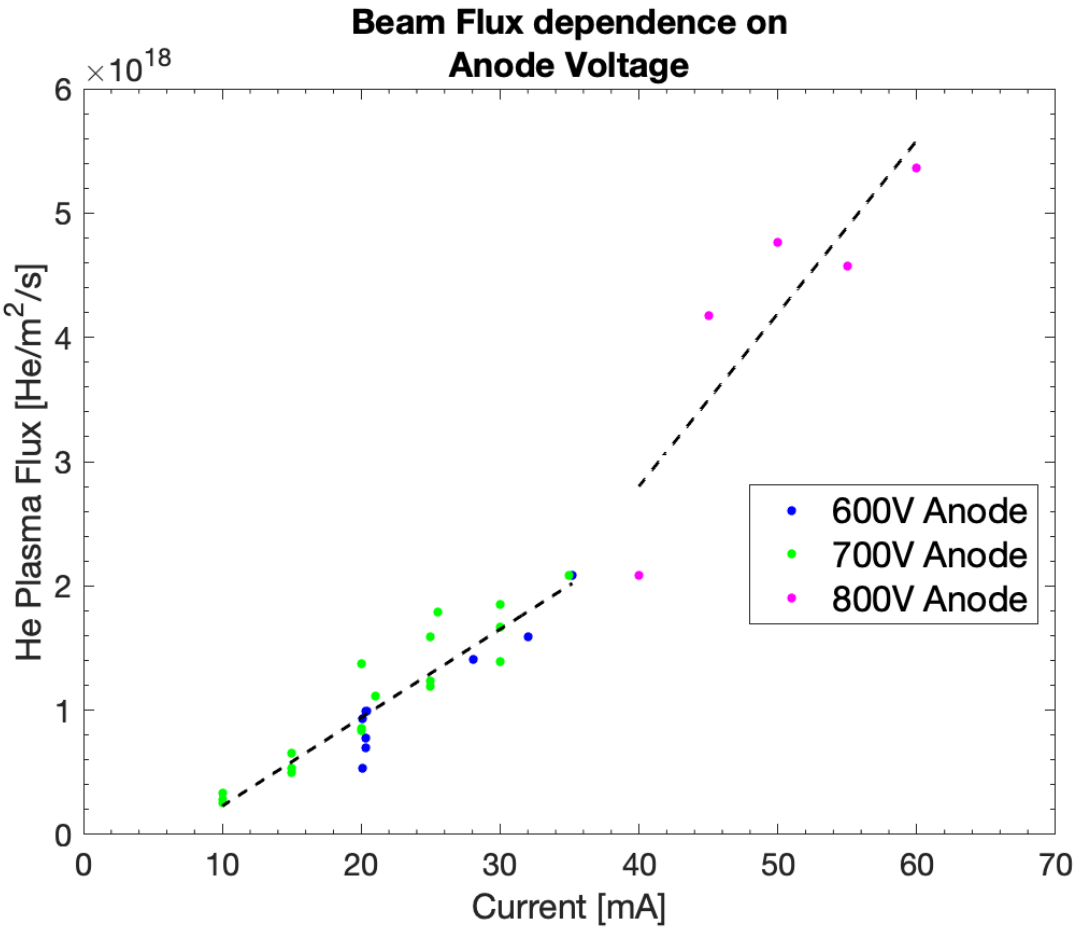

Figure 2.5. University of Tennessee ECR source flux dependence as a function of current and anode voltage.

Looking at Figure 2.5, a roughly linear relationship between the flux and the magnetron current is observed. This further supports the data and observations presented in section 2.2.2. The effect of the anode voltage is expressed as the difference in slopes of the best fit line between the combined 600V and 700V anode voltage data (green and blue) and the 800V anode voltage data (magenta).

The twenty-seven data points below 40mA share the same linear relationship and can be fit by the same linear equation. The five data point above 40mA share linear relationship but differ from the other data set. The data shown in magenta shows a larger degree of flux increment effects compared to the data shown in blue and green. This change in slope is attributed to the larger anode voltage (800 V) used for the plasmas expressed as magenta data points. Even though the magnetron current was also increased to stabilize the plasmas due to changing anode voltages, the effect of the magnetron current on the slope is not considered to be significant given that it has a linear effect on flux (see Figure 2.4). Thus, the change in slope is attributed to the change in anode voltage and not the current increment.

This anode voltage effect on the beam current is consistent with the beam current to anode voltage system testing provided by the ECR manufacturer, SPECS, as shown in Figure 2.6. The anode voltage has a positive relationship on the beam current, meaning the beam current increases as the anode voltage is increased. However, this is not a linear relationship across the entire anode voltage range as is the case for the chamber pressure and the magnetron current. Thus, the anode voltage effect on the beam current can be divided into three regimes. Within each regime it affects the beam current to a different degree. This is indicated by the rate of change in beam current with increasing anode voltage. The rate of change is the largest in the first regime from 0 V to approximately 50 V. The rate of change is reduced to a second intermediate degree of change from 50 V to about 600 V. Finally, the effect of the anode voltage on the beam current is reduced to such a degree that

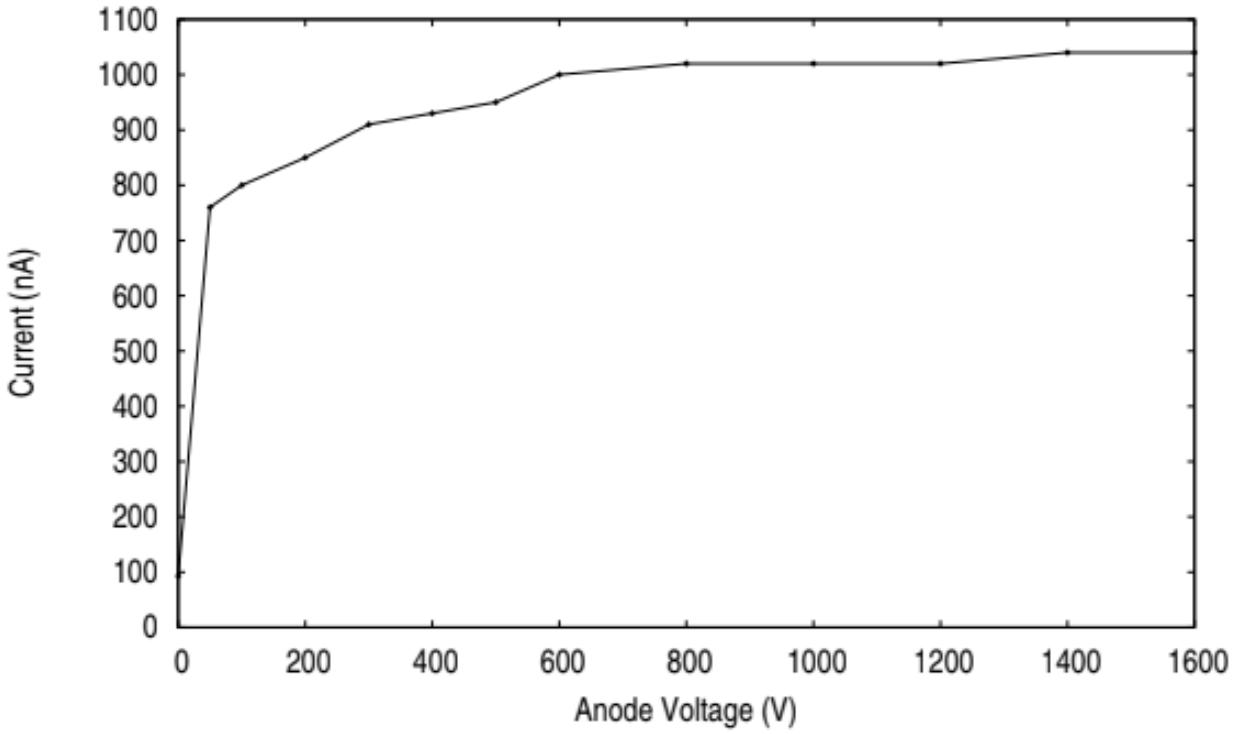

Figure 2.6. SPECS ECR source measured beam current as a function of anode voltage reproduced from Ref. [1].

it nearly plateaus in the third regime running from 600 V to 1600 V. This supports the results obtained during testing of the UTK ECR source where the beam current does not linearly increase across all anode voltages and instead the flux measurements divide into two regimes with different rates of change in beam current to increasing anode voltage. The beam current to anode voltage relationship indicates our system is working according to SPECS manufacturing standard in terms of anode voltage.

2.2.4 Extractor Voltage Effect on Plasma

As mentioned in section 2.2.3, the extractor voltage was set to 200V and remained unchanged throughout the testing of the system. All other parameters and their effect on the plasma beam were studied. With a reasonable understanding of the chamber pressure, the magnetron current, and the anode voltage effects on the plasma; a stable plasma was able to be repeatably sparked and sustained despite not having a thorough understanding of the extractor voltage. This is due to a plasma not depending on solely one parameter but rather a combination of the four parameters. Therefore, even though the extractor was not optimized for the stabilizing of the plasma, all other parameters were, and this allowed the production of stable, and repeatable plasmas.

Due to our system sharing good agreement with the SPECS manufacturer standards for beam current relationship to chamber pressure, magnetron current, and anode voltage; it is safe to assume that the extractor voltage is closely represented by the SPECS test results. Figure 2.7 shows the extractor voltage effects on the total beam current as tested by SPECS. The total beam current increment, as a function of extractor voltage, is on the order of mA as opposed to uA which is the case for chamber pressure and magnetron current, or nA in the case of anode voltage. This means the extractor voltage impacts the beam current significantly and to the

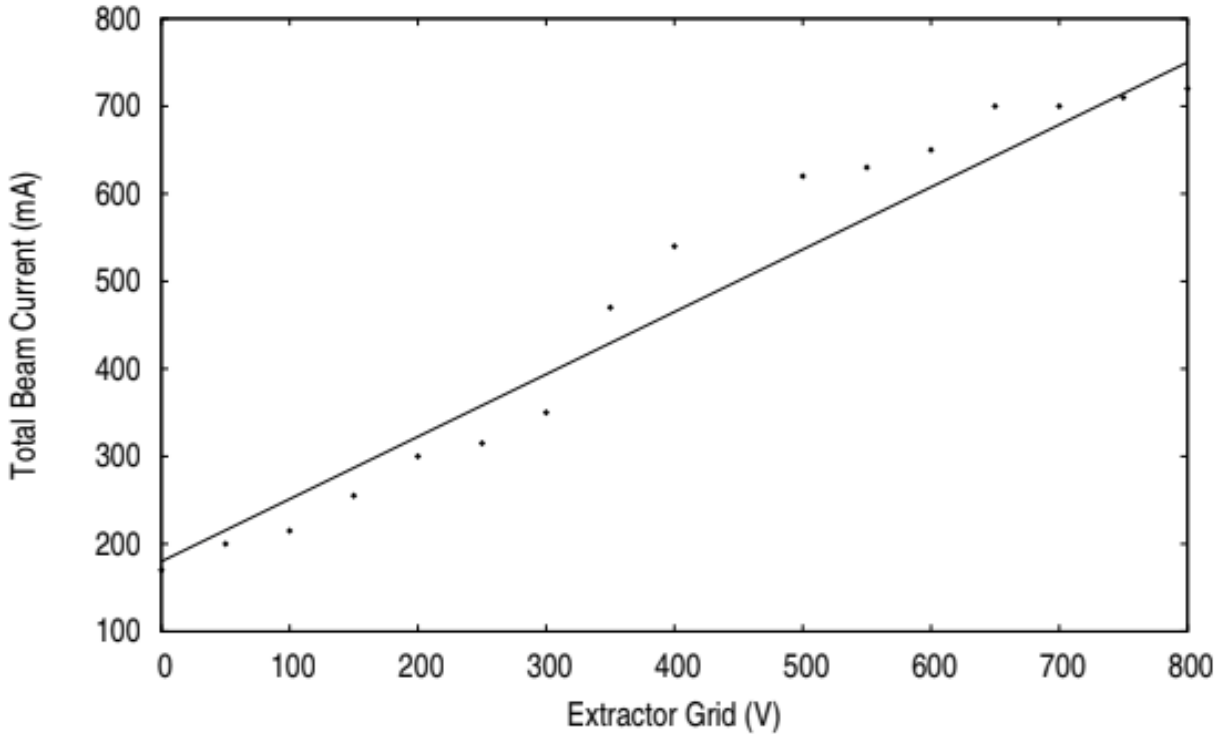

Figure 2.7. SPECS ECR source measured beam current as a function of extractor grid voltage reproduced from Ref. [1].

largest degree of the four parameters. The extractor voltage function depends on the anode voltage.

The effect of the extractor voltage is significant at lower anode voltages. Increase of the extractor voltage significantly increases the ion beam current. However, it appears that at higher energies, above 400V, the effect is reduced and in fact further increasing the extractor voltage can result in a decrease of the beam current. For my experiments this reversal in effect was not of concern given I wanted to achieve a 70eV ion energy plasma beam. This meant that I operated the plasma source in an extractor voltage regime less than 100V where the effect on the beam current is the most significant.

2.3 Ion Energy Readings Performed by a Retarding Field Energy Analyzer (RFEA)

At this point only the flux of the plasma beam had been characterized as a function of plasma conditions. The plasma ion energies remained unknown and needed to be characterized before proceeding with He plasma exposures of the W materials. A Retarding Field Energy Analyzer (RFEA) was used for characterizing the produced plasma ion energies.

An RFEA consists of a series of biased grids that examine the energy distribution of the plasma species[16]. Figure 2.8 describes in detail the workings of a traditional RFEA. The first plate consists of a grounded narrow slit where the particles go through. The plasma forms a sheath over this plate which negatively biases the plate, which repulses electrons only allowing the ions to go through. Some electrons will make it through, but they are later turned around by the suppression grid. Note that for these experiments (unlike what is displayed in Figure 2.8), there was no additional bias applied to the entrance plate ("Ground Slit"). The first

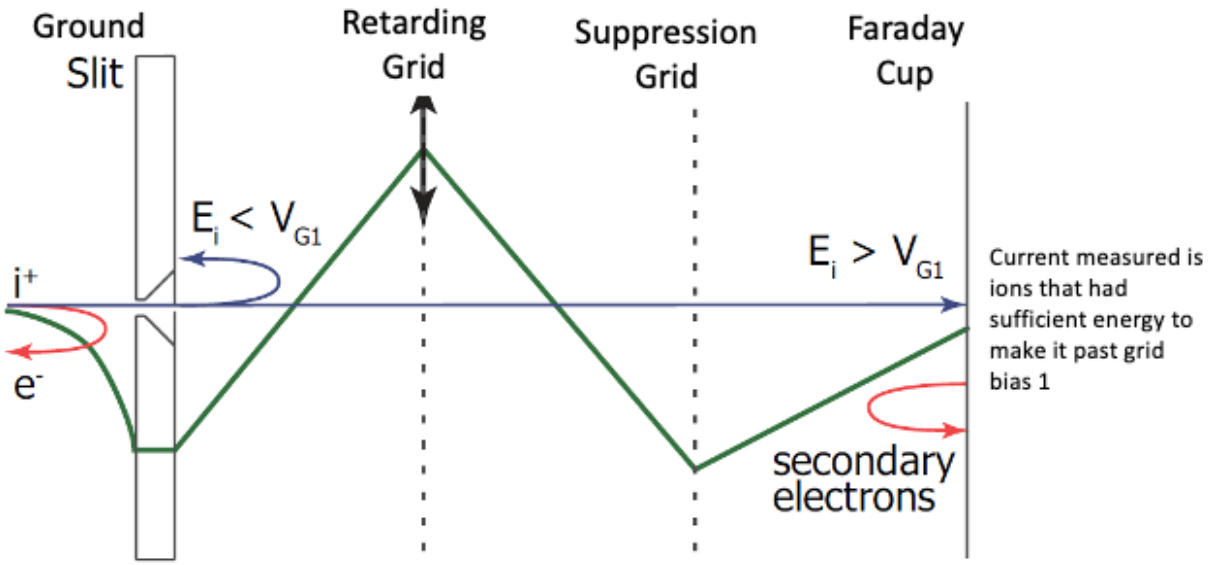

Figure 2.8. Diagram of an RFEA plasma diagnostic used to read current and identify the plasma ion energy peak as reproduced from Ref. [16].

grid is known as the retarding grid. This grid is swept and strongly positively biased to filter out ions without sufficient energy to overcome the positive voltage[16]. This is the grid that characterizes the plasma ion energies and resolves the plasma beam ion energy peak.

The second grid is negatively biased stronger than both the slit plate, and the collector (a faraday cup) to reflect outwards the electrons that transmit past the initial slit plate as well as secondary electrons from the back of the slit plate released from ions rejected by grid 1, and to return secondary electrons formed at the collector as to not charge the collector. Finally, the collector is lightly negatively biased to direct the incoming ions towards it. During ion energy charactering experiments the RFEA grids were biased as follows. The retarding grid was swept from 0 to 80 volts in 2.5V increments. The second grid was negatively biased to 20V, and the collector (faraday cup) was negatively biased to 15V. The current measured at the faraday cup was left in terms of current since ion energy peak is identified through current behavior, instead of flux, as explained in the following section.

2.3.1 Grid Biasing and Voltage Sweeping of the Retarding Field Grid

A Keithley 2260B-80-40 programmable DC power supply was used to continuously sweep the voltage on the retarding grid from 0V to 80V then back down to 0V in 2.5V increments. The suppression grid was biased and held constant at -20V using the 2268-80-10 Keithley power supply. The Faraday cup was biased and held constant at -15V using a Keithley 2400 series. Argon plasma was used to test the RFEA and develop a method of automating the voltage sweeping on the retarding grid, number 1. He plasma was not used during the development stage since helium plasmas are prone to instabilities and sensitive to the RFEA sheath biased slip plate and the biased grids.

During the voltage sweeping the plasma current was read over a period of thirty seconds, at a rate of one data point per second at each voltage. This provided

thirty data points of the beam current as measured by the RFEA for the retarding grid voltage at that moment. The thirty second voltage step increments are more evident in the He plasma RFEA experiments and will be further addressed in section 2.3.3. Although the argon plasma is less susceptible to instabilities and less sensitive to the RFEA, it is quite tumultuous and has large fluctuations, unlike the He plasma, making the voltage increment steps less evident. Given plasmas are highly stochastic by nature, a LabVIEW program was written to automate the retarding grid voltage increments to remove human error and increase the level of systematic measurements. Reducing any additional fluctuations aids in more accurate plasma current readings.

2.3.2 Finding Argon Plasma Ion Energy Peaks as Proof of Method

In order to characterize the plasma and parametrize the system response and test the RFEA, five argon plasmas were produced with a gas flow rate of 30 standard cubic centimeters per minute (sccm), a chamber pressure of 3.14E-04 Torr, a 30 mA magnetron current, a 70 V extractor voltage, and anode voltages ranging from 70 V to 110 V in increments of 10 V. Each plasma only differed in the anode voltage.

The current versus time sweeps of the five plasmas are shown in Figure 2.9. The RFEA measured current is recorded as a negative current and therefore lower currents are plotted closer to the top and larger currents are located lower on the Y-axis. The retarding grid voltage is continuously swept from 0 V to 80 V back to 0 V and so successively. The figure only shows one upwards-downwards voltage sweeping segment with the 80 V turnover point located in the middle, in the form of a peak, at the top of the plot.

The 70 V anode plasma produced the lowest current, plotted as the light blue curve in Figure 2.9. It was sparked and sustained at an initial beam current of -0.6E-7 Amps. As the RFEA retarding grid, grid 1, is biased to increasing higher voltages it

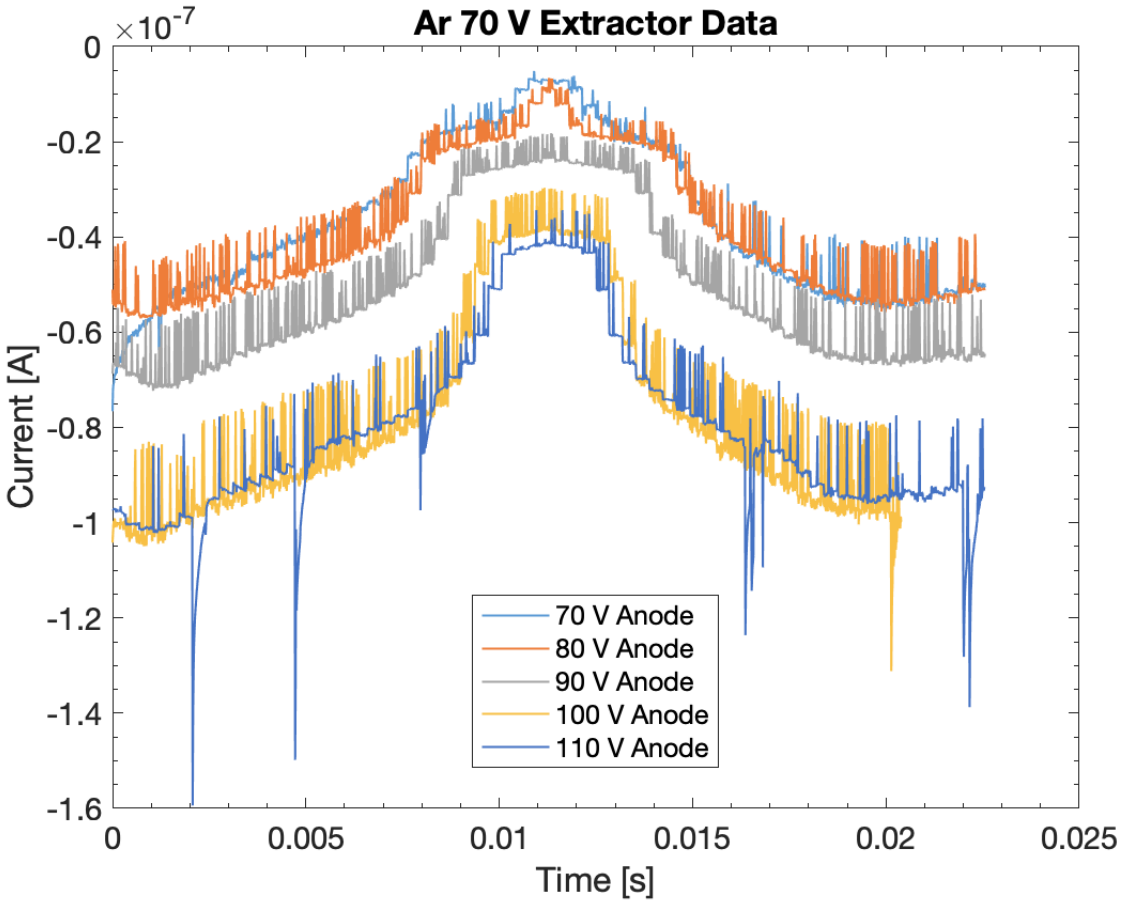

Figure 2.9. Retarding grid voltage sweeps, from 0V to 80V and back down from 80V to 0V, that plot the measured current versus time for five different argon plasmas.

filters out ions with insufficient energy to overcome the potential. The removal of the ions reduces the beam current read by the RFEA, consistent with the current curving towards the top of the plot. When most of the ions are rejected by the RFEA the current is significantly reduced, forming a shoulder in the current curve and later plateauing. The ion energy peak is identified by the emergence of this shoulder since it directly results from filtering the peak of the ion energy distribution. Once the peak of the energy distribution has been filtered out, the energy peak has been identified and can therefore be described by that voltage energy.

As the anode is increased by 10 V for every subsequent plasma, with the extractor voltage unchanged at 70 V, the identified shoulder shifts closer towards the middle of the curve where the 80 V turnover point is located. This indicates the ion energy is impacted and changed by the anode voltage. The increase in ion energy can be due to the difference between anode and extractor voltages where a larger potential difference produces larger ion energies. This is supported by the manufacturer manual describing that the extractor grid function depends on the anode [1]. However, additional studies must be done to further understand the relationship between the extractor and the anode voltages.

Arcing was observed for the highest anode voltages of, 100 V and 110 V. This arcing can be attributed to the larger current resulting from a higher anode voltage. As larger currents are travelling between the RFEA grids sometimes a discharge of electric current jumps from one grid to another causing this arcing phenomenon observed as large peaks.

Thirty current reading data points were taken at each stepwise voltage increase of 2.5 V ranging from 0 V to 80 V back down to 0 V. This allowed sufficient time for the plasma beam to stabilize and resulted in a better current reading resulting from the increase in retarding grid voltage. The thirty data points were averaged at each 2.5 V increment to get a single data point that better represented the average beam current for a specific voltage as shown in Figure 2.10. The averaged

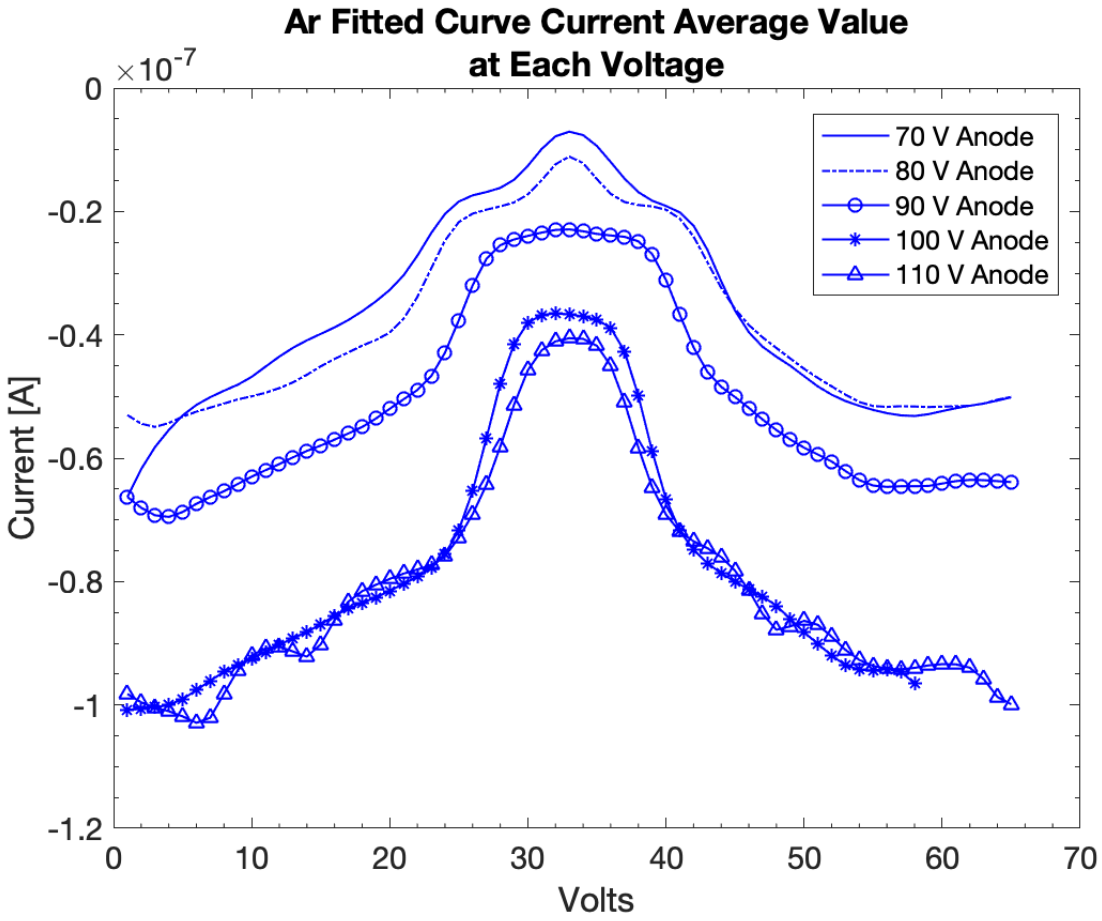

Figure 2.10. Data and best fit curves for the current versus voltage for five anode voltage dependent argon plasmas. Each data point represents a voltage dependent current average over 30 data points.

anode dependent current curves were then fitted with best fit function curves. The best fit curves are represented in Figure 2.10 by the solid line connecting the voltage dependent average current readings.

The energy peak is better resolved by taking the derivative of the current curves as is shown in Figure 2.11 and Figure 2.12. Taking the derivative of each curve translates the shoulder into a peak. Because the derivative peak results from the largest change in current found at a specific standing voltage, we can then conclude that the anode voltage that produces the current curve produces an ion energy peak of the same energy (eV) as the standing voltage. Figure 2.11 and Figure 2.12 show the derivative curves for the upwards voltage sweep and the downwards voltage sweep, respectively. A comparison of these figures indicates that the ion energy peaks for the upwards and downwards voltage sweep were adequately acquired, repeatable, and consistent. The reproducibility of the ion energy peaks for the upwards and downwards voltage sweeps demonstrate the stability of the plasma beam as well as the successful profiling of the whole system within the investigated parameters ranges; Anode Voltage 70 V to 110 V, Extractor Voltage 7 0V, Magnetron Current 30 mA, and chamber pressure 3.24E-04 to 3.41E-04 Torr.

2.3.3 Finding Helium Plasma Ion Energy Peaks

The He plasma is more susceptible to the plasma sheath formed in front of the RFEA as well as the RFEA itself, and as a result could not be used for the testing of the RFEA in order to develop and automatized voltage sweeping method. Ar plasmas were used during the initial beam characterizing and system profiling tests. Having developed a method for the characterization of the plasma ion beam and resolved the ion energy peaks using an argon plasma, it was now possible to characterize the He

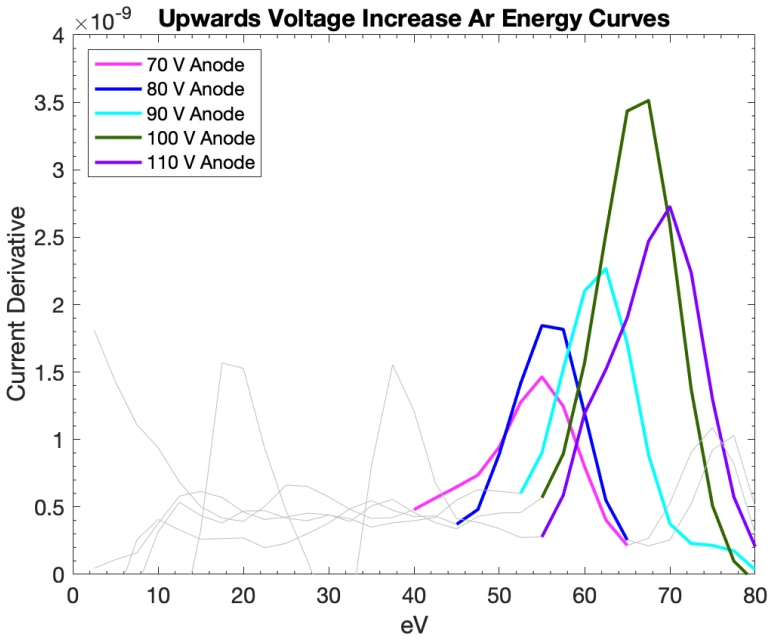

Figure 2.11. Ar plasma ion energy peaks found during the upwards voltage sweep from 0 V to 80. V.

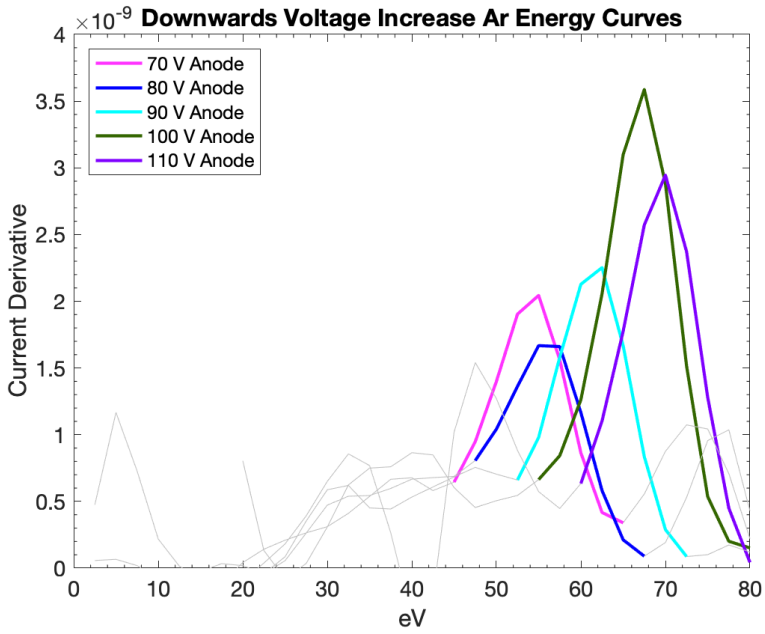

Figure 2.12. Ar plasma ion energy peaks found during the downwards voltage sweep from 0 V to 80 V.

plasma beam and resolve the ion energy peaks. For the Ar plasma a 70 V extractor and a 100 V anode produced a 70 eV energy peak. Because the extractor voltage highly impacts the produced flux at lower voltages and the 70 eV ion energy peak was only found towards the higher volt anode settings, I decided to investigate the He plasma beam at a slightly higher extractor voltage of 80 V and anode voltages ranging from 110 V to 180 V.

Using a higher extractor voltage should produce a higher flux. A higher flux is desirable because it permits larger fluences to be reached within shorter exposure times. Also, similar Ar plasma extractor and anode voltage ranges were used for the He plasma given they had already shown to produce a 70 eV ion energy peak. Fortunately, this selection based on understanding the Ar plasma characteristics provided an adequate starting point of investigation that proved fruitful.

The studied He plasmas are shown in Figure 2.13. A total of seven He plasmas were characterized with an extractor voltage of 80 V and anode voltages of 110 V, 120 V, 140 V, 160 V, and 180 V. Two separate plasmas were studied for the 160 V (lilac curve and dark purple) and the 180 V (green and red curve) anode settings. This was done to investigate the stability and repeatability of the system from day to day and to investigate if setting the system to the same parameters would reproduce a plasma of the same flux and ion energies. The two 160 V anode curves were produced on separate days, between which the entire system was shut down and re-started.. Looking at the 160V curves in Figure 2.13 it is almost impossible to resolve the dark purple curve as it is directly overlapped by the lilac curve. This is a very good indicator that the system has been successfully profiled and characterized to reproduce plasma beams of the same flux and ion energies. The 180 V anode green and red curves also very closely overlap however, to a lesser degree than the 160 V anode currents. This is attributed to the higher anode voltages, for which the higher RFEA potential influences the beam current reading more.

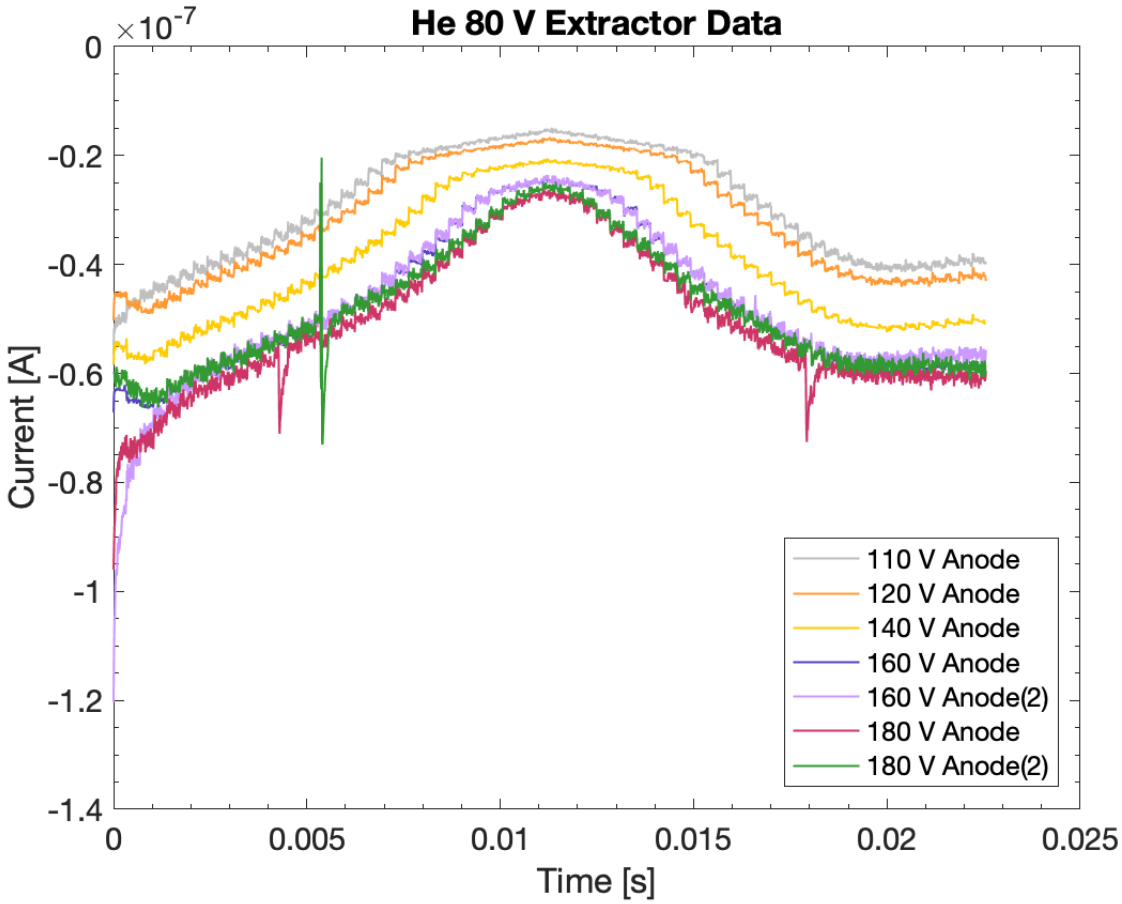

Figure 2.13. Retarding grid voltage sweeps, from 0 V to 80 V and back down from 80 V to 0 V, that plot the measured current versus time for seven different helium plasmas.

Similar to the high anode voltage Ar plasma curves, the high anode voltage He plasmas curves show evidence of arcing behavior. This is particularly observed for both 180 V anode curves. However, unlike the Ar plasma, the He plasma is highly stable as opposed to the Ar plasma which is highly dynamic. This stability is to not be confused with sensitivity to the RFEA biased plates for which He is sensitive to while Ar is more resilient. The stability of the He plasma can be observed in the current curves having low noise to signal ratio, the defined voltage stepwise increments, and the clear emergence of the shoulder that indicates the ion energy peaks.

As was done for the Ar plasma voltage sweeps, thirty current data points were taken at each stepwise voltage increment of 2.5 V from 0 V to 80 V back to 0 V, shown in Figure 2.14. The thirty data points were averaged at each 2.5V increment to get a single value that best represented the average beam current at each voltage increment. The averaged anode voltage dependent current curves were then fitted to determine the best fit function curves.

The energy peak is identified by taking the derivative of the current curves as is shown in Figure 2.15 and Figure 2.16. As previously discussed, the derivative of the curve transforms the shoulder into a peak. This peak shows the ion energy distribution and the ion energy peak. Figure 2.15 and Figure 2.16 show the derivative curves for the upwards and downwards voltage sweep, respectively. Both upwards and downwards voltage sweeps show that an anode voltage of 180 V produces a plasma beam of 70 eV ions, with all other parameters kept constant. Therefore, a He plasma of 70 eV can be produced with an extractor voltage of 80 V, an anode voltage of 180 V, a chamber pressure of 1.05E-3 Torr, and a magnetron current of 30 mA.

2.4 Testing the Temperature Stage

The heating element was tested to ensure it was in working order and to study the temperature dependence of the applied current. Figure 2.17 shows a total of two

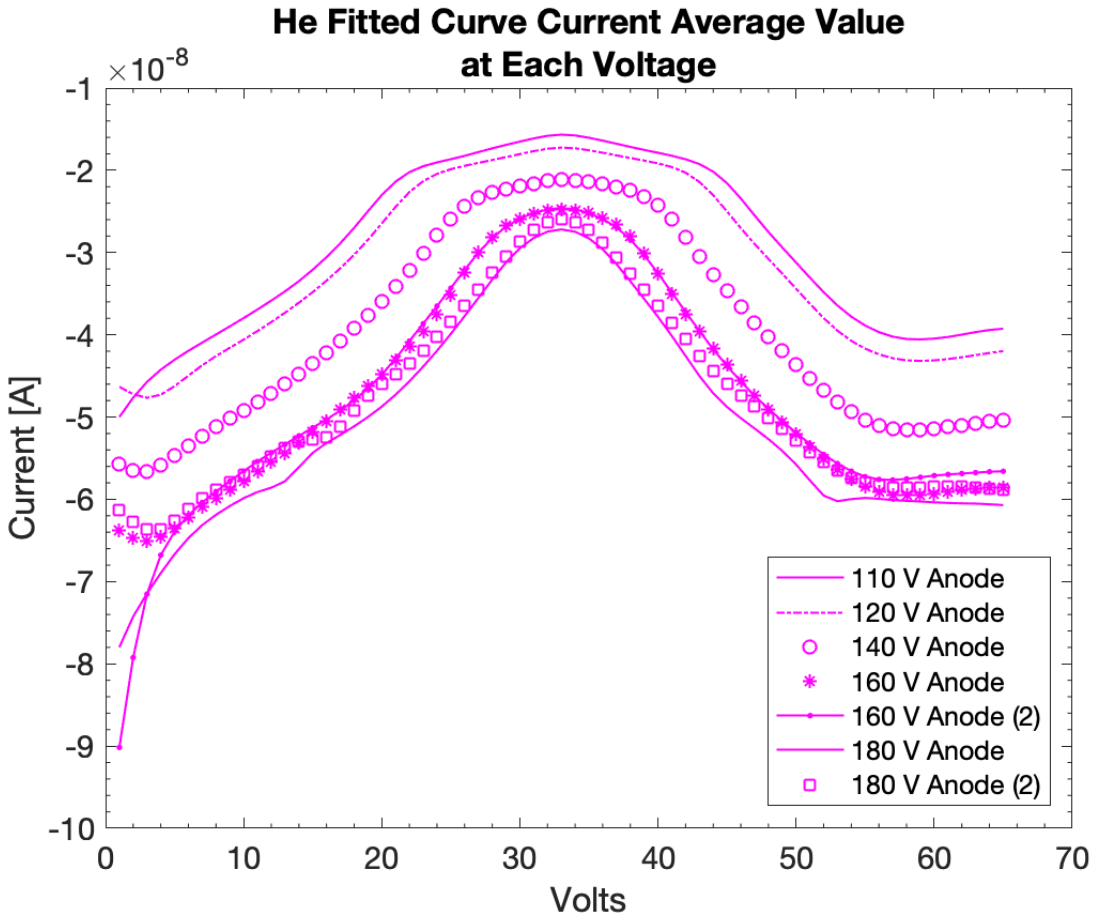

Figure 2.14. Data and best fit curves for the current versus voltage for seven anode voltage dependent helium plasmas. Each data point represents a voltage dependent current average over 30 data points.

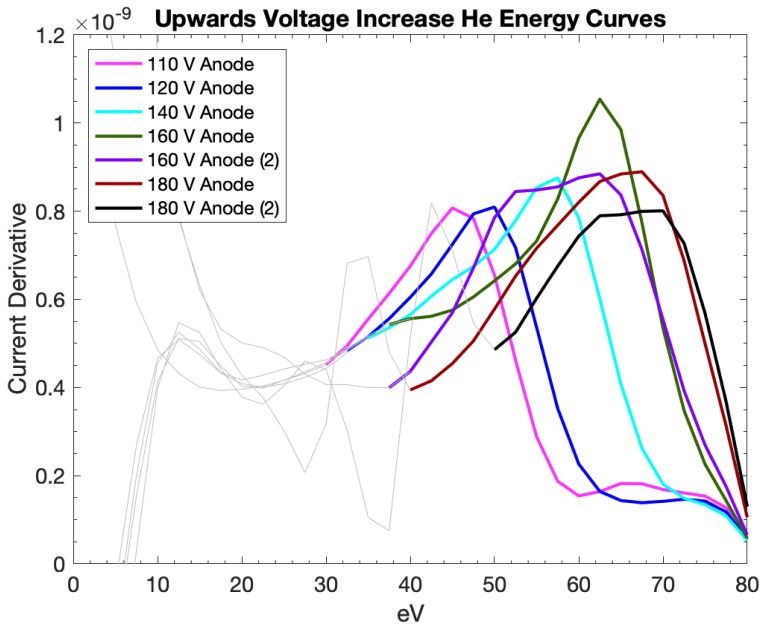

Figure 2.15. He plasma ion energy peaks found during the upwards voltage sweep from 0 V to 80 V.

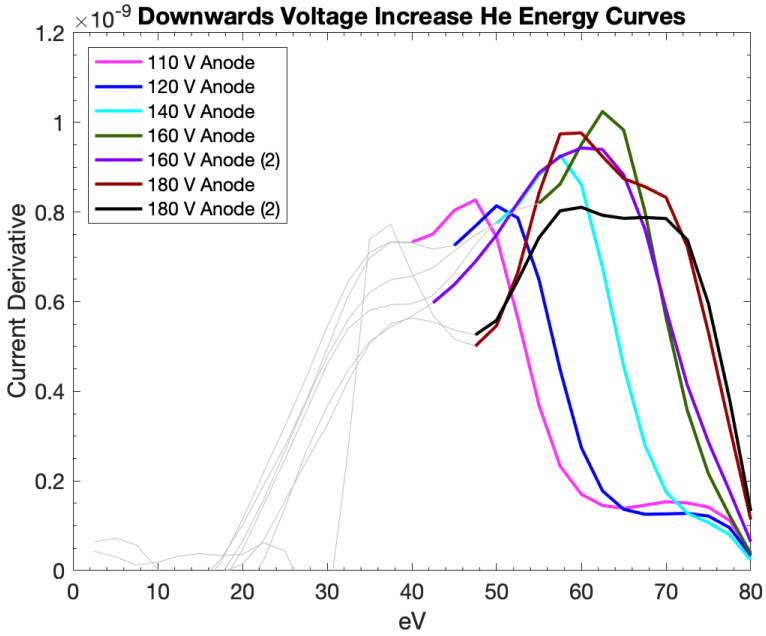

Figure 2.16. He plasma ion energy peaks found during the downwards voltage sweep from 0 V to 80 V.

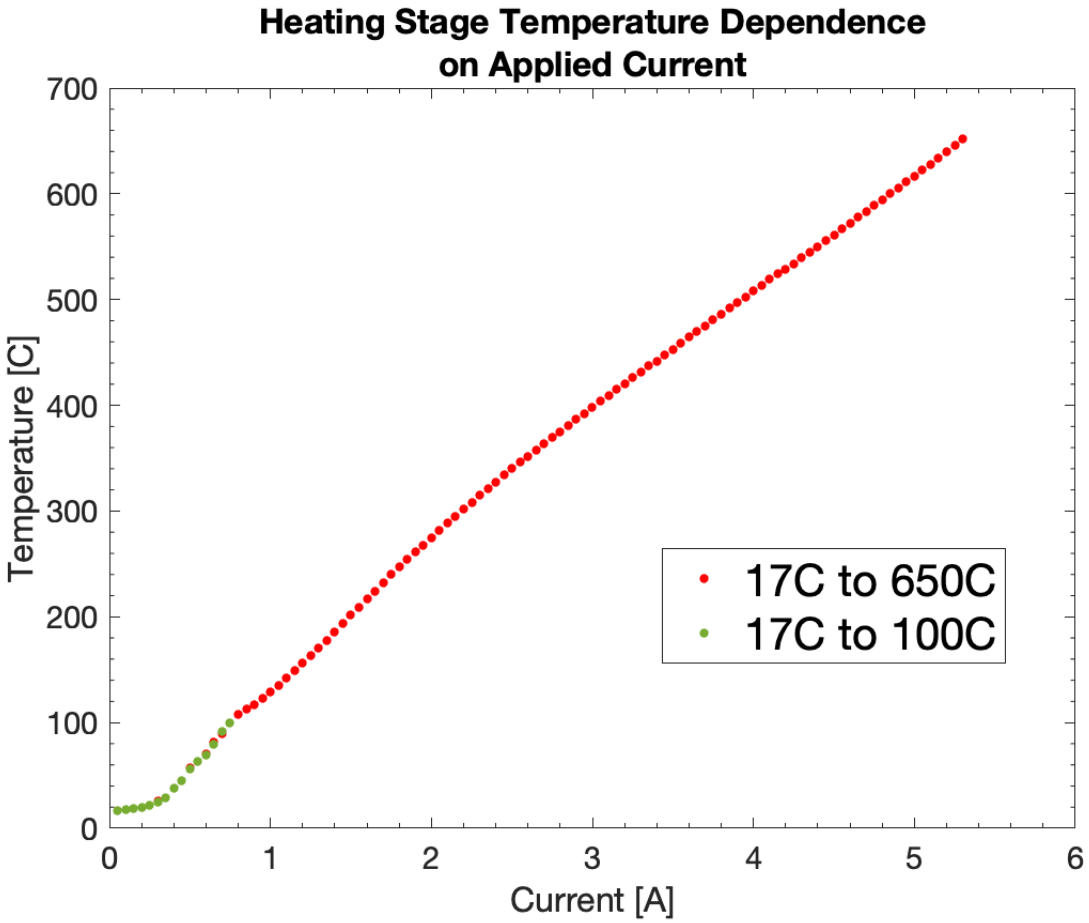

Figure 2.17. Temperature versus current measurements from two heating element tests performed for temperature increments of 0 to 650℃ (Red) and 0 to

tests that were performed to study the consistency and repeatability of the temperature increment as a function of the applied current. An initial temperature sweep from room temperature to 100°C was performed, shown as the green data. The following day an additional temperature sweep was performed from room temperature to 650°C shown in red. Performing the tests over a span of two days ensured the system had been cooled down entirely and the new test readings were not impacted by residual heat from the previous test. The data shows there exists an initial latency period with little to no significant temperature increase. As the applied current nears 0.40 Amps the temperature dependence on the applied current becomes relatively linear with some minor fluctuations taking place. No additional tests were performed given the consistent results between both tests, which also demonstrated that the system was in working order.

Chapter 3 He Plasma Exposures

3.1 Loading Stage Design

With the system parametrized and the plasma beam characterized, He plasma exposures of W were then performed. A circular boron nitride (BN) plate was designed to hold individual W samples centered in front of the incoming plasma beam. Figure 3.1 shows the BN plate design, and measurements in inches, with the outside diameter measuring 2 in. The sample is held in the middle of the plate with the help of a lip cutout. The outside diameter of the lip cutout measures 6 mm with the inside diameter measuring 5 mm. As the 6 mm sample is mounted, a heating element sits behind it to regulate the temperature of the W sample. A thermocouple sits in front of the sample, on the exposed side, but behind the lip cutout to measure the plasma induced current and shield it from direct exposure. The plate contains four additional hole cutouts for the throughput of heating element and thermocouple rods. This BN plate is covered by a secondary BN plate to reinforce the sample and thermocouple positions without putting too much stress on a single plate.

3.2 Sample Preparation

A total of twenty-five 6 mm by 0.5 mm W discs were polished to a 0.05 micron mirror finish by Travis Dixon from the Metallography Laboratory at Oak Ridge National Laboratory. Following polishing, all samples were annealed at 1000°C for 1 hour. High temperature annealing reduces the number of defects within the structure [57]. Once polished and annealed, the samples were exposed using Dr. Donovan's ECR source. Three samples were exposed at each exposure condition. With eight exposure conditions, a total of twenty-four samples were He plasma exposed. The additional W sample was left unexposed to be used as a reference sample.

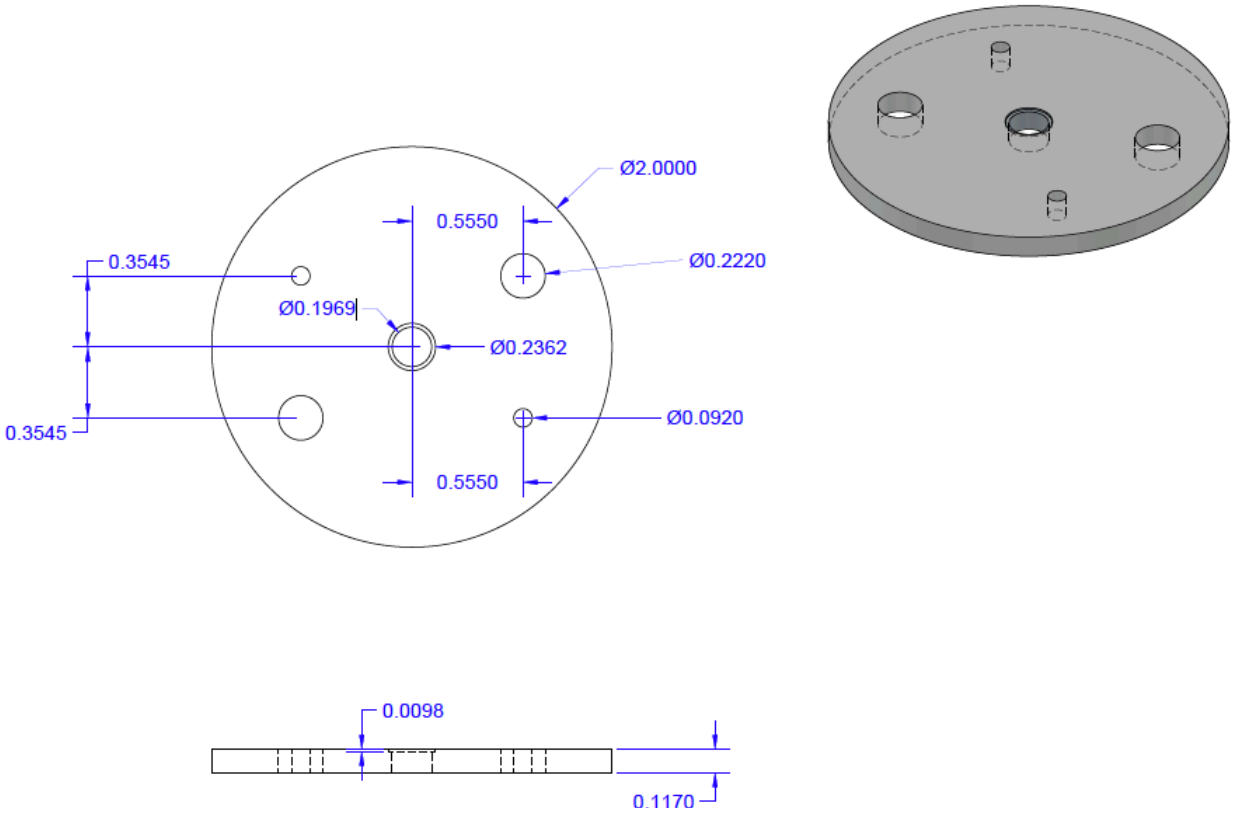

Figure 3.1. Sample holder BN plate design showing the lip cutout and the throughput holes for the thermocouple and heating element rods. All units are shown in inches.

3.3 Sample Loading

Samples were individually exposed one at a time to ensure that the samples were placed in the center of the plasma beam and obtained the largest incoming plasma flux. Additionally, this ensured the W disc received the same fluence throughout the entire surface area. The plasma beam distribution and spatial distribution from the center of the beam was estimated to follow a gaussian distribution based on visual observation of the beam, although it was not characterized. During each sample loading and exposure, the W disc was placed on top of a heating element. The thermocouple was place on top of the exposed sample surface. The BN plate with the lip cutout was placed over the sample and the thermocouple. During each sample loading it was important to secure the thermocouple behind the BN lip cutout. This ensured the current was read from the plasma beam coming into contact with the W surface and not directly with the thermocouple. For samples exposed at 600°C or 900°C, a current was applied to the heating element through two of the rods that intersect the BN plate. The current was supplied by the same Keithley 2260B-80-40 power source used during the RFEA voltage sweeps.

The Keithley 2400, used during the initial Faraday Cup flux measurements, was also used to measure the current incident on the W during experiment exposures. However, unlike the initial Faraday Cup flux measurements, the Keithley 2400 was not negatively biased during experiment exposures. This was to avoid changing the 70 eV energy peak produced using the same system parameters during the preliminary RFEA energy peak measurements. Biasing the Keithley 2400 to a negative voltage would cause the ions to experience an acceleration, thus changing the ion energy peak. Ideally, the energy peak would only be shifted by number of eV's equal to the number of volts the Keithley was biased at, however the degree of change was unknown and therefore it was decided to not incorporate an unknown variable.

3.4 He Plasma Sparking Conditions and Parameters

Although the system parameters that produced a 70 eV ion peak stable plasma had been found, it was extremely difficult to identically replicate during experimental exposures. The reason is the following: the chamber pressure is controlled through a butterfly valve furthermore it is controlled by an open/close switch. When the switch is engaged in the open or close position the valve begins to slowly open or close out of sight inside the chamber. The degree of openness or closeness can only be monitored through an ion gauge measured pressure reading. However, to add complexity to the fine-tuning of the system, when the ion gauge is turned on, it outgasses impurities present on the surface of the filament. As a result, the pressure in the chamber is impacted by the operation of the ion gauge such that observing the pressure impacts the pressure reading.

During RFEA tests it was possible to spark a stable plasma at higher pressures because multiple tests were being conducted throughout the entire day, day after day. Meaning there was not enough time for impurity accumulation on the ion gauge. Therefore, during RFEA tests it was possible to monitor the chamber pressure using the ion gauge. All that was left was to adjust the butterfly valve repeatedly between the open and close position until a pressure of 1.05E-3Torr was reached. This was highly time consuming, it would take a lot of repeated opening and closing of the valve sometimes for up to three hours. During RFEA tests the adequate pressure was only achieved at the end of the day after the system had been pumped down for most of the day.

The system had to be turned off at the end of every day for the safety of the lab equipment and personnel. An entire system pump down, fine-tuning, plasma sparking and stabilizing, and exposure had to be completed within a single workday. Some exposures required a plasma exposure of twelve hours. This meant it was not

possible to pump down the system for an entire day prior to experimental exposures. The chamber conditions for sparking a stable plasma had to be adjusted.

The ion energy peak had been found with the help of the RFEA tests, where it was found an anode voltage of 180 V and an extractor voltage of 80 V produced an ion energy peak of 70 eV. As long as the anode and extractor voltages remained unchanged, the ion energies would remain the same. It was the chamber pressure that required changing to a more easily attainable pressure setting where the butterfly valve was lightly if at all involved. Because the magnetron current required to spark and sustain a plasma is dependent on the chamber pressure, if the pressure was changed the magnetron current also had to be adjusted. During RFEA tests a magnetron current of 30 mA was compatible with a chamber pressure of 1.05E-3 Torr. Omission of closing the butterfly valve would result in a higher vacuum, lower pressure. Following the relationship observed between the chamber pressure and the magnetron current during the RFEA tests meant a lower magnetron current would be compatible with a lower chamber pressure.

A different current and chamber pressure would only result in a lower flux, not a different ion energy. During the initial experimental exposures, it was found that leaving the butterfly valve completely open produced an approximate chamber pressure of 5.8E-5 Torr. This meant a lower magnetron current was needed. After some adjustments between the chamber pressure and the magnetron current, it was determined that the highest current compatible with a chamber pressure of 5.8E-5 Torr was a magnetron current of 13.4 mA. Even raising the current by as much as 0.2 mA, from 13.4 to 13.6 mA, would extinguish the plasma.

After many preliminary tests of the system, and characterization of the plasma beam, it was determined that the highest attainable flux was 1.46E17 He m^{-2} s^{-1} . This was produced by placing the sample ¾ of an inch away from the plasma output head. Maintaining a background current of -9.22E-9 Amps and a live current of -4.6E-7 Amps. The butterfly valve was opened to the full extent.

Chamber pressure reading were not taken during exposures as to not affect the pressure. The anode voltage was set to 180 V and the extractor voltage to 80 V. And lastly, the magnetron current was set to 13.4 mA. These system parameters produced and sustained a plasma for 12 hours at a time. A longer exposure, if desired, would be possible given the stability of the plasma. However, for this dissertation, higher He fluence exposures were not investigated.

3.5 Reading He Flux Measurements and Total Fluence

The Keithley 2400 was connected to a computer with a LabVIEW program was used as a graphical user interface. Through LabVIEW it was possible to view, monitor and plot the current measured by the Keithley. Real-time monitoring of the current provides a real-time survey of the plasma beam and its stability. It is imperative to maintain the plasma beam as stable as possible to ensure the ion energy peak remains as close to 70 eV as possible. In addition to monitoring of the plasma, using Equation (2-1) the beam current was converted to flux and integrated as a function of time to determine the He fluence on the W. The fluence was plotted for the duration of the entire plasma exposure to ensure the desired fluence was reached. Once the fluence was reached, the exposure was complete and the plasma beam turned off.

W samples exposed to accumulated fluences of 5E21 He m^{-2} required an average exposure time of 11 hours. The exposure time was dependent on the plasma beam and flux produced on the day of exposure. Fluences of 5E20 He m^{-2} required a 1 hour long exposure, and 5E19 He m^{-2} only required 5 minutes on average. Samples heated to 900°C required an additional 2 hours of laboratory time for slow temperature ramping. Samples heated to 600°C only required an additional 40 minutes of temperature ramping. The temperature inducing current was increased at a rate of 0.5 Amps per minute as to not stress the heating element or the BN plates. Samples exposed at room temperature required no additional heating. They were exposed to an average room temperature of 17C. Exposures were performed over three months.

Chapter 4
LIBS and LAMS Measurements of Plasma Exposed Tungsten

4.1 A Brief Description of LIBS and LAMS

LIBS is the acronym for Laser Induced Breakdown Spectroscopy and LAMS for Laser Ablation Mass Spectrometry. Both are micro destruction laser-based techniques where a Nd:Yag laser, is focused onto a material of interest. The material quickly heats up and vaporizes (ablates) forming a plasma plume composed of excited ions. Within $0.5\mu s - 10\mu s$ of formation, the plasma quickly begins to recombine and cool down. Distinct emission lines are emitted as recombination takes place. A lens is externally located on a viewport to gather the light coming from the emission lines. With the help of optical fibers, the collected light travels to a filterscope fabricated by the Fusion Energy Division at Oak Ridge National Laboratory (ORNL) [58]. The emission line intensity is measured by photomultiplier tubes (PMTs) fitted with line dependent filters. The filterscope is capable of viewing twelve different emission lines with a total of twelve PMTs. The intensity of the lines is proportional to the quantity of the respective element found within the plasma plume. The line voltage intensities are analyzed to quantify the materials of interest found within the plasma.

LAMS takes place quickly after plasma recombination. With the help of a vacuum pumping system, the plasma forming vaporized particles are removed from the ablation chamber and guided to the quadrupole mass spectrometer (QMS) where they are characterized and measured in the form of a current signal. The current signals are analyzed to quantify the gas species of interest found within the plasma.

Capability of remote operation, in-situ analysis, and good sensitivity to light elements makes LIBS and LAMS an attractive diagnostic for usage in fusion reactors such as monitoring of the wall, divertor, and other plasma facing components (PFCs)[59]. The mass particles move slower than the speed at which the light is emitted and observed; therefore, this allows for the same laser ablation induce plasma plume to be used for both LIBS and LAMS experiments. Use of the same plasma plume by both techniques ensured the experiment conditions were the same. Performing the experiments under the same conditions greatly reduces error and simplifies the data analysis.

4.2 Our LIBS/LAMS System

Our LIBS/LAMS system is located in the LAMDA laboratory at ORNL. Figure 4.1 shows a photograph of our system where the Quantel Big Sky CFR Ultra Q-Switch 532nm Nd:Yag laser can be seen mounted on a plate at the very top as shown in the red circle[3]. The LIBS light collecting Nikon F3 lens is shown in a blue circle while the LAMS QMS is shown towards the back of the system in the yellow circle. The Varian TriScroll 600 oil-free dry scroll vacuum pumps are located on the floor behind the system. These are the initial pumps used to bring the chamber pressure down to $\sim 10^{-3}\ Torr$. At this point the Pfeiffer HiPace 80 turbo-drag-pumps(71 l/s), shown in the green circle, steps in and works in conjunction with the dry pump to bring the chamber pressure further down to $\sim 10^{-8} - 10^{-7}\ Torr$[3].

Figure 4.2 shows a diagram of the LIBS and LAMS system components. The incoming laser beam starts at the top of the system denoted as Section1 laser[1]. Here the Nd:Yag laser produces a laser beam of the desired energy. For W materials the laser is used at 3% energy equivalent to 1.8 mJ. The reasoning behind 3% energy use is explained in section 4.3. The beam is then directed towards the turning mirror where it gets bent 90^{o} downwards to travel through expanding and collimating optics whose focal point can be adjusted using a z translating lens tube[3].

Figure 4.1. Picture of the LIBS and LAMS system found at ORNL. Some of the components are shown in the colored circles for easier identification of them. The turbo pump is shown in green, the light collecting optics in blue, the laser in red, and the QMS in yellow[3]. Image modified from reference [3].

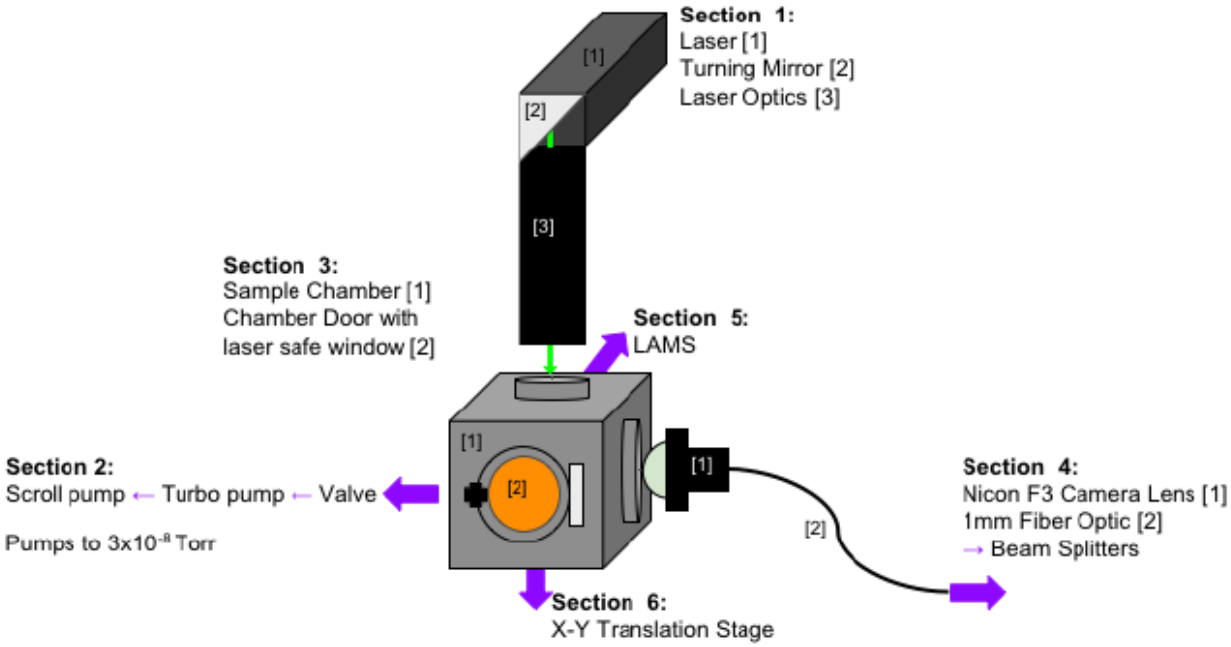

Figure 4.2 Diagram showing the main components pertaining to the LIBS LAMS system located at ORNL in the LAMDA lab[3].

The focal point depends on the height of the sample being ablated. It is best to focus the laser beam just below the surface to stay within focus. As ablation craters accumulate the laser is further focused due to the change in the focal point below the surface. If placed above the surface, the laser will increasingly become unfocused as a function of cumulative ablation craters and as a result, will produce more de-focused, stochastic crater formation.

The left side of the Figure 4.2 diagram, Section 2, shows the location of the valve separating the turbo pump and the scroll pump from the chamber. The sample chamber is shown in Section 3 where the focused laser beam passes through the laser safe window and ablates the material found at the material-laser interface. The emission lines are seen through the porthole, on the right of the diagram, by a light collecting lens where an optical fiber guides the light back to the filterscope as described by Section 4. LAMS takes place in the back portion of the sample chamber, Section 5, where dry pumps guide the particles into the QMS. An X-Y stage allows the user to move the sample in an X-Y plane for additional spots of interest to be ablated as shown in Section 6[3].

4.3 Preliminary System Testing

Preliminary testing was done by Dr. Guinevere Shaw to better understand the capabilities and limitations of the system[3]. The crater formation as a function of laser energy was tested to determine the lowest energy at which W break down occurs and reproducible craters are formed. Small ablation energies are preferred to produce shallow depth craters. Formation of shallow craters provides higher depth resolution. A thorough description of this experiment and iterations is found in Dr. Shaw's dissertation [3] and will not be further described here. The results of the experiments detailing crater depth and width evolution are shown in Figure 4.3. Plot a) shows the ablated depth dependence as a function of accumulated ablations. The first few ablations are best represented by a small cubic growth instead of linear.

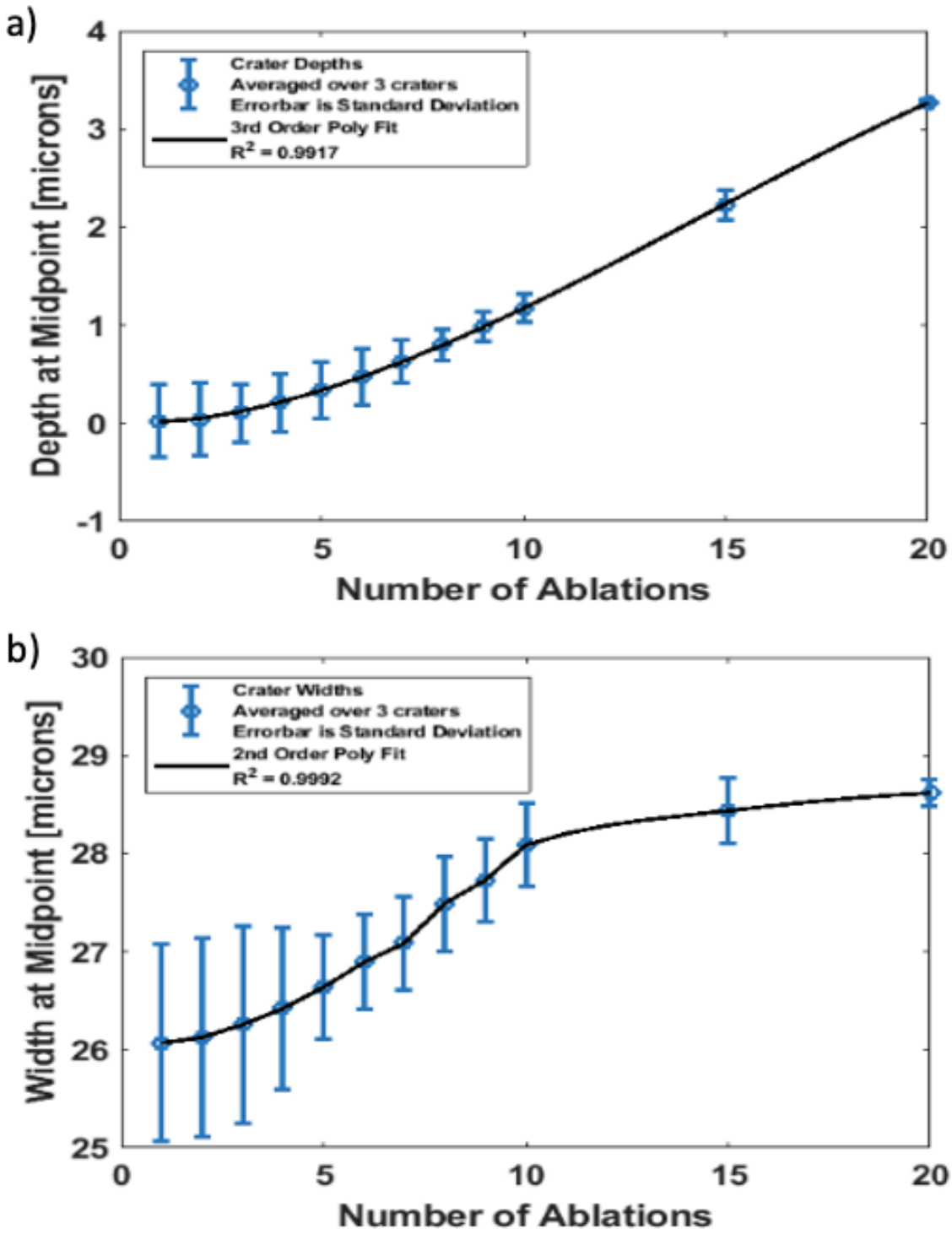

Figure 4.3. Plots showing the crater depth dependence on number of ablations(left) and the crater width dependence on number of ablations(right). Both are fir with polynomials to interpolate values between 10, 15, and 20, as reproduced from Ref.

From the 5th ablation and above the depth growth approaches a linear dependence as a function of subsequent laser ablations. Plot b) shows the crater width dependence as a function of the same accumulated ablations. It is evident there is significant crater widening taking place within the first 10 ablations. Crater Widening effects have been previously observed in LIBS experiments[60]. This crater widening must be accounted for during data analysis as is shown in section 4.5.

4.4 LIBS/LAMS Calibrations

Each LIBS and LAMS system has to be calibrated to maintain high accuracy of data acquisition. Both require different independent calibrations. The LIBS calibration is quite involved and as a result, it is performed every two years. The LAMS calibration is a simpler standard leak calibration that can be performed every 6 months to a year or as frequent as the user desires. In the following sections the LIBS and LAMS calibrations are described in detail.

4.4.1 LIBS Gain Calibration

The LIBS gain calibration needs to be performed for each individual PMT tube. All of the calibration directions for the filterscope can be found in the ORNL Filterscope Manual with the gain calibrations in Appendix B.3[58]. The total gain(G_{Tot}) of a PMT tube is dependent on the PMT gain(G_{PMT}) and the amplifier gain(G_{AMP}). However, the amplifier gain is assumed to be linear and is therefore not calibrated. For the LIBS system at ORNL the G_{AMP} is kept at 1 for all applications as recommended per the filterscope manual. The G_{PMT} is best described as the current amplification in the PMT or the ratio of the anode current to the photo-electron current. G_{PMT} has a non-linear relationship to the input control voltage the PMT is operated at. Therefore, its relationship has to be investigated and calibrated against. This simplifies the G_{Tot} dependence to G_{PMT} only.

The initial gain calibration is done through the use of ND filters. ND filters are neutral density filters that reduce the amount of light passing through the lens and reaching the optics in this case the PMT. By doing so, the PMT control voltage can be increased without overloading the PMT. The G_{PMT} relationship to the input control voltage is investigated through filterscope tube dependent light voltage measurements taken as a function of ND filters and the control voltage. The exact instructions to this procedure can be found in the ORNL filterscope manual appendix B.3 page B-4 through B-7[58].

Shots taken at every control voltage must be recorded in an excel sheet as shown in Figure 4.4. It is recommended to use the format year/month/date/00, example for 2022 February 05: 22/05/20/00. This format is to omit overwriting of older data. Since the shot number is based on a calendar format it will never repeat itself thus avoiding accidental overwriting of data. In order to process the gain calibration data, the user needs access to the GitHub/ORNL-Fusion/Fscope repository. Once having done so, the user can find and pull the "fscope_gain_calibration.py" script. Importing fscope_gain_calibration as fgc allows the user to execute the "main" function as fgc.main(2, 'LIBS_2021_gain_calib.xlsx', 'Sheet1', fitPower=False) with 2 pertaining to the Tube number, LIBS_2021_gain_calib.xlsx the excel sheet where the gain calibration shot numbers are found Figure 4.4 is provided as an example, and Sheet1 referring to the sheet tab the shots are recorded in the excel document. The output will consist of the same plots shown in Figure 4.5 with the top plot providing the G_{PMT} to control voltage relationship polynomial fit coefficients. The middle plot shows a goodness of fit measurement, the Median Percentage Error (MPE). The MPE provides the median of the absolute percentage error of the data. Mathematically, MPE is defined as the fraction of the difference between the data and the fit of the data over the data. A fit with an MPE < 5% is desirable however, not likely with older PMT's which are currently installed in the filterscope. The third plot shows the MPE percentage value at every control voltage used during the gain calibration.

	A	B	C	D	E	F	G
1	V_cont	TUBE01_On	TUBE01_Off	TUBE02_On	TUBE02_Off	TUBE03_On	TUBE03_Off
2	0.05	21051300	21051301	21051340	21051341	21051380	21051381
3	0.10	21051302	21051303	21051342	21051343	21051382	21051383
4	0.15	21051304	21051305	21051344	21051345	21051384	21051385
5	0.20	21051306	21051307	21051346	21051347	21051386	21051387
6	0.25	21051308	21051309	21051348	21051349	21051388	21051389
7	0.30	21051310	21051311	21051350	21051351	21051390	21051391
8	0.35	21051312	21051313	21051352	21051353	21051392	21051393
9	0.40	21051314	21051315	21051354	21051355	21051394	21051395
10	0.45	21051316	21051317	21051356	21051357	21051396	21051397
11	0.50	21051318	21051319	21051358	21051359	21051398	21051399
12	0.55	21051320	21051321	21051360	21051361	21051400	21051401
13	0.60	21051322	21051323	21051362	21051363	21051402	21051403
14	0.65	21051324	21051325	21051364	21051365	21051404	21051405
15	0.70	21051326	21051327	21051366	21051367	21051406	21051407
16	0.75	21051328	21051329	21051368	21051369	21051408	21051409
17	0.80	21051330	21051331	21051370	21051371	21051410	21051411
18	0.85	21051332	21051333	21051372	21051373	21051412	21051413
19	0.90	21051334	21051335	21051374	21051375	21051414	21051415
20	0.95	21051336	21051337	21051376	21051377	21051416	21051417
21	1.00	21051338	21051339	21051378	21051379	21051418	21051419

Figure 4.4. Excel sheet recording of every shot taken during the 2021 Gain calibration of the ORNL filterscope.

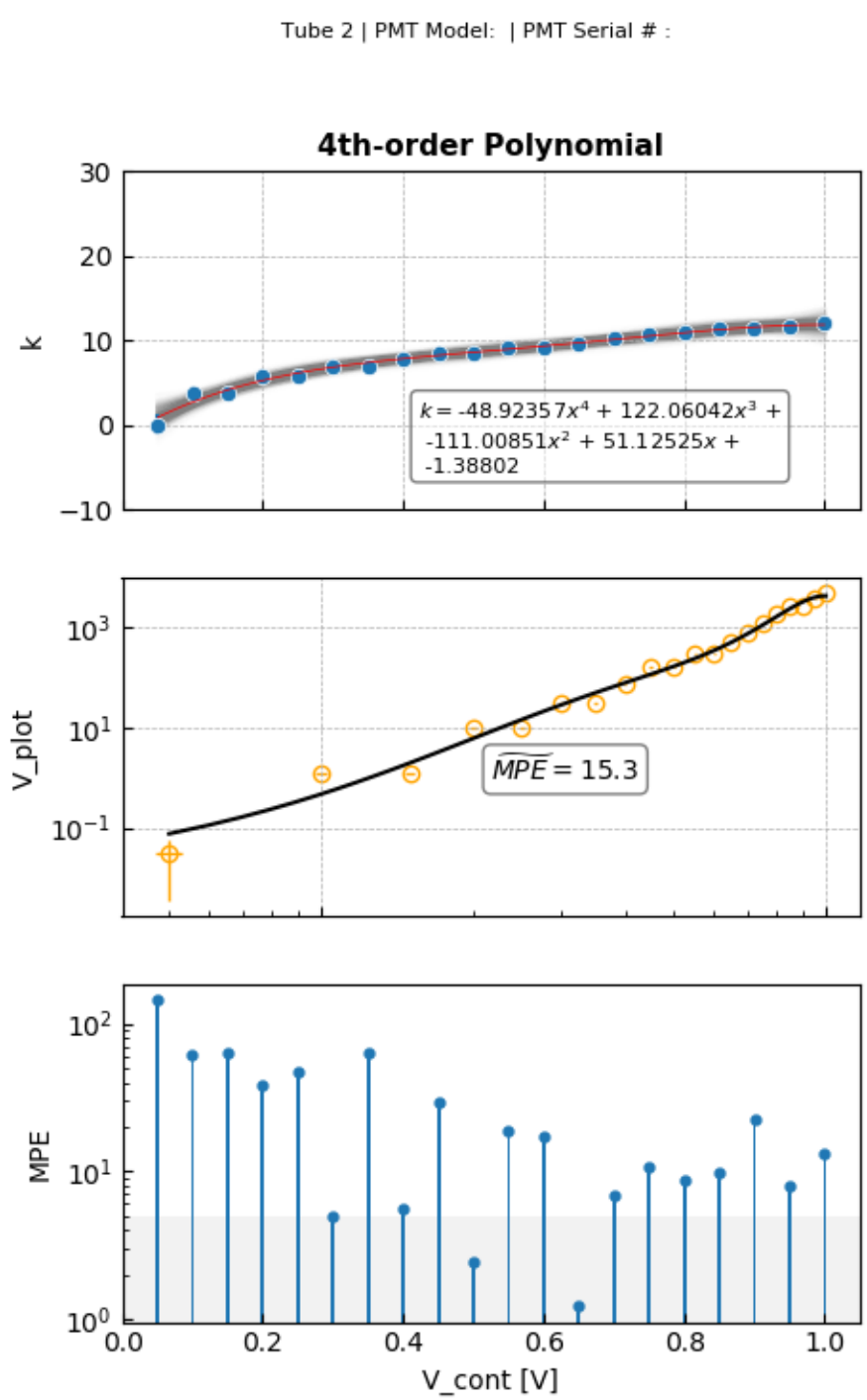

Figure 4.5. ORNL filterscope Tube 2 output plots produced from executing the fscope_gain_calibration.py main function. Polynomial fit coefficients shown in the first plot (top).

At this point the gain calibration portion is complete, and the user must continue with the absolute calibration to solve Equations (4-1) and (4-2). The fit coefficient values found in the top plot of Figure 4.5 are used to solve for G_{PMT} by solving the following equation

$$G_{PMT} = e^{k} \tag{4-1}$$

Where,

$$k = A_0 + A_1 * V_{cont} + A_2 * V_{cont}^2 + A_3 * V_{cont}^3 + A_4 * V_{cont}^4 \tag{4-2}$$

Any voltage can be chosen for V_{cont}. However, it is best to choose one based on the final setup the system is to be used at. To calculate and find the G_{PMT} values, V_{cont} can be found during the absolute calibration portion of the system, discussed in section 4.4.2.

4.4.2 LIBS Absolute Calibration

A filterscope is different to a spectrometer and should not be confused with one. A filterscope is a radiometer that measures the total radiant power passing through a band-pass filter. The radiant power is related to spectral information found inside the entire band-pass range, not just the line of interest. The exact photo-emission line radiation is inferred rather than directly measured, unlike a spectrometer. However, a particle flux can still be determined through line-normalized radiance and by solving Equation (4-3)

$$\Gamma_{A_{i\to k}} = 4\pi \cdot L_{A_{i\to k}} \left(\frac{S}{XB}\right)_{i\to k} \left[\frac{atoms}{\text{sec} - m^2}\right] \tag{4-3}$$

The first term 4π, is used to convert the radiant source from solid angle to spherical and do away with steradian units. The second term $L_{A_{i\to k}}$ is the line-normalized

radiance that permits the conversion of radiative power to photons per second per steradian per centimeter squared, as described in Equation (4-4).

The line-normalized radiance $L_{A_{i\to k}}$ is further extended into its individual components, shown in Equation (4-4).

$$L_{A_{i\to k}} = 5.03 \times 10^{24} \cdot \lambda_{i\to k} \cdot \frac{\Delta\lambda_{i\to k}}{\Delta\lambda_{PN}} \cdot L_{PN}[\frac{ph}{s-str-m^2}] \qquad (4\text{-}4)$$

The line normalized radiance equation can be divided into four components. The first, 5.03×10^{24} is the value resulting from the inverse Planck's constant[Joules] times the speed of light[meters]. Planck's constant is not to be confused with hbar. This is shown in Equation (4-5) for clarity.

$$^{1}/_{1.98644E-25}\,[^{1}/_{J*m}] = 5.03 \times 10^{24} \qquad (4\text{-}5)$$

There is no unit transformation performed on the 5.03×10^{24} value. The second term, $\lambda_{i\to k}$ is the value of the line of interest in units of meters. The third term, $\frac{\Delta\lambda_{i\to k}}{\Delta\lambda_{PN}}$ is the ratio of the line-normalization band pass to the peak-normalization band-pass. Given that this is a ratio, this term is unitless. Lastly, the fourth term L_{PN}, is the peak-normalized radiance. This is the term that incorporates the LIBS voltage signal experimentally measured that is later converted to a particle flux. Additionally, L_{PN} is also dependent on $R_{PN}(\lambda_{PN})$, found during the absolute calibration of the filterscope. All the terms for L_{PN} are shown in Equation (4-6)

$$L_{PN} = [\frac{V_{PMT}}{G_{TOT}}]_{sig} \cdot \frac{1}{R_{PN}(\lambda_{PN})} \qquad (4\text{-}6)$$

L_{PN} is in units of $\frac{W}{sr\cdot m^2}$. These units are a result of the $1/R_{PN}(\lambda_{PN})$ where,

$$R_{PN}(\lambda_{PN}) = [\frac{V_{PMT}}{G_{TOT}}]_{cal} \frac{1}{L_{filter-TOTAl}} \qquad (4\text{-}7)$$

When taking the inverse of $R_{PN}(\lambda_{PN})$ and multiplying by $[\frac{V_{PMT}}{G_{TOT}}]_{sig}$, the voltage and gain units cancel out leaving only $L_{filter-TOTAL}$ in units of $[\frac{W}{sr \cdot m^2}]$. $L_{filter-TOTAL}$ is the integrated filtered radiance described in detail in the following section. With all the components written in the units mentioned above, $L_{A_{i\to k}}$ has units of $[\frac{ph}{s-str-m^2}]$. It must be mentioned that in the filterscope manual $L_{A_{i\to k}}$ is in terms of $[\frac{ph}{s-str-cm^2}]$ not per m^2 as written here. $L_{A_{i\to k}}$ can be written in either units, per cm^2 or per m^2 however, the final flux units will depend on the chosen unit.

Both the band-pass ratio and the integrated filtered radiance are obtained from the absolute calibration of the filterscope. During the absolute calibration, a calibrated light sphere, with a known calibration curve, is used. The filtered radiance consists of each filter transmission fraction curve multiplied by the light sphere calibration curve range found within the respective filter wavelength range. The filter transmission curve is either given by the manufacturer or can be found using a spectrometer. For this work, the McPherson measuring microscope, located in the Fusion Energy Division building at ORNL, was used to find the transmission fraction curves for all the filters. The calibration light sphere was provided by Dr. Theodore Biewer. The light sphere calibration curve values are shown in the Appendix.

Multiplication of the filter transmission fraction and the light sphere calibration curves provides the filtered radiance L_{filter} shown in page 35 of the filterscope manual[58]. It is the light sphere calibration curve units that determine the units of the $L_{filter-TOTAL}$ which consequently determine the L_{PN} units, then the $L_{A_{i\to k}}$ units, and eventually the final flux units, $\Gamma_{A_{i\to k}}$. For the light sphere used, the original units are in $[W/(sr \cdot cm^2 \cdot nm)]$. It was decided to change cm^2 to m^2 early in the derivation to avoid any unit conversion errors later in the derivation. Note, multiplication of the curve by the transmission fractions does not change the units. Therefore, it is important to ensure the transmission fraction is a fraction and not a percentage. Integration of the newfound filtered radiance does away with the nm

units and results in an integrated filtered spectral radiance with unis of $[W/(sr \cdot m^2)]$, same contributing units found in $L_{A_{i\to k}}$ and $\Gamma_{A_{i\to k}}$.

The absolute calibration is paired with an experimental campaign. The experimental campaign must be performed in order to solve the above-mentioned equations. Without this the final flux cannot be determined. During the experimental campaign, the system must be arranged in the final state it will be used at so that we calibrate against that exact arrangement and reduce systematic error.

A channel consists of a PMT in combination with the pertaining band-pass filter. Every channel must be individually calibrated. There are natural variations in every PMT with some developing over time. It cannot be assumed that all PMTs will produce the same voltage output at the same V_{cont}. Additionally, there exist external factors that can differently impact the light reaching the PMT. Beam splitters will reduce the amount of light reaching the PMT depending on what transmission percentage is allowed. Filters will also alter the amount of light and the light wavelengths reaching the PMTs.

In our filterscope system there are only three channels currently in use, meaning three PMT tubes in combination with their respective filters. Tube 1 is used in combination with a helium filter to identify 706.53 nm line. Tube 2 is used in combination with a deuterium or an oxygen filter to identify line 656.3 nm or 777.4 nm, respectively. Finally, Tube 3 is used in combination with a tungsten filter to identify line 400.1 nm. All three channels are connected by a beam splitter containing a single light collecting optical fiber entry port. An optical fiber is used to connect the filterscope channels with the light sphere. One end of the optical fiber is attached to the beam splitter entry port and the other to the light sphere entry port. Each channel is governed by a control voltage (V_{cont}) independent to the other channel's control voltages. The calibration control voltages were chosen based on the voltage that produced an output voltage closest to a minimum of 1 V. In our filterscope system Tube1 V_{cont} = 0.45, Tube2 V_{cont} = 0.50V, Tube3 V_{cont} = 0.75 V. After incorporation of

the beam splitter and filters light is reduced significantly by the time it reaches Tube 3 so the Vcont is set to a higher voltage of 0.75 V.

The light sphere is turned on to the recommended calibration settings. The calibration parameters at the moment of use were 5.579 A for the lamp current and 4302 fL for luminance. One to two filterscope shots are taken with the light sphere connected and turned on. The shots data is analyzed to determine the output voltage as a function of the control voltage for each channel. With the integrated filtered radiance and the experimental campaign output voltage and control voltage (V_{cont}) known, Equation (4-7) and (4-6) can be solved, in that order.

In addition to the integrated filtered radiance, Equation (4-7), $R_{PN}(\lambda_{PN})$, requires the output voltage and the absolute calibration gain total. The output voltage is found during the absolute calibration experimental campaign. The gain total can be calculated with the control voltage used during the absolute calibration experimental campaign in combination with the fit coefficients found during the gain calibration. Equation (4-6) is solved similarly except gain total is dependent on the V_{cont} used during LIBS-LAMS experiments (not absolute calibration experimental campaigns) and the V_{PMT} is the output voltage signal seen during LIBS-LAMS experiments. Multiplying by inverse $R_{PN}(\lambda_{PN})$ solves Equation (4-6). The calculations can be simplified by operating the system at the control voltages it was calibrated at. It is important to note that in the filterscope manual the peak-normalized responsivity is interchangeably referenced as $R_{PN}(\lambda_{PN})$ or R_{PN-MAX} because the peak by default is the max. From this point forth it will be references as R_{PN-MAX}.

The line-normalization band-pass and the peak-normalization band-pass are key component quantities that convert the filterscope system from a qualitative to a quantitative measuring diagnostic. The band-pass ratio is directly related to the ratio of the peak(max) responsivity to the line-normalized responsivity. To find this ratio, first the spectral peak-normalized responsivity $R_{PN}(\lambda)$ has to be determined. $R_{PN}(\lambda)$ is to not be confused with $R_{PN}(\lambda_{PN})$. $R_{PN}(\lambda)$ is the spectral peak-normalized

responsivity over the entire filter wavelength range while $R_{PN}(\lambda_{PN})$ is the maximum of the peak-normalized responsivity.

$R_{PN}(\lambda)$ is arbitrarily defined by setting the filtered spectral radiance L_{filter} to unity. That is, dividing the entire L_{filter} curve by the maximum value of the L_{filter} curve. This returns a unitless value. The newfound unity curve is then multiplied by R_{PN-MAX}, where R_{PN-MAX} is the same as Equation (4-7) or the maximum of the $R_{PN}(\lambda)$. Both values should be equal. The resultant $R_{PN}(\lambda)$ curve is in units of $V \cdot str \cdot m^2/W$. The manual shows an example of an $R_{PN}(\lambda)$ in Figure A4 [58].

The peak-normalized band-pass is defined from the peak-normalized spectral responsivity curve as given by Equation (4-8)

$$\Delta\lambda_{PN} = \frac{\int R_{PN}(\lambda)d\lambda}{R_{PN-MAX}} \tag{4-8}$$

And the line-normalized wavelength band-pass is defined in Equation (4-9) as

$$\Delta\lambda_{i\to k} = \frac{\int R_{PN}(\lambda)d\lambda}{R_{PN}(\lambda_{i\to k})} \tag{4-9}$$

Where the responsivity $R_{PN}(\lambda_{i\to k})$ is the R_{PN} value, in the peak-normalized spectral responsivity curve, at the wavelength of interest. Taking the ratio of both band passes with the line-normalized wavelength band-pass divided by the peak-normalized spectral responsivity curve cancels out both integrals leading to equation

$$\frac{\Delta\lambda_{i\to k}}{\Delta\lambda_{PN}} = \frac{R_{PN-MAX}}{R_{PN}(\lambda_{i\to k})} \tag{4-10}$$

It is in this manner that the two band-pass ratios are directly related to the ratios of the maximum and line responsivities. Again, as a ratio, this term is unitless. At this point all of the equations can be solved in the reverse order up to Equation (4-4), the line-normalized radiance $L_{A_{i\to k}}$.

To solve Equation (4-3), and find the particle flux, the S/XB coefficient must be determined. This can be found through the relationship $\left[\frac{S}{XB}\right]_{i\to k}$.

Where S is the ionization rate coefficient,

$$S \equiv < \sigma_I \nu_e > [\frac{m^3}{s}] \qquad (4\text{-}11)$$

X is the excitation rate coefficient,

$$X \equiv < \sigma_{Exg} \nu_e > [\frac{m^3}{s}] \qquad (4\text{-}12)$$

and B is the branching ratio,

$$B \equiv \frac{A_{i\to k}}{\Sigma_{k\leq i} A_{i\to k}} \qquad (4\text{-}13)$$

the ratio of the probability of a transition from a specific upper level to a lower level ($A_{i\to k}$) to the total probability of transition from the same upper level to any other lower level ($\Sigma_{k\leq i} A_{i\to k}$).

S/XB quantities can be obtained from the ADAS database for an array of common elements. In order to retrieve the correct values, the electron temperature (T_e) and electron density (n_e) of the produced plasma must be known. The S/XB values used in our LIBS-LAMS experimental setup were obtained by Dr. Guinevere Shaw [3] from a paper written by Farid et al [61] for a plasma produced by a ~1E15 W/m^2, 532nm ND:YAG laser operated at ambient pressure on polycrystalline tungsten. It was estimated these conditions produced a plasma plume of ~1E17 cm^{-3} n_e and 2eV T_e[3, 61]. However, these plasma characteristics were found for a plasma produced at ambient pressures. So, to find the plasma characteristics under high vacuum conditions Dr. Shaw consulted a secondary paper by Farid [62] where the electron density and temperature pressure dependence was studied in the range of 1 ATM to 1E-6 Torr where Cu was ablated. Cu is assumed to have similar electron density to that of tungsten as well as temperature trends and so using Cu in place of W, for pressure dependence analysis, was deemed viable. The pressure dependent Cu density and temperature trends were then spline fit. Using the estimated W electron

density and temperature in the fit function determined an estimated plasma of density equal to $4E18\,cm^{-3}$ and a temperature of 2.2 eV in ultra-high vacuum conditions.

To summarize, the first paper by Farid [61] provided electron density and temperature values. The second Farid paper [62] provided the electron temperature and density pressure dependent trend for Cu. Cu is a substitute for W based on the similar electron density. Using the Cu pressure dependence trend provided electron density and temperature values for W in ultra-high vacuum conditions.

Now, the S/XB values for a plasma density of $4E18\,cm^{-3}$ and a temperature of 2.2 eV are not available on the ADAS database. Instead, Dr. Shaw retrieved them from the FLYCHK data base [3, 63, 64]. It is important to note that the S/XB coefficients used in our LIBS have never been directly measured, only inferred based on other works. The significance of this will be further be explained in section 6.3.

Finally, upon reaching this point in the absolute calibration, all the terms are known to solve Equation (4-3), and the particle flux. From the particle flux equation, it is possible to find the total number of atoms per second by multiplying Equation (4-3) by an area in units of m^2. This area pertains to the plasma plume cross section area as observed by the light collecting lens show in Figure 4.2, section 4, item [1]. Doing so returns number of atoms per second. This value can then be time integrated to find total number of atoms. Every laser induced ablation produces a $2-10\mu s$ [60] voltage signal that directly translates to a flux, therefore total number of atoms/s can be found for every ablation. By performing time integration over the $10\mu s$ voltage it is possible to solve for total number of removed atoms at every ablation. The total number of He atoms can then be divided by the removed W volume and converted to an atomic part per million quantity as described in Section 4.5.

4.4.3 LAMS Standard Leak Calibration

The LAMS calibration is much simpler and can be performed in 30 minutes. Processing the calibration data is also quite fast and simple. Therefore, the system can be calibrated before each experiment, or as often as desired. It is best to calibrate the system in the same arrangement as operated during experiments. Meaning the pathway of the particles during calibration should be as close as possibly to the pathway during experiments. Figure 4.6 shows a QMS spectrum obtained during a calibration run. The X-axis is in terms of the nth data point. The axis name "location" pertains to the nth number that data point holds in the output file, therefore location in the output file. This is just the preferred x-axis used to simplify the data analysis. Using time instead of data point location can complicate the analysis because every particle reaches the QMS detector at slightly different times. So analysis as a function of time can become convoluted when dealing with multiple species since they all have different times of travel as a result of different masses. The Y-axis is the QMS recorded current readings during the calibration run, also during experiments but in this section only the calibration is described in detail. The Y-axis is shown in logarithm scale given it spans several orders of magnitude.

The LAMS system was calibrated against two gasses, He, and D_2. The calibration was done using the standard leak method. A standard leak consists of a compressed gas specific cylinder that has been calibrated by the parent company to release a pre-determine gas leak when the valve is opened [65]. The gas leak rate is provided by the company in terms of atm-cc/s or mol/s. For our purposes we use the unit mol/s. As the valve is opened it produces a spectrum similar to the one shown in Figure 4.6. Each calibration campaign will yield slightly different spectrums since the system changes with time. It is precisely because of these small fluctuations that the system needs to be calibrated every 6 months or as needed.

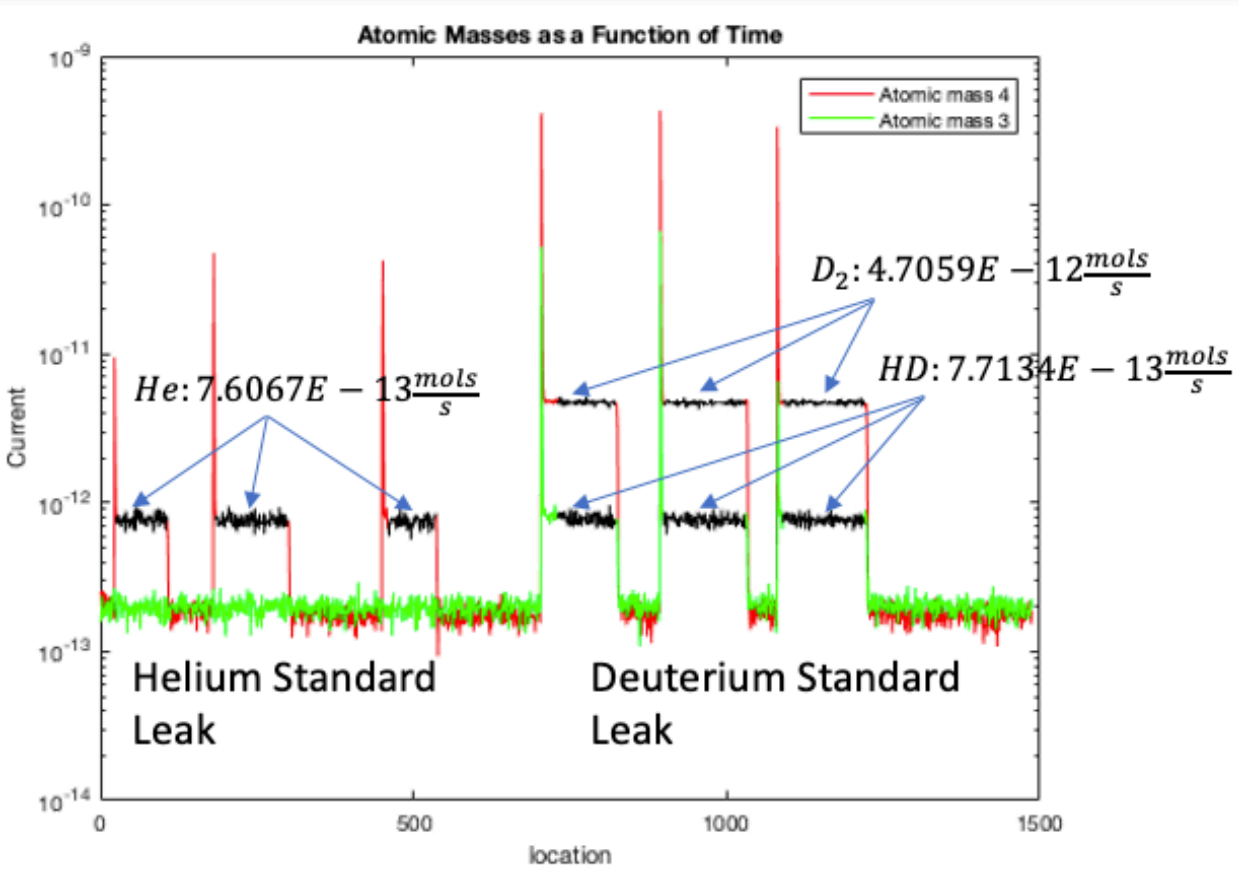

Figure 4.6. QMS output during calibration of the LAMS system performed on February 4th 2022.

The He calibration was performed first to avoid any deuterium attaching to the walls and impacting the helium calibration if performed after the deuterium calibration. Three readings were taken for each gas, He and D. A reading consists of opening the cylinder valve fully and allowing gas to flow for a period of time. This is then followed by fully closing the valve for a smaller period of time to allow the current reading to reach background levels. This is performed at least three times to obtain a statistically reliable calibration. The three helium readings can be observed in Figure 4.6 from location 0 to location 500.

The He cylinder valve is closed for the last time and some time is allowed for the system to return to background current levels. At this point the D calibration can take place. Similarly, to the He calibration, three readings are taken during the deuterium calibration. These three readings for the D calibration are shown from estimated location 600 to location 1500 in Figure 4.6. The preceding peak in every reading is due to the initial pressurized gas rushing into the ultra-high vacuum chamber before stabilizing. This peak should not be considered in the analysis of the data.

Finding the He calibration coefficient is simpler than the D coefficient. First the three He current readings (shown in black) must be averaged to find a single He current value. During this calibration, our He current value was 7.6067E-13 mols/s. The cylinder standard leak rate determined by the company is 4.38E-13 mol/s. Dividing the He current value by the gas release rate yield a value of 0.5758 mol/C. This is shown in Equation (4-14) for clarity.

$$\frac{4.38E-13\,\frac{mol}{s}}{7.6067E-13\,A} = 0.5758\,\frac{mol}{C} \qquad (4\text{-}14)$$

During LAMS experimental data analysis, the LAMS signal is multiplied by this calibration coefficient and Avogadro's number to yield the number of atoms per second. This is shown in Equation (4-15) for clarity.

$$Signal[A] * 0.5758\frac{mol}{s \cdot A} * 6.022E23\frac{atoms}{mol} \Rightarrow \frac{atoms}{s} \qquad (4\text{-}15)$$

Calculation of the D calibration coefficient is similar, but requires additional steps to those of the He calibration.

During the D calibration a current increase is seen on 2 different mass readings, amu3 and amu4. The amu4 signal contains both He and D_2 information. Our QMS cannot distinguish between amu = 4.0026 (He) and amu = 4.0282 (D_2). The amu3 signal measures HD. Therefore, this relationship can be utilized to differentiate the D signal from the He signal in amu4. Dividing the D_2 current by the HD current, during calibration, provides a ratio that is used in conjunction with the amu3 signal to determine the D in amu4. During this calibration that ratio was 6.101 as shown in Equation (4-16)

$$\frac{D_2}{HD} = \frac{4.7059E-12\frac{mol}{s}}{7.7134E-13\frac{mol}{s}} = 6.101 \qquad (4\text{-}16)$$

This means that for every HD, 6.101 D_2 are registered. Therefore, during experiments, the amu3 (HD) signal is multiplied by 6.101 to determine the D_2 signal. Now knowing the D_2 signal, this can be subtracted from amu4. The difference is deemed to equal the He signal in amu4. These relationships are shown in the below equations.

$$HD_{signal} * \frac{D_2}{HD} = D_{2_{signal}} \qquad (4\text{-}17)$$

Substituting with the ratio value,

$$amu\,3_{signal} * 6.101 = D_{2_{signal}} \qquad (4\text{-}18)$$

Provides the final He signal in amu4.

$$He_{signal} = amu\,4_{signal} - D_{2_{signal}} \qquad (4\text{-}19)$$

4.5 Crater Volume Analysis

4.5.1 Volume Analysis Algorithm Correction

The volume of the ablation induced crater is not accurately represented by any single shape. The shape of choice must resemble the surface roughness of the crater surface to best calculate the removed volume during an ablation. This is achieved through a combination of three shapes, cylinder, cone, and truncated cone in which the resultant shape possesses an irregular surface topography. Figure 4.7 shows how superimposing these shapes produces a final shape that most closely represents the resulting crater with a rough surface.

The observed crater widening must be accounted for in the volume analysis. Figure 4.8 shows a visual representation of the volume correction that takes place for each shape. Each consecutive ablation is represented by a different color. Starting with the first ablation shown in pink, followed by the second ablation shown in green. The removed volume that results from the third ablation is shown in cyan. With the fourth and fifth ablation volumes shown in yellow and gray, respectively. Concluding with the sixth and last ablation shown in purple. The removed material (colored layer) per ablation is not composed of a flat layer found at corresponding ablation depth. Instead, it consists of a volume that closely resembles the shape of a U (or a V) which will be used from this point forward when addressing the removed volumes per ablation. The portion of the U found at the corresponding ablation depth will be denoted as the bottom portion of the U from here on. An example of the bottom of the U corresponding to ablation 3 (cyan) is shown in Figure 4.8 by the area shaded in diagonal dark cyan lines. A thorough explanation of the volume correction analysis is given using the simplest shape of the three, the cylinder, due to its top and bottom diameters being the same size. For the cone, and the truncated cone, the top and

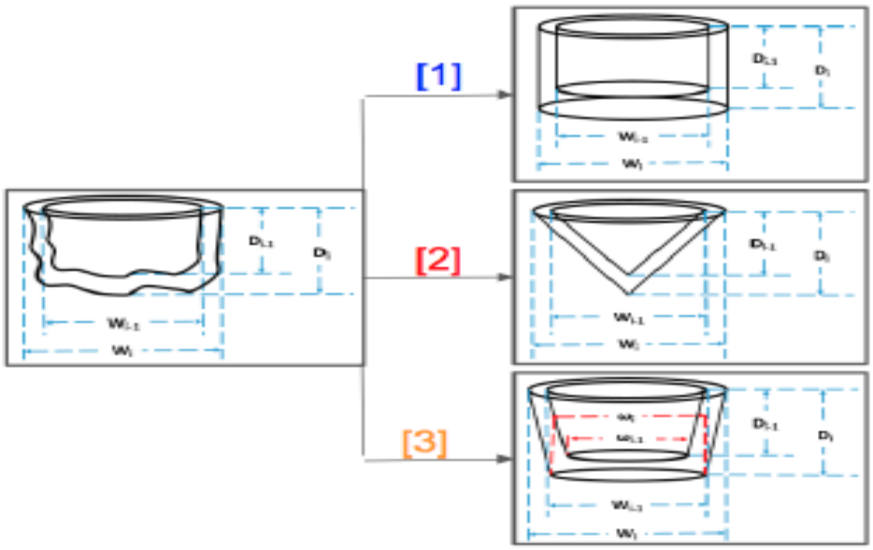

Figure 4.7. Diagram demonstrating the shape of a crater by averaging over 3 shapes, cylinder, cone, and truncated cone, of the same dimensional proportions, as reproduced from Ref.[3].

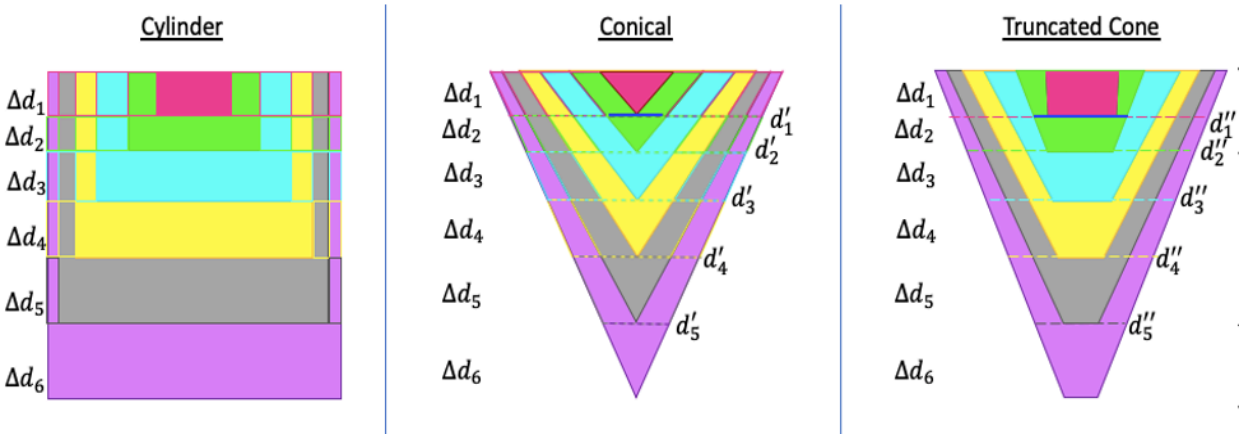

Figure 4.8. Visual representation of the volume analysis for the three different shapes (cylinder, cone, and truncated cone) to be used in creating the final shape that most closely resembles that of the ablation induced crater.

bottom diameters are not the same and as such require additional trigonometric calculations. This derivation is explained in section 4.5.2

For the cylinder, both the top and the bottom diameters are the same. This makes finding the volume difference simple. Starting with level 1, the volume of the two cyan blocks can be found simply by finding the difference in volume between cylinder 3 and cylinder 2 in level 1. Cylinder 3 is calculated using the cylinder formula $\pi r^2 h$, where the radius is that one pertaining to the crater of the 3rd ablation and a height pertaining to Δd_1. The volume of cylinder 2 is calculated using the same formula but with its respective radius. That is, the radius pertaining to the crater of the 2nd ablation, and the same Δd_1 due to being on the same level 1. The same steps are followed for finding the volume of the cyan blocks in level 2 however, $\Delta d_2$is now used in place of Δd_1. Finding the volume of the bottom of the U (purple cylinder in level 6) is even simpler. This volume is composed of a single cylinder rather than a difference between two cylinders. The cylinder is found using the same cylinder formula where the radius is that of the 3rd ablation but with height is Δd_6. The volume of all the individual blocks at each level and bottom of U's for every level must be found before incorporating the a SRIM based concentration profile in the data analysis. Each individual block and bottom of U must be divided by its corresponding total U volume to convert the volumes to a volume weighting factor in the form of a fraction. The crater width correction for the truncated cone, and conical cone is similar to the cylinder with exception of the top and bottom diameters of the shapes found at every level. When a cylinder is cut at different heights, the diameter remains the same at every height. That's why when the cylinder is divided into different levels (level 1, level 2, etcetera) the top and bottom diameters of each newly created cylinder are the same. However, when a truncated cone or a cone is sliced at different heights, the bottom and the top of the newly created trapezoids are not the same. Furthermore, a sliced cone is a combination of trapezoids and an additional cone at the bottom, making crater volume corrections even more complex. Additionally, the

difference between the top and the bottom diameters will increase as a function of consecutive ablations. This is because as ablations are accumulated, the crater will become increasingly more conical. The initial ablations serve to create the crater and widen it while the later ones significantly increase the depth of the crater with little effect on the crater width. This means a pseudo diameter must be calculated at each depth for each ablation for both the truncated cone and the conical cone. A thorough explanation of the pseudo diameter calculation for the truncated cone is described in detail in section 4.5.2

4.5.2 D Prime (Pseudo Diameter) Derivation

A pseudo diameter in this work is a diameter that is not measured but rather derived. The top and bottom diameters of craters can be measured, diameters at intermittent heights cannot. Intermittent diameters are those found along the diagonal distance connecting the top and the bottom of the truncated cone.

Calculation of pseudo diameter is only necessary for the truncated cone and the conical cone crater formation shapes. The pseudo diameter calculation is very similar between the conical cone and the truncated cone with the truncated cone being the simplest of the two. For both shapes, every level (except for the last one on the conical cone) can be described by a truncated cone and therefore the pseudo diameter calculation is the same up to the last level. The shapes differ in that a trapezoid is formed at every level except for the last level of the conical cone where a cone is formed. Given both pseudo diameter calculations are very similar, only the calculation for the truncated cone will be discussed. The calculation for a conical cone is the same with the addition of the volume of a cone at the bottom of every ablation produced crater.

Figure 4.9 shows a total of four nested ablation craters with the pink trapezoid pertaining to the first ablation, the green to the second, the blue to the third, and the yellow to the fourth ablation. The figure is also drawn to show crater formation as a

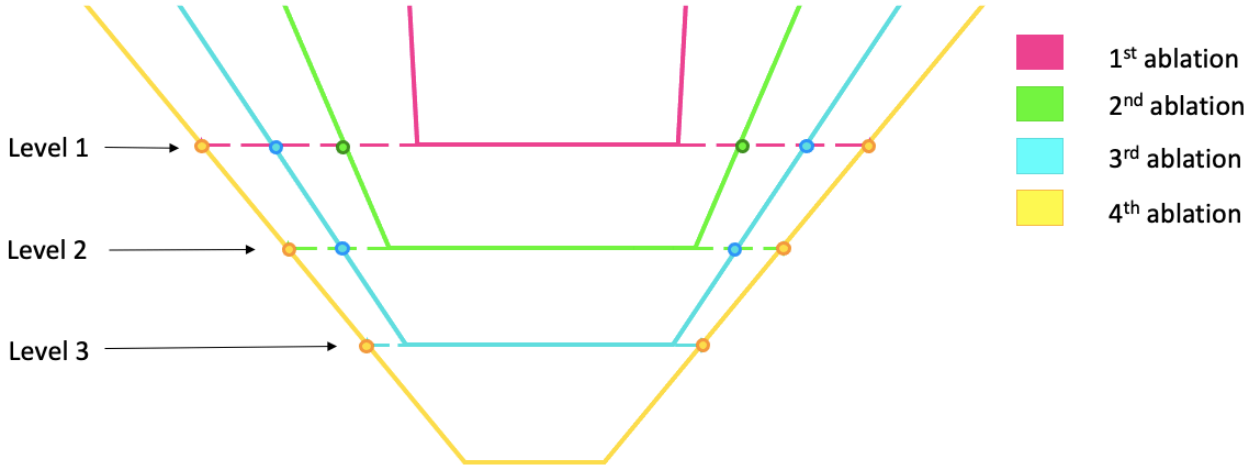

Figure 4.9 Depiction of four accumulated ablations for the truncated cone crater shape approximation.

function of subsequent ablations where the bottom diameter size decreases while the top diameter increases. At the bottom of every ablation crater there is a dashed line of the same ablation color indicating the depth level of that ablation. Level 1 is the bottom of ablation 1, level 2 the bottom of ablation 2, and level 3 the bottom of ablation 3. The bottom of the last ablation is not considered a level in this pseudo diameter derivation given it is measured and not derived.

The first crater does not have a pseudo diameter given it is the first level and there are no previous levels within it. For every crater past the first crater, there are n-1 intermediate diameters where n is the number of ablations at that level. This is shown by the solid dots at each level along the diagonal lines of the truncated cone craters in Figure 4.9. The second crater (green) shows 1 dot on each side at level 1. The distance between the dots on level 1 is the intermediate diameter that needs to be calculated. For the third crater (blue) there are two dots along the diagonal, this is due to there being two previous levels as discussed by n-1 where, for crater three n is 3. Lastly, the fourth ablation (yellow) shows three intermediate diameters at level 1, level 2, and level 3 that need to be calculated.

Only crater one (pink) and two (green) will be used to demonstrate the calculation of intermediate diameters. Figure 4.10 a) shows nested crater one and two along with the geometrical relationship between them. All the solid lines represent values that are measurable. The dashed lines along with the angles must be calculated using trigonometric relationships. The pink dotted line trapezoid is there to show the location of level one which is found at the depth of ablation 1. The depth of each ablation is shown by solid black lines on the right side with the total depth, from surface to bottom, of ablation 2, shown as Tot depth$_2$. The top and bottom diameters for ablation 2 are shown by the solid black horizontal lines. The distance between the two solid green circles is d', the intermediate diameter that we will be calculating for. To find d' we can take advantage of geometrical relationships between right triangles.

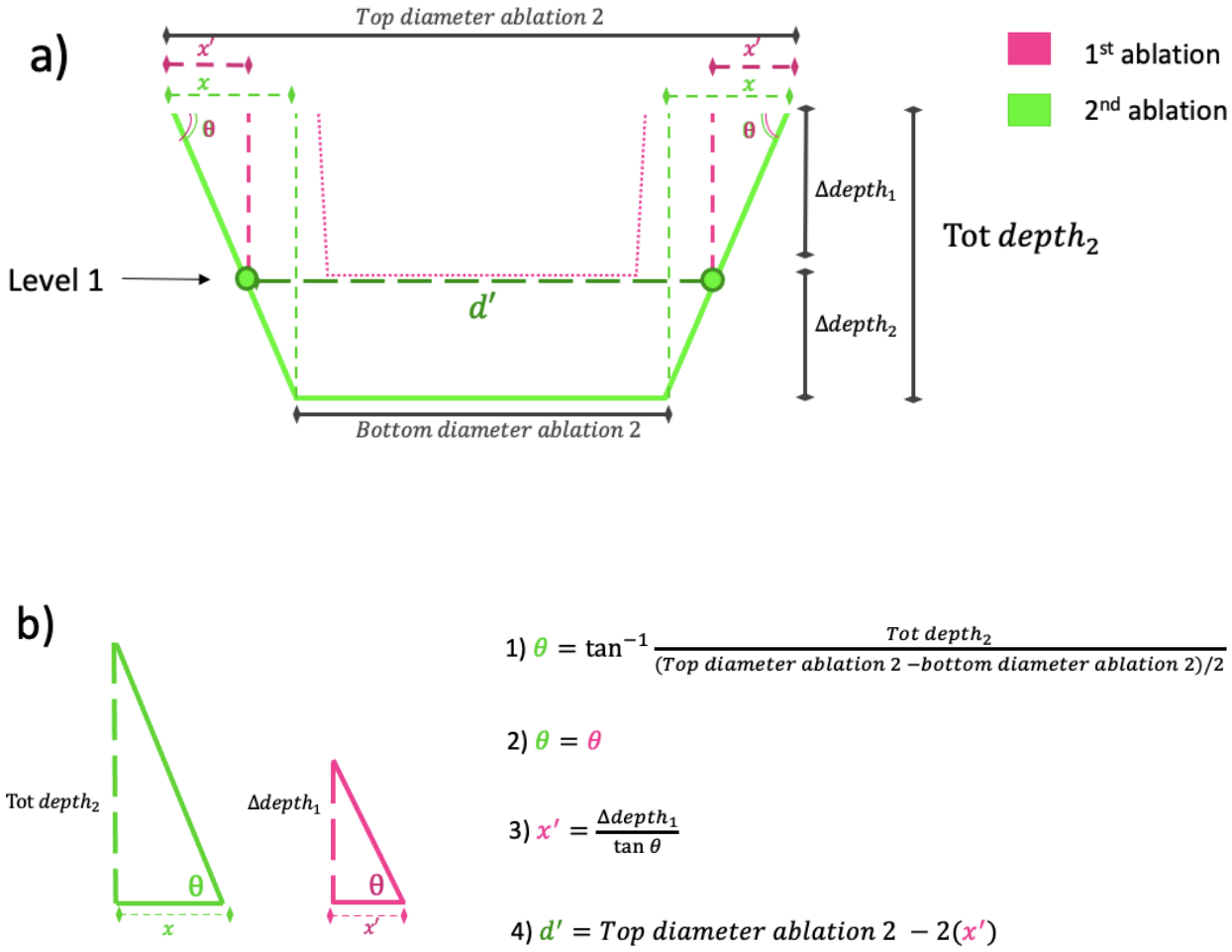

Figure 4.10 Graphics showing the derivation of intermediate diameter found at level 1 for the second ablation crater. Figure a) showsthe geometrical relationship between crater 1 and two. Figure b) shows the trigonometry formulas needed for derivations of d' (intermediate diameter).

To begin, the top diameter of ablation 2 can be divided into three segments composed of the bottom diameter distance plus the two x distances (green). The two x distances are simply the distance between top diameter minus bottom diameter divided by 2 as shown in Equation (4-20).

$$x = (Top\ diameter - bottom\ diameter)/2 \qquad (4\text{-}20)$$

For each green x on either side, a right triangle can be formed by connecting the distance x with the bottom diameter. The newfound triangles (green) are shown on both sides by the two dashed green lines and the solid hypotenuse line. Likewise, two additional related triangles (pink) can be formed by connecting the solid circle point to the top diameter as shown by the vertical pink dashed line. The distance between the top of the vertical pink dashed line and the top of the hypotenuse line is denoted as x'(x prime) also shown in pink. Given the pink and green triangles are both right triangles sharing the same hypotenuse, the angle between the hypotenuse and the base of the triangle is the same for both triangles. A visual of the pink and green triangles is shown in Figure 4.10 b). Using trigonometric relationships, we can deduce the angle θ is the same and therefore can use it to calculate for d'.

The angle θ for the green triangle can be solved by taking the arctangent of the vertical line (total depth) for ablation 2 divided by x as expressed in Equation (4-21).

$$\theta = tan^{-1}\frac{Tot\ depth_2}{(Top\ diameter\ ablation\ 2\ -bottom\ diameter\ ablation\ 2)/2} \qquad (4\text{-}21)$$

Due to the angle between the base of the triangle and the hypotenuse being the same for both the green and the pink triangles, the newfound θ can now be used to calculate for x' in the pink triangle. X' can be calculated by dividing the depth of the current level, in this case level 1, by the tangent of the calculated θ as shown in Equation (4-22).

$$x' = \frac{\Delta depth_1}{\tan\theta} \qquad (4\text{-}22)$$

From this point d' can be calculated by taking the top diameter of ablation 2 and subtracting two times the x' distance as shown in Equation (4-23).

$$d' = Top\ diameter\ ablation\ 2\ - 2(x') \qquad (4\text{-}23)$$

Figure 4.10 b) shows formulas used, in the order executed, and color coded alongside the derived triangles for ease of understanding.

All d' values can be solved in the same manner for all ablations, at all levels. However, solving d' at deeper levels requires the calculation of d' in previous levels as these will act as the top diameter for the created trapezoids at each level. Once d' has been found for every ablation past the first, those d' can be used to calculate the volume of the trapezoids and find the difference between them to find the volume created by an ablation at a specified level. Figure 4.11 shows the calculated volume, at each level, produced by the third ablation (blue). For diagram a) the volume of the two light blue shaded regions is found by taking the difference between the trapezoid created by the top diameter ablation 2, bottom diameters $d'_{1,2}$ and the trapezoid created by top diameter ablation 3, bottom diameter $d'_{1,3}$. Diagram b) shows how $d'_{1,2}$ and $d'_{1,3}$ become the top diameter for the middle level trapezoids and how ablation 2 doesn't have a calculated bottom d' since the bottom of ablation 2 is found at level 2 and therefore is a measured value, not a derived one. Diagram c) shows the volume at the last level which consists entirely of ablation 3 removed material. Therefore, no difference of trapezoids has to be taken into account and only the volume of the single trapezoid has to be calculated. For this trapezoid, the top diameter is the last derived d' and the bottom diameter is the bottom diameter of the ablation 3 crater which is measured, not derived. Summing all the blue shaded regions produces the total volume removed by the 3rd ablation as shown in Figure 4.12.

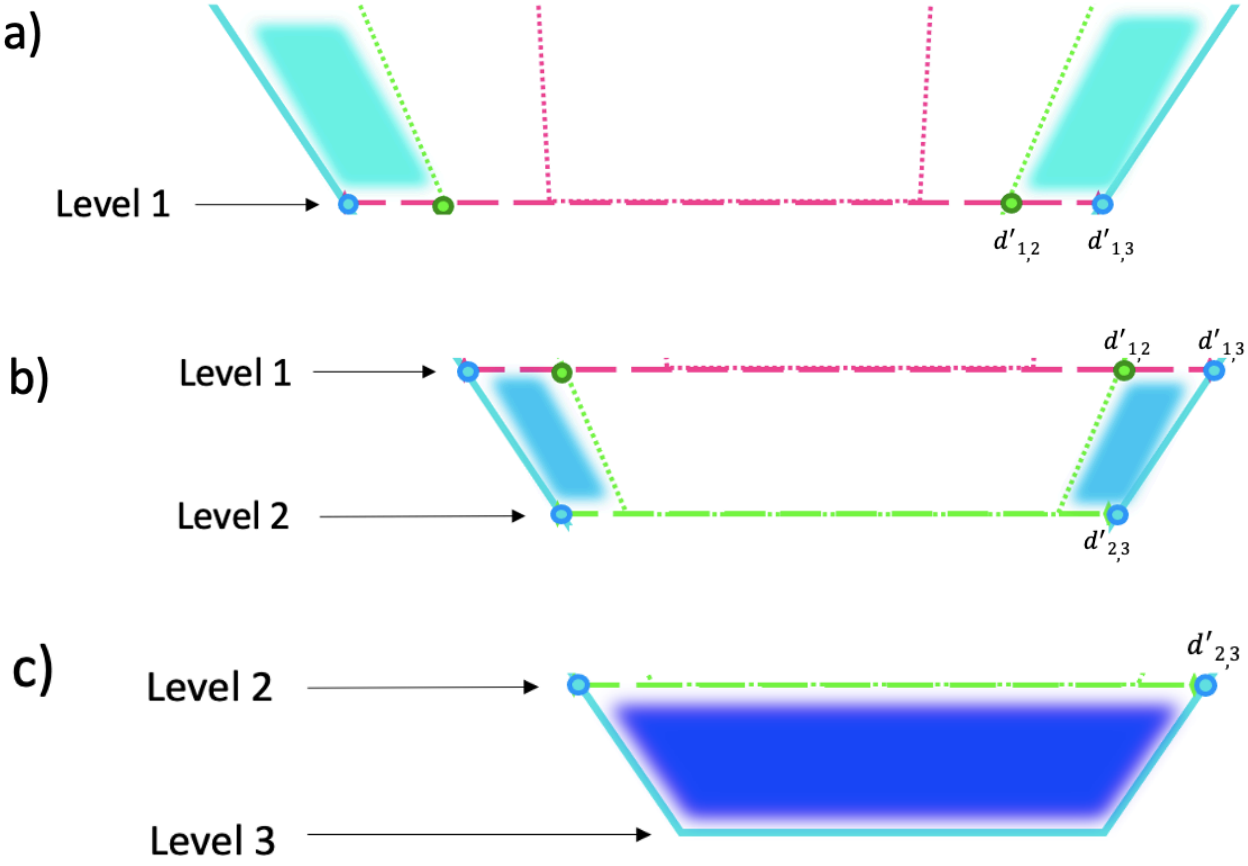

Figure 4.11 Diagrams showing the removed volume (at different levels) as a result of the 3rd consecutive ablation. Additionally, intermediate diameters are shown to demonstrate the need for them and how they are useful in volume calculations.

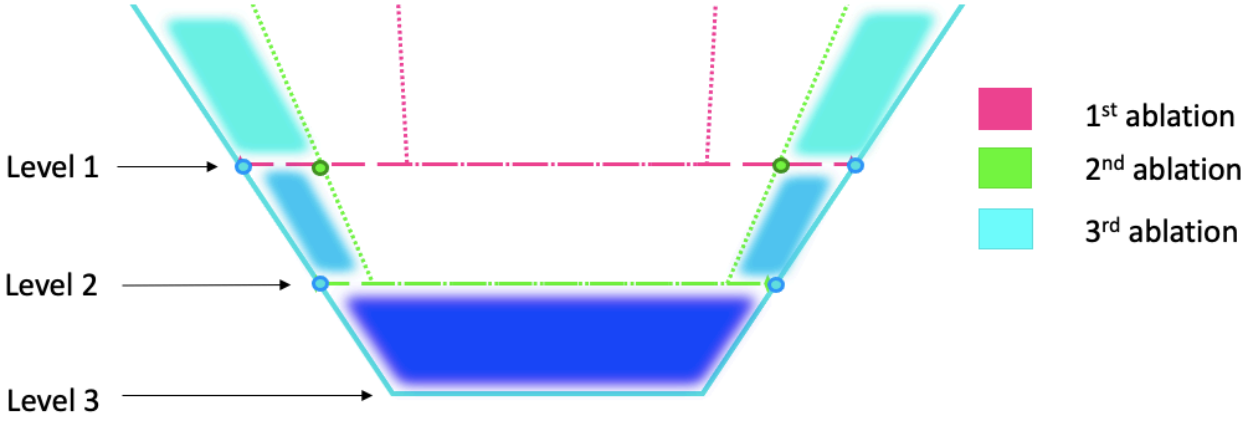

Figure 4.12 Demonstration of the volume removed by the 3rd ablation, found by summing all the blue shaded regions.

4.6 SRIM Implantation Profile Correction

4.6.1 SRIM Profile Implementation

Once the volume correction calculation has been performed, the concertation profile correction can be implemented. Figure 4.13 shows the difference between an assumed linear concentration profile and a near-surface peaked concentration profile. The linear concentration profile (depicted by the dark purple profile) implies that the same number of element specific atoms are found throughout the bulk of the material while the near surface profile indicates that there are more element specific atoms at a certain depth than the rest of the bulk (depicted by the dark green profile). A linear profile is used to represent the W concentration throughout the W matrix. He is best represented by a near surface profile calculated using SRIM. Due to the linear dependence of the W concentration as a function of depth, concentration weighting factor is one and thus does not affect the previously calculated volumes when multiplied.

The concentration weighting factors for helium are calculated by integrating the concentration found at each level (Δd) and then dividing those values by the total concentration. The total concentration is calculated by integrating the SRIM near surface implantation profile from the surface of the material to the depth of the last ablation, in this experiment the last ablation being the 6^{th} one. Each level will have a concentration weighting factor that applies to all the previously calculated volume values within that level (Δd). The LIBS and LAMS signal resulting from the nth ablation is corrected by multiplying said signal by the volume fraction weighting factor times the near surface concentration profile fraction weighting factor. This results in a signal corresponding solely to the number of ablated He atoms that were found at that depth. Volume blocks removed during the n^{th} ablation pertaining to previous levels are added to their corresponding levels. Meaning those volume blocks other than the bottom of the U.

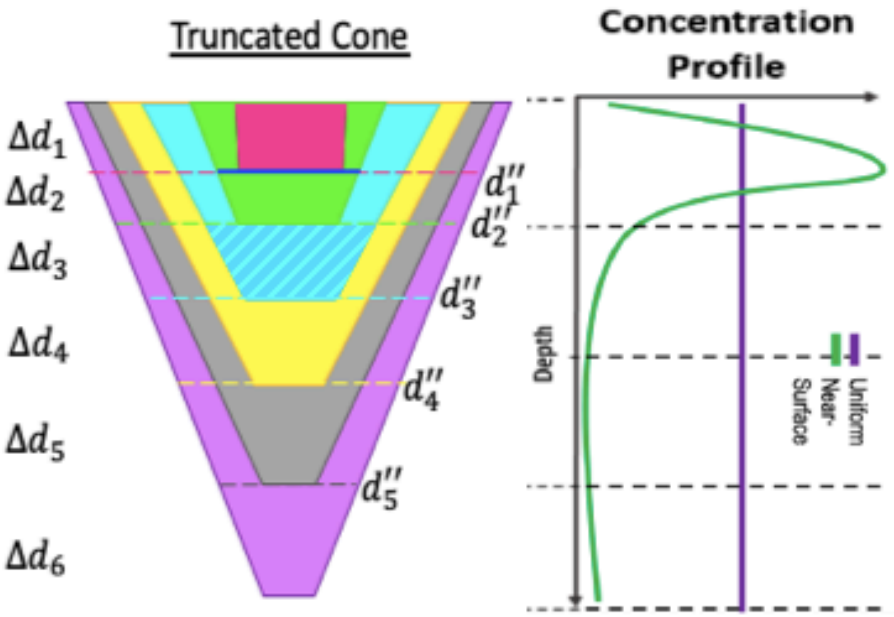

Figure 4.13. Diagram showing the linear and near surface concentration profiles alongside the truncated cone representation of a crater. Linear profile as

4.6.2 Addressing the Heat Affected Zone in Future Experiments

Incorporating crater widening volume and concentration profile corrections into the data analysis allows for a more accurate characterization and quantification of the depth profile thorough subsequent ablations. The bulk material experiences heating and melting due to the relatively long ns laser pulse. The heat goes beyond the bounds of the crater to the surrounding material where enough energy is deposited resulting in desorption. The area heated beyond the bounds of the crater is best described as the heat affected zone. Because He is insoluble in W and assumed to be contained within bubbles, the heat affected zone does not have a significant effect on the He atoms located within it. However, in the case of deuterium, which is highly mobile in W, the heat affected zone can provide sufficient energy for deuterium to diffuse outwards and contribute to the signal associated with that ablation. The heat affected zone correction has not been developed nor incorporated into the data analysis. However, there are plans in progress to limit if not mitigate the heat affected zone surrounding the craters. The incorporation of a fs laser in place of the current ns laser is currently being studied and will take place after this dissertation. Section 9.2.3 provides an analysis of the benefits and differences of a fs laser compared to a ns laser. Evidence of the heat affected zone produced by our current system is shown in Section 7.3.1.

4.7 Benchmarking LIBS/LAMS

The depth profiling characterization capabilities of the LIBS-LAMS systems were benchmarked using an approximately flat top helium concentration profile as shown in Figure 4.14. The flat top was created by carrying the He ion implantation energies from 400 keV to 80 keV in tungsten. The rest of the energies used are shown in the insert within the plot. Both LIBS and LAMS were performed on this sample to observe the extent of depth profiling and characterization abilities.

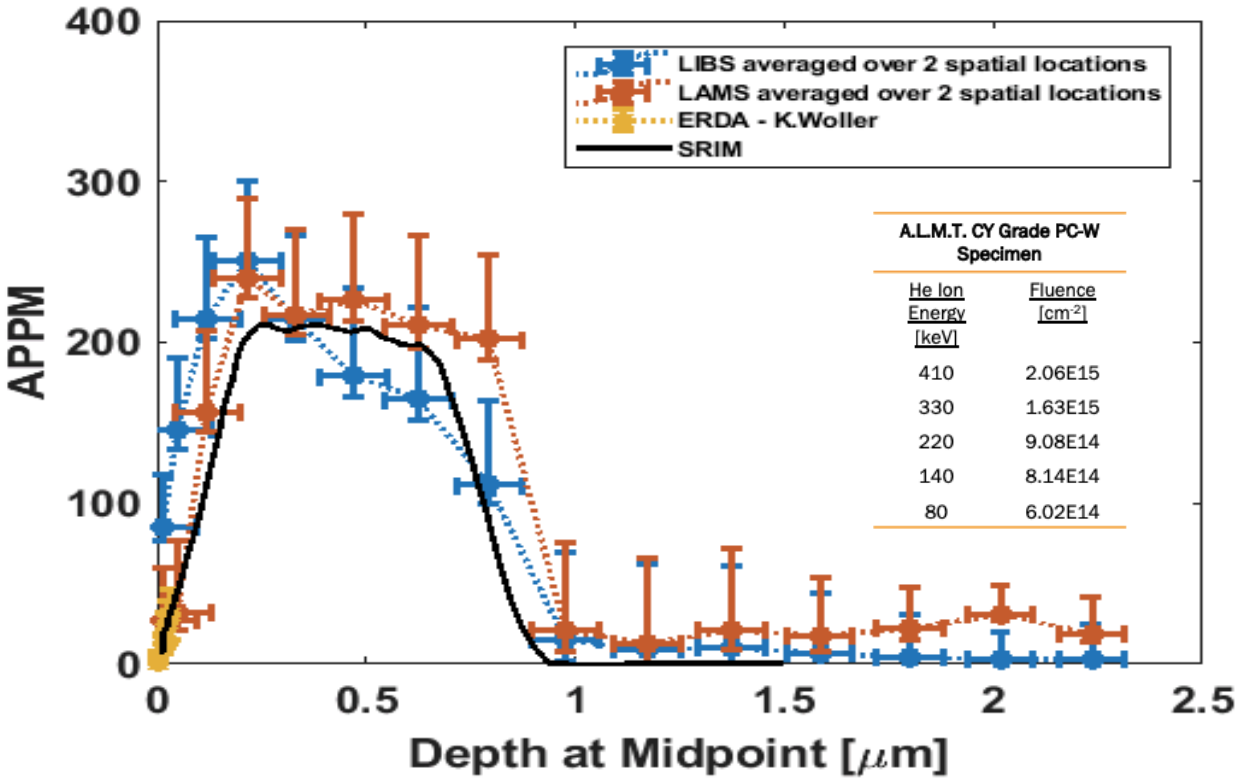

Figure 4.14. Results from LIBS, LAMS, and ERDA experiments performed by Dr. Shaw on a W flat top sample to benchmark the LIBS/LAMS system depth profiling characterization abilities. Good agreement is seen amongst all four data sets, as reproduced from Ref. [3].

LIBS volume corrected results are shown in blue while the LAMS volume corrected results are shown in orange. Both results are plotted against the SRIM predicted implantation profile. Good agreement is seen between LAMS and the SRIM profile where the top hat profile is clearly evident in the LAMS results. LIBS results initially are in good agreement with the SRIM profile near the surface but deviate at deeper depths. The phenomenon of this behavior has been consistently observed in other experiments and as a result was investigated. The details of this behavior are explained in section 6.3. Additionally, ERDA measurements were performed by Kevin Woller (MIT) on the flat top sample. Although ERDA is surface limited and unable to resolve the entire flat top profile, it was able to resolve the first few nanometers of the sample to a high degree of agreement with LIBS, LAMS, and SRIM.

4.7.1 Top Hat LIBS Data Using Updated Volume Correction Algorithm

These preliminary results were produced during the initial development of the crater volume analysis algorithm. At this stage of the algorithm development the cone and the truncated cone volume calculations possessed a significant degree of error, specially at deeper depths, due to no existing pseudo radii (r prime) derivations. The top and bottom radii was assumed to be the one spanning the entire crater. There were no intermediate radii considered. As a result, a negative ablated volume was calculated from time to time.

In an effort to understand the degree of change the new algorithm has on the data analysis, I performed analysis of the same data viewed in Figure 4.14 using the new volume algorithm I developed. Figure 4.15 shows the results of the data analysis using the new crater volume evolution algorithm. In this analysis the volume is calculated using intermittent radii, r prime. The analyzed LIBS data is shown in blue while the simulated SRIM profile is shown in the solid black line. Not only is good agreement evident between the two, but a higher degree of agreement has also been achieved from the previous volume analysis where the r primes were not used.

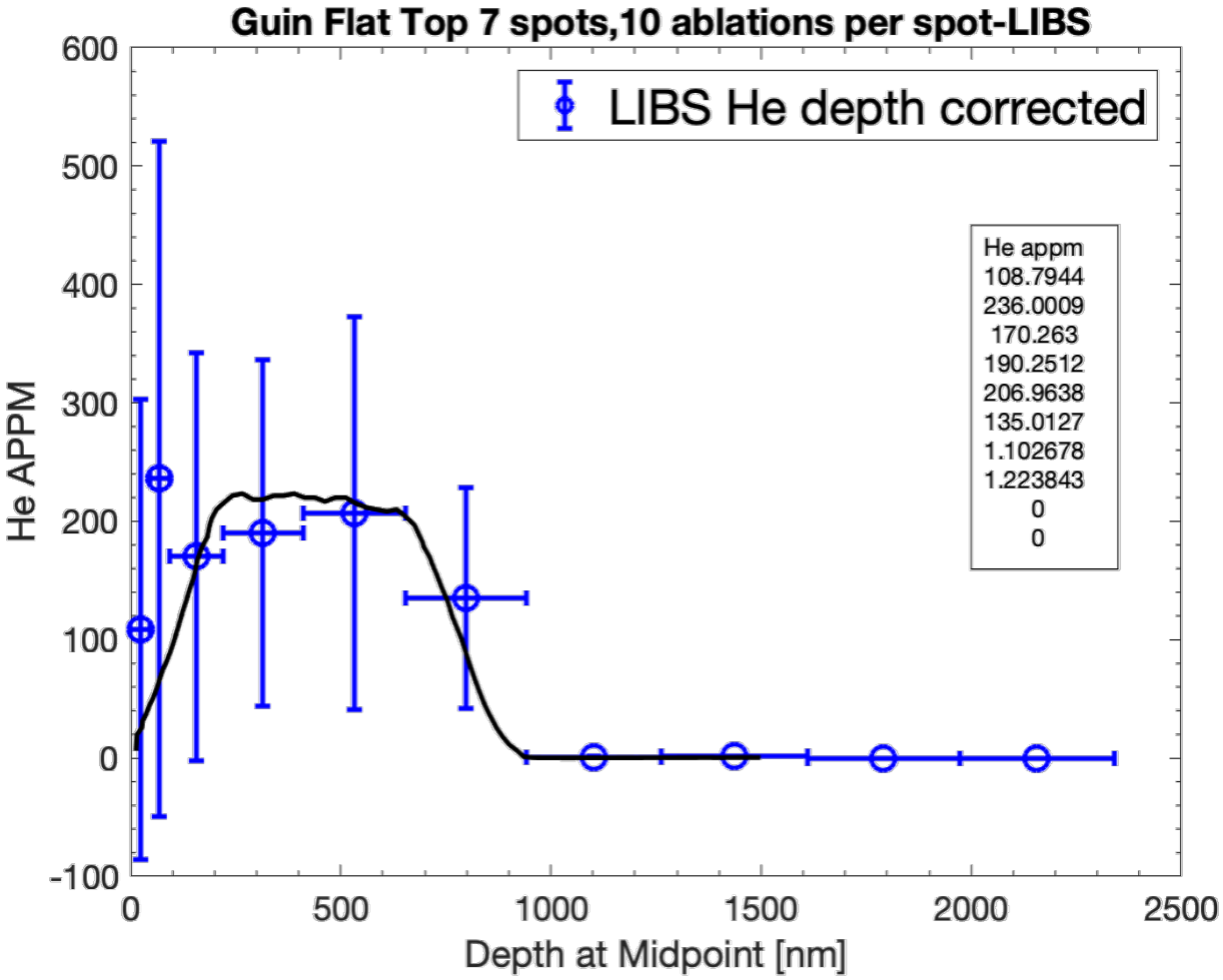

Figure 4.15. LIBS results for Dr. Shaw's flat top sample used to initially benchmark the LIBS-LAMS systems. Profile is composed over the average of seven different spots ablated to ten cumulative ablations.

4.7.2 LAMS Comparison to Cluster Dynamics Experiments Results

Good convergence between LIBS and LAMS experiments has been demonstrated through the usage of a specifically designed experiment where the He implantation profile was known and controlled prior to resolving it. However, in order demonstrate the full qualitative and quantitative capability of the system an unknown profile should be resolved. Figure 4.16 shows LAMS data and cluster dynamics modeling data results for an experiment where the implantation profile was unknown, only predicted by SRIM. The experiment consists of PCW specimens that were implanted at room temperature with 10keV He ions to a fluence of $1E20\ He\ m^{-2}$. The SRIM profile of the anticipated depth dependence of the implanted He concentration is shown in both plots as a solid black curve. LAMS data obtained from the sample following He implantation is shown in blue in the left plot where it can be seen that He is only detected within the first two ablations, consistent with the predicted SRIM profile. The error bars show the standard deviation across 7 laser ablation locations in the annealed sample, and over 9 laser ablation locations for the case of the implanted sample. This analysis serves as further evidence of the ability the LIBS-LAMS system to spatially resolve and quantify depth dependent He in W.

A separate sample was He implanted under the same conditions, and then subsequently annealed to $1000°C$ for one hour. The LAMS measurements of this sample following annealing are shown in magenta where a reduced helium concentration is observed. Cluster dynamics simulations were performed for PCW implanted and annealed under the same conditions. The cluster dynamics results shown on the right plot show general agreement with LAMS regarding the He depth dependence and decrease in He after annealing. Although additional LIBS and LAMS measurements are needed before a detailed comparison can be made, this experiment showcases that the qualitative trends are consistent. The depth dependent profile resolving capabilities of the system have been demonstrated.

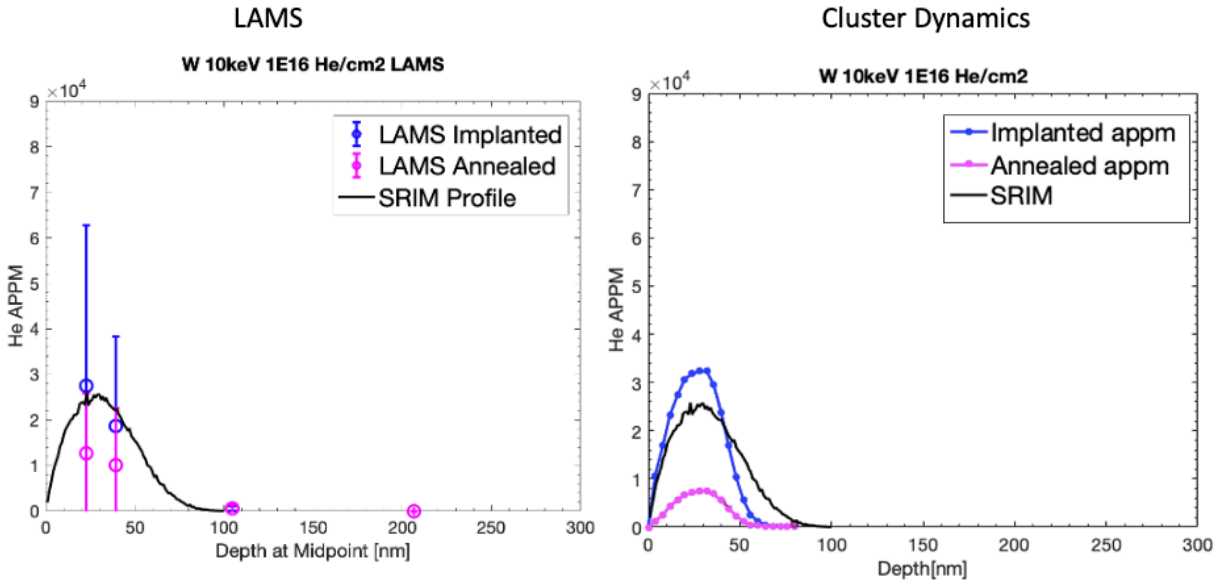

Figure 4.16. LAMS and Cluster Dynamics result for He implanted and annealed PCW samples. Good agreement is seen between the predicted SRIM depth dependence profile and the implanted He results. Agreement for a reduced magnitude of the annealed curve is also evident amongst LAMS and cluster dynamics results.

Chapter 5
Permeability Measurements of Hydrogen Isotope

5.1 Gas Permeability in Metals

Permeability is the measure of which a material allows a secondary liquid or gas, to pass through it when diffusion-limited transport dominates[66]. The rate at which one material permeates through another is influenced by a multitude of factors such as the electron structure of the permeating material, the surface chemistry of the material that is being permeated, and internal defects and traps[45]. A material permeability is defined as the point at which the steady-state diffusional transport, specified by the flux, is achieved in a material where a differential pressure of the permeating gas exists[43]. The steady state permeation flux (J_∞) is related to the square root of the upstream gas pressure as shown in

$$J_\infty = \phi \frac{\sqrt{p}}{\delta} \qquad (5\text{-}1)$$

Where, J_∞ is the steady state deuterium flux, ϕ is the permeability value of interest, $\sqrt{p}$ is the square root of the upstream permeating gas pressure, and δ is the sample thickness before any secondary material has permeated through the sample.
Given that the pressure, sample thickness, and steady state flux are known values, permeability can easily be calculated by Equation (5-2).

$$\phi = \frac{\delta}{\sqrt{p}} J_\infty \qquad (5\text{-}2)$$

Figure 5.1 shows permeation data for Eurofer 97 steel from measurements performed at temperatures ranging from 350 °C to 550°C in increments of 50°C [7]. For all temperature regimes, a clear linear relationship is obtained between the steady state permeation flux in units of $mol \cdot s^{-1}m^{-2}$, and the square root of the upstream gas pressure in units of $Pa^{-\frac{1}{2}}$. The distinct linear relationship reveals that the deuterium permeation at each temperature is a result of deuterium bulk diffusion and that the surface effects have a negligible impact. The increase in magnitude indicates an increase in diffusivity as temperature increases; meaning diffusivity and permeability are a function of temperature where at higher temperatures the gas is able to permeate the steel matrix more easily. There is also a clear increase in slope as a function of temperature. This observation indicates that upstream pressure enhances permeation to a greater degree at higher temperatures.

5.1.1 Arrhenius Dependence

The temperature dependence of permeability follows an Arrhenius dependence described by Equation (5-3)

$$\kappa = Ae^{-\frac{Ea}{RT}} \qquad (5\text{-}3)$$

where κ is a rate constant, A is a pre-exponential factor, E_a the average activation energy it takes a gas atom to move through crystal lattice in units of J/mol, R is the universal gas constant $\frac{8.314J}{K*mol}$, and T the absolute temperature in kelvin.

Translating Equation (5-3) to the permeability variables produces the following equation

$$\phi = \phi_o * e^{-\frac{Ea}{RT}} \qquad (5\text{-}4)$$

where ϕ is the permeability of the material and ϕ_o is the pre-exponential factor. Taking the natural log of Equation (5-4) produces Equation (5-5).

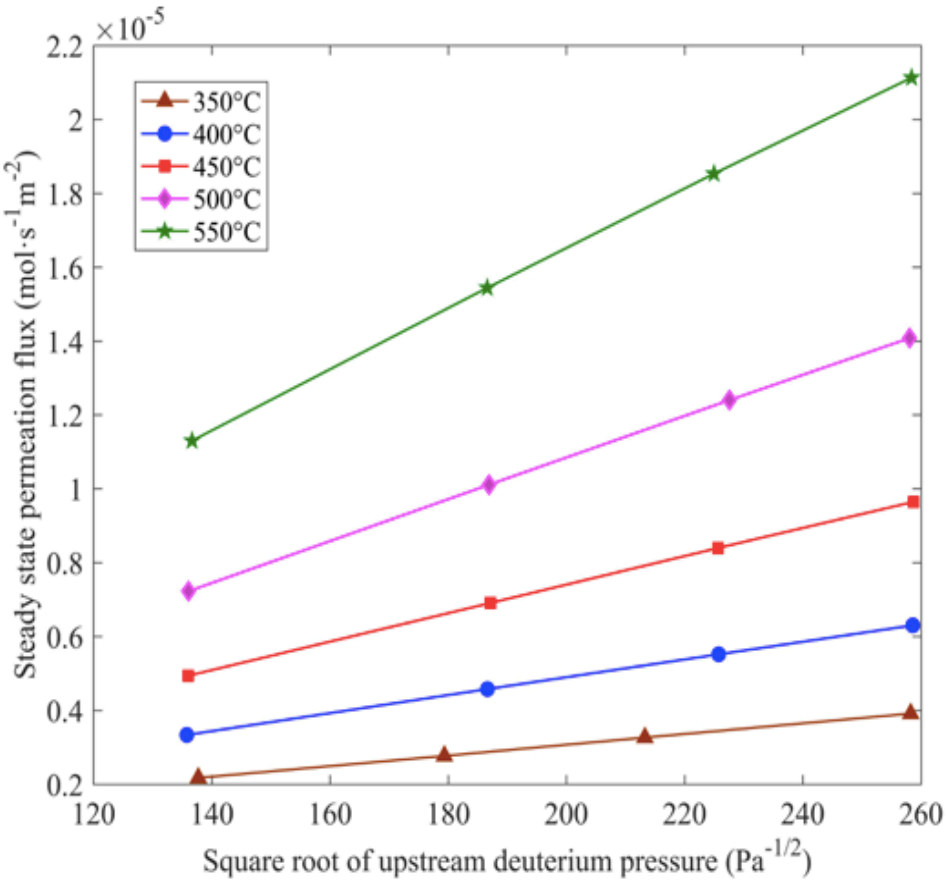

Figure 5.1 Permeation data for Eurofer 97 steel, showing a linear relationship between the steady state permeation flux and the square root of the upstream gas pressure. Permeability measurements for performed for 5 temperatures shown from bottom to top 350°C (brown), 400°C (blue), 450°C (red), 500°C (magenta), 550°C (green), as reproduced from Ref. [7].

$$\ln(\phi) = \ln(\phi_o) - \frac{E_o}{R} * \frac{1}{T} \qquad (5\text{-}5)$$

Equation (5-5) is best described by the linear equation $y = mx + b$ where $\ln(\phi)$ is y, $\ln(\phi_o)$ is the y intercept b, $-\frac{E_o}{R}$ is the slope m, and $\frac{1}{T}$ is the x axis values.

Plotting Equation (5-5) produces an Arrhenius plot as shown in Figure 5.2 [9] where the permeability (ϕ) is plotted on the natural log y-axis in units of $mol \cdot m^{-1}Mpa^{-\frac{1}{2}} \cdot s^{-1}$, and the x-axis in units of inverse temperature 1/T. A total of seven permeation data values (ϕ) (red data points) are plotted as a function of inverse temperature, and a clear exponential trend is observed (red solid line). Finding the y intercept of this linear fit yields the permeability coefficient ϕ_o, and the slope equal to $-\frac{E_o}{R}$, where $R = \frac{8.314J}{K*mol}$, yields the activation energy E_o value in units of Joules/mol. The experimental methods and steps for finding the permeability ϕ values is discussed in detail in section 5.4

Consistency of diffusivity measurements has been seen amongst different works for hydrogen diffusivity values at high temperatures, however, at low temperatures, the diffusivity values are not only inconsistent amongst one other but also significantly lower than the Arrhenius predicted values[43]. Given permeability is a function of diffusivity, the same is said for the extrapolation of permeability values at low temperatures[67]. The increase in scatter of permeability measurements at low temperatures could be due to the hydrogen trapping effects being more significant at lower temperatures where traps have not been removed through heating/annealing. Therefore, the movement of the permeating gas is affected to a greater degree. This permeability to temperature relationship is discussed in detail in Section 5.2. Given the mentioned temperature effects on permeability measurements, caution should be taken when extrapolating the permeability trend to lower temperatures.

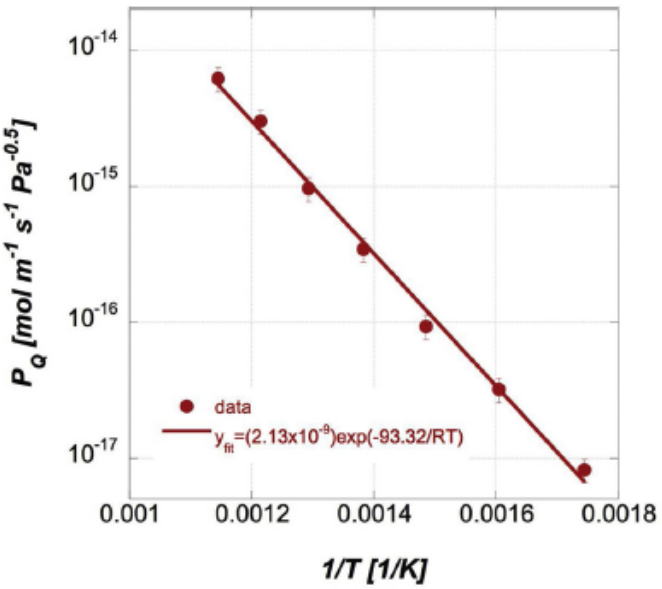

Figure 5.2 Arrhenius plot of tritium permeability in polycrystalline W. Permeability measurements performed at 573K, 623K, 673K, 723K, 773K, 823K, and 873K at 100Pa HT gas pressures. As reproduced from Ref. [9].

5.2 Comparison of Permeability Literature

Several permeability experiments have been performed for hydrogen isotopes in polycrystalline tungsten[9]. A comparison of these investigations is shown in Figure 5.3 which includes the work of Shimada (red solid line), Frauenfelder(1968, blue dashed line) and (1969, purple dashed line), Zakahrov(1973, dark green dashed line), Benamati(2000, lime green dashed line), Esteban(2001, yellow and brown dashed lines), and Buchenauer(2016, gray dashed line).

Shimada's work covers the lowest temperature range and although it does not directly overlap with the literature data, likely due to the different temperature range investigated, the extrapolated data (dashed red line) very closely agrees with Frauenfelder (1 and 2), Zakahrov, and Buchenauer in the higher temperature range 1,111K-1,666K. The lower extrapolated permeability could be due to the fact that the extrapolation was performed from permeability values taken at lower temperatures where permeability is lower in general. Good agreement is also seen for the aforementioned hydrogen isotope permeability slopes, which indicates similar activation energies. The slopes from measurements of Benamati and Esteban differ from the rest of the literature but agree with one another. This could be due to the fact that these experiments used tungsten discs at lower temperatures while tungsten foils or tubes were used in the initially mentioned research. However, the reasons for this difference will not be further discussed here.

The parameters for the experiments mentioned in Figure 5.3 are shown in Table 5-1. In order from left to right, the first column shows the composition of the W samples used in the experiments. The second column lists the H isotope used in the respective temperature range, provided in column three. The H isotope permeability partial pressure, observed in the upstream side of the experiment, is shown in column four. The permeability pre-exponential factor and permeability activation energy values acquired from experiments are shown in column four and five, respectively.

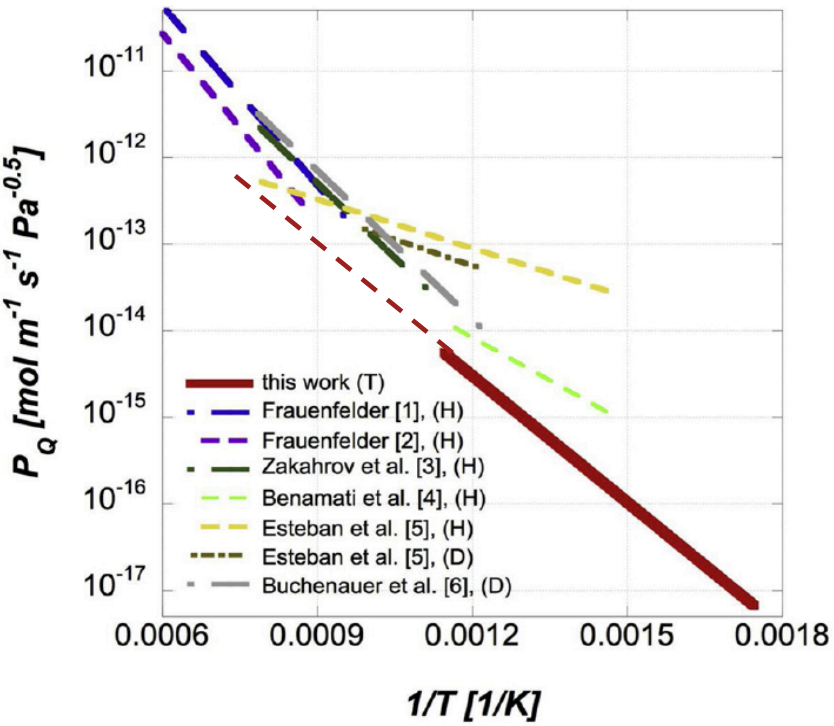

Figure 5.3 Comparison of Hydrogen isotope permeability in tungsten as function of sample type (tungsten tubes, rolled sintered tungsten rods, tungsten discs), permeability experiments(gas-driven permeation, gas desorption/evolution, isovolumetric gas-phase desorption), and temperatures (555K - 1666K), as reproduced from Ref [9]

Table 5-1 Parameters and experimental conditions for Hydrogen permeability in tungsten as a function of temperature, as reproduced in Ref [9]

composition	Hydrogen isotope[a]	temperature [K]	hydrogen isotope partial pressure [Pa]	pre-exp. factor for permeation: P_Q^0 [mol $m^{-1}s^{-1}$ $Pa^{-0.5}$]	activation energy for permeation: E_P [kJ mol^{-1}]	reference
99.95% W	T	573 - 873	$5.8 \times 10^{-2} - 6.8 \times 10^{-2}$	2.13×10^{-9}	93.32	this work
99.95% W	H	1050 - 2000	$1.3 \times 10^{-4} - 2.6 \times 10^{4}$	7.63×10^{-7}	131.80	[1]
99.90% W	H	1120 - 2080	8.0×10^{4}	6.07×10^{-7}	138.70	[2]
W	H	900 - 1330	$1.3 \times 10^{2} - 2.6 \times 10^{4}$	7.32×10^{-8}	109.79	[3]
W	H	673 - 873	$1.0 \times 10^{4} - 1.0 \times 10^{5}$	7.56×10^{-11}	63.17	[4]
99.98% W	H	673 - 1073	$1.3 \times 10^{4} - 1.0 \times 10^{5}$	1.65×10^{-11}	36.20	[5]
99.98% W	D	823 - 1023	$1.3 \times 10^{4} - 1.0 \times 10^{5}$	1.51×10^{-11}	38.70	[5]
99.95% W	D	823 - 1273	$1.0 \times 10^{4} - 1.0 \times 10^{5}$	1.04×10^{-7}	109.87	[6]

Permeability values for temperatures up to 1223 K, possibly 1323 K, can be replicated by our system (discussed in Section 5.4) for comparison and validation purposes. Validating the H in W permeability results and the impact that He has on the expected permeability behavior will allow us to better understand synergies between H and He as well as give insight into reducing if not mitigating fuel retention in fusion reactor PFCs.

5.3 Permeation System

Our gas permeability measurement system is located in the Low Activation Materials Design and Analysis (LAMDA) lab at Oak Ridge National Lab (ORNL). The image shown in Figure 5.4 shows the furnace component of the system where the heating of the material takes place. This furnace allows us to increase the temperature from room temperature up to 1,100°C. The general rule of thumb used to determine the ramping rate is 20°C per 1 minute. Once the achieved temperature is achieved, this temperature can be held for hours, even days if desirable. This system also allows for multiple temperature ranges to be investigated in sequential order. For example, the system can start at 25°C and ramp to 850°C over 40 minutes following the 20°C/min heating rate. Once the desired temperature of 850°C has been reached, it is then held for an hour or so until the permeability flux reaches equilibrium. At this point a higher temperature, such as 900°C, can be investigated by increasing the temperature at a rate of 20°C/min. All this can be programed into the system to ensure consistency and limit human error in the temperature ramping rates and hold times.

Changing a couple of components in the system allows for it to be used at higher temperatures in the range of 950°C while holding a strong vacuum on the order of 10^{-7} to 10^{-8} torr. It is possible to reach 1050°C while still holding vacuum however, this temperature range has not yet been attempted.

Figure 5.4 Gas driven permeation system for deuterium permeability in structural materials, or tungsten, analysis. Located in the Low Activation Materials Design and Analysis at Oak Ridge National Lab.

Figure 5.5 shows a schematic of our permeability system. On the left side H_2, D_2, and He gas tanks are joined to the system through bellows valves. Opening the valve pertaining to the gas of interest will allow this gas to travel towards the chamber adjacent to it where a pressure gauge is located. This is the pressure that is used in (5-2) to determine the permeability of the system. Prior to the gas bellows valves being opened this chamber is pumped down to a vacuum of $10^{-7}\,Torr$. The pumping system shown below the chamber has a gate valve connecting the chamber to the turbo pump which is connected by a secondary valve to the scroll pump also known as a dry pump.

The permeating gas moves through the chamber and fills it as it travels in the direction of the furnace. It then moves through the flexible bellows shown by the small vertical lines on both ends of the furnace. These flexible bellows allow for different sized components, such as tubes, and gauges, to be swapped out in order to allow for different experiments, with different temperature ranges, to be performed. Once the gas travels through the left most flexible bellow it will enter the portion of the tube located within the furnace. It will continue to travel unrestricted until it comes in contact with the sample. The W sample is loaded to hold a vacuum seal such that the path of least resistance for the gas is through the samples. Once the gas permeates through the sample it exits the furnace area on the right side of the system called the downstream side. It travels through a second flexible bellow into another chamber similar to the initial chamber. This chamber is initially also pumped down to a high vacuum with the help of a turbo pump and a scroll pump as shown on the bottom of the downstream portion of the system in Figure 5.5. The gas continues to travel into the QMS where it gets characterized and quantified. An element and quantity dependent signal is outputted from the QMS and observed on the computer connected to it. This signal is given in terms of a quantity dependent current signal with units of [C/s]. The QMS signals are then converted to permeability values to develop Arrhenius dependent plots.

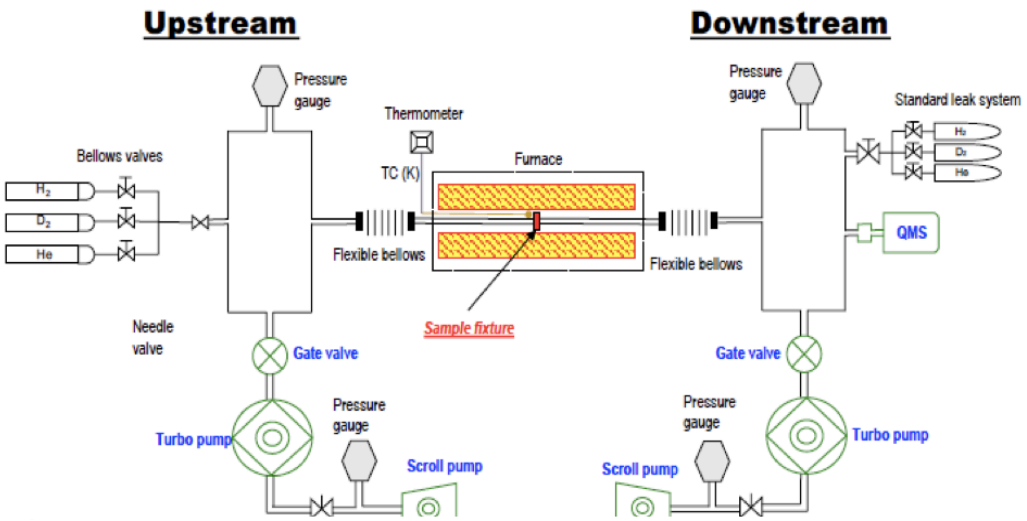

Figure 5.5 Diagram showing all the essential upstream, sample heating, and downstream components of our permeability system. The standard leak calibration system is also included in the diagram even though it is only used when calibrating the system and not as a part of every permeability experiment.

5.3.1 Standard Leak Calibration

Calibration of systems is important across all experimental techniques because components, seals, joints, and materials change over time. Calibration of diagnostics must take place in order to translate their outputs to a useful value. Our permeability system and the QMS are calibrated with a frequency of every 6 months to a year through a standard leak system. The standard leak system consists of gas tanks that have already been calibrated by their parent company to release a specified amount of mols of gas per second [$\frac{mol}{s}$]when their respective bellow valves are fully opened. The standard leak system must include calibrated gas tanks of the same elemental composition as the gas being used in the upstream portion of the system. A total of three gas tanks are used, as shown in Figure 5.5, one for H_2, a second one for D_2, and a third for He. Opening the D_2 standard leak tube allows for $X\,\frac{mol}{s}$ of D_2 atoms to move into the QMS and where an elemental and quantity dependent current signal is observed in units of C/sec. Dividing this predetermined mol rate value by the observed current yields a deuterium calibration coefficient of $0.9119\,\frac{mol}{s \bullet C}$. Our system was last calibrated on March, 2022. The standard leak calibration for the permeation system is similar to that of LAMS. For a more detailed walk through of the calibration refer to section 4.4.3.

5.3.2 High Temperature Permeability System Design

When using materials to conduct permeability measurements, precaution must be taken to ensure that those materials are capable of withstanding the temperatures and vacuum conditions during experiments. The melting temperature of stainless steels is in the range of 1500°C making it a viable material for the construction of the sample fixture and tubes in experiments with temperature needs of up to 550°C maybe 600°C. However, for experiments with higher temperature

needs, such as the close representation of hydrogen isotope permeability in fusion reactor tungsten components, stainless steel is not a good candidate. Investigating isotopic hydrogen permeability, and the impacts of He, in tungsten, under conditions that closely resemble those found in ITER, required designing and fabricating high-vacuum, high-temperature resistant components that could be swapped out for the stainless-steel ones inside the furnace. With the assistance of Charles Schaich from ORNL, Inconel alloy 625, was the material of choice to fabricate the high vacuum, high temperature permeability components. This particular alloy is extremely corrosion resistant even at high temperatures with safe operating temperature ranges from the cryogenic to 982°C. ORNL is able to work with this material and fabricate components, therefore, the accessibility of it was another factor for choosing this Inconel alloy over other ones with even higher temperature limits. Charles Schaich developed the initial design of the high temperature components which Thomas Muth, Sr. ORNL scientist developed the later iterations of the high temperature system.

The left image in Figure 5.6 shows the sample loading components consisting of two Inconel flanges positioned at the left and right of the schematic. Each flange contains a cut-out groove where an Inconel C ring(3) is positioned, easily discernable by the C shape ends. The C rings act as a gasket ensuring the incoming upstream pressurized gas moves through the sample rather than around it. The sample is positioned between these C-rings as depicted by the thin black rectangle. As the flanges are brought closer together the C-rings begin to deform and create a vacuum tight seal around the sample allowing the downstream and upstream tubes, through which the gasses travel, to be held under vacuum and pressurized gas, respectively. The copper-colored rectangles are representative of copper gaskets(4) used to account for different sample thicknesses. The high temperature system is designed for a 0.5mm thick sample. This provides a 0.38mm gap between the flanges that, when fully closed, provides just enough load to engage the c-rings to hold a vacuum seal.

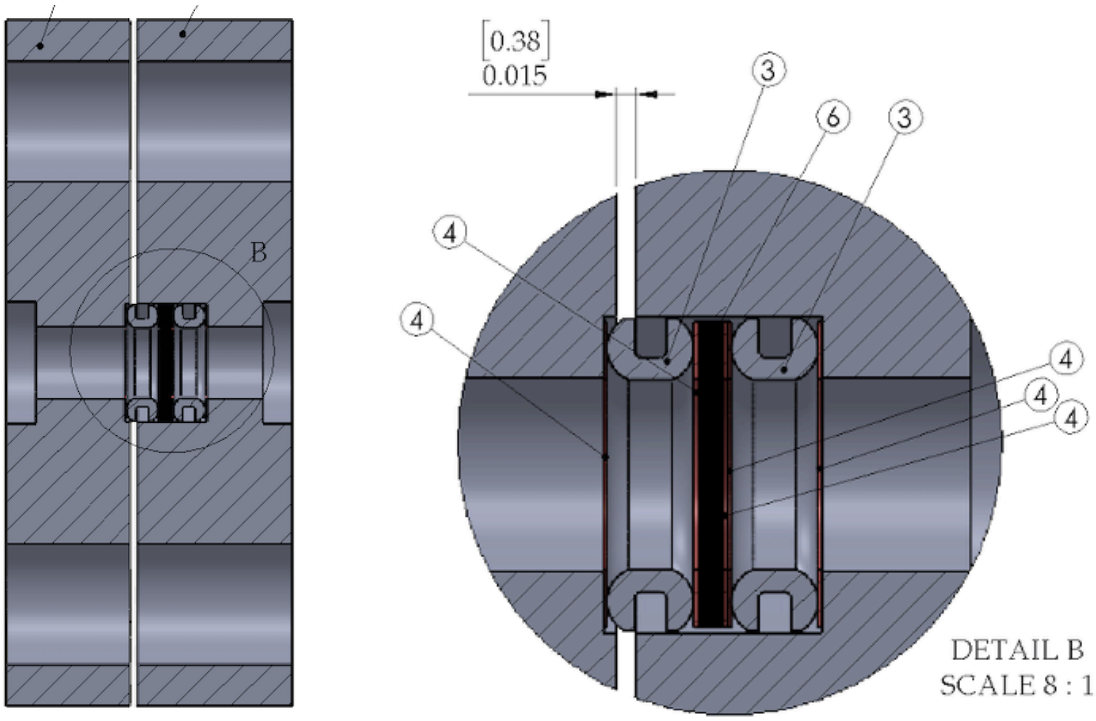

Figure 5.6 Permeation system component found within the heating source. The two inconel flanges hold the sample of interes, copper gaskets, and the inconel C-rings. Image rendered by Thomas Muth Sr. Scientist at ORNL.

Samples thinner than 0.5mm reduce the gap thickness between the flanges and therefore, when fully closed, not enough load is provided to the c-rings. This causes the c-rings to not be fully engaged and therefore a vacuum seal is not attained. The copper gaskets serve to make up for any deviation from 0.5mm due to different sample thicknesses. This provides more flexibility in the samples used and in the tolerated margins of error from initial sample processing such as cutting and additional reduced thickness due to polishing.

Figure 5.7 shows a detailed design schematic of the Inconel C-rings used. The left side shows a side view of the C-rings, with the same side view shown in Figure 5.6. The right side shows a top view along with outer, and inner diameter measurements that are 0.242 inches (06.15mm), and 0.147 inches (03.73 mm), respectively. The top view allows the viewer to more easily understand that the whole C-ring is essentially a hollowed-out ring where a thin ring around the outer most circumference has been removed leaving a C shape when seen from the side

A schematic of the components found inside the heating chamber is shown in Figure 5.8. One Inconel tube(1) is welded onto the outside of each flange(3). The upstream deuterium travels through a tube towards the sample. Once it permeates through it continues to travel downstream through the other tube towards the QMS where it is characterized and quantified. Each flange contains four holes to hold four standard 10-32 by 0.75"by 0.312" across the top Inconel 625 nuts and bolts. It is imperative the nuts and bolts are made of the same material as the flanges or at least made of material with the same thermal expansion coefficient to avoid thermal expansion at different rates between the nuts, bolts, and the flanges. Due to the high operating temperatures, ~900°C, where most fabrication materials, such as stainless steel, begin to show evidence of stress, corrosion and melting; ensuring the same thermal expansion of the components avoids any additional stress between the nuts, bolts, and flanges. Surrounding the flanges is a quartz tube with flowing argon(8). The argon gas was used to dissipate air and reduce high temperature oxidation.

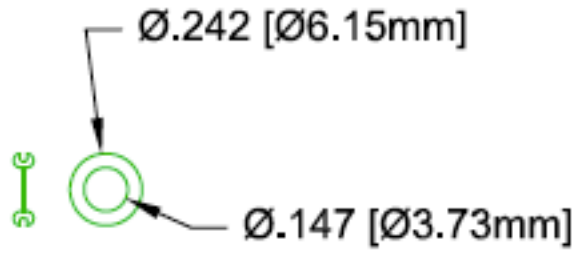

Figure 5.7 Side and top view of Inconel C-rings. Outer diameter is equatl to 0.242 inches (06.15mm). Inner diameter is equal to 0.147 inches (03.73 mm).

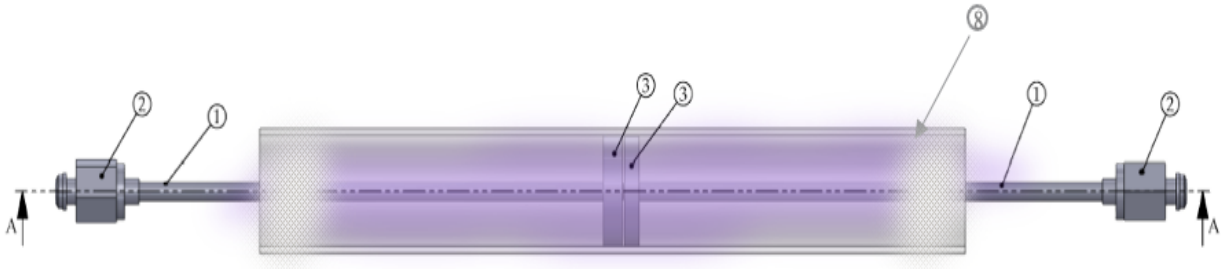

Figure 5.8 High temperature permeation system component showing the inconel tubes welded onto the flange. During this work, the system is surrounded by a quartz tube (8) to hold argon shown in purble.

The quartz wool (shown in white) is positioned at both ends of the tube to contain the argon within and avoid any further inflow of air. This portion of the system will be changed since it appears to have impacted the experimental results. This will further be explained in section Chapter 6.

5.4 Permeability Experimental Methods

The same experimental steps are taken for high temperature as for low/intermediate temperature experiments. Therefore, I provide detailed steps using data from intermediate temperature experiments performed by Ze Chen [7]. It is important that the thickness of the permeated sample be measured prior to the permeability experiment due to expansion that occurs as a result of the permeating gas. Once measurement has taken place the sample is positioned inside of the flanges and encased within the two C-rings. Both sides, that is the upstream and downstream sides must be pumped down to about $10^{-7} Torr$, possibly $10^{-8}\ Torr$. Once vacuum has been achieved, the heating system is turned on and allowed to reach the desired temperature and remain at this temperature.

As mentioned in Section 5.1.1, in order to calculate the activation energy and permeability pre-exponential factors, a series of permeability values for different temperatures must be plotted to obtain the Arrhenius dependence. Figure 5.9 shows Eurofer 97 permeability measurements performed by Chen [7] at each temperature regime starting from $350°C$ and incrementing by $50°C$ up to $550°C$. Multiple permeability values can be calculated using Equation (5-2) by incrementing the upstream permeating gas pressure within the same temperature regime and using their respective flux values in Equation (5-2). For example, at $350°C$ the system is initially under vacuum on both the upstream and the downstream sides. Once the heating chamber has reached the desired temperature, in this case $350°C$, the upstream gas can begin to be let in at a set pressure, in this case 19,600 pascals or 147 Torr.

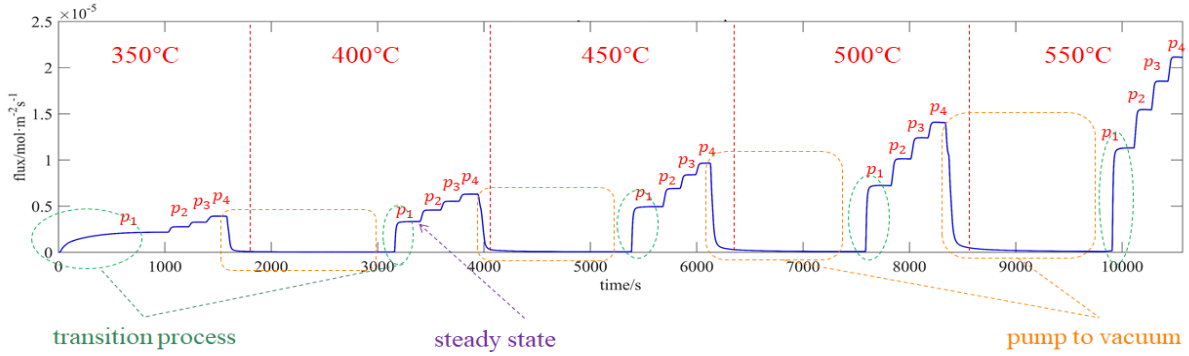

Figure 5.9 Deuterium in Eurofer 97 permeability measurements performed at 350°C, 400°C, 450°C, 500°C, 550°C, and at four different pressures within each temprature regime. As reproduced from Ref [7].

The period prior to steady state permeation, is labeled as the transition process (green). Steady state permeation is shown by the purple arrow. Once a clear steady state period has been achieved, the incoming gas pressure can be increased, in this case it was increased to 243 Torr. The incoming upstream gas pressure was increased a total of four times at the same temperature. Once the fourth permeating flux has been calculated, both sides of the system are pumped back to $\sim 10^{-7} Torr$ and the temperature is increased to $400°C$. The orange dotted line box between $350°C$ and $400°C$ shows the lull period where the system is being pumped back down. Once the desired vacuum has been achieved the same previous steps are taken again at this new temperature. The multiple calculated permeability values are then averaged together into a more statistically accurate average permeability value with error analysis (error bars). This results in a single permeability value at that temperature. It is these averaged permeability values that are plotted as a function of inverse temperature in the Arrhenius dependence plot.

5.5 Preliminary High Temperature System Testing

All previously shown results pertain to the intermediate temperature range where stainless steel components were used. Figure 5.10 plots measurement results of deuterium in tungsten using our system with the initial high temperature design and Inconel components (magenta). The results are compared against available literature. This demonstrates successful design, fabrication, and implementation of the Inconel equipped permeation system, from 450°C to 950°C, while maintaining a vacuum on the order of $10^{-7}\ Torr$.

The left plot of Figure 5.10 shows the recorded steady state permeation flux as a function of pressure. Each temperature is represented by a different color and each pressure by an individual data point. Increase in slope with increasing temperature is present with red being the lowest, blue the intermediate, and green the highest temperature.

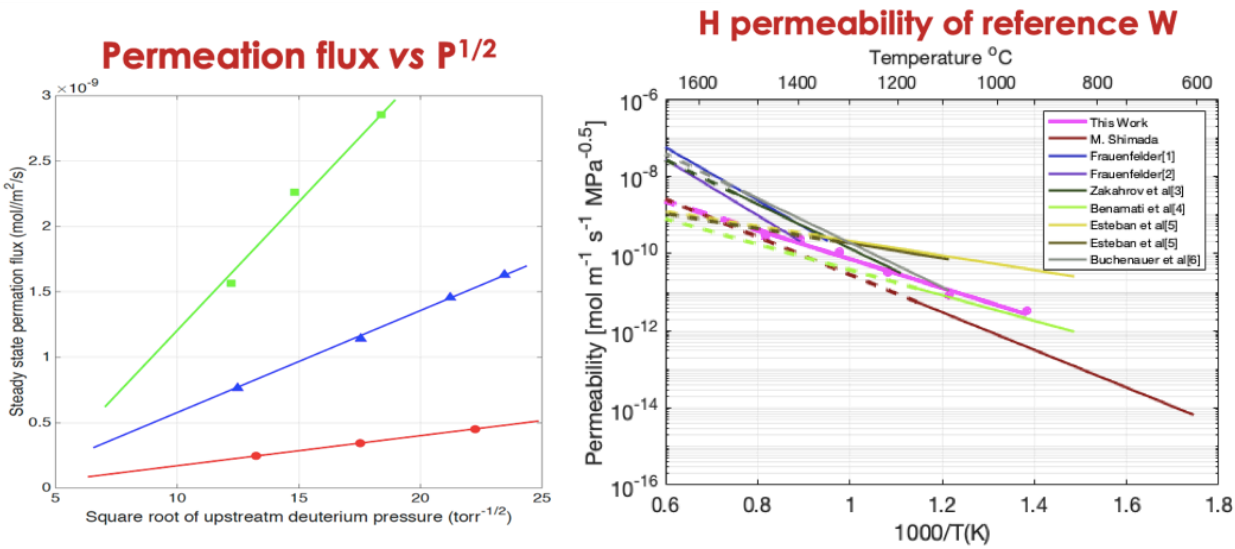

Figure 5.10 Permeation flux vs the square root of the upstream pressure plot (left) showing a clear linear relationship. Deuterium in Tungsten permeability data plotted against previous works within the same temperature regime (right).

The plot on the right shows the average permeability values plotted against previous works performed by Shimada and others. There is good agreement between our work and literature permeability magnitudes with a slight difference in the slope. Our pre-exponential factor is $3.96x10^{-7}$ compared to $2.13x10^{-6}$ obtained by Shimada[9] literature values, listed in table Table 5-1. Our activation energy is 71.60 kJ/mol, compared to 93.32 kJ/mol calculated by Shimada[9]. Permeability can be affected by material fabrication and the additional impurities that result from it. Small variations in measured permeabilities are expected and therefore the work performed by Dr. Xunxiang Hu (magenta) is in good agreement with other literature works.

5.6 Permeability Summary

Further understanding of hydrogen permeability behavior in tungsten is important for reactor design and to further develop the fusion energy field. Good intermediate temperature permeability results for materials such as Eurofer 97 using stainless steel components is shown. Due to the high melting point of tungsten, performing permeability experiments on tungsten requires a much higher temperatures where stainless steel components start to experience heat corrosion. As a result, Inconel based components were designed and fabricated to use for the hydrogen in tungsten permeability experiments.

Preliminary experiments were performed by Dr. Hu to benchmark our hydrogen permeation in tungsten results against available literature[68], including Shimada[9], to demonstrate our systems capability to perform permeability measurements at high temperatures. Both the resulting activation energy and pre-exponential factor are within reasonable agreement, allowing us to continue with future experiments where a helium containing bubble layer is pre-implanted prior to the permeability experiments.

Chapter 6 SEM, Permeability, and LIBS/LAMS measurements of He-plasma exposed Tungsten: pre and post permeation

6.1 SEM Evidence of Successful He Exposure

Given the UTK plasma source system had not been previously parametrized nor the plasma beam characterized, there was uncertainty regarding the presence of He in the W samples as a result of exposures. To assess the success of He exposures Dr. Chad Parish (Research Scientist from ORNL) performed SEM on a He exposed W sample to study if there was any He induced surface damage. The sample exposed to the highest fluence and temperature (5E21 He m^{-2}, 900K) was chosen for the SEM surface characterization. The reason for choosing this sample is that He induced surface damage has been observed to increase with He content and temperature [54]. If He surface damage was not observable on the sample with the highest He content then it would likely not be observable on the lower fluence samples.

Figure 6.1 shows Dr. Parish's produced SEM images of the 5E21 He m^{-2}, 900K exposed W sample. The three images show the center of the sample, at different scales, where the peak of the plasma beam distribution was estimated to be located. Surface damage is evident in image b) and c). Image c) shows very early stage incident damage that give rise to fuzz at larger fluences and temperatures [54]. Evidence of He induced surface damage was promising however, even post SEM, the presence of He was not conclusive and additional surface to bulk characterization was needed.

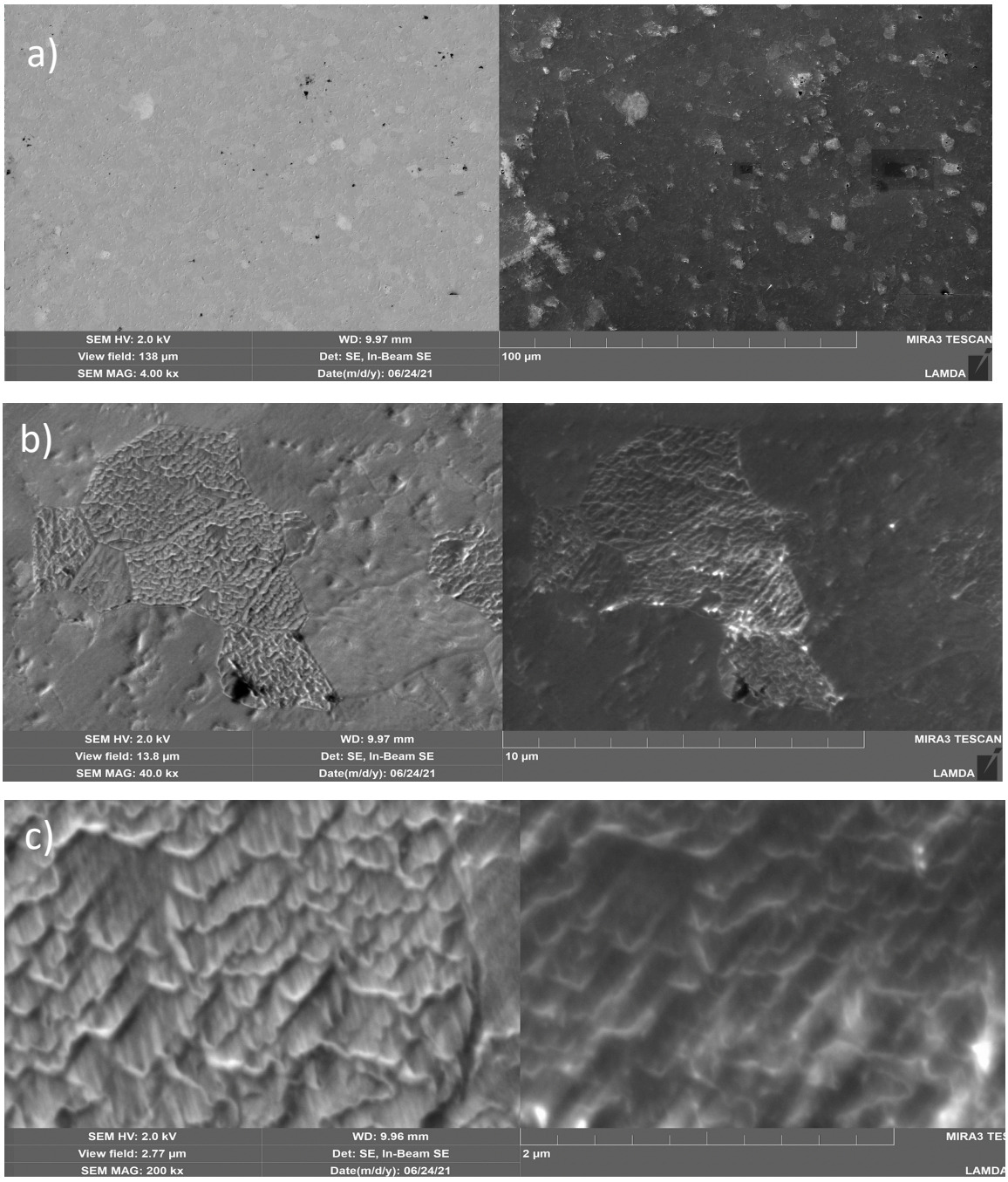

Figure 6.1 SEM images produced by Chad Parish showing the He induced W surface damage.

6.2 LAMS Measurements for He Exposed Samples

LAMS was performed on one sample per exposure condition. Given there are eight different exposure conditions, a total of eight samples were studied using the LIBS-LAMS techniques. Figure 6.2 shows the LAMS results for the UTK He plasma exposed W samples. The plots are organized in increasing temperature order from right to left, and increasing fluence order from bottom to top. Each plot contains a He depth dependent profile where the He content is resolved throughout the bulk. Additionally, each plot also contains an insert that provides the He appm values plotted at each depth specified on the x-axis. A sample with a fluence of 5E20 at 300K was not produced and as such its position in this matrix is blocked by the orange dotted X. The x-axis of every plot is a function of the average depth at midpoint for each ablation. The y-axis is in terms of appm, quantifying the ablated material in atomic parts per million. The top left sample in Figure 6.2 is the one on which the SEM characterization was performed on by Chad Paris. It contains the largest levels of He with an appm of 462,210 in the near surface.

From SEM surface characterization and LAMS results, I could determine with high certainty that the plasma exposures had been successful in positioning He in the W near-surface and, further, that all of the helium was located within the first 50 to 100 nm of the surface. The larger fluences were expected to yield higher quantities of He. This relationship can be viewed within the same matrix column from one row to the next. A correlation between temperature and He content was also expected where higher exposure temperatures would yield larger quantities of He. This relationship is evident from right to left within a single column. The LAMS output results correlate well with the expected He content based on the flux and temperature exposure conditions. These samples can now be used in deuterium permeation experiments to investigate He effect on H permeation behavior.

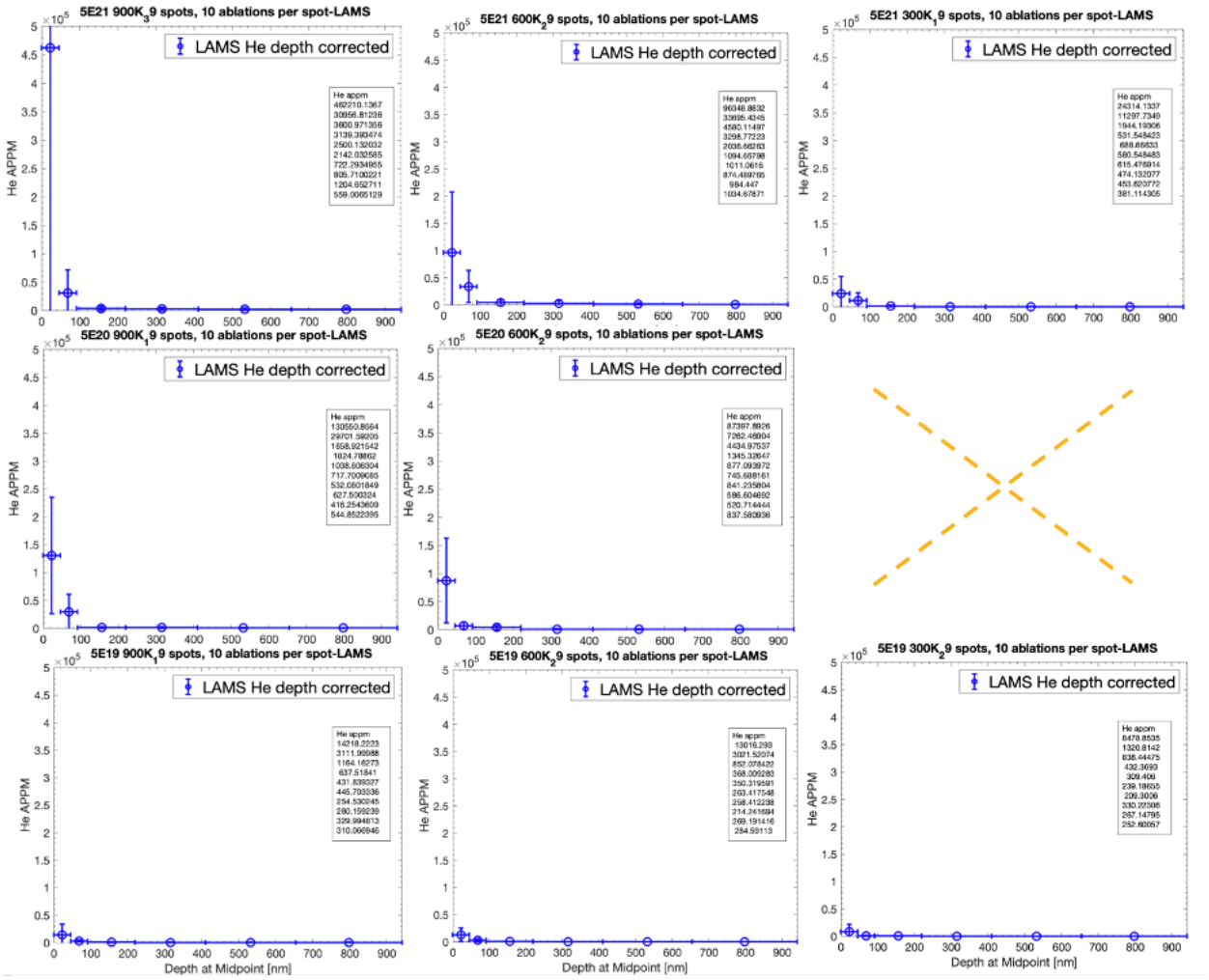

Figure 6.2 LAMS results for all UTK He plasma exposed W samples. Plots arranged in order of increasing temperature and fluence.

6.3 LIBS Plasma Plume Evolution as a Function of He

The LIBS results were very revealing regarding the system capabilities, limitations, and remaining unknowns. In order to fully assess the He exposures, LIBS and LAMS was performed on a sample also characterized by Chad Parish with scanning electron microscopy (SEM). The SEM surface characterization provided evidence of He exposure surface damage consistent with the presence of He in the near-surface region. However, this SEM characterization is only qualitative in nature. This sample was exposed to the largest fluence of 5E21 He/m^2 and highest temperature of 900K. It was chosen as the first one to perform LIBS and LAMS on to ensure a signal was observable. The idea was that if no signal was evident with the largest exposure, it would likely not be observable in the lower fluence, lower temperature sample exposures.

A very clear and significant signal was observed by LAMS for the 5E21 He/m^2 900K sample as demonstrated in Section 6.2. However, when analyzing the LIBS data for the same sample, the raw voltage hovered near 0.18V while it nearly doubled to 0.27V for a reference W sample with no He. Multiple ablations were performed in nearly 30 different spots and analyzed using LIBS. A secondary 5E21 He/m^2 900K exposed sample was also investigated using LIBS and equally a voltage near 0.18V was consistently observed. Similarly, a secondary reference sample was studied using LIBS and likewise a large voltage near 0.27V was obtained. This was counterintuitive to the more common magnitude dependent signals obtained from LAMS and most other systems where larger quantities produce larger signals. This seemingly inverse relationship had to be investigated further in order to further develop the LIBS experimental technique.

Figure 6.3 shows a plot containing the raw voltage values for all UTK He plasma exposures plus an additional reference sample. The raw LIBS voltage signals are plotted as a function of the LAMS quantified He content shown on the x-axis. The

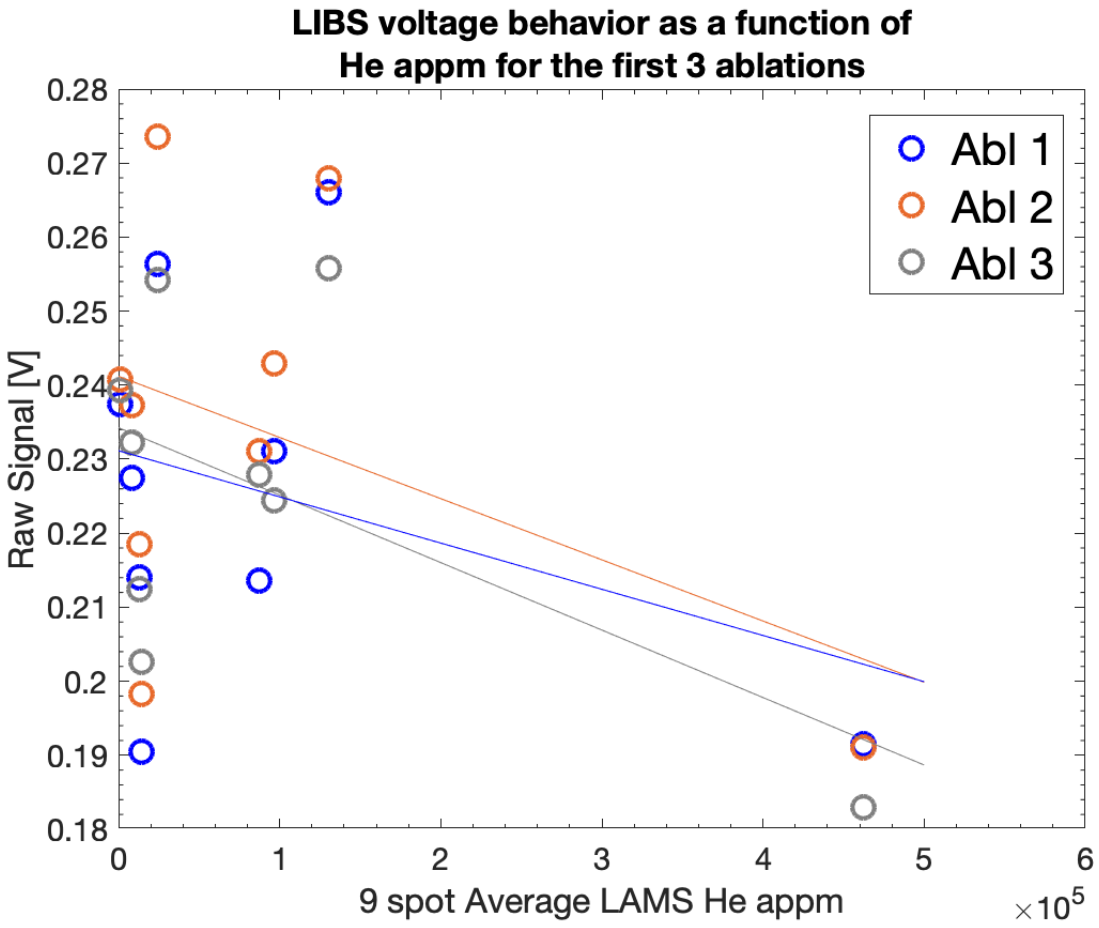

Figure 6.3 Raw voltage signal plotted as a function of LAMS quantified, He in appm. Observable inverse relationship between raw voltage signals and He content.

blue circle data points pertain to the first ablation for all eight exposed samples and the reference sample. The orange circles pertain to the second ablation for all nine samples. Successively, the gray circles pertain to the third ablation for all samples. Ablations past the first one were included to observe if the same inverse relationship was present past the surface or if it was just an initial pristine surface effect. From these comparison studies it is evident there is a consistent inverse relationship between the helium content and the ablation produced voltage signal measured in the filterscope during the LIBS experiment.

Further analysis of the voltage signal to helium content dependence was performed to identify gaps in the understanding of the LIBS system and the data analysis. Identification of these gaps could be the last step in converting LIBS from a qualitative assessment to a quantitative technique. To use LIBS quantitatively the raw voltage signal can be converted to a particle flux through Equation (4-3). Then the particle flux can be simplified to a total particles per second quantity. However, currently, there are two unknowns in Equation (4-3), the plasma plume size and the S/XB coefficients. To convert the particle flux to a particle per second quantity, Equation (4-3) is multiplied by a plasma cross section as observed by the lens. However, the laser produced plasma plume size has never been measured, just estimated by myself. Similarly, the S/XB coefficients in Equation (4-3) have not been measured, just estimated[3]. Given the plasma plume cross section size can systematically vary, it was the initial parameter changed during the analysis of raw voltage signals to He content.

Figure 6.4 shows the plotted LIBS signal calculated by changing the plasma plume size until it equals the LAMS quantified He. The insert in the plot shows the changing, ever increasing, plasma plume size required LIBS to equal LAMS calculated He content. Eventually, a plasma plume cross section of $7m^2$ is required for the largest He content. This plume size is impossibly large which indicates the S/XB coefficients is responsible and highly inaccurate for large He content plasmas.

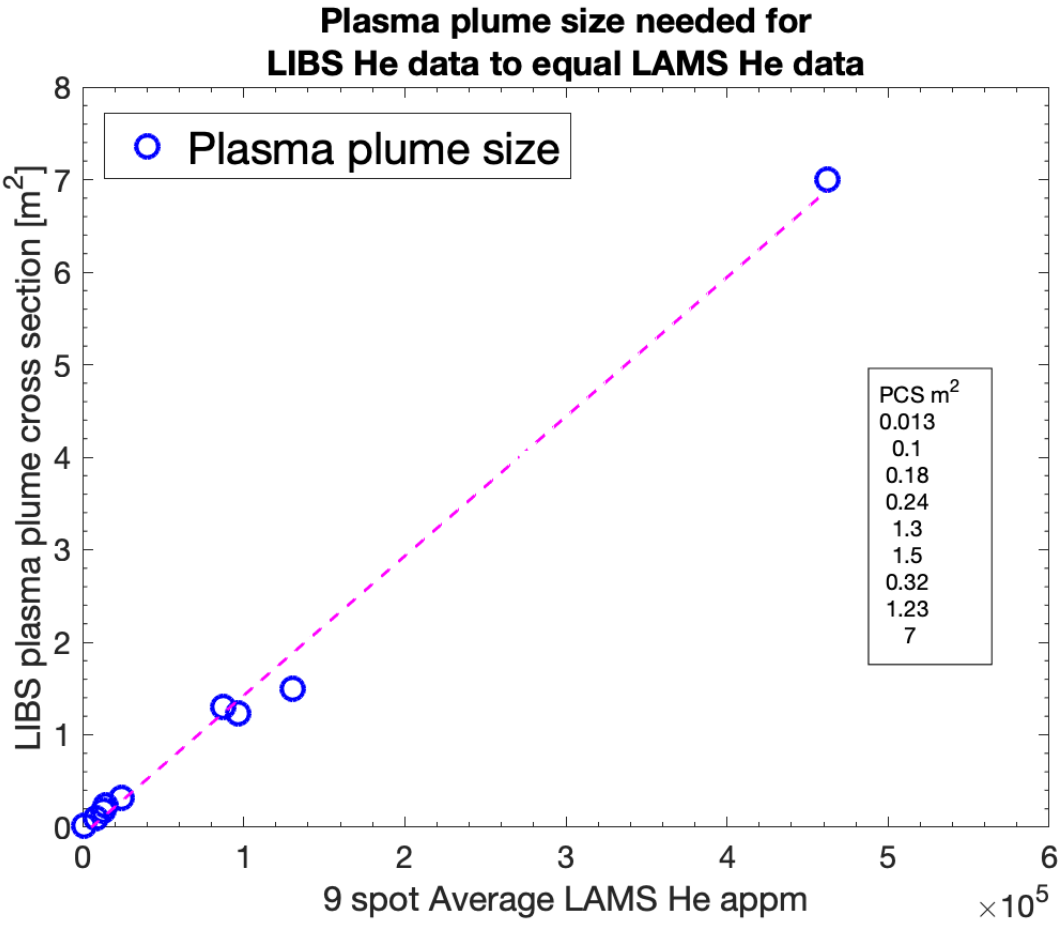

Figure 6.4 Adjusted LIBS calculated He appm to equivalate LAMS He appm by changing the size of the plasma plume cross section.

Fitting the data (magenta dashed line) shows there is a strong linear relationship between the plasma plume size required and the He content. This shows that the LIBS signal can render the same He quantities as LAMS, however, doing so by changing plasma plume size is an incorrect approach and therefore other degrees of freedom must be investigated. The linear relationship is indicative of predictable and repeatable phenomena that needs further investigation.

It is evident from Figure 6.4 that the plasma plume size is not entirely responsible for the conversion of LIBS signal to particles. The S/XB coefficients are the only remaining unknown parameter in the flux equation, Equation (4-3). As mentioned in section 4.4.2, the S/XB coefficients were determined for a static plasma, specifically a pure W plasma that did not contain He. The plasma characteristics of the plasma plume produced in our system has never been directly measured. If the electron temperature and densities are unknown, it is virtually impossible to solve for the correct S/XB coefficients specially when the plasma present element concentrations differ from pure W. This S/XB increasing deviation effect is shown in Figure 6.5 where the ratio of the LAMS signal to the LIBS signal is plotted as a function of He content. In this LIBS calculation the plasma plume size remains unchanged to isolate the effect of the S/XB coefficients on the LIBS resolved He content. The insert in the plot shows the resultant ratio for each of the 8 UT plasma source exposures and the reference sample. This also shows a strong linear relationship between the ratio and the He content.

The systematic grid of He plasma exposures provided unexpected insight of LIBS and remaining gaps in the understanding of its use as a quantitative system. Based on the described analysis, it has been determined that it is imperative to first understand not only the plasma plume evolution but also the plasma properties as a function of He content. Additional experiments are suggested beyond this dissertation to study the electron temperature and density for different element containing W materials. A Langmuir probe will be utilized to determine the electron

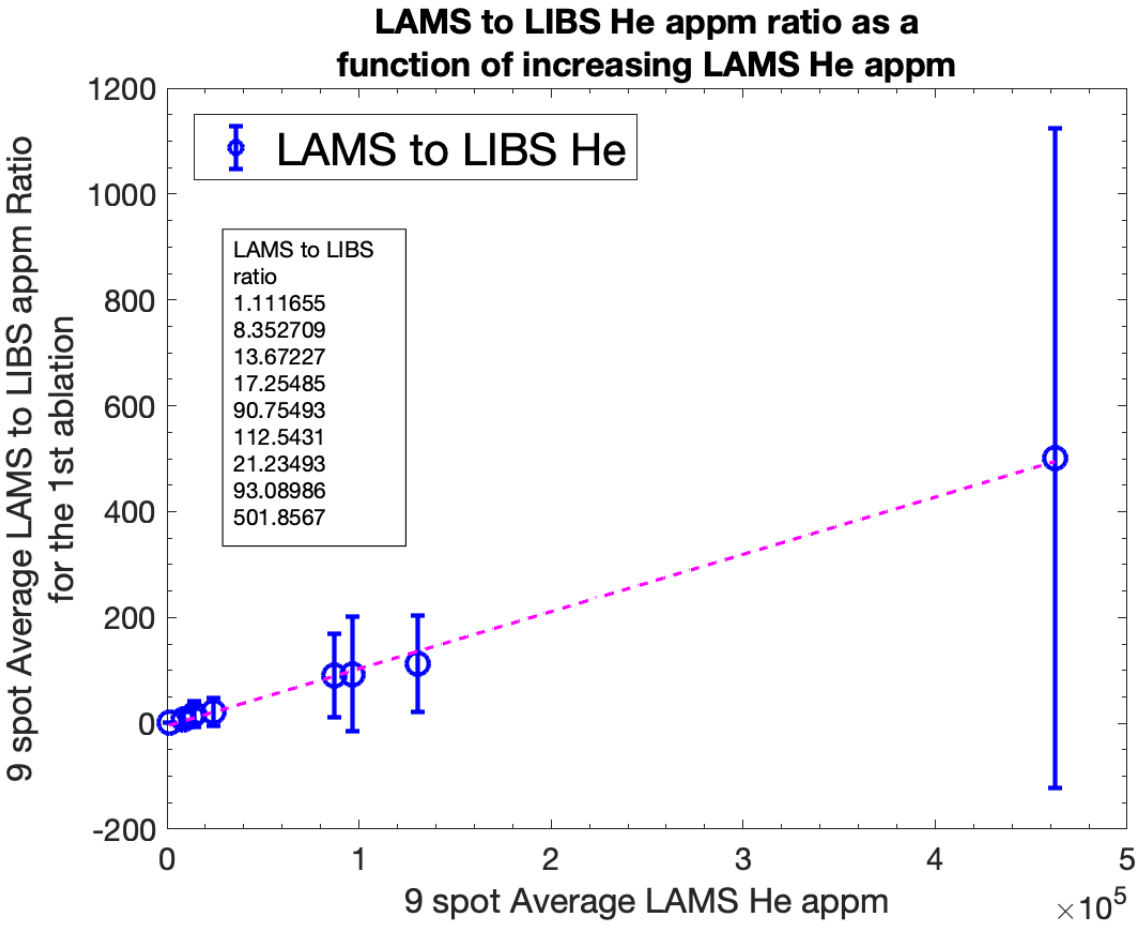

Figure 6.5 Ratio of calculated LAMS He content to LIBS calculated He content while plasma plume size remained unchanged.

temperature and density while an ICCD camera will be used to image the evolving plasma and determine cross sections at different points. This will provide more accurate calculation of the S/XB coefficients and plasma plume size and cross section.

6.4 Permeability Results

During the experiment performed by Dr. Hu using the initial design components, there was significant high temperature oxidation of the flanges and the W samples. For the latest design, we incorporated the use of flowing argon gas to displace air and reduce oxidation. Permeation experiments of the UT exposed W samples were performed with flowing argon and the design described in Section 5.3.2. There were only a total of eight c-rings available for immediate use. With two c-rings per experiment, this meant there were only enough c-rings for four permeation experiments. While additional c-rings have been purchased, due to COVID-19 and material chain supply issues, we were unable to acquire any additional c-rings before the completion of this dissertation work. Thus, due to the limited availability of c-rings, permeation experiments were performed on a total of four samples. One sample was chosen for every fluence (3) at 900K plus an additional reference sample. The steady state permeation flux plots of these permeation works are shown in Figure 6.6. The top left plot shows the results of the reference sample for permeation performed at two different temperatures. The top right shows steady state permeation results for the 5E19 He/m^2, 900K UT exposure performed at three different temperatures. The bottom left shows steady state permeation at four different temperatures for the 5E120He/m^2, 900K UT exposure. Lastly, the bottom right shows steady state permeation at four temperatures for the 5E21 He/m^2, 900K UT exposure. For all samples studied, there is a consistent linear relationship between steady state permeation and the square root of the upstream deuterium pressure. This is indicative of steady state permeation where permeation is controlled

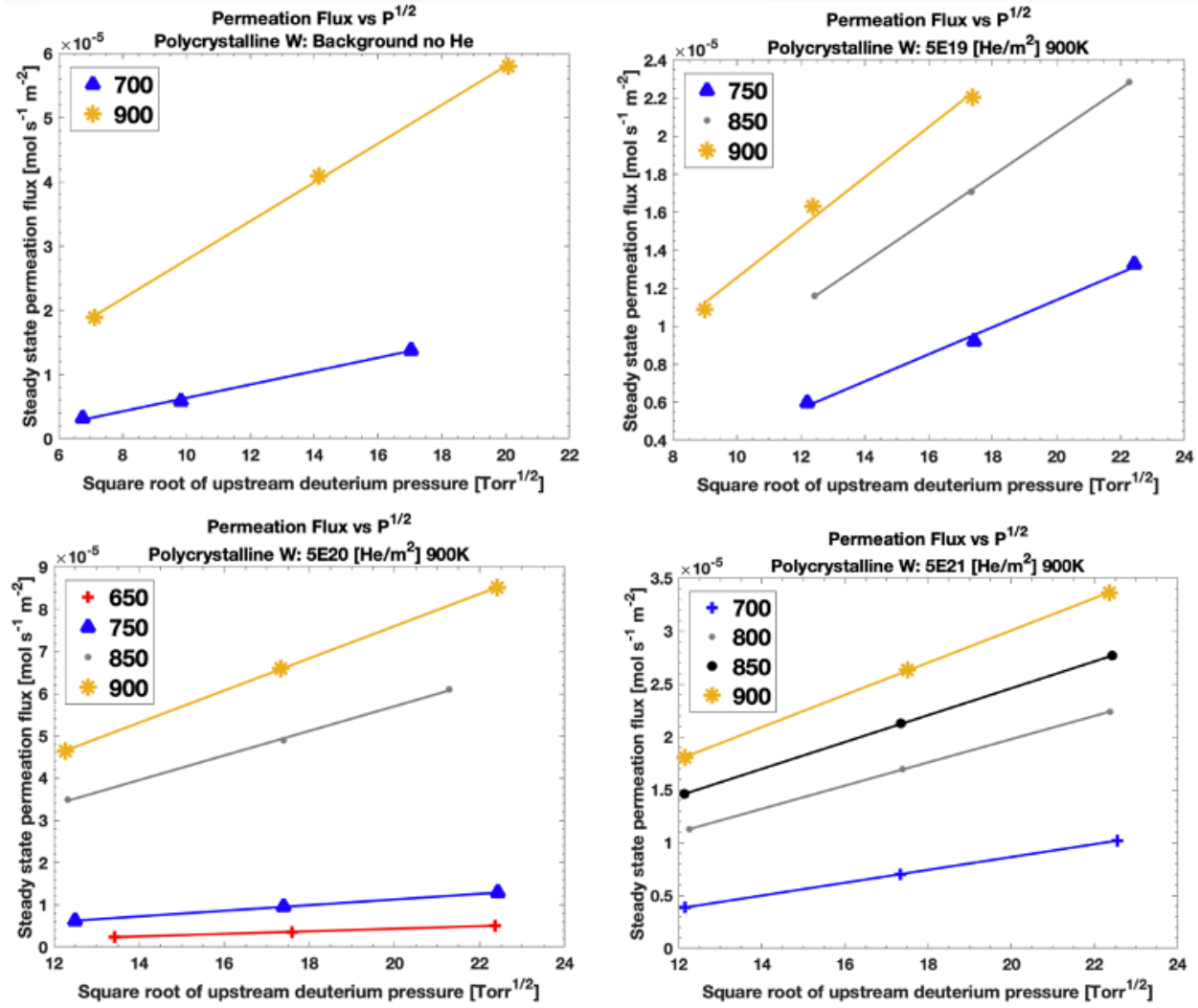

Figure 6.6 Permeation flux to square root of upstream deuterium pressure plots showing the expected linear relationship for steady state permeation.

by deuterium bulk diffusion with negligible surface effects.

Figure 6.7 shows the Arrhenius dependence relationship for all four samples alongside Dr. Hu's initial permeation experiment (magenta), with the initial experimental setup where no flowing argon was present. It must be noted that this data has been normalized for easier, direct comparison between the two different studies. Without normalization, the three UT exposed samples permeability values are larger by two orders of magnitude from both the literature data, and the initial measurement of tungsten by Dr. Hu. This could be due to the presence of argon. In all other works argon is not present and oxidation is able to take place, there is no effort to mitigate it. It is possible that removing the argon and allowing air to surround the flanges, as was the case in Dr. Hu's work, would produce permeability values in closer agreement with all other works. Investigation of the oxidation effects on permeability values is part of the future work to be performed

There is very good Arrhenius dependence agreement between Dr. Hu's reference sample, where no argon was present (magenta), and the normalized reference sample results where flowing argon gas was present (blue). This agreement in permeation behavior is shown by the overlapping magenta and blue lines in Figure 6.7. However, the permeability data should overlap without normalization. A shift in all the new permeation experiments, where argon is present, is indicative of the permeation experiments being equally impacted by an external source present during the entirety of the experiment, potentially the argon gas. Permeation results for He pre-implanted samples, 5E19 900K and 5E21 900K, show higher permeability than the reference sample while 5E20 900K shows reduced permeability. The offset, yet consistent, results for the He pre-implanted samples supports the idea the permeation experiments must pe performed once again but now without the presence of argon.

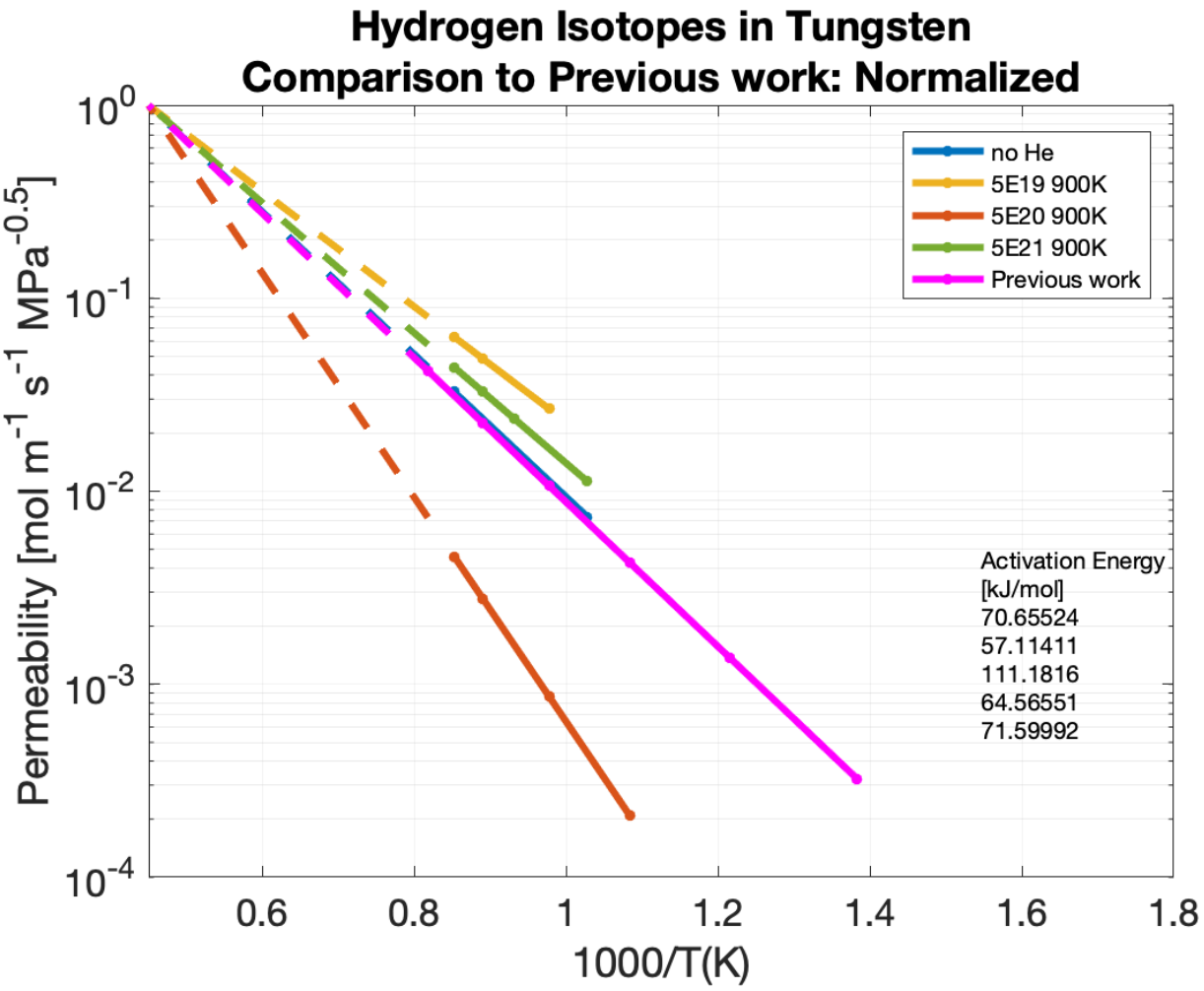

Figure 6.7 Arrhenius dependence shown for all work alongside Dr. Hu's work. The data has been normalized for direct comparison between all works.

6.5 Post-permeation LAMS Results

Although the permeation measurements are not fully consistent with prior measurements, steady state permeation was reached as evident by the strong Arrhenius dependence shown in Figure 6.6. This means deuterium was driven through the W material and thus deuterium retention as a function of He can still be investigated. Additionally, an interesting question to address is the amount of deuterium remaining in the samples.

As discussed previously in Section 6.3, the LIBS measurements and analysis currently can only provide qualitative assessment, and thus for the remainder of this Chapter, the focus will be on the LAMS measurement results. LAMS measurements were performed on the W samples almost immediately after permeation experiments to measure He and D quantities. Once permeation experiments were finished, the sample was left inside the permeation sample loading component until room temperature was reached. The samples were allowed to reach room temperature over a period of approximately three hours. The system lingers near ~150°C and the rate of cooldown decreases. Therefore, when the whole system reaches this temperature, small fans are employed to expedite the cooling process. Once the sample holder has cooled sufficiently to handle, the samples are removed and put into the LIBS/LAMS chamber. The whole LIBS/LAMS system is pumped down over night, or days, until a high vacuum level of ~ 5E-7 Torr achieved.

Post-permeation results for LAMS are shown in Figure 6.8 and Figure 6.9. Plots on the left of both figures show He measurements in appm units while plots on the right show D measurements in appm units. The first set of plots in Figure 6.8 show results for the reference sample where no He was present. The bottom plots in Figure 6.8 show results for 5E19 He m^{-2} 900 K exposures. The first set of plots in Figure 6.9 show results for 5E20 He m^{-2} 900 K exposures and the second set of plots Figure 6.9 show results for 5E21 He m^{-2} 900 K exposures.

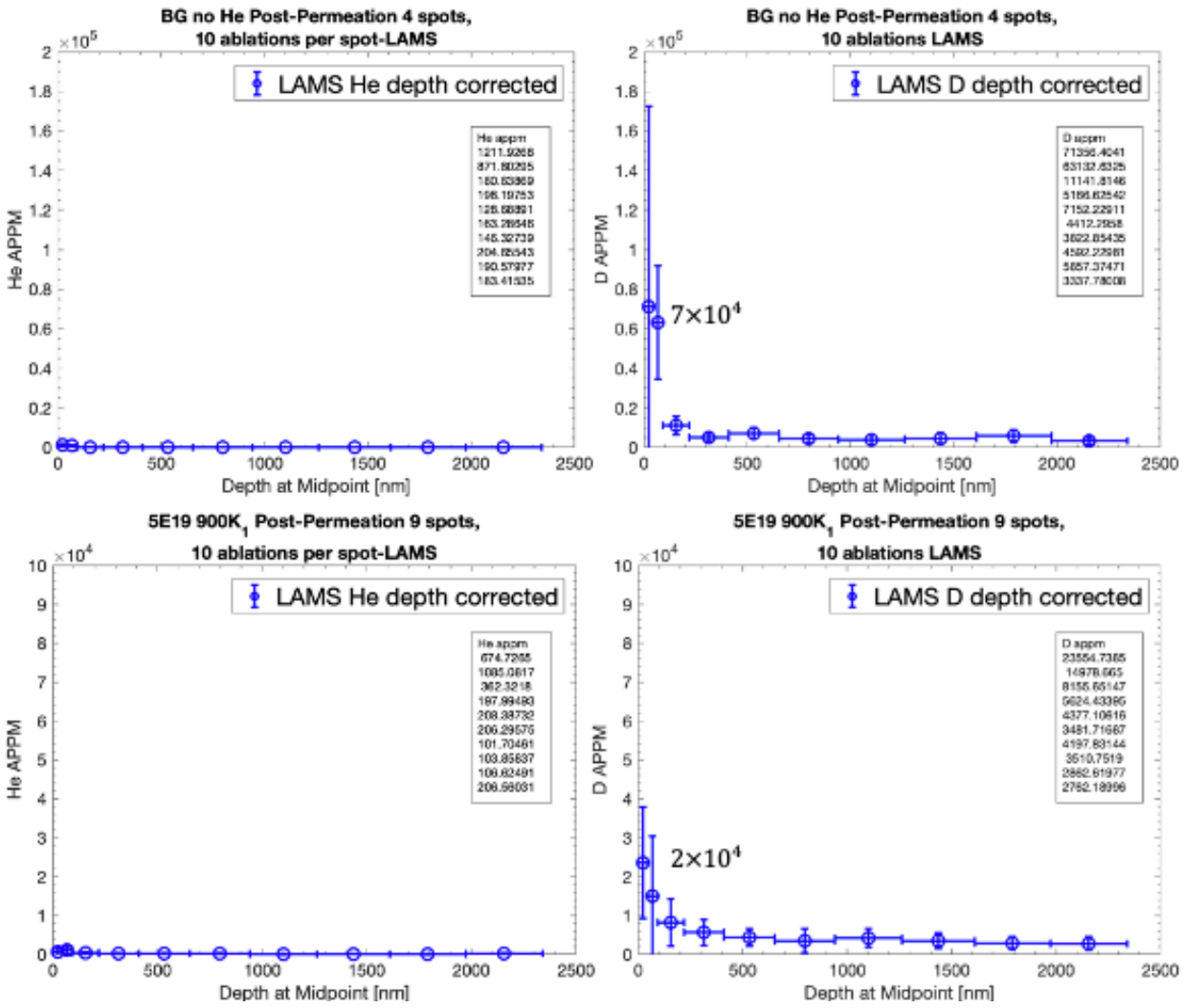

Figure 6.8 Post-permeation LIBS/LAMS measurements for UTK He exposed samples. He quantities in appm (left), D quantities in appm (right). Reference sample results (top), 5E19 He m^{-2} 900 K results (bottom).

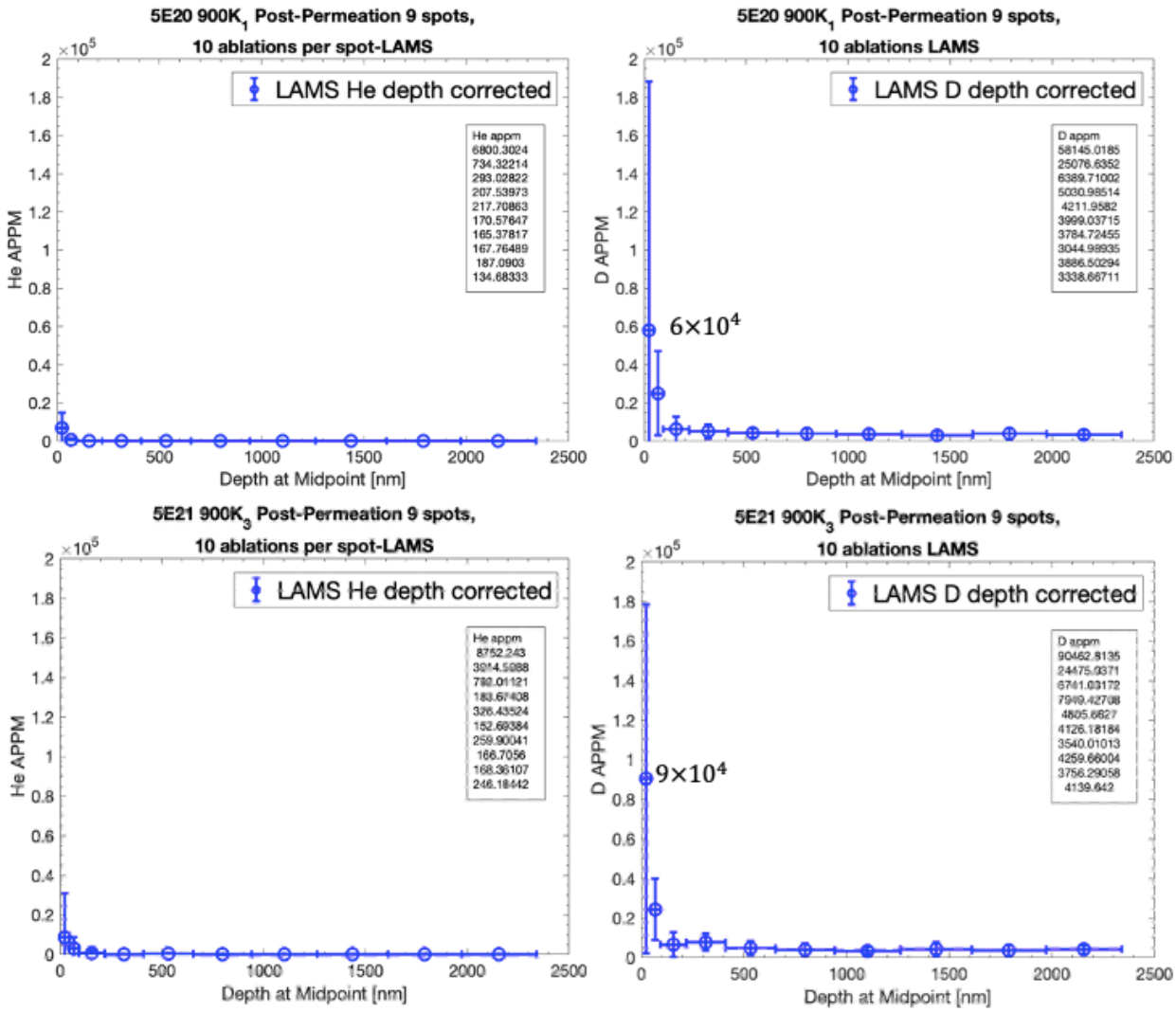

Figure 6.9 Post-permeation LIBS/LAMS measurements for UTK He exposed samples. He quantities in appm (left), D quantities in appm (right). 5E20 He m^{-2} 900 K sample results (top), 5E21 He m^{-2} 900 K results (bottom).

Figure 6.10 shows pre and post-permeation LAMS results for He content for the first ablation a) and sum of first three ablations b), plotted as a function of He exposure fluences. It is evident from Figure 6.10 that there is a significant decrease in the He content post-permeation compared to the as exposed, pre-permeation samples. Decrease in He content is observable for all samples. Loss of He could be due to a combination of bubble bursting and He desorption resulting from the extreme near surface location (~2 to 10 nm) of the 70 eV He and the high temperature (900°C) to which the sample was exposed during the permeation measurement.

Post-permeation LAMS results revealed first ablation appm He contents of 1.2E3, 0.6E3, 6.8E3, and 8.7E3 for the reference sample, 5E19, 5E20, and 5E21 He m^{-2} 900 K, respectively. Although the reference sample He content is higher (1.2E3 appm) than the lowest He exposure (0.6E3 appm), it is close to background values. In previous reference sample LAMS analysis an average of 1,200 appm is seen as the He background quantities for a pristine sample. This is essentially a system calibration factor that should be subtracted from all data. However, it has not been subtracted here since more LAMS reference sample analysis as a function of sample preparation is necessary. This means that essentially all the He content was desorbed from the lowest He exposure (5E19 He m^{-2} 900 K). Despite He desorption during high temperature permeation, the relative He content to exposure fluence relationship remained qualitatively the same where He content increased as a function of exposure fluence. The lowest He exposure (5E19 He m^{-2} 900 K) contained the lowest He content, the intermediate He exposure containing intermediate values, and the largest He exposure (5E21 He m^{-2} 900 K) containing the most He.

Based on the LAMS characterization of the He-exposed, and D-gas permeation exposed samples, an assessment of the He effect on D trapping and retention can be performed. This can be done by contrasting the D appm measured in the first ablation (near-surface) and the third ablation (bulk). The value for the first ablation is

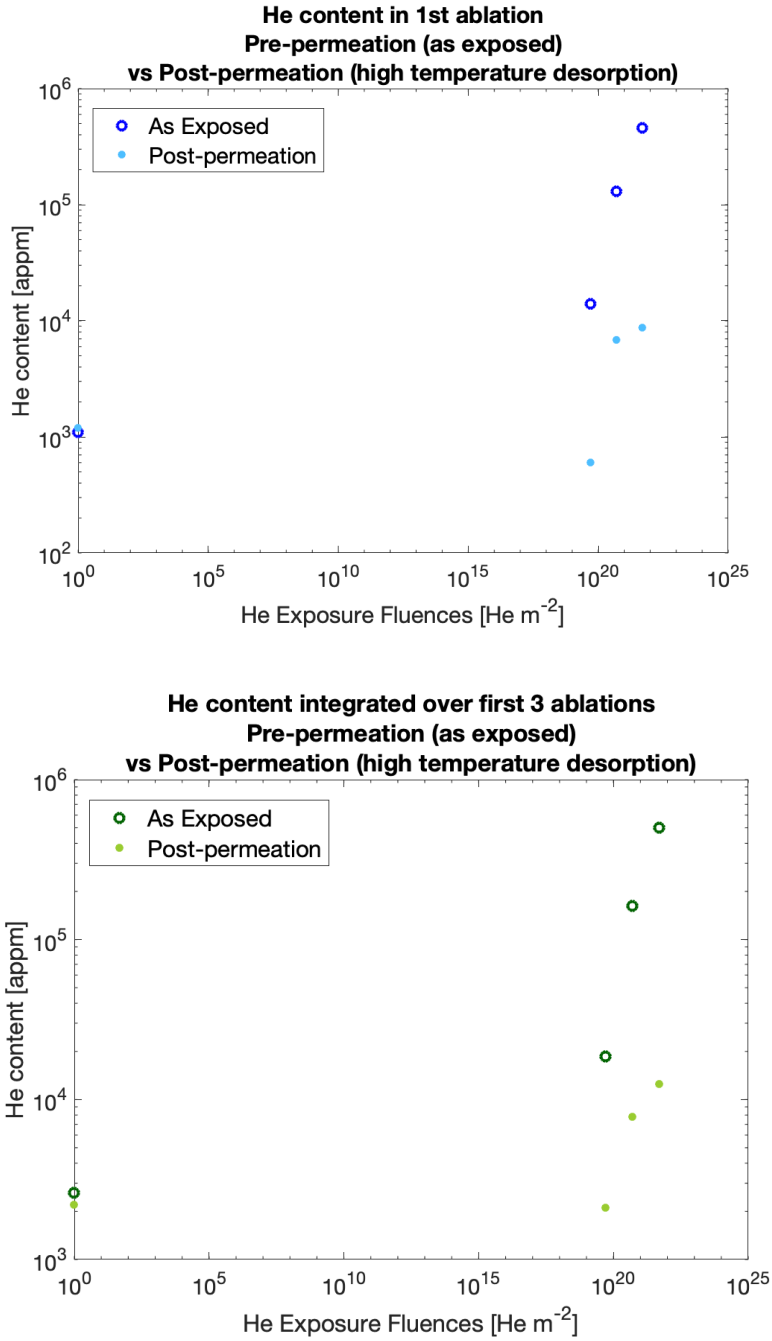

Figure 6.10 Pre and post permeation LAMS measured He content for first ablations a) and sum of first three ablations b), as a function of He plasma exposure fluences. Results shown for a Reference sample, 5E19 He m^{-2} 900 K, 5E20 He m^{-2} 900 K, and 5E21 He m^{-2} 900 K exposed samples.

included within the D plots (right side plots of Figure 6.8 and Figure 6.9). Post-permeation LAMS D measurements for the first ablations and the third are shown in Figure 6.11. LAMS measurements of the reference sample, 5E19, 5E20, and 5E21 He m^{-2} 900 K exposed samples indicated 7.1E4, 2.4E4, 5.8E4, and 9E4 appm D in the first ablation. The same analysis for the third ablation revealed 1.1E4, 8.1E3, 6.4E3, and 6.7E3 D appm, for the reference sample, 5E19, 5E20, and 5E21 He m^{-2} 900 K exposed samples, respectively. Only the surface and the first three ablations are considered as this is where the highest values of the steady-state D concentration profile are expected.

For the reference sample, no He, there are larger quantities of D within the first three ablations when compared to the He exposed samples. As He content increases, the D content found in the first ablation increases while the D measured in the third ablation (further below the surface) is reduced. This shows that D permeation in the bulk was reduced while the near surface D retention increased as a function of increasing near-surface He content. This preliminary observation of the effect of a near surface He layer is consistent with our expectations, and available literature, but will require further confirmation once the remaining samples from our experimental matrix can be characterized.

6.6 LIBS/LAMS, Permeability Results Summary

LIBS/LAMS analysis of the systematic matrix of He exposures provided insightful information regarding the LIBS system capabilities and limitations. Currently, LIBS is a system capable of providing a qualitative analysis, not quantitative. The goal is to develop it further to a quantitative diagnostic. To do so further understanding of plasma plume evolution and its conditions are necessary. Due to COVID-19 supply chain issues, only three UTK He exposed samples were chosen to perform high temperature D permeation experiments on; a sample for each fluence at 900K was chosen.

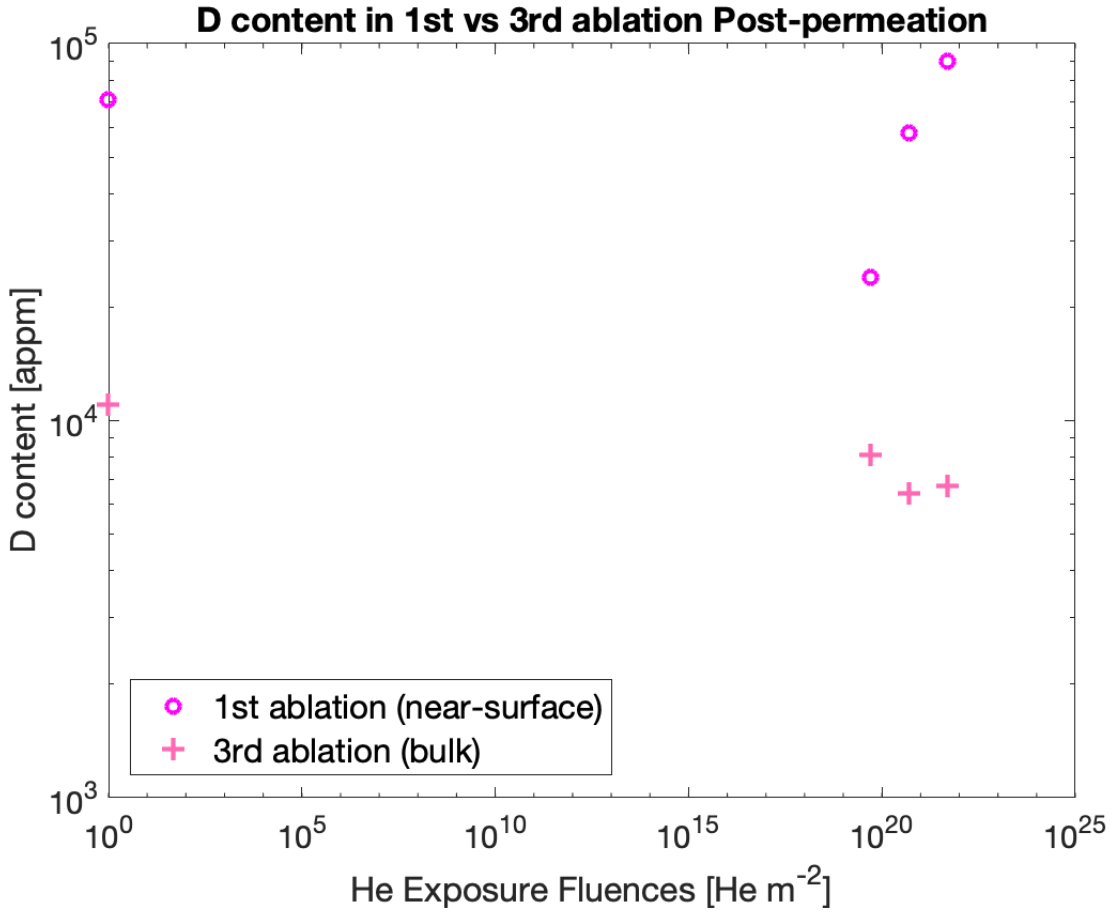

Figure 6.11 First ablation and third ablation LAMS measured D content, as a function of He plasma exposure fluences, for a Reference sample, and 5E19 He m^{-2} 900 K, 5E20 He m^{-2} 900 K, and 5E21 He m^{-2} 900 K exposed samples.

The high temperature components were slightly redesigned to reduce oxidation, improve sample loading, and ensure c-ring engaging success rates. Permeation results are consistent amongst the three UT exposed samples, and the reference sample but larger in magnitude when compared to literature [9] and Dr. Hu's previous work [unpublished]. This could be due to the presence of argon and the absence of oxygen. All works benchmarked against did not use argon gas as an oxidation mitigator. Permitting oxidation of the sample could lead to closer agreement of permeation results. Further work will be performed to investigate the effect of argon on the increase in permeability magnitudes.

Post-permeation LAMS analysis were performed to study He-D synergies in W. LIBS analysis were omitted due to new findings identifying the need for understanding of plasma plume conditions. Post-permeation LAMS measurements for the three UTK He exposed, and the reference samples, showed evidence of He-D synergies. Increase in near surface D retention, with decrease in bulk D, was observed as a function of increasing He content for all samples. Significant He desorption resulted from the high temperature 900°C permeation experiments due to near surface, 70 eV, He ions location. Deeper He bubble layers could reduce desorption during high temperature permeation experiments.

Chapter 7
WEST Samples

Two (111), and one (110) single crystal W discs measuring $6\,mm \times 0.5\,mm$ were selected for the WEST C4 campaign experiments. The W samples were single side 0.5um mirror polished by Tom from the Metallography Laboratory at ORNL. The back (unpolished) side of the samples was subsequently laser engraved as R1, R2, and R3 for identification purposes (R1 and R3 were (111) and R2 was (110) oriented single crystals). Lastly, the samples were annealed for 1 hour at 1000°C. This reduced the amount of defects present in the material. Electron microscopy performed by Chad Parish showed surface formations of nm sized, low density 'coral' structures and a 70 – 100 nm capping surface oxide layer.

7.1 Experimental Setup at WEST

The samples were loaded into the WEST tokamak by Dr. Brian Wirth. During experiments the W single crystals were exposed to He plasma using a reciprocating collector probe. Sample R1, positioned lowest on the collector probe, received the largest flux of 7.8E22 He m^{-2} s^{-1} while R3 was placed highest along the collector probe and therefore received the lowest flux of 1E22 He m^{-2} s^{-1}. R2 was positioned between R1 and R3 and thus received and intermediate flux of 3.1E22 He m^{-2} s^{-1}. The probe was inserted into the scrape off layer (SOL) plasma for approximately 10 seconds of cumulative exposure, and thus estimated fluences of 7.8E23 He m^{-2}, 3.1E23 He m^{-2}, and 1E23 He m^{-2} for R1, R2, and R3, respectively.

7.2 SEM Analysis

Post exposure analysis showed significant surface oxidation on all samples, primarily R1. Chad Parish performed electron microscopy surface characterization on R1. The produced SEM and STEM images, shown in Figure 7.1, show surface formations of nm sized, low density 'coral' like structure and the formation of a 70-100 nm surface oxide 'capping' layer [69]. The coral type features appear to contain cavities which presumably are helium-filled.

7.3 LIBS/LAMS Experiment Details

LIBS/LAMS analysis were performed on R1, R2, and R3 to characterize the surface, quantify the He content, and produce a He depth dependent profile. A total of nine locations were investigated for each sample. This ensured good statistical analysis and a more accurate assessment of the He content throughout the W surface. Six consecutive ablations were performed on each spot location to probe the material to a depth of approximately 900 nm below the surface.

To assess the oxygen content, a 777.4 nm narrow bandwidth filter was used on the second tube of the filterscope. Given the beam splitter can only accommodate three PMTs-filter channels, the D filter was replaced by the O filter in tube 2. This permitted emission line observation of He 706.52 nm in tube 1, O 777.4 nm in tube 2, and W 400.10 nm in tube 1. The S/XB coefficients for oxygen were not explored given prior LIBS analysis demonstrating the need for plasma plume conditions and evolution studies. A similar plasma plume study to the one discussed in Section 6.3 is also performed in Section 7.5 for the WEST samples. LAMS measured oxygen content was not possible due to the lack of an oxygen standard leak calibration component. Additionally, driving oxygen through the entire chamber would lead to significant contamination of the system walls. Therefore, the WEST samples oxygen content is only qualitatively investigated by LIBS rather than quantitatively.

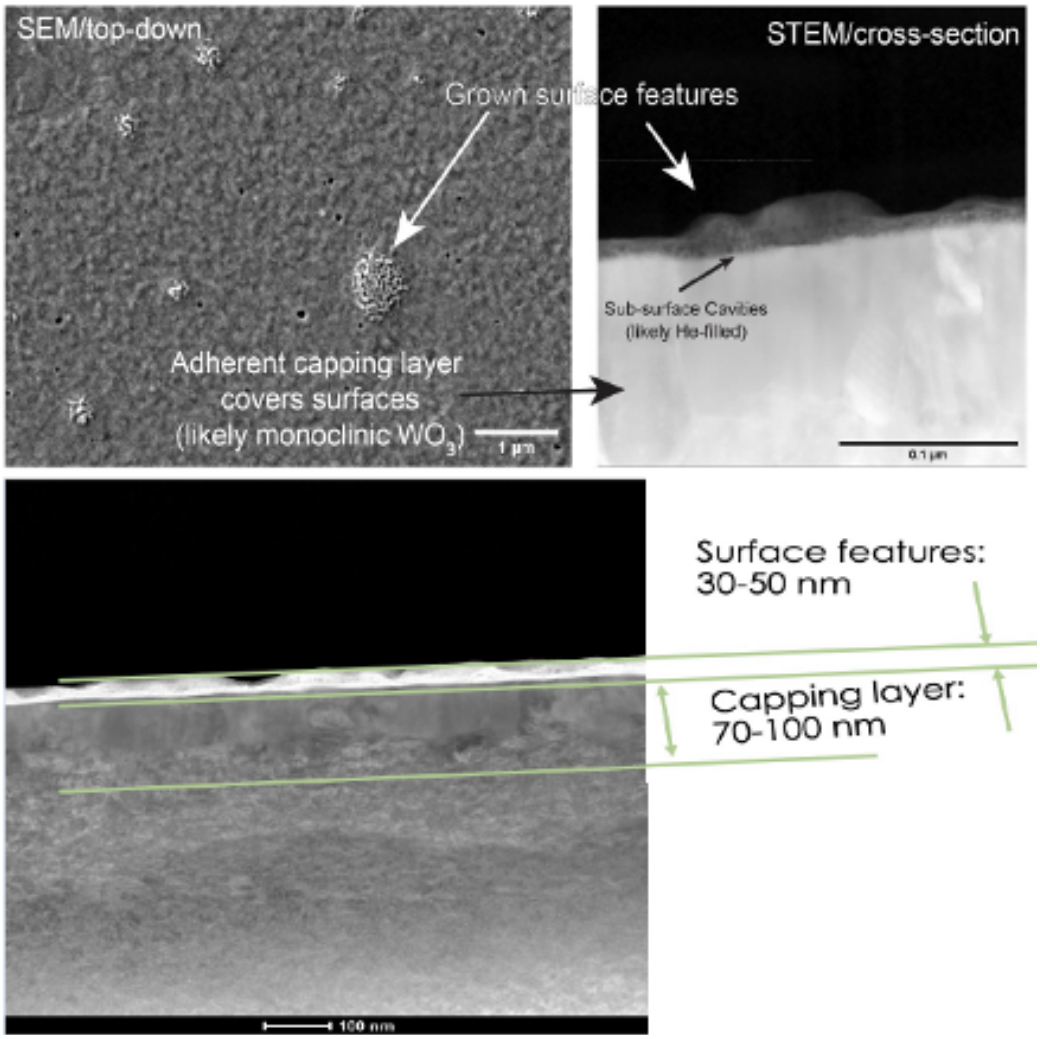

Figure 7.1 SEM and STEM image produced by Chad Parish for the R1 WEST C4 campaign sample. Surface characterization shows evidence of 'coral' type surface features and a 70-100 nm oxide capping layer.

7.3.1 SEM Evidence of Heat Affected Zone through W and O filters

Chad Parish produced additional images using W and O filters. Figure 7.2 presents microscopy images taken by Chad Parish with backscattered electrons corresponding to W and O for the sample R1. 7.2a shows a green image filter of where W is located on the sample surface. Given the sample is nominally pure single crystal W , the whole surface is covered in the green film. 7.2b is a similar analysis but this time using an O filter. The location of O on the surface of b) is identified by the use of a green filter as well. These images were taken after the LIBS/LAMS ablations and TEM analysis which are near surface destructive techniques and thus if is logical to conclude that some portion of the O layer was removed in the surface areas where the techniques were performed. The dark areas in Figure 7.2b) are indicative of the absence of O.

Figure 7.2c and Figure 7.2d are magnified regions from within the area shown in Figure 7.2a and 7.2b, respectively. Within Figure 7.2c and Figure 7.2d the extent of the ablation induced crater can be appreciated by the pink circle labeled 1. The circular ring formations past the crater are laser produced but not part of the crater. Similar to Figure 7.2a, Figure 7.2c shows the location of W in the form of a green filter. Here the W covers the entire sample surface with stronger saturation (light yellow green) in the ring surrounding the marked ablation area. This means that all though W is present in equal quantities throughout the entire surface, the filtered image is able to resolve it with better clarity in the rings surrounding the crater.

Figure 7.2d shows a similar ring covered surface area surrounding the ablation crater. The ring covered area surrounding the ablation crater appears dark indicating the near complete absence of O. With increasing distance beyond these rings, a significant presence of O is evident. The consistent reproducible pattern of oxide layer removal surrounding the ablation craters indicates this ring area is laser induced. Thus, it is logical to conclude that the oxide layer is surface desorbed due to

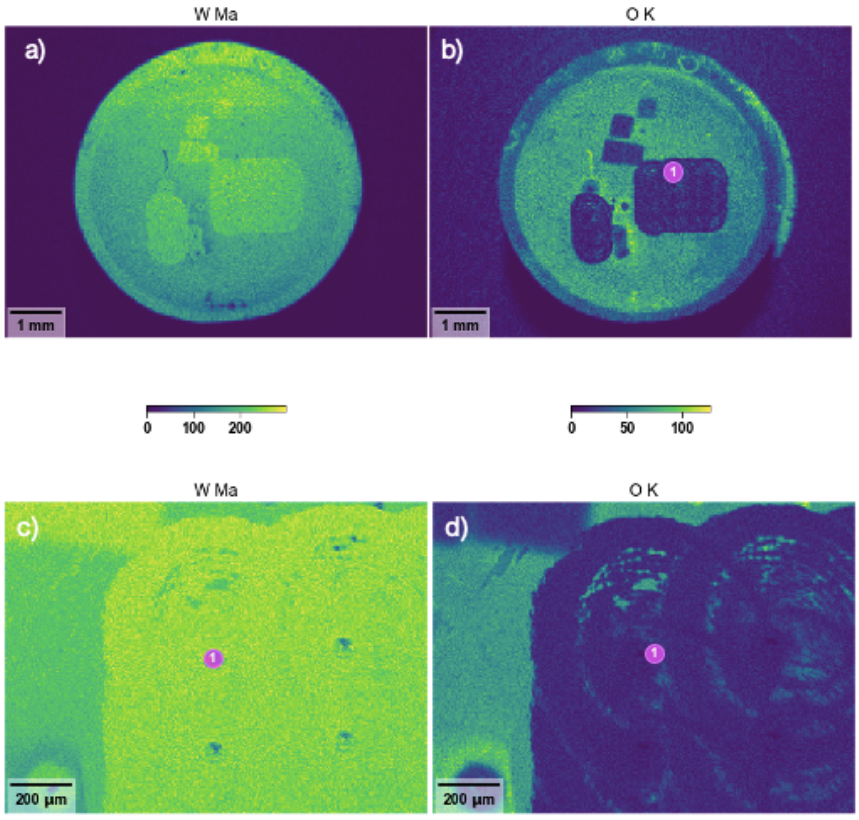

Figure 7.2 SEM images produced by Chad Parish using a W filter (a) and an O filter (right). Image c) and d) are zoomed in images of a) and b), respectively.

the produced laser heat. This surrounding ring area is better known as the heat affected zone. Efforts to mitigate or significantly reduce the heat affected zone are underway.

7.3.2 LIBS Qualitative Assessment of Oxide Layer and Content

The filtered images produced by Chad Parish demonstrated the oxide layer had been desorbed during LIBS/LAMS ablations. Figure 7.3 shows the raw LIBS signal for the first ablated spot on the R1 sample. This first spot is the same one depicted by the magenta circle with the number one engraved within Figure 7.2. Being the first spot meant the oxide layer was pristine and had not been altered by previous ablation induced heat affected zones. Figure 7.3 includes LIBS signals for He (rainbow colors) O(red), and W (black). Since the S/XB coefficients and the plasma plume cross section size are unknown, the signals are in terms of ph s^{-1} str^{-1} m^{-2}. There are a total of 10 ablations plotted as a function of relative time. Within each ablation the He, O, and, W signals overlap since they are read simultaneously during a single ablation. Although the signals are not in terms of appm or quantitative, they are qualitative. Comparison of ablation signals for the same spot can provide insight on the content present relative to one another. The W signal is relatively constant for all ablations with an average of 5E17 ph s^{-1} str^{-1} m^{-2}. The He signal is a bit harder to make a qualitative analysis of from this plot given the scale and the overlap with other larger signals. A separate plot would have to be analyzed to make a qualitative assessment of the He signals. However, for O, a qualitative analysis is possible and quite insightful. The left most signal is the nearest surface ablation (first ablation) followed by the second signal (second ablation) and so on until reaching the most far right tenth signal (10^{th} ablation). Comparison of the red signals shows that the first signal is clearly higher than the subsequent values. Now, it is important to note that in addition to an oxide layer, oxygen was present in the near surface region of the sample in the form of WO_3. Therefore, observation of O signals deeper in the bulk (2^{nd} through

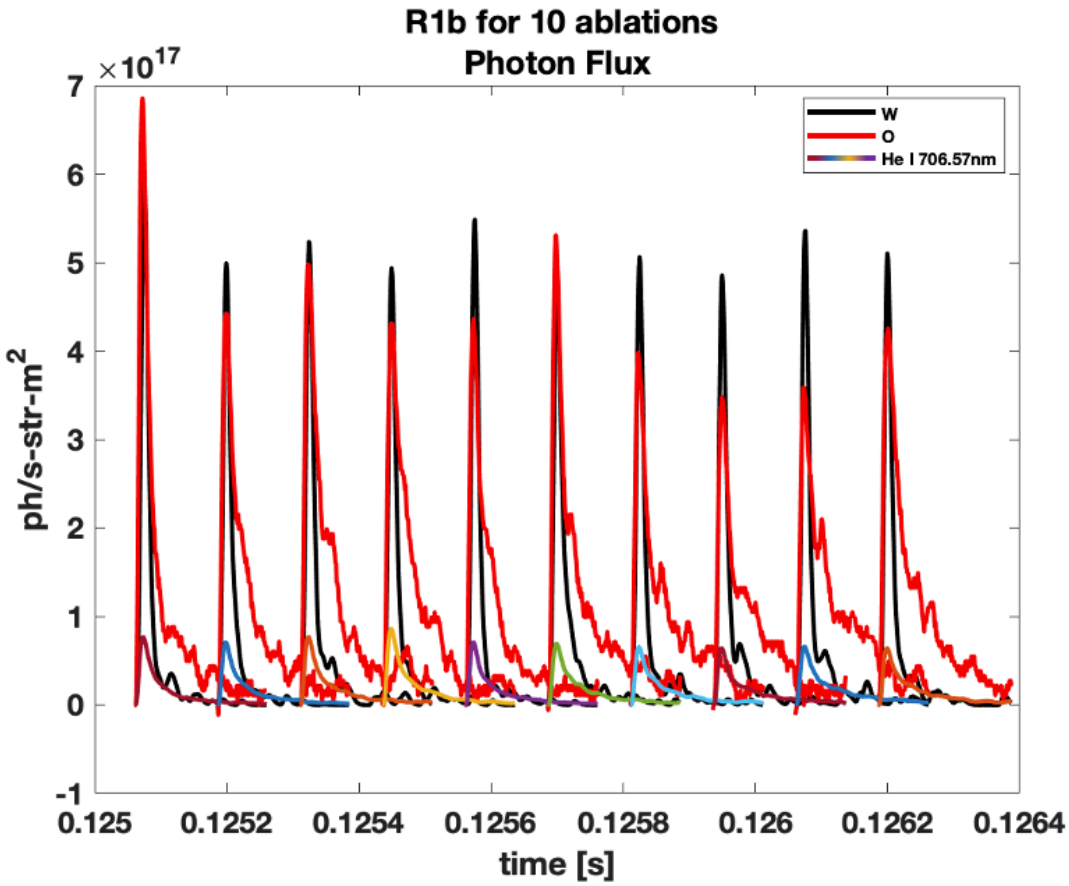

Figure 7.3 Relative O signals (red) as a function of consecutive ablations (left to right). The W signals are shown in balck and the He signals are shown in an array of rainbow colors near 1E17 ph/s-str-m².

10th ablation) is consistent with the fact that oxygen was present throughout the material and a larger first ablation signal is consistent with higher O levels on the surface possibly due to an oxide layer.

7.4 LAMS Measured He content

LAMS was used to quantify the He content. The O content could not be quantified due to the absence of a standard leak calibration. Calibration of O gas is difficult due to the high reactivity. It would lead to severe chamber contamination and therefore an experimental campaign solely dedicated to the quantifying of O would have to be designed.

Therefore, only He was measured during these LAMS measurements. LAMS results for R1, R2, and R2 are shown in Figure 7.4. A total of fifteen spots were studied on sample R1, twelve spots on sample R2, and twelve spots on sample R3. For every sample, all the investigated spots were averaged to get total He content per ablation. The y axis error bars are the standard deviation of the studied spots from the average He content value for that particular sample.

For all samples, the He content is found very near the surface with significant decrease at the second ablation and even more at the third ablation. Additionally, the LAMS output correlates well with the He content expected based on the flux at each location. With R1 being lowest on the collector probe, and therefore closest to the plasma separatrix, it received the largest flux and therefore the largest relative He content was expected. R3 received the lowest flux as it was positioned highest on the collector probe and therefore it was expected to have the lowest He content relative to the rest of the samples. R2 received an intermediate flux and thus an intermediate He content value was expected. It is reassuring to see this general relationship amongst the three samples.

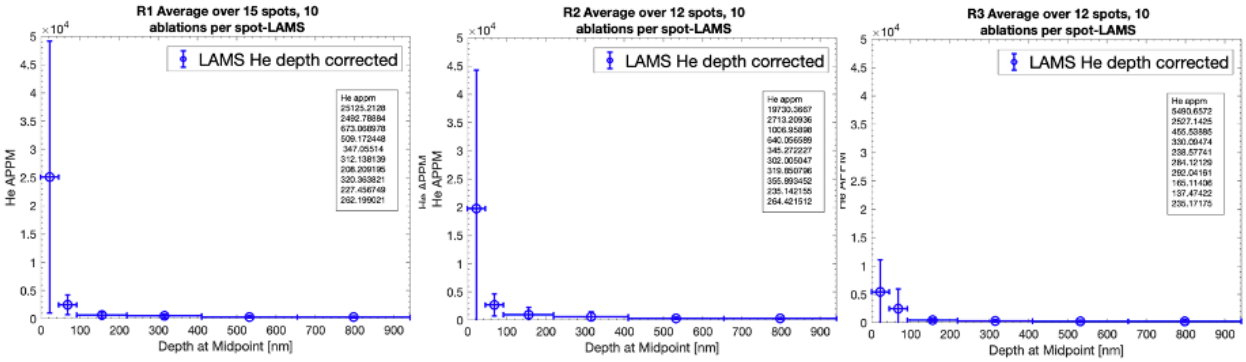

Figure 7.4 LAMS measured He content and depth dependent profiles for R1 (left, R2 (middle), and R3 (right).

7.5 LIBS Plasma Plume Evolution as a Function of He

Due to the findings of plasma plume evolution studies discussed in section 6.3, the same analysis were performed for the three WEST C4 experimental campaign W samples in addition to a reference sample.

Figure 7.5 shows results for the WEST samples LIBS plasma plume analysis. Plot a) shows the LIBS raw voltage signal plotted as a function of LAMS measured He content for a reference W sample and the three WEST samples. The first ablation for all samples is shown as the blue circles, the second ablation in orange circles, and the third ablation as the gray circles. The solid lines are best fit lines for each set of data (ablation 1, ablation 2, and ablation 3). The best fit lines show a clear inverse relationship between the raw voltage signal and the He content measured by LAMS. As the He content in the laser ablated plasma plume increases, the produced voltage signal decreases. This is contrary to most quantity dependent signals produced by most systems. Given this very atypical relationship further analysis were performed as a function of changing plasma plume cross section size.

Plot b) shows plasma plume size as a function of LAMS measured He content. As explained in Section 6.3, both the S/XB and the plasma plume cross section size are not known. However, the plasma plume size can be systematically changed to address the effect on the LIBS measurements. For each sample, the plasma plume size is increased until the LIBS calculated He content is equal to the LAMS measured He content. As He increases a larger LIBS plasma plume is necessary. Eventually a plasma plume of 0.62 m^2 is necessary for the R1 sample LIBS values to equal LAMS. The dotted dash line is a best fit line for the reference sample, R3, and R2. The fourth data point pertains to R1 and is seen to significantly deviate from the linear trend. This could be due to the surface oxide layer changing the laser produced plasma plume conditions. Additionally, the oxide layer could also be changing the way the laser interacts with the sample surface covered. This further supports the need for

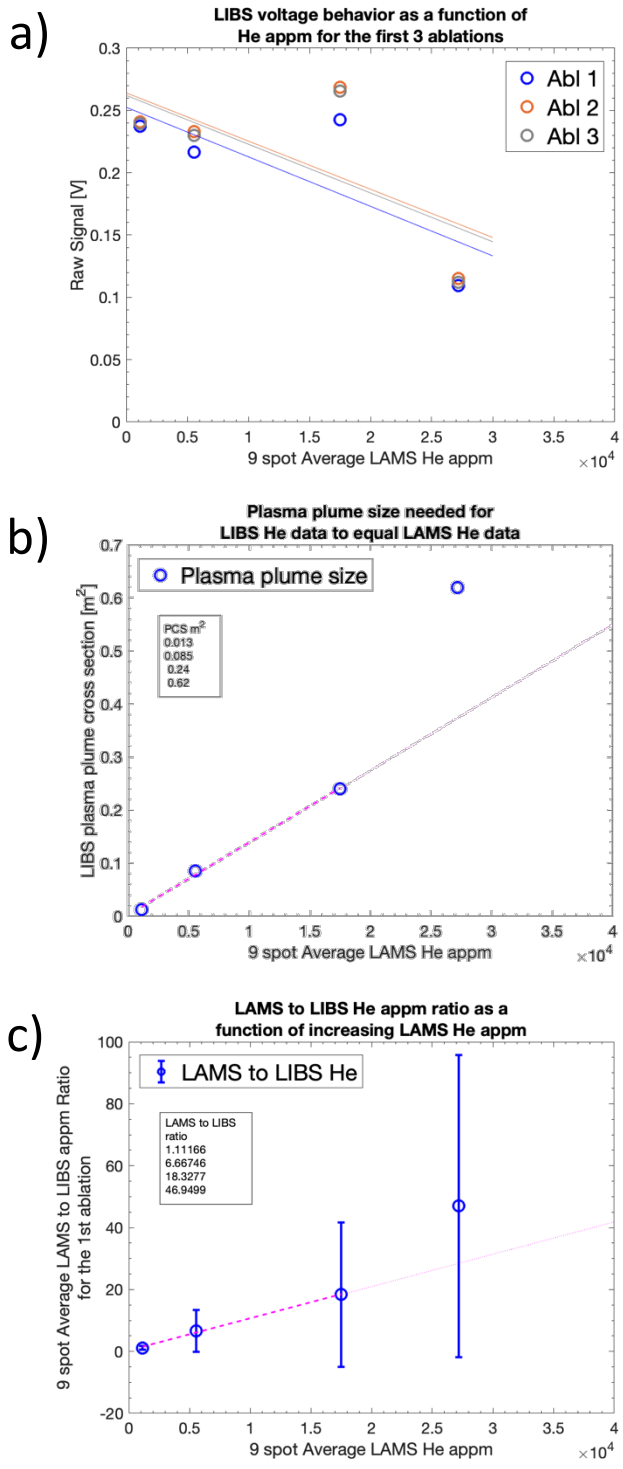

Figure 7.5 LIBS plasma plume analysis as a function of He content for the three WEST samples and a reference W sample.

plasma plume studies as in terms of different gasses, gas content, and plasma evolution.

Finally, plot c) shows the LAMS to LIBS ratio as a function of LAMS measured He content. In this analysis no parameters were changed. The plasma plume size was left the same at 0.013 m^2 for all analysis.

The raw signals were then analyzed as described in Chapter 4, in which the LAMS and LIBS values were calculated using their raw signal. Similarly, the magenta line is a best fit line to illustrate the linear trend. The reference sample, R3, and R2 all follow the expected linear relationship. R1 deviates from this relationship which means there is higher level of disagreement between LIBS and LAMS for this sample. This deviation could be the result of the present oxygen. Thus, further analysis of sample oxidation and its effect on plasma plume formation is necessary to be able to convert the LIBS system from qualitative to quantitative.

A comparison between the UTK and WEST plasma plume analysis is shown in Figure 7.6. UTK samples were exposed in a controlled and monitored lab environment limiting the number of unknown factors. Therefore, the plasma plume evolution is equally impacted for all UTK samples. This observation can be made in the left plot of Figure 7.6 were the plasma plume size as a function of LAMS He content follows a linear relationship for all UTK samples. For the WEST samples only two of them, in combination with a reference sample, follow the linear relationship. These two samples are R3 and R2 which received the lowest and intermediate He flux. The deviation from the linear relationship seen in sample R1 could be due to the oxide layer found on the surface.

The largest UTK LAMS He content (5E5 appm) is an order of magnitude larger than the largest He content for WEST (2.7E4 appm). This required a 7 m^2 size plasma plume in the LIBS analysis to equate to the LAMS measured amount of He for this UTK plasma exposed sample, whereas the WEST exposed sample required a 0.62 m^2 size plasma plume. The difference between plasma plume sizes is also an order of

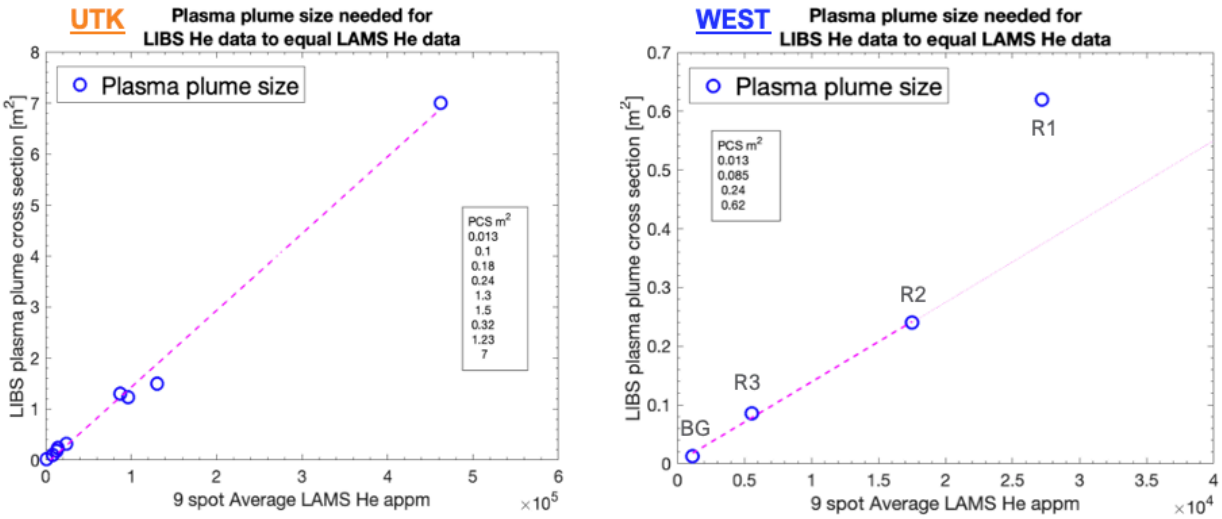

Figure 7.6 Comparison of LIBS plasma plume volume evolution for UTK He plasma source exposures and WEST He exposures.

magnitude with UTK being larger. This means that that the plasma plume evolution is consistent between both exposure experiments when pertaining to He in W only, or at least primarily. However, when incorporating a third element, like oxygen, the plasma plume evolution linear relationship no longer holds. This comparison further justifies the need for understanding the plasma plume evolution as a function of different elements.

7.6 WEST C4 Campaign LAMS Summary

LIBS and LAMS analysis were performed on the samples in combination with a reference sample. LAMS measurements revealed near surface He concentration profiles with significant drop off in He content at the second and third ablation. LAMS results also provided evidence of different He content as was expected due to different exposure fluxes for every sample. The sample that received the largest flux contained the largest He, the lowest flux sample contained the lowest amount of Helium, and the intermediate flux sample contained intermediate levels of He as measured by LAMS. LAMS output correlate well with He content expected based on the flux at each location.

LIBS summary measurements provided qualitative analysis of O content in the near surface vs bulk. The first ablation (surface) showed a larger O 777.4 nm signal than deeper (bulk) signals. O signal in the bulk is consistent with the presence of oxygen in form of $W0_3$. LIBS measurements also provided insight on the plasma plume evolution for WEST exposed samples. Additionally, comparisons of plasma plume evolutions between tokamak exposures vs controlled lab exposures were possible. Plasma plume sizes required as a function of LAMS measured He content were consistent between UTK and WEST exposures.

Chapter 8 DIIID

8.1 Experiment Details

This chapter describes the characterization of tungsten samples, which were loaded with helium at the PISCES-A linear plasma device, and subsequently exposed in the DiMES probe of the DIII-D tokamak at General Atomics. The purpose of this experiment, coordinated by Greg Sinclair of General Atomics, was to investigate the effect of sub-surface helium bubbles on the recycling and retention of deuterium during exposure to both L-mode and ELMy H-mode plasma conditions on DIII-D. A total of eight samples with varying exposure conditions, in addition to a reference sample, were evaluated.

Edge-localized-modes (ELMs) are a phenomenon present during H-mode operation in tokamaks [70]. As gradients in the transport barrier grows, once they exceed the MHD stability limit the ELM instability bursts resulting in transport of energetic particles along open field lines and onto material surfaces. As a result, high heat flux is deposited onto material surfaces, the divertor, and the main chamber. Therefore, it is imperative to study and understand ELM effects on He and D retention in W since it will impact many component inside the tokamak. This project explores the effects of ELMs on He and D through H-mode plasma exposures in DIII-D.

8.1.1 PISCES and DIII-D Exposures

Exposure details are shown in Table 8-1 and Table 8-2. PISCES-A exposures consisted of 70 eV He ions with a flux of $10^{21} – 10^{22}$ m^{-2} s^{-1} and a total fluence of 10^{25} m^{-2}. Average electron temperature and density were 4 -7 eV and $10^{17} – 10^{18}$ m^{-3}, respectively. Two samples were exposed at room temperature, three at 600 K, and

Table 8-1 PISCES-A (He) and DIII-D (D) exposure conditions, as reproduced from Ref. [8]

Parameter	PISCES-A	DIII-D (L-mode)	DIII-D (H-mode)*
Species	He	D	D
Impact energy (eV)	70	175	150
Flux ($m^2 s^{-1}$)	10^{21}-10^{22}	7.5×10^{21}	4.5×10^{21}
Fluence (m^{-2})	10^{25}	1.9×10^{23}	1.6×10^{23}
Surface temperature (K)	600, 800	< 400 K	< 550 K
T_e (eV)	4-7	35	30
n_e (m^{-3})	10^{17}-10^{18}	3.5×10^{19}	2.0×10^{19}

Table 8-2 Sample specific exposure conditions and their identification labels, as reproduced from Ref. [2]

Old Sample ID	New Sample ID	PISCES			DIII-D	
		He ion energy (eV)	Sample temperature (K)	He+ fluence (m^-2)	D+ fluence (m^-2)	L-mode or H-mode
W-pristine	W-pristine	N/A	N/A	N/A	N/A	N/A
W-2 He only	W-He600	60	600	1.2E+25	N/A	N/A
W-3 He only	W-He800	60	800	1.0E+25	N/A	N/A
W-1	W-DH	N/A	N/A	N/A	1.61E+23	H-mode
W-2	W-DL	N/A	N/A	N/A	1.88E+23	L-mode
W-He-1	W-He600-DH	60	600	1.2E+25	1.61E+23	H-mode
W-He-2	W-He800-DH	60	800	1.0E+25	1.61E+23	H-mode
W-He-3	W-He600-DL	60	600	1.2E+25	1.88E+23	L-mode
W-He-4	W-He800-DL	60	800	1.0E+25	1.88E+23	L-mode

the remaining three at 800 K, for a total of eight exposed samples. Notably, these conditions are very similar in temperature to those studied previously in this dissertation, although the helium flux and fluence are different. For UTK exposures He flux was 1.3E17 m^{-2} s^{-1} and surface temperature 900K vs He flux of 1E21 m^{-2} s^{-1} and 800K surface temperature for PISCES exposures.

Following initial He plasma exposure at PISCES/A, the samples were loaded into the DiMES probe within DIII-D for D exposures. In L-mode the D ion energy was 175 eV, flux 7.5E21 m^2 s^{-1}, fluence 1.9E23 m^{-2}, exposure temperature less than 400 K, electron temperature 35 eV, and electron density 3.5E19 m^{-3}. During H-mode all parameters decrease slightly compared to L-mode. Impact energy was 150 eV, flux 4.5E21 m^2 s^{-1}, fluence 1.6E23 m^{-2}, exposure temperature less than 550 K, electron temperature 30 eV, and electron density 2.0E19 m^{-3}. The discrepancy between Table 8-1 and Table 8-2 regarding the ion energy, 70 vs 60 eV, can be ignored given the close proximity of both values and neither being above the sputtering threshold. Through these He, D exposures of W we can study deuterium recycling and retention in helium-implanted W.

8.2 ERDA Results

ERDA analysis of the nine samples was performed by William Wampler from Sandia National Laboratory [5]. Figure 8.2 shows a table with He content as measured from the ERDA results alongside sample exposure conditions. Concentration profiles are shown on the right for samples W-2 (W-DL) and W-He-4 (W-He800-DL). This is to demonstrate that for both samples, exposed under different conditions, the concentration profile is similar with most of the He content located in the first 15 – 20 nm. This is consistent with LAMS produced concentration profiles, which will be described in the next section.

Although sample W-2 was not pre-loaded with He in PISCES, ERDA measured He concentrations for W-2 that are similar to that of PISCES He exposed W samples.

Sample	PISCES			DIII-D		He content (ERDA)
	He ion energy (eV)	Sample temperature (K)	He+ fluence (m^-2)	D+ fluence (m^-2)	L-mode or H-mode	(atoms cm^-2)
W-pristine	N/A	N/A	N/A	N/A	N/A	0
W-2 He only	60	600	1.2E+25	N/A	N/A	3E+15
W-3 He only	60	800	1.0E+25	N/A	N/A	3.97E+15
W-1	N/A	N/A	N/A	1.61E+23	H-mode	3.04E+15
W-2	N/A	N/A	N/A	1.88E+23	L-mode	2E+15
W-He-1	60	600	1.2E+25	1.61E+23	H-mode	3.75E+15
W-He-2	60	800	1.0E+25	1.61E+23	H-mode	2.53E+15
W-He-3	60	600	1.2E+25	1.88E+23	L-mode	2.9E+15
W-He-4	60	800	1.0E+25	1.88E+23	L-mode	3.55E+15

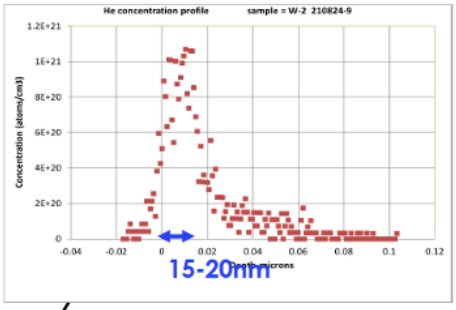

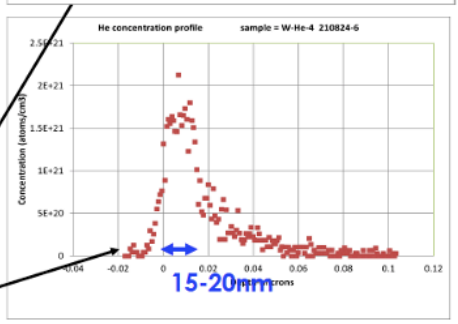

Figure 8.2 ERDA results of PISCES-DIII-D W sample exposures alongside He concentration profiles demonstrating the location of implanted He layer, as reproduced from Ref. [5]

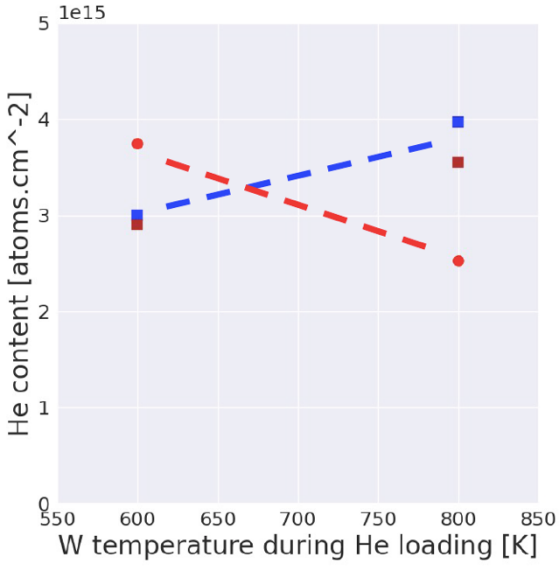

Figure 8.1 He content in W samples as a function of W temperature for PISCES, DIII-D H mode and L mode, as reproduced from Ref. [5]

For example, ERDA measured He content in W-1, which was not He pre-loaded, of 3.04E15 atoms cm^{-2}. This He content is larger than the measured He content of 2.53E15 atoms cm^{-2} in W-He-2 which was He exposed in PISCES at 800 K to a fluence of 1E25 m^{-2}. The presence of He in samples not exposed in PISCES could be due to the long He glow discharge between each plasma shot in DIII-D. It is estimated that the glow discharge He exposes the W samples at low temperatures and a large fluence [5].

Additional analysis of ERDA results is shown in Figure 8.1. He content for samples only exposed in PISCES, no D plasma, and samples exposed in DIII-D under L-mode are shown by the blue dashed line and by the two dark red squares alongside the blue dashed line, respectively. Both relationships show He content increases with W temperature during He loading. The dashed red line with circle endpoints shows the He content during He loading for samples exposed to D plasma in DIII-D H-mode. In this case the He content decreases with W temperature during He loading when exposed H-mode D plasma in DIII-D. This inverse relationship could be due to thermal release of He during plasma exposure.

8.3 PISCES DIII-D LAMS He and H Results

LAMS analysis were performed on all nine samples to produce He and D content concentration profiles. Figure 8.3, Figure 8.4, and Figure 8.5 show He, and D LAMS results for all nine samples. Plots in Figure 8.3 pertain to He exposures performed at 800 K. Plots in Figure 8.4 are results of samples He exposed at 600 K, plots in Figure 8.5 are results for room temperature or non PISCES exposures. For all figures the top row shows He content in appm and the bottom row shows D content in appm. The first column of plots shows PISCES He exposures at their respective temperatures. The second column (middle) displays results for DIII-D exposures in H-mode, and the third column for L-mode. All figure are organized as described except for the first

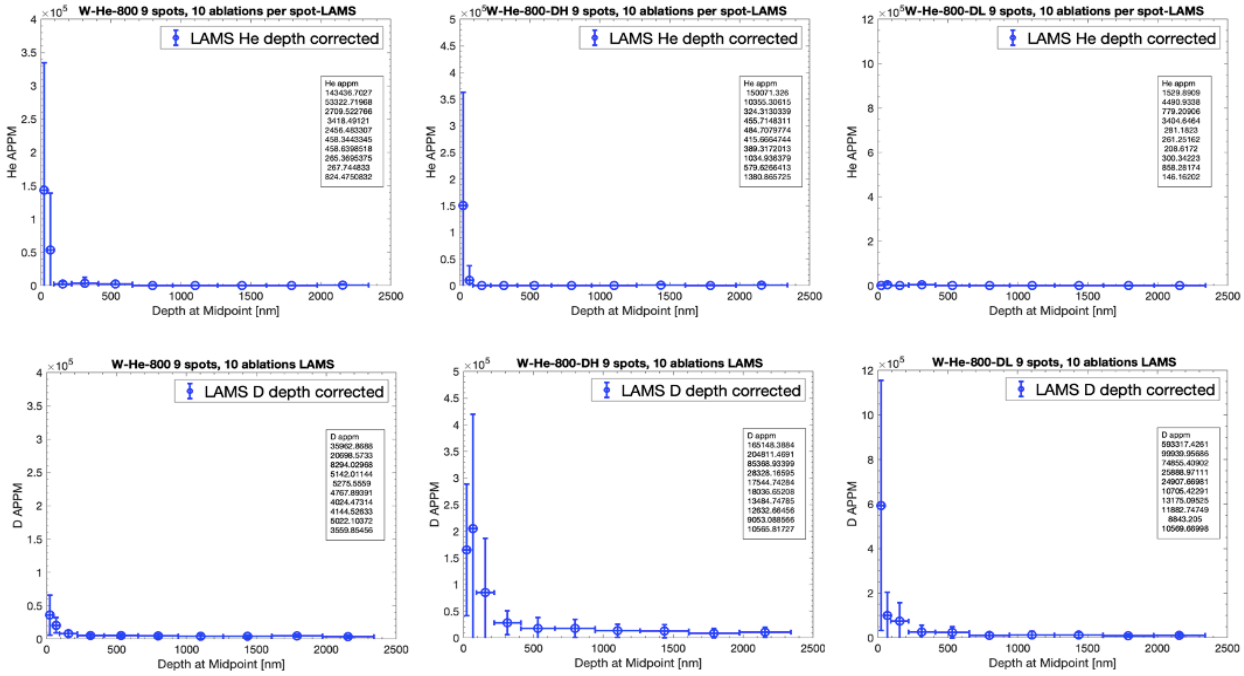

Figure 8.3 LAMS results for PISCES samples exposed at 800 K.

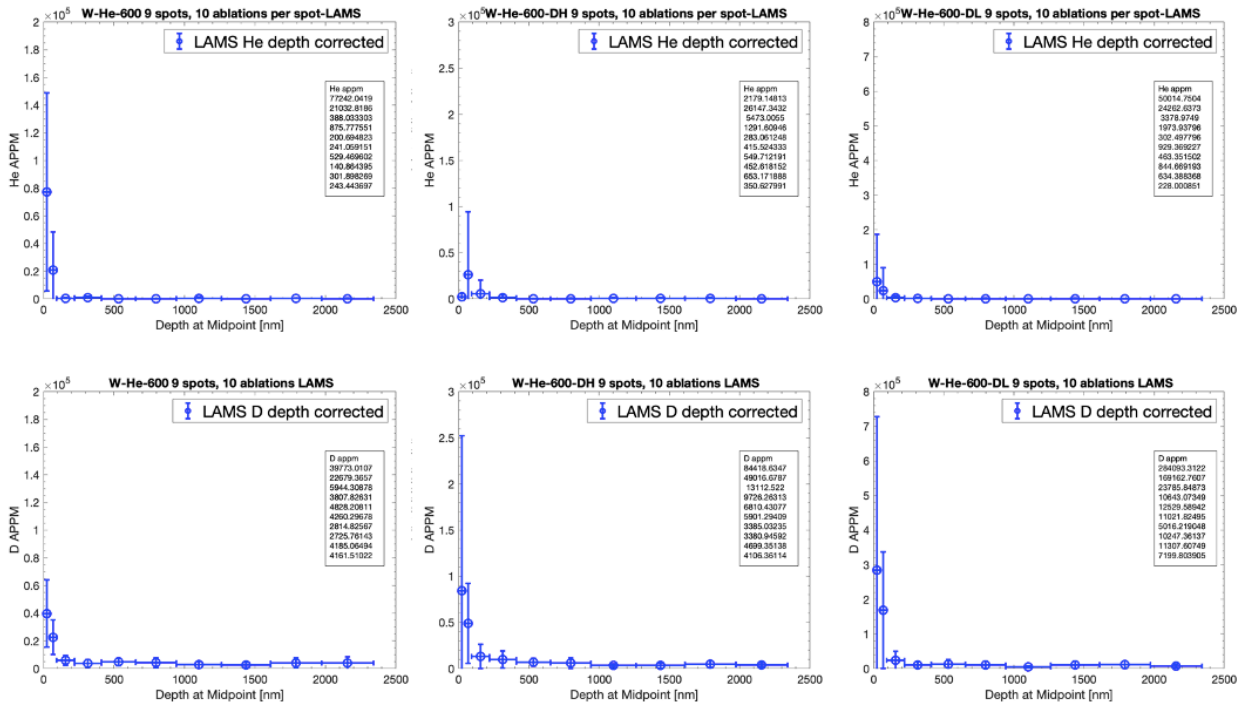

Figure 8.4 LAMS results for PISCES examples exposed at 600 K.

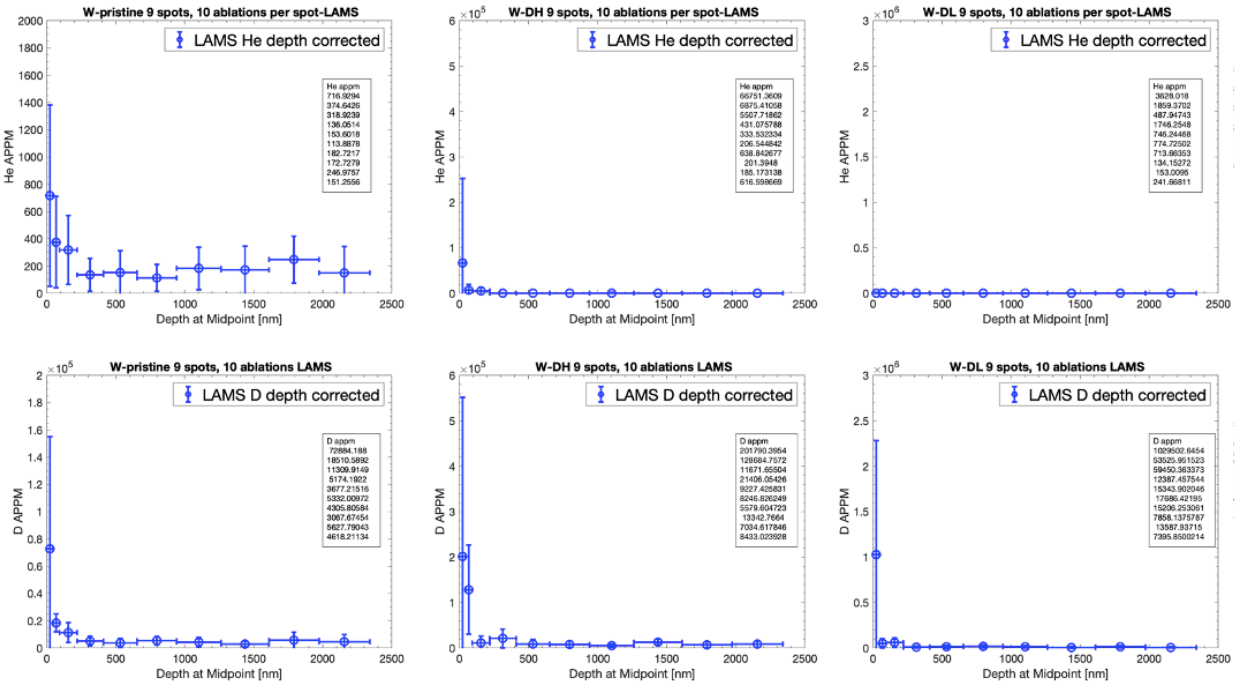

Figure 8.5 LAMS results for the reference sample and samples not exposed in PISCES, only DIII-D.

column in Figure 8.5 where this is not a PISCES He only exposed sample but rather the reference W sample.

Similar to ERDA, LAMS produced a very near surface He and D concentration profile with the concentration peak located within the first 50 nm for all samples. Due to LAMS resolution limitations, it is unable to render a 15 – 20 nm peak location however, detection of the peaks in the first ablation (50 nm) agrees with ERDA resolved peak location. The top middle plot in Figure 8.5 and the top middle plot in Figure 8.3 shows LAMS He content results for samples W-1(W-DH) and W-He-2(W-He800-DH), respectively. W-1(W-DH) is the sample discussed in Section 8.2 where He was present in quantities larger than W-He-2(W-He800-DH) even though it had not been He preloaded. LAMS measured significant He quantities of 6.6E4 He appm (for the non He loaded sample) just like ERDA however, it was not in larger quantities than sample W-He-2(W-He800-DH) where LAMS measured a He content of 15E4 He appm. LAMS measured He content in W-1(W-DH) is consistent with the He present in DIII-D due to the glow discharge. This is in agreement with ERDA measurements of He in W-1(W-DH).

However, measurement of lower He quantities in the non-preloaded sample compared to the He exposed sample is reasonable given that He plasma exposure in a linear plasma device is expected to lead to larger He content than an intermittent, non-direct, glow discharge. However, it is hard to make either argument given the He fluence during the glow discharge is unknown. More studies have to be made to identify the ERDA and LAMS differences in measured He content.

8.3.1 PISCES DIII-D LAMS H Results

Deuterium LAMS measurements were simultaneously performed with the experiments pertaining to the previously discussed He Results. Using filterscope tube 2, in combination with a D 656.3 nm filter, D quantities were measured. The results are shown in the second row of Figure 8.3, Figure 8.4, and Figure 8.5. For example,

for the 800 K exposures in Figure 8.3 the He only exposure (bottom left plot) shows D quantities of 3E4 appm while the H-mode exposure (middle plot) shows 1.6E5 appm and the L-mode (right plot) shows 5.8E5 appm.

For the top row of the same Figure 8.3, integrating He content over the first two ablations returns He quantities of 2E5 appm for He only (left), 1.6E5 for H-mode (middle), and 6E3 for L-mode (right). For the He only exposure, the He content is the highest of the three 800 K exposed samples at 1.4E5 appm. For the H-mode exposure the He content is lower at 1.5E5 appm and and even lower for L-mode at 1.5E3 appm. There seems to be an inverse relationship between the He and D near surface content. As He content decreases near the surface, D content increases as evident by the He and D plots for sample W-He-800-DL in Figure 8.3. Here, D is seen in the largest quantity relative to the other two mentioned samples in Figure 8.3 while He is seen in the lowest quantities relatively to the other samples. Similarly, the opposite is true, for sample W-He-800, He content is the largest of the three while the D content is the lower of the three.

The same relationships are evident in Figure 8.4 and Figure 8.5 where He content is higher, D content is lower, and vice versa. Samples with intermediate values of He, relative to the other exposures, have intermediate values of D. This relationship is evidence of H-He synergies.

8.4 Comparison of ERDA and LAMS He Results

Table 8-4 draws a clearer comparison between ERDA and LAMS He measurements in atoms · cm^{-2} units for ERDA and in both atoms · cm^{-2} and appm for LAMS. Appm units are included for LAMS since they are the traditional units used during discussion of LAMS results in previous sections. However, for direct comparison against ERDA, LAMS appm values were changed to atoms · cm^{-2}. The conversion was done by multiplying the first ablation appm values (for every sample) by 6E22 (the W atomic density in cm^{-3}) and diving by 1E6 (1 million due to the million

Table 8-4 ERDA measured He content in atoms cm^{-2} units compared against first ablation LAMS He content measurements in atoms cm^{-2} and appm.

New Sample ID	ERDA [atoms cm^{-2}]	LAMS [atoms cm^{-2}]	LAMS [appm]
W-pristine	0	9.45E+13	716
W-He600	3E15	1.02E+16	77,242
W-He800	3.97E15	1.89E+16	143,436
W-DH	3.04E15	8.81E+15	66,751
W-DL	2E15	4.82E+14	3,648
W-He600-DH	3.75E15	2.88E+14	2,179
W-He800-DH	2.53E15	1.98E+16	150,071
W-He600-DL	2.9E15	6.60E+15	50,014
W-He800-DL	3.55E15	2.02E+14	1,529

unit in appm) the resultant value was then multiplied by the depth of the first LAMS ablation induced crater. From the volume analysis described in Chapter 4.5 we can determine the first ablation crater depth to be 2.20E-6 cm, equal to 22 nm. ERDA only characterized the first 100 nm with the location of the peak found in the first 15-20nm as is shown in Figure 8.2 and discussed in Ref. [5]. Therefore, only the first ablation in LAMS is considered in this table in comparison with the ERDA peak results. Comparison of LAMS measurements (in atoms · $cm^{-2)}$ against ERDA measurements shows that there is close agreement between the two techniques. The level of agreement varies between samples but the measured He content is in close proximity for both techniques with ERDA consistently measuring values of approximately 2E15 atoms · cm^{-2} and LAMS ranging from 9E13 to 1.9E16 atoms · cm^{-2}. A He content of 716 appm for the pristine (reference) sample is considered background levels, this background signal has not been subtracted from the LAMS results for the rest of the samples.

Background He measurements depend on the sample processing and composition. For samples used in my UTK and WEST exposures, a background He content of ~1,200 appm was measured. Those samples were mirror polished and of similar composition. PISCES - DIII-D DiMES samples are processed differently and not mirror polished. These conditions result in a background He measurement of 716 appm. Given LAMS analysis has only been performed on one reference sample of these conditions, there are insufficient measurements of reference samples to determine a repeatable background signal. Further background measurements have to be performed for reference samples manufactured in the same manner in order to accurately subtract a He background measurement from all other exposed samples processed in the same manner.

Degree of agreement between ERDA and LAMS is shown in Figure 8.6. LAMS is plotted in the y-axis against ERDA (in the x-axis). The orange dotted line serves to guide the eye to what would be a perfect one to one relationship. As evident from the

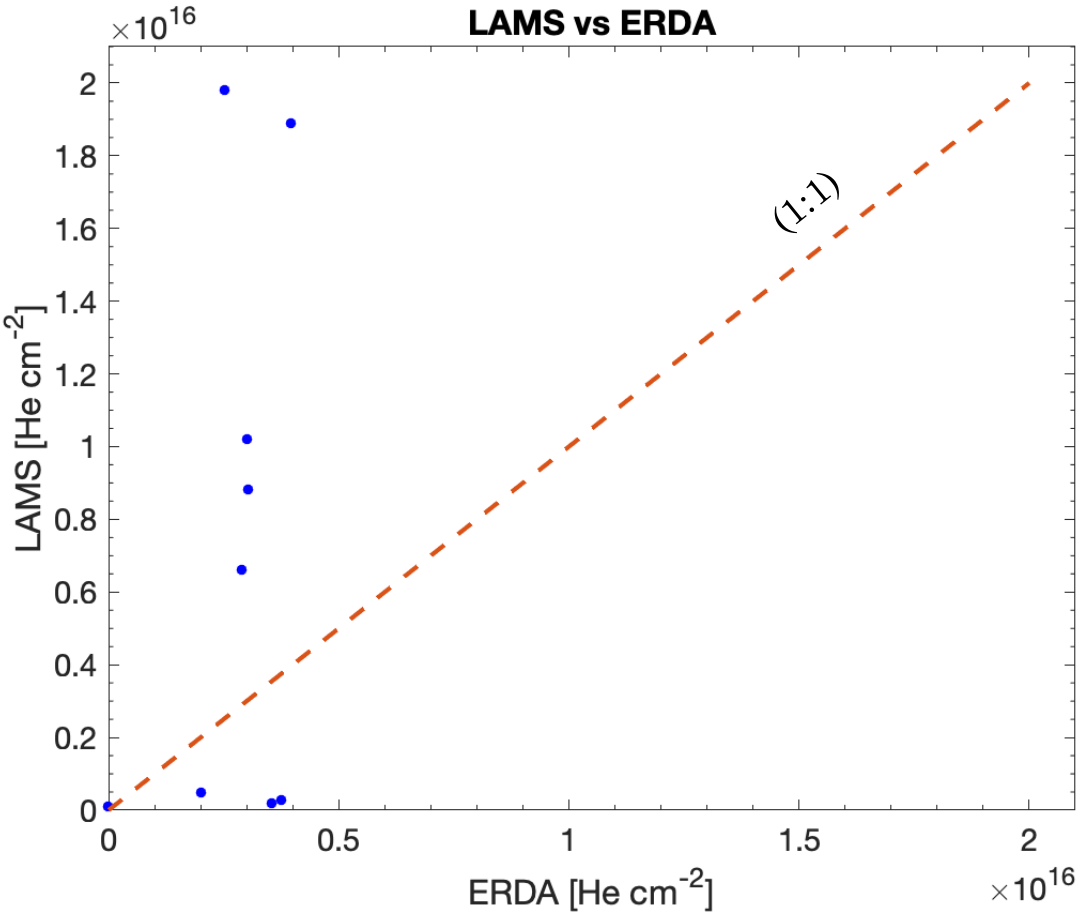

Figure 8.6 LAMS vs ERDA measurements showing degree of agreement. Dotted line is representative of a perfect one to one relationship.

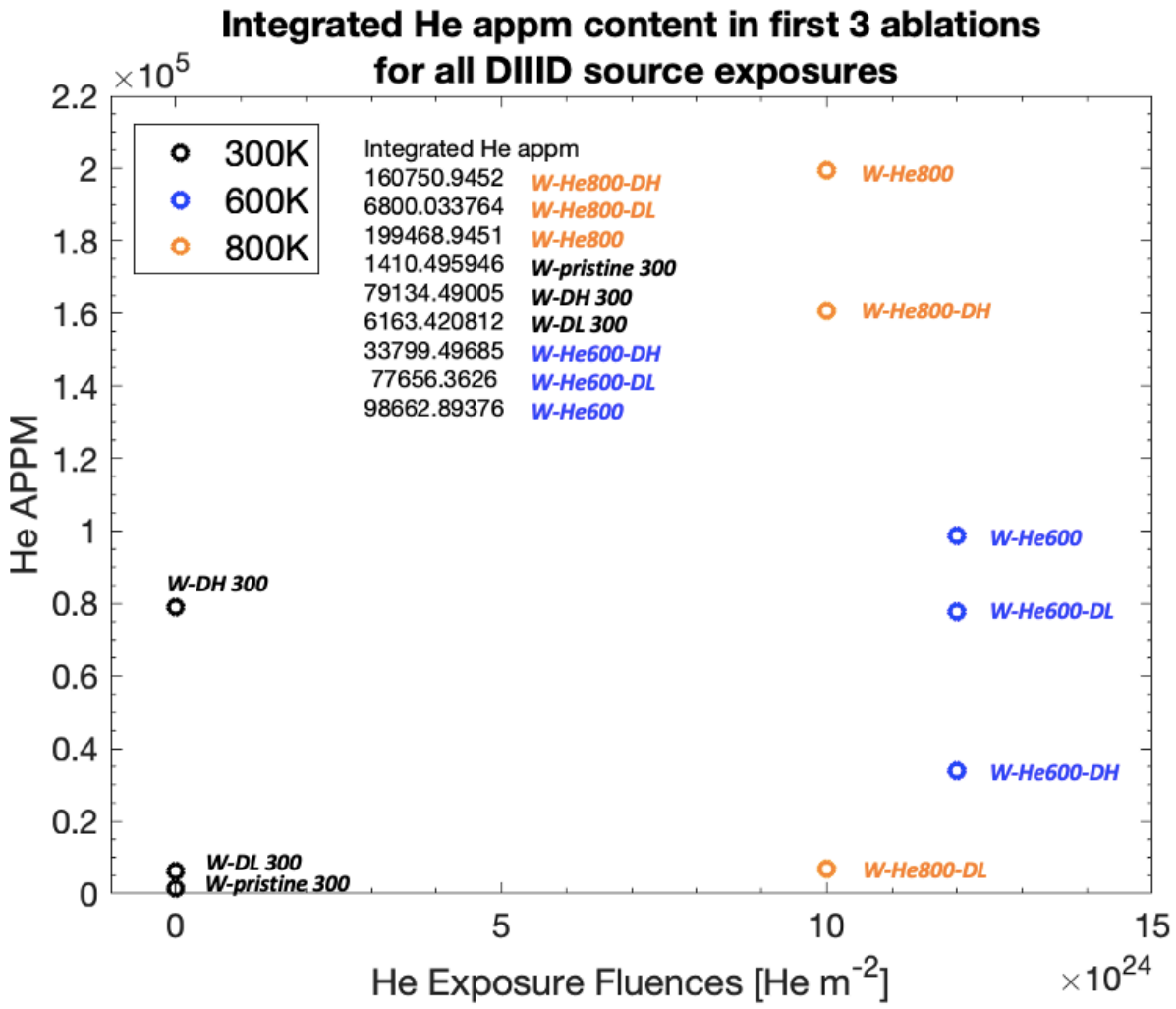

Figure 8.7 PISCES-DIII-D LAMS measured He content integrated over the first three ablations.

data points, there is significant deviation in LAMS vs ERDA results; shown by the scatter of LAMS results above and below the one-to-one relationship. This means that LAMS tends to predict larger He content when compared to ERDA.
Figure 8.7 shows LAMS results integrated over the first three ablations to encompass the entire region where He is present. The relative spread of the data remains the same between the first ablation and integration over the first three ablations except for W-He800 and W-He800-DH where W-He800 is lower in the first data points, there is significant deviation in LAMS vs ERDA results; shown by the scatter of LAMS results above and below the one-to-one relationship. This means that LAMS tends to predict larger He content when compared to ERDA.

Figure 8.7 shows LAMS results integrated over the first three ablations to encompass the entire region where He is present. The relative spread of the data remains the same between the first ablation and integration over the first three ablations except for W-He800 and W-He800-DH where W-He800 is lower in the first ablation but larger when integrated over the first three ablations. For both room temperature and 800 K exposures, H-mode (DH) exposures showed larger quantities of He than DL. This is opposite to 600 K exposures where the L-mode (DL) exposure shows larger He quantities. As mentioned in Section 8.2, He content is expected to be lower following H-mode exposures due to the thermal release that takes place during ELMs. The 600 K exposures are consistent with this trend, not the room temperature nor the 800 K exposures.

8.5 PISCES-DIIID Exposures Summary

W samples were exposed to a combination of He only, D only, and He followed by D plasmas. Exposures for He and D were performed in PISCES and DIII-D, respectively. ERDA and LAMS analysis were performed on all nine samples. There is agreement between both characterization techniques as to the location of the He peak content within the first 20 nm. There is general agreement on the magnitude of

He content however, there is significant scatter in this data and a direct one to one relationship is not observable. LAMS tends to predict larger He contents than ERDA in similar samples by one to two orders of magnitude. More analysis and experiment are required to address the quantitative agreement.

Chapter 9
Summary and Future Work

9.1 Summary

During this dissertation, LAMS depth profiling of He content in W has been demonstrated. He content in W under different exposure conditions as well as He-D synergies in W have been studied. Figure 9.1 shows a comparison of all of the LAMS experimental measurements performed in this dissertation.

LAMS measurement results for UTK plasma exposures, WEST tokamak C4 campaign, PISCES DIII-D, and 10 keV He exposures have been plotted on Figure 9.1 for easier analysis. The LAMS measured He content is plotted in the y-axis, in units of appm, as a function of He exposure fluence [He m^{-2}]. Exposures range from 5E19 He m^{-2} to 5E25 He m^{-2} while He content ranges from 1E3 to 5E6 appm. A general trend is observed where He content increases with larger fluences however, not linearly. For example, the 5E21 He m^{-2} 900 K UTK exposure shows larger He quantities (5E5 appm) than WEST and DIII-D exposures. This could be due to the higher temperature during the UTK exposure. Additionally, exposures in a controlled lab setting where plasma current is monitored, and plasma fluctuation and contamination is limited, can lead to more accurate estimate of total He fluence. There are some uncertainties in the PISCES DIII-D exposures in terms of the temperature they are being implanted at due to heat up during exposure and samples not holding constant temperature. Due to variation in exposure conditions, it is difficult to make direct comparisons. WEST results are at intermediate fluence, they do not appear to be on the same trend curve as the UTK plasma source and PISCES data, this is likely due to the thick oxide layers found in the WEST samples.

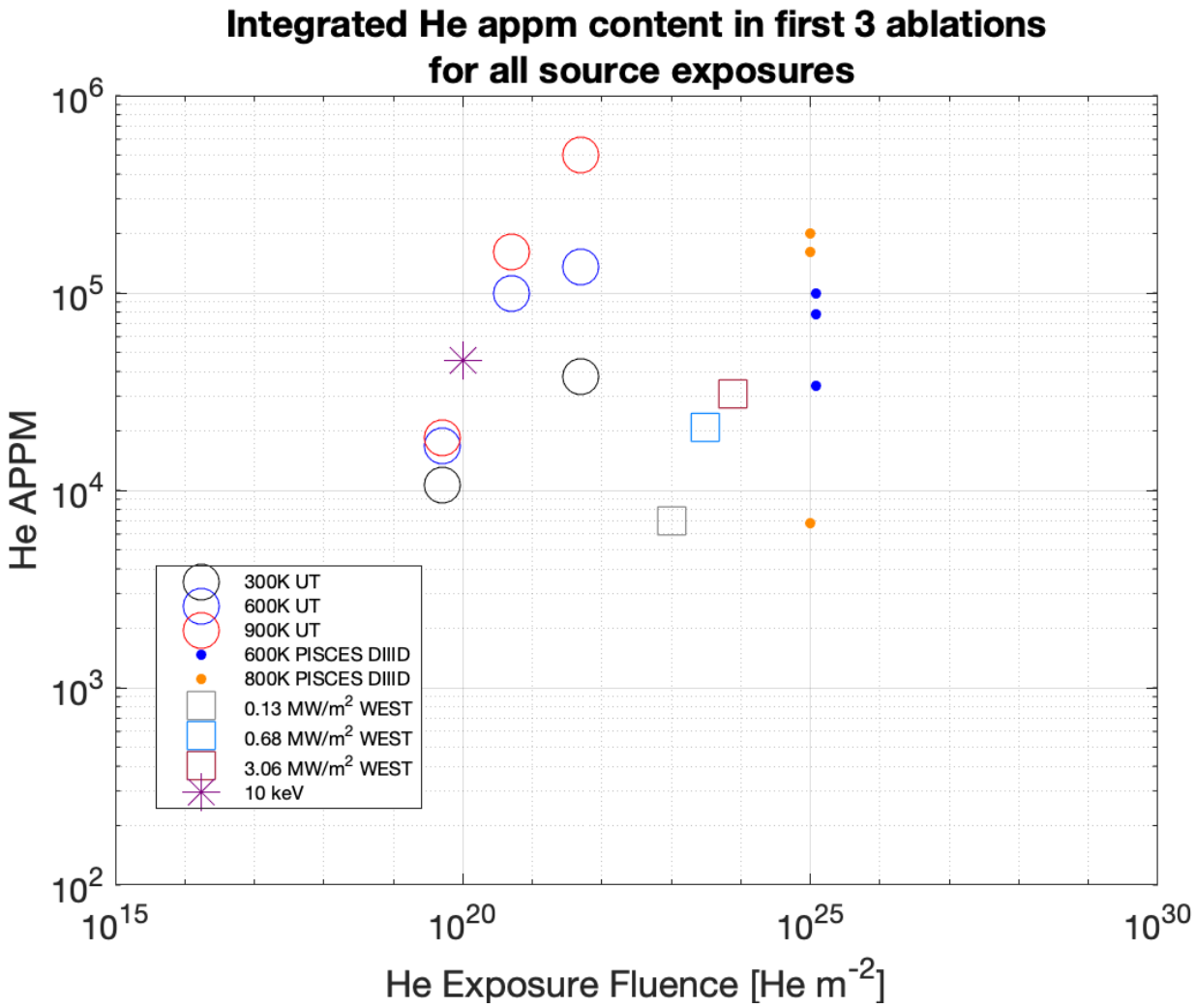

Figure 9.1 All the LAMS analysis results in this dissertation work plotted as a function of He fluence during exposures. Specific data sources include UTK exposures, PISCES - DIII-D, WEST C4 campaign, and 10 keV He exposures.

Lower He content in WEST could be due to oxygen in the scrape off layer. Even though a total He fluence was estimated, based on He flux and exposure time, the resulting He content could have been reduced through sputtering of the near surface region by the present oxygen. Similarly, PISCES DIII-D exposure fluences were not directly monitored but rather estimated based on He flux and exposure time and therefore exposure conditions could differ from estimated conditions. Additionally, PISCES measurements could be lower due to not being isothermal during exposures. It is difficult to assess the temperature in PISCES measurements but if we assume near He saturation dependent upon temperature, PISCES results are in range of what we expect given they held a nominal 800 K temperature. LAMS measured He content for the 10 keV He3 He4 study is also comparable to UTK, WEST, and PISCES DIII-D results. The He content value is found in the lower range of the data scatter where He values for UTK room temperature exposure are located. This is consistent given the 10 keV exposures were performed at room temperature.

Overall, a positive He content to exposure fluence trend is observed for all data shown in Figure 9.1. Higher He content is expected as a function of increasing temperature and fluence; experimentally we are seeing higher retention at higher temperatures, except for 1 of the DIII-D samples. While there is some disagreement, in general the trend between He content and exposure fluence is good for all data. It largely follows the trend of increasing He content with increasing temperature and exposure fluence. There is reasonably good agreement amongst all the samples of the total accumulated He

9.2 Future work

9.2.1 Continued work on He-D synergies

The impact of an oxide layer on D permeability in W will be studied. This will be attained by performing permeability experiments on reference W samples in the

presence, and in the absence of argon. Argon reduced oxidation significantly almost to a null point. It is possible that permeability in the studied UTK exposed W samples (described in Section 6.4) was increased due to the absence of an oxide layer. If this is the case, argon could allow us to study permeability in W in the absence of oxidation. Permeation work will continue on the UTK exposed samples to complete the matrix of intended permeations. This will allow us to systematically study He-D synergies in W. Additionally, the role of oxide on the laser absorption characteristics and what that does to the laser ablation profiles will also be investigated.

9.2.2 Characterizing plasma plume evolution in future experiments

Evolution of the laser produced plasma plume will also be investigated. In this dissertation it was shown that laser produced plasma plume is not constant and evolves significantly. Furthermore, it changes as a function of the type and content of elements present. To demonstrate the extent of plasma evolution, results from Sankar et al are shown in Figure 9.2. They performed plasma plume evolution experiments to study the evolution of femtosecond (fs) and nanosecond (ns) laser produced plasmas[13]. Figure 9.2 shows aluminum plasmas produced using a 100fs ultrashort laser pulse (top) and a 7ns short pulse laser (bottom). Intermediate images were taken using an ICCD camera to image the plasma at different growth stages. The color map is indicative of changing density throughout the plasma. It is evident that the plasma plume changes significantly in a span of 5 microseconds for both the fs and ns laser produced plasma plumes. Although the discussed plasmas result from laser ablation of aluminum, this work exemplifies that it is not accurate to assume a static plasma plume. Additionally, it demonstrates the need for understanding plasma plume evolution, measurements of plasma plume size, and measurement of electron temperature and densities at different stages of evolution. Crater formation can be further improved through the implementation of a femtosecond laser. This would require separate plasma plume evolution analysis as their resultant plasmas

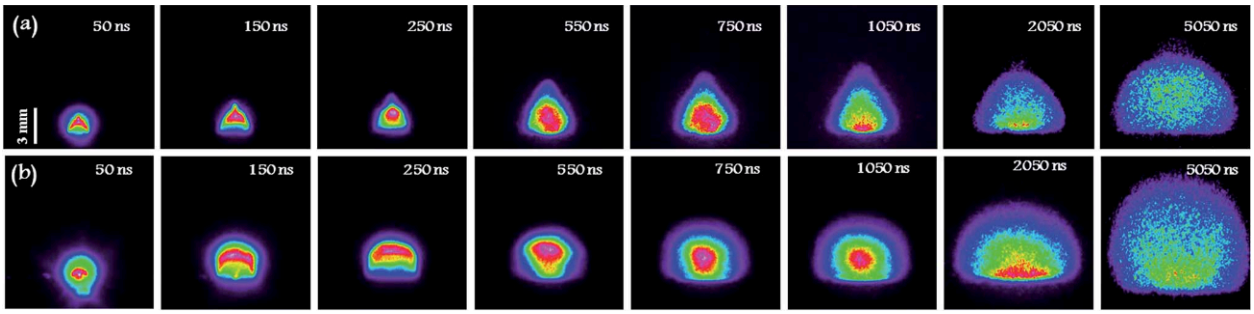

Figure 9.2 ICCD camera resolved images of plasma plume evolution. Top images a) evolution of fs laser ablation produced plasma plume. Bottom images b) evolution of ns laser ablation produced plasma plume. Figure reproduced from Ref. [13]

differ slightly. The extent of this difference is unknown and should be further investigated.

9.2.3 Nanosecond vs Femtosecond Laser Ablations

Work on the nanosecond vs femtosecond LIBS will also continue. Laser induced crater formation can be improved by using a Ti-Sapphire(800nm) femtosecond laser. A shorter, quicker laser pulse will mitigate the amount of splash back material due to the laser beam coming into contact with the W surface for only ~60 fs as opposed to 5ns. The shorter pulse limits the amount of time that the material is heated, providing just enough time for the material to evaporate and form the plasma plume but not enough to cause melting or splash back. A shorter laser-W surface contact time would also reduce the heat affected zone.

Figure 9.3 shows experiments performed by Dr. Balooch from Berkley where he ablated separate W surfaces using repeated pulses of either a ns laser or a fs laser. The images on the left shows the ns laser plasma plume (LPP) expanding symmetrically in every direction forming a more spherical plasma. AFM produced surface images and profiles directly to the right of the ns LPP show the surface roughness that results from the laser melting the material. Even at a depth of 800 nm following many hundreds of consecutive ablations have been performed, a surface roughness persists. It is very difficult to accurately represent this crater formation due to the extreme surface roughness left throughout the depth profile. The images on the right show the same information for a fs laser. Here the plasma plume forms in a more cylindrical direction normal to the material surface. Directly adjacent to the ICCD image are the corresponding AFM produced surface and profile images. It is clear that this crater formation is much cleaner and absent of the splash back rings thus making it an attractive upgrade to our existing system. Studies of both ion flux and kinetic energy show that ns laser plasma plumes provide narrower energy

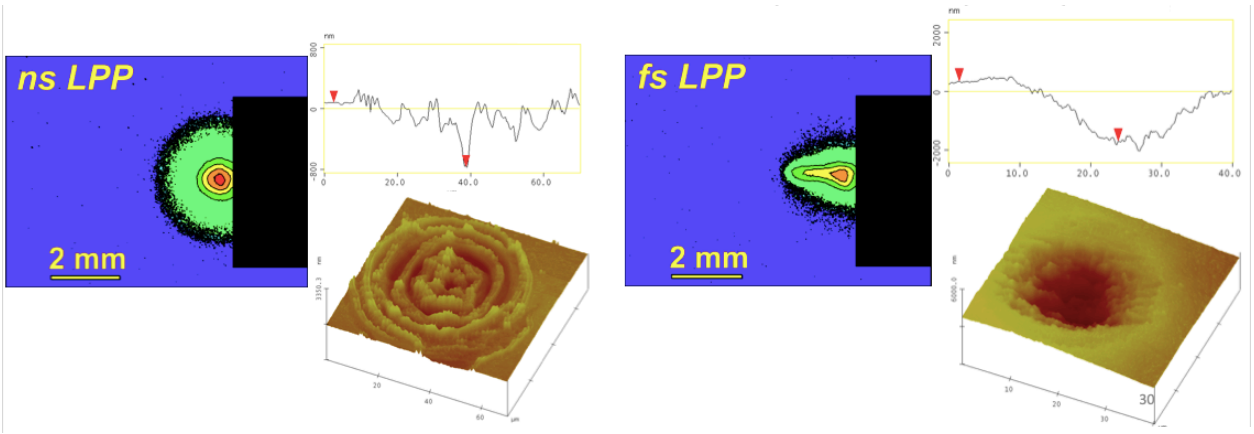

Figure 9.3 LPP images taken by an ICCD camera showing the difference in plasma formation for a ns vs a fs laser. Next to them are the corresponding AFM produced images of the surface morphology and topography. Ref [14], [20](Unpublished)

distribution while fs laser plasma plumes have narrower angular distribution. Therefore, more research has to be conducted to better understand the way in which a fs laser will impact our LPP, crater formation, depth profile, and data analysis.

Improvement on Laser plasma plume formation is expected with the fs laser system upgrade. LIBS qualitative measurements have been demonstrated. However, there is more work to be done to make it quantitative. The plasma plume size and evolution need to be well understood as well as the electron temperature and density. This is required to determine the correct S/XB coefficients for LIBS to become a quantitative system.

List of References

1. SPECS, *SPECS User Manual*, in *PCS-ECR Plasma Cracker Source*. February 13, 2013.
2. Sinclair, G., *LIBS/LAMS Analysis Proposal for DIII-D Experiment 2019-53-03*, W. Garcia, Editor. 2022.
3. Shaw, G., *Quantification of Hydrogen-Helium Retention in Tungsten Using Laser Induced Breakdown Spectroscopy Coupled with Laser Ablation Mass Spectrometry*. 2018.
4. DOE/EIA. *International Energy Outlook 2017*. Available from: https://www.eia.gov/todayinenergy/detail.php?id=32912.
5. Guterl, J. *Modeling of He and D reention in W samples exposed to DIIID plasma using Xolotl*. in *American Physical Society (APS)*. 2022. Virtual.
6. Nave, R. *Nuclear Fusion*. Nuclear; Available from: http://hyperphysics.phy-astr.gsu.edu/hbase/NucEne/fusion.html.
7. Chen, Z. *Hydrogen Isotope Behavior in RAFM Steels*. in *The Nineteenth International Conference on Fusion Reactor Materials*. 2019. San Diego, California, USA.
8. Sinclair, G. *Deuterium recycling and retention in helium-implanted tungsten exposed to ELMy H-mode plasmas in the DIII-D tokamak*. in *25th International Conference on Plasma Surface Interaction in Controlled Fusion Devices*. 2022. Virtual.
9. Shimada, M. and R. Pawelko, *Tritium permeability in polycrystalline tungsten*. Fusion Engineering and Design, 2019.
10. Christian. *Plotting nuclear fusion cross sections*. July 10 2018; Available from: https://scipython.com/blog/plotting-nuclear-fusion-cross-sections/.
11. DOE/EIA. *December 2019 Monthly Energy Review*. U.S. Energy Information Administration 2019; Available from: https://www.eia.gov/todayinenergy/detail.php?id=40013.
12. Bergstrom, Z.J., M.A. Cusentino, and B.D. Wirth, *A Molecular Dynamics Study of Subsurface Hydrogen-Helium Bubbles in Tungsten*. 2017. **71**(1).
13. Sankar, P., Nivas, J.J.J., Smijesh, N., Tiwari, G.K., Philip, R., *Optical emission and dynamics of aluminum plasmas produced by ultrashort and short laser pulses*. Journal of Analytical Atomic Spectrometry 2017. **32**: p. 1177–1185.
14. Harilal, S.S., et al. *Comparison of nanosecond and femtosecond LIBS*. OSA.
15. Wirth, B.D., et al., *Challenges and opportunities of modeling plasma–surface interactions in tungsten using high-performance computing*. Journal of Nuclear Materials, 2015. **463**: p. 30-38.
16. Brunner, D., et al., *Scanning retarding field analyzer for plasma profile measurements in the boundary of the Alcator C-Mod tokamak*. Review of Scientific Instruments, 2013. **84**(3): p. 033502.
17. Ogorodnikova, O.V., et al., *Deuterium retention in tungsten exposed to low-energy pure and helium-seeded deuterium plasmas*. Journal of Applied Physics, 2011. **109**(1): p. 013309.

18. Doerner, R.P., et al., *Retention in tungsten resulting from extremely high fluence plasma exposure.* Nuclear Materials and Energy, 2016. **9**: p. 89-92.
19. Uemura, Y., et al., *Effect of helium irradiation on deuterium permeation behavior in tungsten.* Journal of Nuclear Materials, 2017. **490**: p. 242-246.
20. Balooch, M.
21. Esen, Ö. and M. Bayrak, *Does more energy consumption support economic growth in net energy-importing countries?* Journal of Economics, Finance and Administrative Science, 2017. **22**(42): p. 75-98.
22. DOE/EIA. *International Energy Outlook 2019 with projections to 2050*. Office of Energy Analysis September 2019; Available from: https://www.eia.gov/todayinenergy/detail.php?id=12251.
23. Agency, E.U.S.E.P. *Sources of Greenhouse Gas Emissions*. July 27, 2021; Available from: https://www.epa.gov/ghgemissions/sources-greenhouse-gas-emissions.
24. Energy, O.o.N. *Advantages and Challenges of Nuclear Energy*. March 29, 2021; Available from: https://www.energy.gov/ne/articles/advantages-and-challenges-nuclear-energy.
25. Solutions, C.f.C.a.E. *Renewable Energy*. Energy November 10,2021; Available from: https://www.c2es.org/content/renewable-energy/#:~:text=Renewables%20made%20up%2019.8%20percent,come%20from%20wind%20and%20solar.
26. Tong, D., et al., *Geophysical constraints on the reliability of solar and wind power worldwide.* Nature Communications, 2021. **12**(1).
27. Desantis, D., et al., *Cost of long-distance energy transmission by different carriers.* iScience, 2021. **24**(12): p. 103495.
28. Analysis, U.S.E.I.A.-E.-I.S.a. *Wind Explained*. Wind energy and the environment December 17, 2021; Available from: https://www.eia.gov/energyexplained/wind/wind-energy-and-the-environment.php.
29. Analysis, U.S.E.I.A.-E.-I.S.a. *Hydropower explained*. Hydropower and the environment December 9,2021; Available from: https://www.eia.gov/energyexplained/hydropower/hydropower-and-the-environment.php.
30. Dhar, A., et al., *Geothermal energy resources: potential environmental impact and land reclamation.* Environmental Reviews, 2020. **28**: p. 415+.
31. Administration, U.S.E.I. *Biomass and the environment*. December 9, 2020; Available from: https://www.eia.gov/energyexplained/biomass/biomass-and-the-environment.php.
32. *Global electricity demand is growing faster than renewables, driving strong increase in generation from fossil fuels*, iea, Editor. July 15, 2021.

33. energy-CCFE, C.C.f.f. *Bringing the power source of the stars down to Earth could give us low-carbon electricity for millennia to come.* March 18,2019; Available from: https://ccfe.ukaea.uk/fusion-energy/fusion-in-brief/.
34. Wu, Y. and S. Şahin, *3.13 Fusion Energy Production*, in *Comprehensive Energy Systems*, I. Dincer, Editor. 2018, Elsevier: Oxford. p. 538-589.
35. Grisham, L.R., *Chapter 10 - Nuclear Fusion*, in *Future Energy (Second Edition)*, T.M. Letcher, Editor. 2014, Elsevier: Boston. p. 199-211.
36. Haider, Q., *Nuclear Fusion: Holy Grail of Energy* 2019.
37. Iter. *External Heating Systems*. Available from: https://www.iter.org/mach/Heating#:~:text=The%20temperatures%20inside%20the%20ITER,the%20fusion%20reaction%20to%20occur.
38. *Comprehensive measurement of pp-chain solar neutrinos.* Nature, 2018. **562**(7728): p. 505-510.
39. A. Hassanein, V.S., *Potential design problems for ITER fusion device.* Scientific Reports, 2021.
40. Gunn, J.P., et al., *Surface heat loads on the ITER divertor vertical targets.* Nuclear Fusion, 2017. **57**(4): p. 046025.
41. Hirai, T., et al., *Use of tungsten material for the ITER divertor.* Nuclear Materials and Energy, 2016. **9**: p. 616-622.
42. Loarer, T., et al., *Gas balance and fuel retention in fusion devices.* Nuclear Fusion, 2007. **47**(9): p. 1112-1120.
43. Rion A. Causey, R.A.K., Christopher W. San Marchi, *Titium Barriers and Tritium Diffusion in Fusion Reactors.* 2012: p. 511-546.
44. Hammond, K.D., F. Ferroni, and B.D. Wirth, *Simulation of Helium Behavior Near Subsurface Prismatic Dislocation Loops in Tungsten.* Fusion Science and Technology, 2017. **71**(1): p. 7-21.
45. Lässer, R., *Tritium and Helium-3 in Metals*, ed. SpringerLink. 1989: Berlin, Heidelberg : Springer Berlin Heidelberg.
46. Kirillov, I.R., et al., *Liquid lithium self-cooled breeding blanket design for ITER.* Fusion Engineering and Design, 1998. **39-40**: p. 669-674.
47. Ullmaier, H., *The influence of helium on the bulk properties of fusion reactor structural materials.* Nucl.Fusion, 1984. **24**(1039).
48. Marian, J., et al., *A review of helium–hydrogen synergistic effects in radiation damage observed in fusion energy steels and an interaction model to guide future understanding.* Journal of Nuclear Materials, 2015. **462**: p. 409-421.
49. Liu, P.P., et al., *Effect of helium and hydrogen synergy on vacancy migration energy in Fe-10Cr model alloy.* Journal of Alloys and Compounds, 2019. **788**: p. 446-452.
50. Huang, J., et al., *Helium-Hydrogen Synergistic Effects in Structural Materials Under Fusion Neutron Irradiation.* Frontiers in Materials, 2022. **9**.

51. Monterrosa, A.M., Z. Jiao, and G.S. Was, *The influence of helium on cavity evolution in ion-irradiated T91.* Journal of Nuclear Materials, 2018. **509**: p. 707-721.
52. Zakharov, A.P., Sharapov, V.M. & Evko, É.I., *Hydrogen permeability of polycrystalline and monocrystalline molybdenum and tungsten.* Mater Sci, 1975.
53. Shaw, G., et al., *Investigating helium–deuterium synergies in plasma-exposed tungsten using laser ablation techniques.* Physica Scripta, 2020. **T171**: p. 014029.
54. Dasgupta, D., et al., *On the origin of 'fuzz' formation in plasma-facing materials.* Nuclear Fusion, 2019. **59**(8): p. 086057.
55. Brown, K.L. and G.W. Tautfest, *Faraday-Cup Monitors for High-Energy Electron Beams.* Review of Scientific Instruments, 1956. **27**(9): p. 696-702.
56. Gerdin, G., W. Stygar, and F. Venneri, *Faraday cup analysis of ion beams produced by a dense plasma focus.* Journal of Applied Physics, 1981. **52**(5): p. 3269-3275.
57. Tanure, L., et al., *Effect of annealing on microstructure, texture and hardness of ITER-specification tungsten analyzed by EBSD, vickers micro-hardness and nano-indentation techniques.* Journal of Nuclear Materials, 2019. **524**: p. 191-199.
58. Unterberg, E.A., Garren, Edward W., Davda, Kirtan M., Neff, Anton L., Ray, Holly R., and Fehling, Dan T., *The Filterscope: A Technical Guide & User's Manual.* 2019.
59. Li, C., et al., *Review of LIBS application in nuclear fusion technology.* Frontiers of Physics, 2016. **11**(6).
60. Singh, J.P. and S.N. Thakur, *Laser-induced breakdown spectroscopy*. 1st ed. 2007, Amsterdam ;: Elsevier.
61. Farid, N., et al., *Laser-induced breakdown spectroscopic characterization of tungsten plasma using the first, second, and third harmonics of an Nd:YAG laser.* Journal of Nuclear Materials, 2013. **433**: p. 80–85.
62. Farid, N., et al., *Emission features and expansion dynamics of nanosecond laser ablation plumes at different ambient pressures.* Journal of Applied Physics, 2014. **115**(3): p. 033107.
63. Chung, H.-K., Chen, M.H., Morgan, W.L., Ralchenko, Y., Lee, R.W., *FLYCHK: Generalized population kinetics and spectral model for rapid spectroscopic analysis for all elements.* High Energy Density Physics 2005. **1**: p. 3-12.
64. Ratko K., J.D., LangerDouglass E., PostJr.Kenneth EvansJr., *Elementary Processes in Hydrogen-Helium Plasmas Cross Sections and Reaction Rate Coefficients*. Atoms + Plasmas, ed. S. Series. 1987.
65. Chen, Z., et al., *Deuterium transport and retention properties of representative fusion blanket structural materials.* Journal of Nuclear Materials, 2021. **549**: p. 152904.

66. Le Claire, A.D., *Permeation of Gases through Solids*. Defect and Diffusion Forum, 1991. **33**: p. 1-0.
67. Liu, F., et al., *Deuterium gas-driven permeation and subsequent retention in rolled tungsten foils*. Journal of Nuclear Materials, 2014. **455**(1): p. 248-252.
68. Frauenfelder, R., *Permeation of Hydrogen through Tungsten and Molybdenum*. The Journal of Chemical Physics, 1968. **48**(9): p. 3955-3965.
69. Wirth, B.D., *Measuring and Modeling Helium Accumulation in Single Crystal Tungsten Specimens Exposed to He pLasma Discharges in WEST Reciprocating collector Probe*, in *IAEA-FEC*. 2020.
70. Leonard, A.W., *Edge-localized-modes in tokamaks*. Physics of Plasmas, 2014. **21**(9).

Appendix

Light sphere calibration curve values

Wavelength (nm)	Spectral Radiance [W/(sr cm2 nm)]
350	8.679E-07
360	1.147E-06
370	1.443E-06
380	1.887E-06
390	2.376E-06
400	2.987E-06
410	3.691E-06
420	4.453E-06
430	5.254E-06
440	6.125E-06
450	7.071E-06
460	8.132E-06
470	9.196E-06
480	1.029E-05
490	1.143E-05
500	1.261E-05
510	1.381E-05
520	1.503E-05
530	1.628E-05
540	1.755E-05
550	1.886E-05
560	2.011E-05
570	2.135E-05
580	2.258E-05
590	2.388E-05
600	2.498E-05
610	2.627E-05
620	2.755E-05
630	2.871E-05
640	2.989E-05
650	3.103E-05
660	3.211E-05
670	3.313E-05
680	3.414E-05

690	3.512E-05
700	3.603E-05
710	3.687E-05
720	3.772E-05
730	3.842E-05
740	3.907E-05
750	3.959E-05
760	4.012E-05
770	4.061E-05
780	4.115E-05
790	4.162E-05
800	4.208E-05
810	4.246E-05
820	4.280E-05
830	4.304E-05
840	4.337E-05
850	4.369E-05
860	4.401E-05
870	4.430E-05
880	4.461E-05
890	4.487E-05
900	4.521E-05
910	4.551E-05
920	4.569E-05
930	4.577E-05
940	4.583E-05
950	4.605E-05
960	4.620E-05
970	4.631E-05
980	4.637E-05
990	4.643E-05
1000	4.648E-05
1010	4.649E-05
1020	4.643E-05
1030	4.621E-05
1040	4.594E-05
1050	4.579E-05
1060	4.553E-05

1070	4.521E-05
1080	4.489E-05
1090	4.468E-05
1100	4.425E-05

Vita

Wendy Angelica Garcia was born and raised in El Paso, TX. She attended Mission Early College High School where she received an Associate of Arts degree with concentration in Physics along with her high school diploma. She formed part of the school's FIRST robotics team for two years becoming the mechanical engineering team captain in her senior year. After high school she attended New Mexico State University where she received a Bachelor of Science in Physics, a minor in Math, and another minor in Astronomy. After completing undergraduate school Wendy moved to Knoxville, TN to pursue a Doctor of Philosophy degree in Nuclear Engineering. Her research consisted of laser ablation mass spectrometry and laser induced breakdown spectroscopy characterization of fusion materials as well as investigation of helium-hydrogen synergies in tungsten under fusion conditions. She will continue her research career at Sandia National Laboratories where she will pursue Ion Beam Analysis research and continue work on fusion materials.